TRACE GAS TRANSPORT IN THE UT/LS

SEASONALITY, STRATOSPHERE-TROPOSPHERE EXCHANGE AND IMPLICATIONS FOR THE EXTRA-TROPICAL MIXING LAYER DERIVED FROM AIRBORNE O_3 AND H_2O MEASUREMENTS

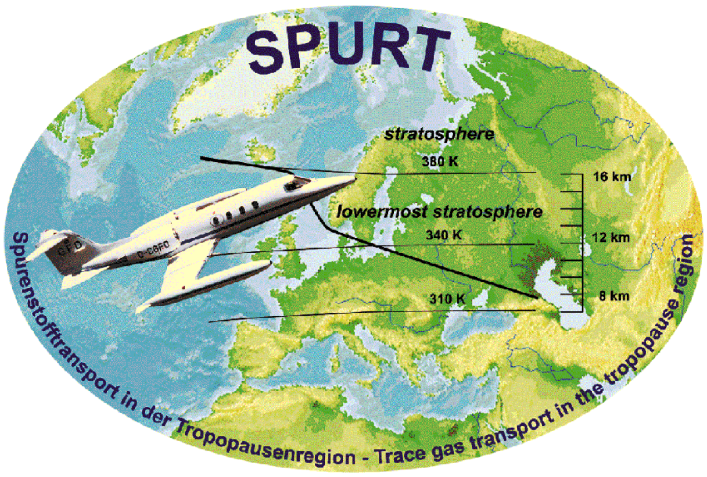

Dissertation

for the acquisition of the doctor degree (Dr. rer. nat.)
of the Faculty C: Mathematics and Natural Sciences
University of Wuppertal

submitted by

Marc Krebsbach

March 2005

prepared at the

Institute for Chemistry and Dynamics of the Geosphere I: Stratosphere
Research Centre Jülich

WUB-DIS 2005-03

UNIVERSITY OF WUPPERTAL
FACULTY OF MATHEMATICS AND NATURAL SCIENCES

1st supervisor	:	Prof. Dr. Martin Riese University of Wuppertal and Institute for Chemistry and Dynamics of the Geosphere: Stratosphere, Research Centre Jülich
2nd supervisor	:	Prof. Dr. Heini Wernli Institute for Atmospheric Physics, Johannes Gutenberg University Mainz
Day of submission	:	30. March 2005
Day of oral examination:		30. May 2005

para Glua-Lua,

a verdadeira amiga da minha vida,

a rainha dos provérbios

Abstract

This doctoral thesis gives new insights into the trace gas transport in the tropopause region and in processes controlling the chemical composition of the upper troposphere and lowermost stratosphere (UT/LMS). It thus contributes to an improved understanding of the governing processes in that atmospheric region. Several questions are addressed concerning the seasonal and latitudinal coupling between UT and LMS, trace gas distribution and variability, identification of undergoing transport and mixing processes and their impact to the trace gas composition. This will be achieved by airborne high resolution *in situ* measurements as well as by model calculations.
In the experimental part of this thesis, I performed airborne high resolution *in situ* measurements of H_2O and O_3 in the UT/LMS in the frame of the AFO 2000 project SPURT. The analysing components in this work focus on these measurements in the European sector between November 2001 and July 2003. As a milestone for an innovative campaign concept, SPURT is the first project in the UT/LMS with an extensive data coverage of each annual season within a broad latitude range between 20 and $80°$N. In several campaigns, distinct cross-tropopause exchange events and characteristic features for specific meteorological situations could be identified. Significantly enhanced H_2O of several 10 ppmv near the tropopause and even higher up in the LMS have been year-round detected. For a comprehensive insight into processes and trace gas variability, correlations, frequency distributions as well as 2-dimensional probability distribution functions were determined using chemical, thermal and dynamical coordinates. Beneath the reflected seasonal cycles of H_2O and O_3 in the UT and LMS in the distributions, both trace gases show the most compact arrangement and are best correlated in the view of potential vorticity (PV) and distance to the tropopause.
Using tracer distributions in the potential temperature/equivalent latitude space and trajectory calculations, an extra-tropical mixing layer (ML) following the shape of the tropopause and/or surfaces of PV could be identified. This layer with H_2O mixing ratios well above 5 ppmv, indicative for significant tropospheric contribution, ranges several $10°$ poleward in equivalent latitude and several 10 K above the tropopause in potential temperature. Using tracer-tracer correlations, the extent of the ML is estimated to reach to $\approx 8-9$ PVU, i.e. well within the LMS, independent on season. Based upon Lagrangian long-term simulations using the Jülich CLaMS model, tropospheric influence with enhanced H_2O values even beyond this ML could be reproduced which originates from transport processes on longer time scales.
Based upon Northern Hemisphere ECMWF analyses, a quasi 2-year "climatology" of H_2O and meteorological parameters at the tropopause is performed to compare to the *in situ* measurements and to put the observed data in a climatological context. The seasonal cycle of H_2O in the LMS is mainly determined by its entry value at the tropopause, and thus by seasonal and latitudinal variability of tropopause temperatures. The highly variable H_2O is traceable to temperatures the air parcels suffered recently. In conjunction with backward trajectories, the SPURT measurements indicate occurrence of and potential for (super)saturation and cirrus cloud formation in and even above the tropopause region. Hence, observed troposphere-to-stratosphere transport (TST) is probably associated with freeze-drying. Using the RDF technique in a case study, fine scale sub-synoptic structures in fields of PV and ice saturation, which are not resolved by the used meteorological analyses, were reconstructed successfully. Thereby, TST and ongoing freeze-drying in the UT/LMS could be identified.
The high resolution SPURT measurements contribute significantly to the data coverage of the UT/LMS and provide thus a basis for model approaches. O_3 climatologies obtained during SPURT were used for CLaMS initialisations to study the seasonal tracer variability relative to the jet core. Thereby, jet stream maximum wind speeds are used as a natural coordinate centre. Besides the effectiveness of the jet as a barrier to quasi-isentropic transport, it is investigated in which manner the strength is linked to the observed distributions and tracer gradients. Quasi-isentropic transport is most efficiently inhibited by the jet stream in winter, whereas during summer young tropospheric air from the (sub-)tropics is transported into the LMS. Due to the integral effect, the respective consequences are most evident at the end of each period, i.e. during spring and autumn.

Zusammenfassung

Die vorliegende Dissertation gibt neue Einsichten in den Spurengastransport in der Tropopausenregion und in Prozesse, die die chemische Zusammensetzung der oberen Troposphäre und unteren Stratosphäre (UT/LMS) bestimmen. Die Arbeit trägt damit zu einem besseren Verständnis der vorherrschenden Prozesse in dieser atmosphärischen Region bei. Verschiedene Fragestellungen werden erörtert, wie saisonale und breitenabhängige Kopplung zwischen UT und LMS, Spurengasverteilung und -variabilität, Identifikation der zugrunde liegenden Transport- und Mischungsprozesse sowie deren Einfluss auf die atmosphärische Spurengaszusammensetzung.
Im experimentellen Teil der vorliegenden Dissertation führte ich im Rahmen des AFO 2000 Projektes SPURT hoch aufgelöste flugzeuggestützte *in situ* Messungen von H_2O und O_3 in der UT/LMS durch. Die Auswertungen in dieser Arbeit basieren auf diesen Messungen im europäischen Sektor zwischen November 2001 und Juli 2003. Mit einem innovativen Kampagnenkonzept liefert SPURT als erstes Projekt einen qualitativ hochwertigen Datensatz mit umfassender saisonaler Abdeckung über einen Breitenbereich von 20 bis $80°$N. In mehreren Kampagnen konnten verschiedene Austauschereignisse durch die Tropopause und charakteristische Strukturen für bestimmte meteorologische Situationen identifiziert werden. Erhöhtes H_2O von einigen 10 ppmv nahe der Tropopause und in der LMS wurde ganzjährig detektiert. Für einen umfassenden Einblick in Prozesse sowie räumliche Spurengasvariabilität wurden Korrelationen, Häufigkeits- sowie 2-dimensionale Wahrscheinlichkeitsverteilungen unter Verwendung chemischer, thermischer und dynamischer Koordinaten erstellt. Neben saisonalen Spurengaszyklen in der UT und LMS zeigen die Verteilungen kompakteste Strukturen und beste Korrelationen in Abhängigkeit von potentieller Vorticity (PV) und Abstand zur Tropopause.
Spurengasverteilungen im Raum der potentiellen Temperatur und der äquivalenten Breite sowie Trajektorienrechnungen zeigen die Existenz einer extra-tropischen Mischungsschicht, die der Tropopause bzw. PV-Flächen folgt. Diese Mischungsschicht, mit einer strengen troposphärischen Kopplung, erstreckt sich einige $10°$ polwärts in äquivalenter Breite und einige 10 K in potentieller Temperatur über die Tropopause. Mittels Spurengaskorrelationen wurde kürzlicher troposphärische Einfluss bis weit in die LMS auf $\approx 8-9$ PVU abgeschätzt, unabhängig von der Jahreszeit. Langzeitsimulationen mit dem Jülicher CLaMS Modell konnten diesen Einfluss auch oberhalb der Mischungsschicht auf größere Transportzeitskalen zurückführen.
Für eine Vergleichsbasis der *in situ* Messungen und deren klimatologische Einordnung wurde auf Basis nordhemisphärischer ECMWF Analysen eine etwa 2-jährige "Klimatologie" von H_2O und Parametern an der Tropopause erstellt. Der H_2O-Zyklus ist primär durch Eintrittswerte an der Tropopause bestimmt und somit durch saisonale und breitenabhängige Temperaturänderungen. Die H_2O-Variabilität ist demnach über die Temperaturhistorie der Teilchen verfolgbar. In Verbindung mit Rückwärtstrajektorien wurde der Einfluss von Transport durch die extra-tropische Tropopause untersucht. Die SPURT Messungen zeigen Auftreten von und Potential für (Über-)Sättigung und Zirrenbildung in und oberhalb der Tropopausenregion. Dies indiziert, dass Troposphären-Stratosphären Transport (TST) mit Gefriertrocknung verbunden ist. Anwendung der RDF-Technik auf Felder der PV und der Eissättigung konnte feinskalige Strukturen, die in den verwendeten meteorologischen Analysen nicht aufgelöst werden, erfolgreich rekonstruieren. Daneben wurden TST und frische Gefriertrocknungsprozesse in der UT/LMS identifiziert.
Die hoch aufgelösten SPURT-Messungen tragen erheblich zur Datenabdeckung der UT/LMS bei und liefern einen Grundstock für Modellsimulationen. Die gewonnenen klimatologischen O_3-Verteilungen wurden in CLaMS initialisiert, um die saisonale Spurengasvariabilität relativ zum Strahlstrom (Jet) zu studieren. Neben der Effektivität des Jets als quasi-isentrope Transportbarriere untersucht die Studie den Einfluss der Jetstärke auf die beobachteten O_3-Gradienten. Dabei dient der Jetkern als Ursprung eines natürlichen Koordinatensystems. Quasi-isentroper Austausch wird im Winter effektiv reduziert, wobei im Sommer junge troposphärische Luft aus den (Sub-)Tropen in die LMS transportiert wird. Die jeweiligen Auswirkungen werden aufgrund des integralen Effekts zum Ende einer Periode, das heißt im Frühling und Herbst, am deutlichsten.

Contents

List of Figures

List of Tables

Chapter 1

Introduction

Human activity and its impact on climate has significantly increased with the beginning of the Industrial Age. Related keywords are ”global warming” and ”ozone hole”. The relevant effects and changes have direct and indirect response to fauna, flora and human being. Beneath the Montréal Protocol (1987), the Kyoto Protocol, which has very recently gone into force on February 16, 2005, is the most important global environmental agreement. Alongside its relevance as a milestone in global climate protection, concerning development politics, it has large effects and it is a new element of global-economic order. A challenging task for scientists is to analyse consequences of and responses to past and future activities and to provide solutions for tomorrow. On this account it is essential to understand the contributing factors and the governing processes in nature.

1.1 Water vapour, ozone and atmospheric dynamics

Water vapour (H_2O) and ozone (O_3) are the most important and major absorbers of solar irradiance and emitters/absorbers of terrestrial radiation. They play therefore a prominent role for the radiative budget of several atmospheric regions, for chemistry and climate. Water vapour has its main source at the Earth’s surface and has no harmful consequences there. In the atmosphere it is an important greenhouse gas. On average, the Earth’s surface is above the freezing-level as a result of the ”natural” greenhouse effect mainly produced by water vapour in the atmosphere. Concerning the positive and/or negative radiative feedback mechanisms of water vapour, in particular for climate prediction, the understanding of water vapour distributions is a deciding issue in atmospheric research. For instance, increasing air traffic and the increase in atmospheric aerosols has large effects on climate conditions. As a direct effect, aerosols reflect incoming solar radiation, thus cooling the Earth’s surface. Since aerosols act as condensation nuclei for water vapour, increasing atmospheric aerosols en-

hance cirrus cloud formation. This indirect effect leads to a warming at the Earth's surface. Persistent cirrus, in particular in regions with cold temperatures and high atmospheric humidity, can have an additional greenhouse effect. In the global mean, a gain in energy for the atmospheric radiation budget is supposed, however there are still large uncertainties (IPCC, 1999, 2001). Moreover, stratospheric water vapour has increased over the last decades (SPARC, 2000) which can attribute to stratospheric cooling (Forster and Shine, 1999). Several global warming scenarios (e.g., Lindzen, 1990; Rind et al., 1991; Yang and Tung, 1998; Inamdar and Ramanathan, 1998) discussed the impact of enhanced surface temperatures. They may lead to greater evaporation and to an elevating amount of water vapour, thus increasing the absorption of outgoing terrestrial radiation. Despite that, the accrete of dry large-scale subsidence regions can contribute to a delay of greenhouse warming due to the deficit in absorbed radiation (Pierrehumbert, 1995).

The penetration of shortwave solar UV (ultraviolet) radiation in the UVB ($280 - 320$ nm) and UVC (> 220 nm) is hindered by O_3 in the atmosphere to reach the Earth's surface. The ozone layer acts as the primary shield against the biologically damaging solar UV radiation. Absorption of UV radiation by O_3 leads to a conversion of energy to heat. Hence, temperatures increase with height in the stratosphere. Decreases in stratospheric ozone enhances solar UVB at the Earth's surface and can thus aggravate detrimental effects on life. Moreover, changes in atmospheric O_3 are also important for climate change. As direct effects, a decrease in stratospheric O_3 has a negative radiative forcing, leading to a reduction of the vertical stability in that atmospheric region (Rind and Lonergan, 1995), whereas increase in tropospheric O_3 implies a positive radiative forcing. Furthermore, there are indirect effects such as e.g., an increase in certain photolysis rates which affect tropospheric O_3 and its oxidation capacity.

At almost all Northern Hemisphere ozone stations at middle and high latitudes significant decreases in stratospheric ozone were observed from 1970 to 1990 (Logan et al., 1999), and this was also reported on the global scale by Fioletov et al. (2002). The observed ozone trend may be explained by several contributing processes. For instance, an observed increase in Arctic tropopause height was related to stratospheric cooling (Highwood et al., 2000). Changes in tropopause heights can affect the ozone column, since a low tropopause is correlated with high total O_3 and vice versa (Steinbrecht et al., 1998; Forster and Tourpali, 2001). A further dynamic cause could be an increased transport of O_3-poor air from lower to higher latitudes (Reid et al., 2000). Additionally, chemical O_3 destruction should be important, especially during winter within the polar vortex with a subsequent downward and equatorward transport (Bregman et al., 2000). Since H_2O is an important source of odd hydrogen, enhanced H_2O increases the O_3 loss rates in the HO_x (reactive hydrogen) catalytic cycles (Dvortsov and Solomon, 2001). The participation of H_2O and nitrogen oxides (NO_x)

compounds in heterogeneous chemical reactions, and particularly at high latitudes in winter, reactions on Polar Stratospheric Clouds and chlorine activation can take place controlling ozone destruction in the stratosphere. Cirrus clouds near and above the tropopause have the ability to enhance the conversion of chlorine reservoir species ($ClONO_2$ and HCl) into active, ozone destroying molecules (ClO) (Solomon et al., 1997). In the upper troposphere (UT), ozone and chlorine reservoir species have minimal concentrations. Therefore, the potential of the conversion mechanism is critically dependent on the penetration of clouds into the stratosphere (Pfister et al., 2003). Thus, cold aerosols and/or cirrus clouds can affect the catalytic destruction of ozone at mid-latitudes (Solomon et al., 1999). A detailed review concerning O_3 trends is given by Staehelin et al. (2001).

In a large-scale perspective, the meridional circulation is characterised by the so called Brewer-Dobson circulation (Brewer, 1949). Non-locally Rossby and gravity wave breaking in the extra-tropical middle atmosphere act as an extra-tropical ”suction pump”, leading to the so termed downward control principle (Haynes et al., 1991). It causes up-welling of tropical upper tropospheric air into the stratosphere (Plumb, 1996; Mote et al., 1996), transport within the stratosphere to the extra-tropics (Waugh, 1996) and downward transport from the stratosphere into the troposphere at middle and higher latitudes (Holton et al., 1995). To account for the tropical up-welling the wave breaking must extend into the sub-tropics (Plumb and Eluszkiewicz, 1999).

Hoskins (1991) structured the lower atmosphere in three major parts. In the region above the 380 K isentrope, which coincides with the tropopause in the tropics depending on cloud top heights ($\approx 15-18$ km, Holton et al., 1995; Highwood and Hoskins, 1998; Seidel et al., 2001), surfaces of potential temperature lie entirely in the stratosphere. This part of the atmosphere was termed ”overworld”. Towards the poles the tropopause slopes down to $290-320$ K ($\approx 6-8$ km). Thus, in the ”middle world” isentropes lie partly in the troposphere (in the tropics) and partly in the stratosphere (at high latitudes), hence intersecting the tropopause which separates the stratosphere and the troposphere. Quasi-isentropic bi-directional stratosphere-troposphere exchange (STE) is enabled on relative fast time scales (Chen, 1995). The atmospheric region below was termed as the ”underworld”. Holton et al. (1995) defined the stratospheric part of the middle world as the lowermost stratosphere, more precisely the lowermost extra-tropical stratosphere, hereafter referred to as LMS. Transport from the overworld to the troposphere and vice versa requires diabatic cooling and heating, respectively, which implies transport processes on larger time scales. At the extra-tropical tropopause a strong isentropic gradient of potential vorticity (PV) implies a strong Rossby wave ”restoring force”, and Rossby waves tend to follow the strongest PV gradient. This limits cross-tropopause displacements of air even on isentropes. A sketch of

transport pathways between the lowermost stratosphere and the troposphere is illustrated in Figure 1.1.

The global ozone distribution is essentially conditioned by its production and transport mechanisms. The fundamental production rates occur in the tropics due to the strong solar insolation. With the Brewer-Dobson circulation ozone is transported poleward and downward. Thus, extra-tropical ozone has its main source in the stratospheric overworld. The fact that the whole stratosphere is extremely dry is related to the passing of air through the cold regions at the tropical tropopause. There the air is freeze-dryed to the ice saturation mixing ratio corresponding to the low temperatures. Thereby, this water vapour signal is maintained by the air parcels on their transport pathways. Hence, seasonal differences in tropical tropopause temperatures are recorded by the atmosphere as a layering of H_2O mixing ratios up to heights at 20 hPa (atmospheric tape recorder, Mote et al., 1996; Jackson et al., 1998).

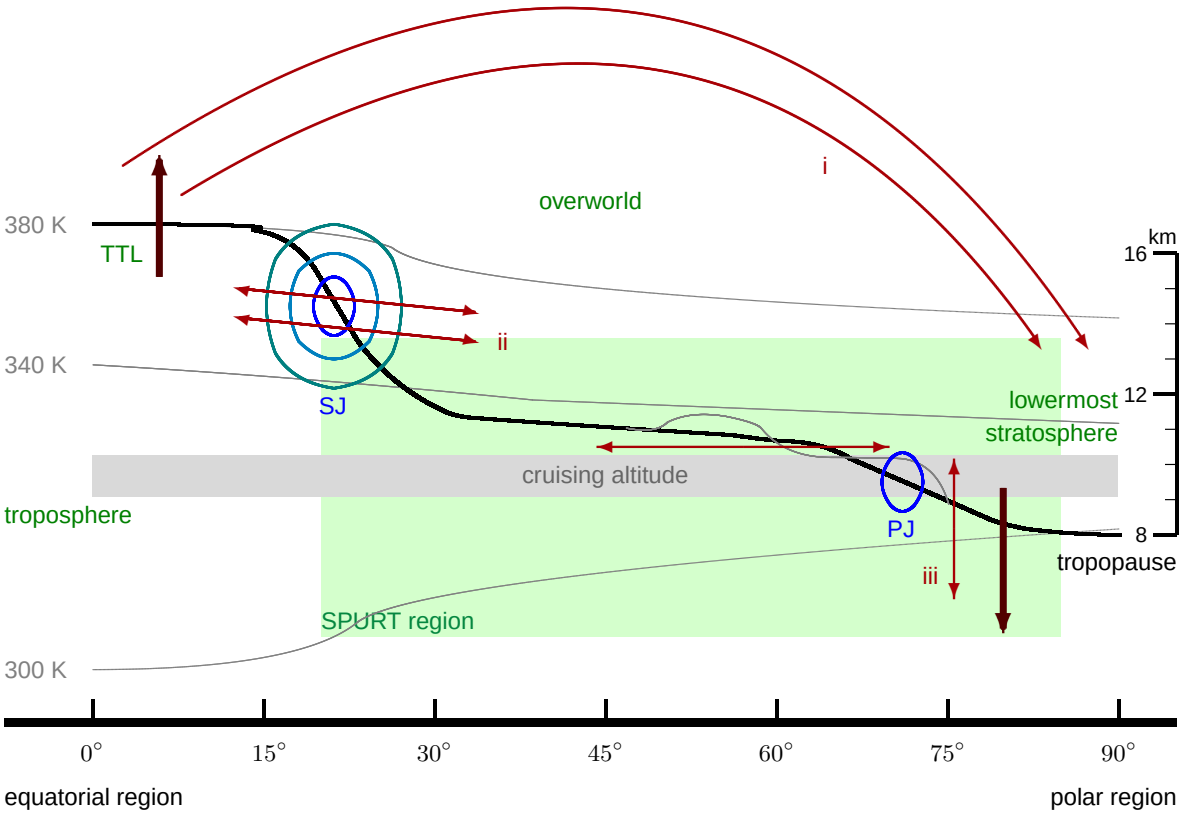

Figure 1.1.: Sketch of the mean atmosphere (cf. Holton et al., 1995; Hintsa et al., 1998). Thin grey lines denote different isentropes, the thick black line reflects the tropopause with the troposphere below that surface. The lowermost stratosphere is defined to range from the tropopause up to ≈380 K, the mean tropical tropopause height. The overworld is the region above that isentrope, where surfaces of potential temperature lie entirely in the stratosphere. Stratosphere-troposphere exchange via the Brewer-Dobson circulation from the tropical transition layer (TTL) to the polar regions is indicated by the thick dark red arrows. Thin red arrows denote different pathways by which air enters the lowermost stratosphere as well as of bi-directional exchange: (i) descend from the overworld, (ii) quasi-isentropic transport from and to the upper troposphere, (iii) diabatic ascent/descend (e.g., convection, stratospheric intrusion). The thin grey line around the mean tropopause at mid-latitudes reflects tropopause deformations, most probably associated with the polar front, so that pathway (ii) is also possible at these latitudes. The sub-tropical and polar jet streams (SJ, PJ) are illustrated by the coloured ellipses, reflecting their strength. The operation region during the SPURT project (see chapter 2) is denoted by the greenish shading. The usual cruising altitude of passenger aircraft is reflected by the light grey shading.

However, zonal mean tropical tropopause temperatures can not explain the extreme dryness of the stratosphere. Thus, Newell and Gould-Steward (1981) suggested transport within so called stratospheric fountains, i.e. restricted regions of very low tropopause temperatures. Within the large-scale ascent in the tropical tropopause region dehydration can also be realised by the formation of widespread (sub-visible and ultrathin) cirrus clouds which have been detected recently (Jensen et al., 1996b; McFarquhar et al., 2000; Peter et al., 2003; Luo et al., 2003). Dehydration mechanisms by gravity waves triggering stratospheric cloud formation upwind of convective regions (Potter and Holton, 1995) are also considered. Anyhow, in tropical cyclones (Baray et al., 1999) or through breaking Kelvin waves (Fujiwara et al., 1998) there could also occur tropical transport directed from the stratosphere to the troposphere.

The tropopause in the extra-tropics is not impermeable to bi-directional transport. Synoptic- and meso-scale processes are frequently combined with injection of stratospheric air into the troposphere. Stratosphere-to-troposphere transport (STT) was observed in association with tropopause folding events near both the polar jet (PJ, e.g., Danielsen, 1968; Vaughan et al., 1994; Langford et al., 1996) and the sub-tropical jet (SJ, e.g., Baray et al., 2000). As part of baroclinic wave life-cycles, STT has further been detected within filamentation events (e.g., Bithell et al., 1999) and cut-off lows in regions of upper-level troughs (e.g., Danielsen and Hipskind, 1980; Shapiro, 1980; Ancellet et al., 1991; Price and Vaughan, 1993; Eisele et al., 1999). Inflow of stratospheric air into the troposphere was also evidenced to occur in the presence of clouds with associated latent heat release (Lamarque and Hess, 1994; Wirth, 1995). Additionally, breaking gravity waves can effectuate STT (Lamarque et al., 1996). This transport was further observed within meso-scale convective complexes (Poulida et al., 1996). Deep subsidence of stratospheric intrusions into the troposphere have been observed by Stohl and Trickl (1999). These can enhance O_3 concentration in the boundary layer (Stohl et al., 2000; Wernli and Bourqui, 2002) and also affect tropospheric chemistry and subsequently the radiation budget (e.g., Roelofs and Lelieveld, 1997). Generally, filamentary structures form and cascade down to smaller scales (Appenzeller et al., 1996a). STT processes are very intermittent and a variety of mechanisms has been identified.
Extra-tropical troposphere-to-stratosphere transport (TST) has also been observed, albeit less frequent. However, many observations show relatively moist regions in the LMS which evidence for transport via extra-tropical paths. Model studies by Rood et al. (1997) and Zierl and Wirth (1997) suggest radiative effects, especially in anticyclones, to induce upward transport. Meso-scale high reaching complexes, as considered by Poulida et al. (1996) or Wang (2003), can contribute to TST by overshooting the tropopause at the anvil outflow or through breaking of gravity waves above cumulus clouds, respectively. The high stability of the LMS requires a large increase in potential temperature to establish TST. Radiative heat-

ing, however, can not affect this. Thus, tropospheric injections do typically not reach high stratospheric levels and especially not the overworld. Anyhow, Stohl (2001) and Wernli and Bourqui (2002) accentuate rapid transport of tropospheric air into the lower stratosphere, established by so called warm conveyor belts (Wernli and Davies, 1997).
Due to the generally large-scale downward transport in the extra-tropics, TST has to be considered against that background (Haynes et al., 1991). The LMS is hence an atmospheric region where the trace gas composition is a mixture of aged stratospheric overworld air and recently intruded tropospheric air. In the recent years a so called mixing layer just above the tropopause has been identified (Fischer et al., 2000; Dethof et al., 2000; Zahn, 2001; Hoor et al., 2004c). This layer is rather an extra-tropical transition layer where upward transported tropospheric air is mixed with down-welling stratospheric air. Tracer-tracer correlations have been used to infer information on mixing (Fischer et al., 2000; Parrish et al., 2000; Zahn, 2001). However, correct quantification as well as the amount and seasonality of mixing is still a challenging task.
Model climatologies by James et al. (2003b) and Sprenger and Wernli (2003) infer net STT only in the sub-tropics and at middle latitudes. Net TST was derived in the polar regions. From analyses of balloon-borne *in situ* measurements Ray et al. (1999) deduced strongest transport from the overworld during spring and transport of tropospheric air into the LMS being probably most efficient during autumn.

In contrast to the well-known cycle of the large-scale downward circulation as well as the boundary conditions of water vapour and ozone in the overworld, there are large uncertainties concerning transport processes across the lower boundary of the LMS, in particular at the extra-tropical tropopause (Pan et al., 1997). Ozone and water vapour are suitable trace gases to investigate and understand processes in the UT/LMS. Stratospheric trace gas distributions depend strongly on the interaction between dynamical and chemical processes near the tropopause, since this part of the atmosphere is to a large extent affected by dynamics, in particular by STE. Changes in the chemical composition of the UT/LMS region have a strong impact on atmospheric radiation. A detailed understanding of the governing processes, particularly the variability, the chemical composition and the transport processes of natural and anthropogenic emissions, is especially essential to assess important implications for climate and life conditions. The upper troposphere and lowermost stratosphere and especially the tropopause region is thus of severe scientific interest.

1.2 Overview of this thesis

The objective of this doctoral thesis is to contribute to an improved understanding of the governing processes in the UT/LMS. To identify and quantify atmospheric transport processes

it is profitable in experimental field campaigns to record as many species as possible with different sources and sinks. At the ICG-I of the Research Centre Jülich specific instruments were developed or modified for implementation on research aircraft. These are in particular the FISH (Zöger et al., 1999) and the JOE (Mottaghy, 2001) instruments measuring total water and ozone, respectively. As part of this thesis, high resolution *in situ* measurements of these species were performed within the SPURT project. The project in the European area was especially designed to establish a climatology of trace gas composition in the UT/LMS without focussing on special meteorological events. A total of 8 airborne measurement campaigns, evenly distributed over 2 years, were performed to obtain a sufficient amount of data to analyse ongoing processes in the UT/LMS region. A campaign overview is given in chapter 2.

Based on this data set seasonal cycles of measured O_3 and H_2O are analysed in chapter 3. To get a comprehensive insight into processes and trace gas variability in the region of the UT/LMS, the measurements are put into the frame of different reference coordinates. Thereby, especially 2-dimensional probability distribution functions serve as a powerful tool to illustrate and investigate the seasonal trace gas distribution with high spatial and temporal variability.

Using a distinct coordinate system, which is especially favourable for climatological objectives, the measured O_3 and H_2O data are represented in chapter 4. Using this coordinate system, spanned by potential temperature and equivalent latitude, characteristic trace gas distributions and seasonal differences in transport processes are inferred. An extended part in chapter 4 deals with characteristics of the extra-tropical mixing layer. Tracer-tracer correlations of measured and model-derived parameters are used to estimate the seasonal extent of that layer into the LMS and how its isentropic thickness varies with season. The studies are supported by extensive 3-dimensional trajectory studies with the Jülich CLaMS model (e.g., McKenna et al., 2002b). For this, a preprocessor to derive the isentropic vertical velocity in a more precise approach was designed, which works more sufficient, especially in the tropopause region.

A quasi 2-year "climatology" of H_2O and meteorological parameters at the tropopause based upon Northern Hemisphere ECMWF analyses is introduced in chapter 5. Thereby, the H_2O *in situ* measurements are related and compared to the model climatology. Especially, the amount of H_2O entering the LMS is assessed. During the SPURT campaigns significantly enhanced H_2O of several 10 ppmv near the tropopause and even higher up in the LMS has been detected during all seasons. Concerning supersaturation and cirrus cloud formation in the tropopause region and in the LMS as well as the tropospheric ozone budget, effects of TST and STT are discussed in chapter 6, respectively. In conjunction with the former, the RDF technique is applied in chapter 7 to analyse a specific flight during SPURT in more detail. Within this mission significant saturation in the LMS was encountered.

The derived climatologies for O_3 during SPURT are used in a long-term simulation with CLaMS in chapter 8. In this model run, purely based on transport and mixing, the effectiveness of the sub-tropical jet as a barrier to quasi-isentropic transport is studied. To account for this aspect, a natural coordinate centre based upon maximum jet stream wind speeds is used. Thereby, it is investigated how the observed trace gas distributions and gradients are linked to the jet stream strength.
Conclusions with future objectives are given in an extended summary in chapter 9.

It should be mentioned that within this thesis the annual seasons winter, spring, summer, and autumn are considered as the month-triples December, January, February (DJF), March, April, May (MAM), June, July, August (JJA), and September, October, November (SON), respectively. Statements given for seasons are related to measurements during these months. Even when using backward trajectories this terminology is maintained. This is justified since (i) the backward trajectory calculations are performed for a maximum of 30 days and (ii) the air parcels are never initialised within the first month of each season.

Chapter 2

SPURT - trace gas transport in the tropopause region

Satellite observations are a powerful tool for a global data coverage of the whole atmosphere. However, there are several disadvantages and limitations given by nature and technology. For instance, clouds provide a handicap for some trace gas measurements in the UT/LMS. The spatial resolution, particularly in the vertical, is restricted by technological facilities and not sufficient enough to resolve fine-scale structures. Due to the limitations and the lack of satellite measurements in this atmospheric region, high sensitive and high resolution observations of the UT/LMS can only be provided by aircraft, balloon or even rocket *in situ* measurements. Observations over limited geographical regions, different height regimes and seasons offer a suitable data base for case and process studies as well as for the generation, evolution and variability of atmospheric trace gas distributions. Despite the lower spatial coverage due to the 1-dimensional measurements along the individual flight tracks, data compositions (e.g., Emmons et al., 2000) enable a compilation of trace gas climatologies. A further advantage is the coverage of a wide range of spatial scales (local, meso and even global scale). Obtained tracer distributions and variability can be compared to satellite measurements. Additionally, the data benefit for implementation and initialisation in models, e.g., to compare to tracer variability, particularly in models with Lagrangian transport and mixing parameterisations, such as CLaMS (e.g., McKenna et al., 2002b). Accurate description and representations of tracer gradients in the tropopause region are especially important for the chemical and radiative balance of climate simulations (McLinden et al., 2000).

In the recent years and decades several projects using research aircraft were carried out to investigate the region of the UT/LMS concerning different objectives. Funded by the BMBF (German: Bundesministerium für Bildung und Forschung, German Ministry for Education and Research), the POLSTAR (polar stratospheric aerosol experiment) campaigns

in 1997 and 1998 were performed to investigate causes of O_3 loss near the polar tropopause and, in particular, the formation and composition of cirrus clouds. Objectives in the EU (European Union) campaigns STREAM (stratosphere-troposphere experiment by aircraft measurements, $1993-1998$) were the study of the chemical composition of the UT/LMS with latitude and season as well as the extent and role of cross-tropopause exchange. Thereby, the focus was on biomass burning emissions and the influence of transport of polar vortex air into the mid-latitudes. The BMBF funded project CONTRACE (convective transport of trace gases into the middle and upper troposphere over Europe, $2001-2003$) exploits the overall impact of convective processes on the distribution and budgets of trace gases in the UT over Europe, which is presently poorly known. Additionally, inter-continental transport of air pollution on the regional trace gas budget is addressed. A further recent EU campaign UTOPIHAN-ACT (upper tropospheric ozone: processes involving HO_x and NO_x, the impact of aviation and convectively transported pollutants in the tropopause region, $2002-2004$) investigates the influence of aviation and convectively transported pollution on O_3 in the UT. Whereas the above mentioned projects used more or less special research aircraft, the 1994 started program MOZAIC (measurement of ozone on airbus in-service aircraft, Marenco, 1998) and the project CARIBIC (civil aircraft for the regular investigation of the atmosphere based on an instrument container, $1997-2002$, from December 2004 up to now, Brennikmeijer et al., 2005) use commercial and passenger aircraft to measure routinely O_3, H_2O and other chemical species in the tropopause region. However, thereby only the lower part of the LMS is reached.

2.1 The SPURT project

A cutting edge for a new concept of aircraft based campaigns was introduced by the project SPURT (German: Spurenstofftransport in der Tropopausenregion, trace gas transport in the tropopause region). In the frame of AFO 2000 (German: Atmosphärenforschungsprogramm 2000, federal atmospheric research program 2000) the joint research project SPURT was funded by BMBF ($2001-2004$) under contract No. 07ATF27. Fast payload integration on the used aircraft and flexible flight-planning allowed short-term operational facilities to investigate specific meteorological events. The project with its aims, instrumentation and performance is introduced in more detail in the following.

2.1.1 Key objectives

The SPURT project intended to investigate dynamical and chemical transport processes in the region of the UT and LMS. The governing processes in that atmospheric region should

be studied within a broad latitudinal range from the sub-tropics to the Arctic. A further aim was to obtain a good seasonal coverage of airborne high resolution *in situ* measurements of chemical tracers. A sketch of the considered operational atmospheric region is indicated by the greenish shading in Figure 1.1 in chapter 1.

2.1.1.1 Experimental intentions

Major objective of the SPURT project was the data acquisition of a large set of trace gases with huge latitudinal and seasonal coverage in the UT/LMS. The climatological distribution and variability of chemical species with different sources, sinks and life times in the UT and LMS should be obtained by aircraft based measurements. Long-term observations should be performed by a series of short-term campaigns. Thus, special demands and requirements to the aircraft and the instrumentation had to be fulfilled (cf. subsection 2.1.2 and 2.1.3). Chemical species to sample were the tropospheric tracers total water (H_2O), carbon monoxide (CO), carbon dioxide (CO_2), nitrous oxide (N_2O), methane (CH_4), sulfur hexafluoride ($SF6$), and the chlorofluorocarbons CFC11 and CFC12. Stratospheric trace gases considered were nitric oxide (NO), total reactive nitrogen (NO_y) and ozone (O_3). This results in a total of 11 species. Beneath the collection of climatological data dedicated case studies should be performed.

2.1.1.2 Purposes of data analyses

The measurements provide the basis for various data analyses to investigate the state of the UT and LMS. Several scientific aspects should be addressed concerning the

- trace gas distribution and their variation as a function of latitude, altitude and season,
- degree of trace gas variability and the underlying processes,
- identification of these processes on the local, meso, and global scale,
- analyses of actual variability on these scales,
- assessment and causation of transport and mixing processes and their effects on trace gas budgets,
- coupling between the UT and the LMS with regard to latitude, altitude and season.

Beside the experimental analyses model application are applied to investigate atmospheric processes. Using the RDF (reverse domain filling, cf. chapter 7) technique in case studies

helps to interpret observations during flight missions and to identify recent stratosphere-troposphere exchange. With long-term simulation using the Jülich CLaMS dynamical causes, temporal evolution and trace gas structures on different scales are studied. Furthermore, coupling processes of dynamical and chemical processes in the tropopause region are examined using different chemical transport models. Beneath the analysing character, the data set with climatological distribution and variation of considered chemical species provide a valuable basis for modelling purposes, in particular to improve models and their parameterisations but also to compare to satellite data and tracer variability.
Additional aspects are covered by the theory group at the Johannes Gutenberg University of Mainz. The tropopause sharpness during baroclinic wave development is studied. Further, with the so-called contour-advective semi-Lagrangian (CASL) algorithm the evolution of passive tracers in the tropopause region is investigated with very high spatial resolution.

The large amount of information and, up to the present, the unique data set of high resolution *in situ* measurements of several chemical species in the European sector offers a vast quantity of potentialities and options for data analyses and investigations of scientific problems. Since the SPURT data set provides the basis for this thesis, several questions mentioned above are addressed.

2.1.2 Instrumentation and project partners

SPURT was a cooperative project of several institutes and companies. A total of 8 single 1-week measurement campaigns evenly distributed over all seasons were planned. In order to achieve a key objective of long-term observations from short-term campaigns a Learjet 35A, which was supposed to be appropriate for the campaign strategy, was equipped with high resolution *in situ* instruments. The Learjet 35A D-CGFD was provided by the company enviscope GmbH in co-operation with GFD (German: Gesellschaft für Flugzieldarstellung) in Hohn, Germany. The used aircraft is depicted in Figure 2.1 with some technical details. Depending upon the meteorological conditions, the aircraft's ceiling altitude is of ≈ 14 km and thus allows sampling in the lowermost stratosphere during all seasons, even at sub-tropical latitudes. Beneath the meteorological data recording, 6 instruments of 4 different research groups were integrated into the measurement platform to probe different tracers within the cross-sectional flights. A short overview of the instrumentation and participating institutes is given in Table 2-I.

Two instruments aboard the aircraft are in service of the ICG-I (Institute for Chemistry and Dynamics of the Geosphere I: Stratosphere) of the FZJ (German: Forschungszentrum Jülich, Research Centre Jülich GmbH). Total water (H_2O), measured as the sum of vapour and vaporised ice, was measured with the photofragment-fluorescence technique by the

Figure 2.1.: Aircraft used to perform the SPURT campaigns: Learjet 35A D-CGFD, provided by GFD (Hohn, Germany) in co-operation with the company enviscope GmbH (Frankfurt/Main, Germany). Some technical data are drawn in the photograph. Further information can be found under the uniform resource locater address `http://www.enviscope.de/home_campaign.html`. (Photo by M. Krebsbach)

Table 2-I: SPURT instrumentation on the Learjet 35A D-CGFD and responsible research groups. Additionally, the measurement principles with resolution and uncertainty (including precision and accuracy) are listed. Species which were measured twice during some flights are highlighted in bold letters. Abbreviations used are as following for the measuring principles: Ly-α ≡Lyman-α fluorescence, UVA≡UV absorption, TDLAS≡tunable diode laser absorption spectroscopy, NDIR≡non-dispersive infrared-absorption, CL≡chemiluminescence, GC≡gas chromatography. The SPURT partners are shortened as: FZJ≡Institute for Chemistry and Dynamics of the Geosphere I: Stratosphere of the Research Centre Jülich (Germany), MPI≡Max Planck Institute for Chemistry, Mainz (Germany), IACETH≡Institute for Atmospheric and Climate Science of the Swiss Federal Institute of Technology Zürich (Switzerland), and JWGU≡Institute for Meteorology and Geophysics, Johann Wolfgang Goethe University of Frankfurt/Main (Germany).

chemical species	**partner**	**instrument**	**principle**	**resolution in s**	**uncertainty in %**	**reference**
total H_2O	FZJ	FISH	Ly-α	1	< 3	Zöger et al., 1999
O_3	FZJ	JOE	UVA	10	5	Mottaghy, 2001
CO, **N_2O**, CH_4	MPI	TRISTAR	TDLAS	5	1.5, 1, 2.5	Wienhold et al., 1998
CO_2	MPI	LiCor-6262	NDIR	1	< 0.1	Gurk, 2003
NO, NO_y, **O_3**	IACETH	CLD 790 SR	CL	1	4.5, 16, 5	Hegglin, 2004
CO, CFC11/12, SF6, **N_2O**	JWGU	GHOST II	GC	90,45	< 1	Bujok et al., 2001

FISH instrument (fast *in situ* stratospheric hygrometer, Zöger et al., 1999). Ozone (O_3) was measured with UV absorption by the JOE instrument (Jülich ozone experiment, Mottaghy, 2001). For most flights (from the 3^{rd} campaign on), O_3 was additionally measured by the CLD 790 SR instrument of the IACETH (Institute for Atmospheric and Climate Science of the Swiss Federal Institute of Technology). A comparison of O_3 measurements by JOE and the CLD 790 SR show good agreements with a mean correlation coefficient of ≈ 0.99. No significant systematic differences were detected. Anyhow, a slight impact of photomultiplier temperatures of the CLD 790 SR to its O_3 signal is evident but not essential (Hegglin, 2004).

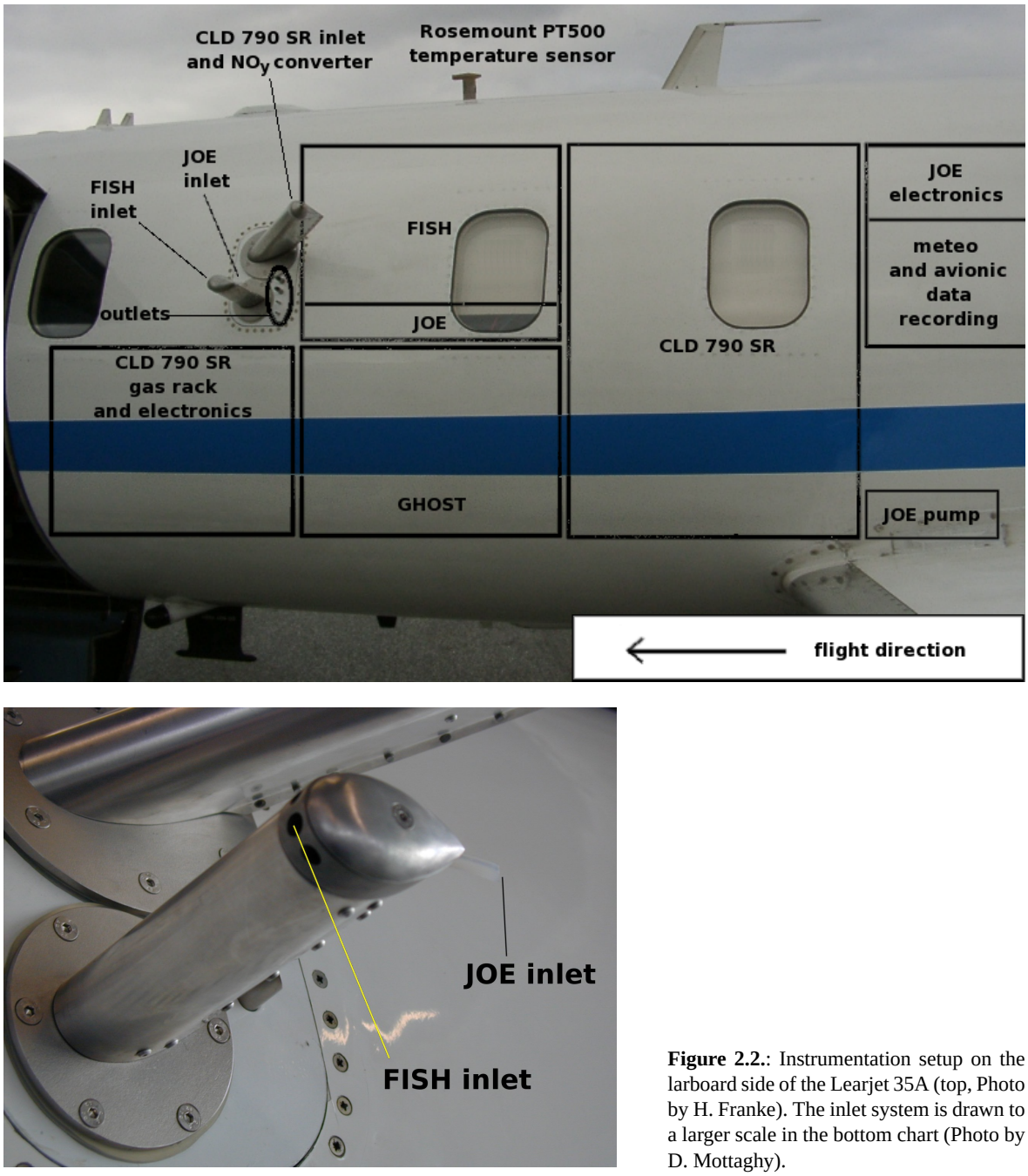

Figure 2.2.: Instrumentation setup on the larboard side of the Learjet 35A (top, Photo by H. Franke). The inlet system is drawn to a larger scale in the bottom chart (Photo by D. Mottaghy).

The approximate locations of the instruments on the larboard side of the Learjet 35A, including the equipment in service of the ICG-I, is shown in Figure 2.2. Whereas the flow and data recording system of the total water measurement instrument is totally integrated in the FISH, both components are separated for the ozone measurements by JOE. The FISH inlet is forward facing, the JOE inlet is backward facing with a PFA-teflon tubing to reduce artificial O_3 destruction by air contact with metallic surfaces. To ensure sufficient air convection in the flow system of JOE, an external pump is placed below the rack for the meteorological and avionic data recording system. The inlet system is drawn to a larger scale in the bottom chart in Figure 2.2.

2.1.3 Concept and campaign performance

Performance of long-term observations in short-term campaigns can only be established with a request of the aircraft on short notice and with integration of the instruments within a short time. The opportunity of a fast availability of the Learjet 35A, its medium range capability of ≈ 4000 km and a ceiling altitude of ≈ 14 km were outstanding advantages to achieve the project goals. The single campaigns should be seasonally distributed over 2 years. Thereby, each campaign should be carried out in a time frame of only 1 week to occupy the aircraft as short as possible, thus keeping costs low. The time period includes integration of the payload, performance of research flights, and de-installation of the equipment.
To keep the planned time schedule both the aircraft and the instruments have to fulfill specific conditions. The payload weight was restricted to ≈ 1000 kg. Thus, the instruments have to be implemented in special designed lightweight and robust racks and within fast-locking systems. Beneath the payload and the minimum flight crew, i.e. pilot and co-pilot, there was room for two additional operators aboard the Learjet 35A. After a preparation phase a test campaign with instrument integration as well as safety and electromagnetic compatibility tests was performed in April 2001, resulting in a successful certification and a short test flight.

The succeeding high-resolution *in situ* measurements of the set of trace gases listed in Table 2-I took place over Europe between November 2001 and July 2003. This main research part of the SPURT project was divided into 8 single campaigns with a duration of $5-6$ days. Main base was the military base in Hohn, northern Germany ($9.53°$E, $54.31°$N), where the Learjet 35A and the GFD is resident. On $2-3$ subsequent days, $4-6$ flights were carried out. On one day northbound flights, on the other southbound flights were performed. Thereby, the flight routes were restricted by aerial surveillance and aircraft restrictions. Each flight had a duration of about 4 hours, resulting in a total number of 147 flight hours. Details of the performed research flights are given in Table 2-II. Stop criterions of a flight mission or rather

a strong reduction of flight duration should be applied if neither GHOST II nor TRISTAR were operating or if no ozone measurements were available. However, only once a flight was shifted by one day due to problems with GHOST II.

With this innovative measurement concept, with fast integration and testing of the measurement equipment within $2-3$ days and a quick and flexible flight planning, a good seasonal coverage was obtained. Each annual season was investigated within 2 campaigns in the region around the polar jet covering a broad latitude range between $\approx 20-80°$N.

Table 2-II: Overview of the performed SPURT campaigns. Listed are the campaign with the corresponding time period, the flight day, locations of take off (TO) and touch down (TD), the covered longitudinal and latitudinal range as well as the flight duration. In the last row the single flight times are summed up. The flight times are given in the format hours:minutes. The used abbreviation IOP denotes Intensive Operation Phase, reflecting the chronological order of the performed campaigns. H_2O and O_3 data are available for all missions, except for the 2 flight missions on August 23, 2002, (missing H_2O data) and on the last 2 flight missions on February 16, 2003, (missing O_3 data). However, since O_3 was measured twice (from IOP3 on), O_3 data are totally disposable.

campaign: time period	**flight day**	**destinations: TO → TD**	**longitudinal range**	**latitudinal range**	**flight time**
IOP 1: 07-12 Nov 2001	10	Hohn → Faro	09.83°W-09.56°E	35.78-54.32°N	04:13
	10	Faro → Hohn	08.42°W-09.53°E	37.01-54.29°N	04:23
	11	Hohn → Kiruna	09.37°E-21.39°E	54.29-68.66°N	02:44
	11	Kiruna → Hohn	09.68°E-25.24°E	54.19-73.12°N	04:11
IOP 2: 15-20 Jan 2002	17	Hohn → Casablanca	08.22°W-09.56°E	33.49-54.34°N	04:27
	17	Casablanca → Cran Canaria	14.44°W-07.77°W	27.50-33.33°N	01:56
	18	Cran Canaria → Lisbon	15.39°W-07.69°W	27.92-38.60°N	02:32
	18	Lisbon → Hohn	09.14°W-09.56°E	38.77-54.14°N	03:35
	19	Hohn → Tromsø	00.11°E-19.20°E	54.31-73.20°N	04:35
	19	Tromsø → Hohn	00.10°E-19.07°E	54.39-73.13°N	04:23
IOP 3: 13-17 May 2002	16	Hohn → Jerez	08.68°W-09.63°E	36.13-54.32°N	04:52
	16	Jerez → Hohn	13.92°W-08.85°E	36.72-54.22°N	04:31
	17	Hohn → Tromsø	09.25°E-24.00°E	54.28-75.10°N	04:39
	17	Tromsø → Hohn	05.02°E-18.97°E	47.85-69.75°N	04:45
IOP 4: 19-24 Aug 2002	22	Hohn → Monastir	09.52°E-13.60°E	33.80-54.32°N	03:53
	22	Monastir → Hohn	08.33°E-11.86°E	35.72-54.52°N	03:33
	23	Hohn → Keflavik	27.21°W-09.76°E	54.31-65.05°N	03:46
	23	Keflavik → Hohn	22.63°W-09.75°E	53.34-63.99°N	03:47
IOP 5: 14-19 Oct 2002	17	Hohn → Seville	07.03°W-09.56°E	36.50-54.32°N	04:30
	17	Seville → Hohn	08.00°W-09.89°E	35.42-54.27°N	04:39
	18	Hohn → Keflavik	26.27°W-09.56°E	53.71-63.71°N	04:18
	18	Keflavik → Hohn	26.60°W-09.40°E	54.27-64.11°N	03:53
IOP 6: 12-17 Feb 2003	15	Hohn → Faro	12.00°W-09.68°E	36.84-54.32°N	04:39
	15	Faro → Hohn	07.97°W-10.02°E	36.99-54.25°N	04:32
	16	Hohn → Tromsø	09.54°E-18.54°E	54.31-69.86°N	02:59
	16	Tromsø → Longyearbyen	10.02°E-30.08°E	69.54-82.07°N	03:43
	16	Longyearbyen → Hohn	09.33°E-19.08°E	54.36-78.26°N	03:43
IOP 7: 23-29 Apr 2003	27	Hohn → Kiruna	09.37°E-21.00°E	54.29-72.99°N	04:21
	27	Kiruna → Hohn	08.43°E-20.35°E	49.99-70.53°N	04:50
	28	Hohn → Lisbon	10.39°W-09.55°E	38.50-54.31°N	04:32
	28	Lisbon → Hohn	10.19°W-13.44°E	37.95-54.51°N	04:17
	29	Hohn → Hohn	09.42°E-15.60°E	53.27-66.09°N	04:18
IOP 8: 07-10 Jul 2003	09	Hohn → Faro	08.07°W-09.56°E	35.88-54.32°N	04:04
	09	Faro → Hohn	05.05°W-09.55°E	35.87-54.47°N	04:27
	10	Hohn → Tromsø	09.30°E-21.82°E	54.29-73.25°N	04:15
	10	Tromsø → Hohn	06.54°E-21.75°E	49.90-69.69°N	04:15
				total flight time	**147:00**

A typical operational sequence of a campaign started with the arrival of the research and engineering groups. The whole equipment was shipped to Hohn and back to the home base of each group for all campaigns. The aircraft was prepared for instrument integration in the hangar by enviscope GmbH and GFD and the research groups arranged their instrumentation. On the second day the whole payload was integrated into the aircraft, including the installation of racks, instrumentation, data acquisition system and first tests. The third day started with the aircrafts weighing and leak tests. The rest of the day was reserved for final instrument tests, repairs, if necessary, and calibrations as well as preliminary flight planning and crew briefing.The first campaign flights took place on the fourth day. After the flight preparation, fore-runnings of the instruments and final crew briefing, two flight missions, each of an approximate duration of 4 hours, were conducted. Thereby, a short break for fuel refilling, status report and eventual troubleshooting in contact with the home base was established at the destination airport. Back in Hohn a de-briefing, data retrieving, some instrument calibrations and quick-look discussions were accomplished, as well as the preparation for the next operation day. The following flight day starts with the same process sequence. After the missions and data collection, the payload was partly uninstalled from the aircraft. On the sixth day final de-installations were performed, the whole equipment was packed and the groups departed. Within this compact campaign concept, the Learjet 35A was blocked only for 4 days. Thus, the operation schedule in the SPURT project was maintained very well.

2.1.4 Meteorological preflight and post-flight support

For the flight planning extensive meteorological support with forecasts and analyses was provided by IACETH, adapted from 3 h operational ECMWF (European Centre for Medium-Range Weather Forecasts) data with 60 vertical levels (T511L60). Based upon the PV fields the flight levels as well as planned crossings of air masses of different origins were adjusted. Thereby, during most SPURT missions a typical flight structure was applied (cf. Figure 2.3).

Due to the different time resolutions of the single instruments the whole measurement data were merged to 5 s data by IACETH. For an average aircraft flight speed of approximately $150 - 200$ m s^{-1} this results in an average spatial resolution of about $0.75 - 1.00$ km. Based upon the achieved meteorological and avionic data during the flight missions, the IACETH supplied meteorological post-flight analyses. These contained pressure cross-sections along the flight path and information of 10-day backward trajectories. The latter were included into the merged data set. The trajectories were initialized every 10 seconds along the flight track (Wernli and Davies, 1997) to get detailed history information of the probed air masses.

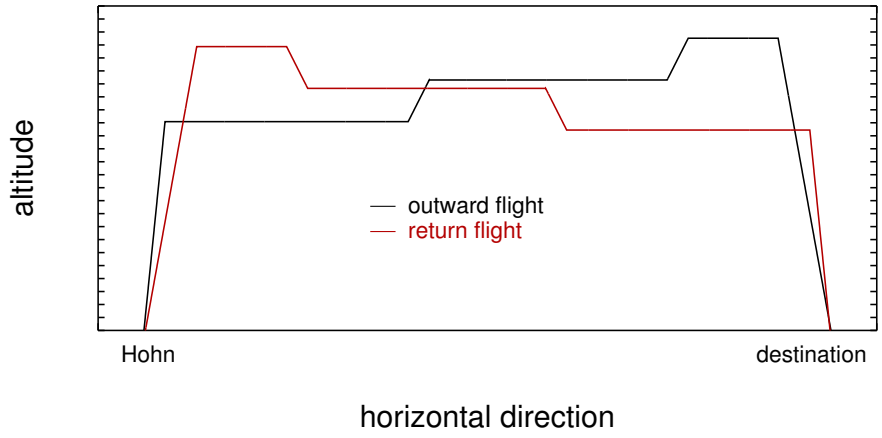

Figure 2.3.: Sketch of a typical flight pattern during SPURT. During take off and approach for landing slow ascents and descents were performed to obtain highly resolved vertical profiles. The first flight leg at constant pressure altitude was located in the tropopause region, the second deeper within the LMS. At the end of each mission, a climb to maximum altitude was carried out. The flight pattern of the outward flight was mirrored on the return flight to the home base.

In this thesis, trajectory information are used from calculations with the trajectory module of the Jülich CLaMS (Chemical Lagrangian Model of the Stratosphere, McKenna et al., 2002b,a). Thereby, Northern Hemisphere ECMWF analyses with a time resolution of 6 hours and a grid resolution of $1^\circ \times 1^\circ$ in latitude and longitude on 21 pressure levels (1000, 925, 850, 700, 500, 400, 300, 250, 200, 150, 100, 70, 50, 30, 20, 10, 7, 5, 3, 2, 1 hPa) were used. Since CLaMS operates on isentropic surfaces, the hybrid data set of each analysis was first of all interpolated to 25 isentropic surfaces, located between 280 and 400 K in 5 K steps, according to the Poisson-equation

$$\Theta = T \cdot \left(\frac{p}{p_0} \right)^{-\kappa}. \tag{2.1}$$

Hereby, T is the temperature in K, p is the pressure in hPa, p_0 is the reference pressure (here set to 1000 hPa) and $\kappa = R/c_\mathrm{p}$ is the Poisson-constant with $R = 287.04$ J kg^{-1} K^{-1} as the individual gas constant and $c_\mathrm{p} = 1004$ J kg^{-1} K^{-1} as the specific heat constant, both for dry air (e.g., Pichler, 1997).

2.2 The H_2O and O_3 SPURT data set

The FISH and JOE measurements during the SPURT project provide the main data base for this thesis. Beneath the maintenance of the measurement equipment, the instruments had to be prepared for their application on the research flights. In order to assure a high data accuracy, the servicing included several instrument calibrations in the laboratory before and after each campaign, as well as calibrations during the campaigns in the hangar. The sampled data during the single SPURT campaigns were prepared and archived. Thereby, the huge amount of achieved H_2O and O_3 data reflect the successful performance of the SPURT project and the reliability of the FISH and the JOE instrument.

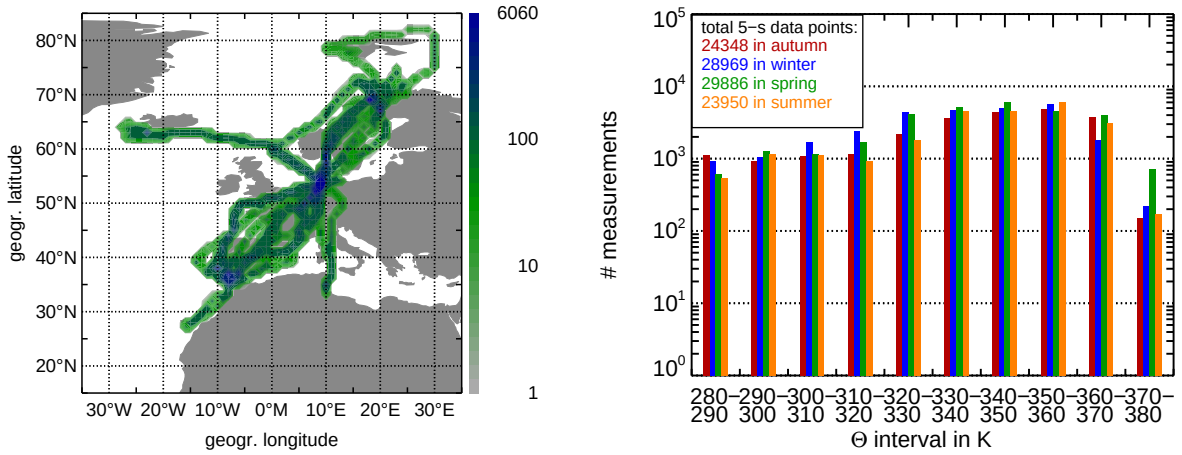

Figure 2.4.: In the left chart, the distribution of the SPURT measurements with a 5 s time resolution in the geographical ($1^\circ \times 1^\circ$ grid) space is displayed. Thereby, the colour bar reflects the number of 5 s data points in each geographical bin. The right chart shows frequency distributions of the sampled SPURT data in the potential temperature space. Hereby, a seasonal separation is performed (autumn, winter, spring, and summer corresponding to red, blue, green, and orange, respectively). The total number of merged data points during each season is given in the upper left corner.

As mentioned above, for a consistent SPURT data set the final data of all measured species were merged by IACETH to a uniform time resolution of 5 s. An overview of the obtained coverage of the 5 s trace gas measurements in the geographical and potential temperature (Θ) space is given in Figure 2.4. Beneath the campaign base Hohn in northern Germany, the two main inter stations, Faro in southern Portugal and Tromsø in Norway, are identifiable in the geographical distribution. Each annual season (autumn, winter, spring, and summer, corresponding to the months SON, DJF, MAM, and JJA) was investigated in two campaigns. The frequency distribution of data points in potential temperature intervals from 280 K to 380 K in steps of 10 K indicates winter and spring with ≈ 29000 and ≈ 30000 data points as the best captured seasons within the SPURT project. With ≈ 24000 data points also the autumn and summer seasons are probed quite well. The lower boundary of 280 K is a sampling result, since the inlet of the FISH instrument was only opened below a pressure value of ≈ 400 hPa. Also the JOE instrument provides high qualitative data rather below that pressure level.

The distribution of measurements in the potential temperature space reflects the flight concept of the SPURT missions. Slow ascents and descents led to a good coverage of the vertical structure between $280 - 310$ K. Within each flight two flight legs at rather constant pressure altitude were performed, one near and the other above the tropopause (cf. numbers of data points within $320 - 340$ K and $350 - 370$ K). In a final step, a climb to maximum altitude (> 370 K) was performed to sample generally undisturbed stratospheric background air. Due to fuel consumption and thus the lower mass of the aircraft, the climb took place at the end of each mission. The altitude flight profile was mirrored on the mission back to Hohn to sample the meteorological condition at two different height regimes. Additional informa-

tion about the SPURT concept can be found up to now in Hoor et al. (2004a,c) and Hegglin (2004).

Chapter 3

Seasonal cycles and variability of O_3 and H_2O during SPURT

The SPURT data set provides information of both climatological and individual processes. In this chapter the *in situ* measurements of ozone and total water are first used to derive the seasonal cycles of both chemical species in the upper troposphere and in the lowermost stratosphere. However, different meteorological conditions and dynamical impacts affect the trace gas composition in the UT/LMS. The underlying variation, ranging and correlation of both trace gases relative to different chemical, thermal and dynamical coordinates are then investigated in more detail by using 2-dimensional probability distribution functions.
The troposphere and the stratosphere are two atmospheric compartments with substantially different physical and chemical characteristics. Thus, first of all the location of the notedly boundary between both regimes, i.e. the tropopause, is analysed as observed during the SPURT campaigns, in order to derive the seasonal trace gas cycles in the UT and LMS.

3.1 Tropopause heights from SPURT ascents and descents

The determination of the tropopause location is a well known complicacy. There are several tropopause definitions for different purposes. For the extra-tropics definitions of the thermal or lapse-rate tropopause (LRT, Haynes and Shepherd, 2000), based upon the basis of the temperature lapse rate $\partial T/\partial z$, the chemical, deduced from the O_3 profile, and the dynamical tropopause, derived from the PV profile, are widely used. In the tropical regions the tropical thermal tropopause[1] (TTT, Haynes and Shepherd, 2000), the secondary tropical tropopause[2] (STT, Haynes and Shepherd, 2000), the cold-point tropopause[3] (CPT,

[1] typically at 16-17 km
[2] level of maximum convective outflow above the drifting of the lapse rate from the moist adiabat
[3] height of coldest temperature

e.g., Highwood and Hoskins, 1998; Haynes and Shepherd, 2000) the clear-sky radiative tropopause[4] (CSRT, Haynes and Shepherd, 2000) and the hygropause[5] (HP, Kley et al., 1979) are applied. However, up to now there exists still no tropopause definition, based upon physics or chemistry, which is appropriate to suffice in almost all meteorological conditions as well as from the poles to the equator (Wirth, 2000).

After the definition of the World Meteorological Organization (WMO) the thermal tropopause is placed at the lowest level below a pressure of 500 hPa at which the lapse rate falls below -2 K/km and does not exceed that value for at least 2 km further upward (cf. WMO, 1986a; Poulida et al., 1996). As noted by Danielsen and Hipskind (1980) temperature shows systematic changes, but in view of the gradual character of these changes there could also exist a second discontinuity in the temperature profile. Especially in regions with cross tropopause exchange processes most difficulties to derive an exact tropopause location arise. Due to mere reversible dynamical changes the character of the air could change from tropospheric to stratospheric and reverse, which shows one of the disadvantages of the thermal tropopause definition.

Owing to the different concentrations of O_3 in the troposphere and the stratosphere (up to 2 orders of magnitude higher in the stratosphere) and a sharp gradient in the transition region between the troposphere and the stratosphere, a chemical tropopause is most frequently defined as the location at which the O_3 volume mixing ratio (VMR) starts to increase rapidly with height and exceeds 100 ppbv (e.g., WMO, 1986b). There are several studies defining or using the chemical (ozone) tropopause (e.g., Bethan et al., 1996; Thouret et al., 1998; Talbot et al., 1999; Zahn et al., 2004b). Bethan et al. (1996) assigned four characteristics of a chemical tropopause. The ozone gradient in the vertical has to be at least 60 ppbv/km, the O_3 VMR must exceed 80 ppbv, potential vorticity has to be greater than 1.6-2.0 PVU[6] and just above that derived altitude the O_3 concentration must exceed 110 ppbv. The use of O_3 as a chemical species to distinguish between tropospheric and stratospheric air is particularly favourable in winter when there is little photochemical production of O_3 in the troposphere (cf. subsection 3.2.1, Haynes and Shepherd, 2000). Ozone often gives clearer signatures between the troposphere and the stratosphere than the lapse rate tropopause, e.g., in cyclones (Bethan et al., 1996; Haynes and Shepherd, 2000). The tropopause analysis of Bethan et al. (1996) was primarily given for winter and spring where it appears to be located about 800 m below the thermal tropopause.

Beyond the thermal and chemical definition, the tropopause can also be derived by a dynamic quantity. Already Danielsen (1968) proposed the potential vorticity as the most adequate parameter for the identification of the physical boundary between the troposphere and

[4] level with vanishing clear-sky heating

[5] location of the minimum water vapour mixing ratio

[6] PVU denotes Potential Vorticity Unit corresponding to 10^{-6} m^2 s^{-1} K kg^{-1} (Hoskins et al., 1985)

the stratosphere. Potential vorticity reflects by definition[7] the stability of the atmosphere and increases therefore with height. Diabatic heating due to O_3 in the stratosphere and the resulting large stability causes PV values in the stratosphere to exceed those in the troposphere by 1-3 orders of magnitude. In the troposphere the vertical stability is decreased by surface heating and radiative cooling of the tropopause region. At the extra-tropical tropopause a strong vertical gradient of PV is evident. Various threshold values of PV representative for the location of the extra-tropical tropopause are given in the literature. They range from > 1.0 PVU (Bithell et al., 1999), 1.6 PVU (Danielsen, 1984; Price and Vaughan, 1993; Stohl and Trickl, 1999) and 2.0 PVU (e.g., mentioned, used or estimated by Holton et al., 1995; Appenzeller et al., 1996b; Ray et al., 1999; Rood et al., 2000; Wernli and Bourqui, 2002; Pfister et al., 2003; Stohl et al., 2003b; Sprenger et al., 2003; James et al., 2003a; Hoor et al., 2004c) to 3.5 PVU (Hoerling et al., 1991; Hoinka, 1999) and 3-4 PVU (Ovarlez et al., 1999). Many studies exposed a PV value of 2.0 PVU. The PV-based tropopause definition alone could not be maintained since it breaks down in the tropics. Anyhow, this dynamical tropopause definition is more attractive than the WMO thermal tropopause definition, since PV is a conserved quantity under adiabatic and frictionless conditions (Ertel, 1942) and furthermore emphasises the nature of the tropopause as a material surface (Hoskins et al., 1985; Wirth, 1995). However, for estimating fluxes related to stratosphere-troposphere exchange it is essential to know the exact location of the tropopause. There are difficulties in determining the tropopause height (Highwood et al., 2000; Zängl and Hoinka, 2001), and especially subjectivity and the associated sensitivity can be substantial in cases when the tropopause is less sharp (Wirth, 2000; Zängl and Hoinka, 2001). Recapitulating, the extra-tropical tropopause can be located at the basis of the temperature lapse rate, the ozone and the potential vorticity profile.

Since the thermal tropopause has a generally accepted definition, extra-tropical tropopause heights were determined by the WMO criterion (cf. page 22) from temperature profiles during SPURT ascents and descents (a total of 72 profiles) when possible, i.e. when a vertical profile was sufficiently high enough to apply the thermal definition. Additionally, the chemical tropopause definition based on O_3 profiles after Bethan et al. (1996) was applied. For each profile the altitude, the potential temperature, the O_3 VMR as well as the PV value at the derived thermal (TP_{th}) and chemical (TP_{ch}) tropopause heights are given in Table A-I. It is evident in nearly all vertical profiles that PV and O_3 are well correlated (not shown here in detail, refer to subsection 3.4.1 and section 3.5), particularly for cases of recent inflow

[7] The isentropic potential vorticity is defined as

$$PV \equiv -g \cdot (f + \zeta) \cdot \frac{\partial \Theta}{\partial p}, \tag{3.1}$$

where g is the gravity acceleration, f is the Coriolis parameter, $\zeta = \frac{\partial v}{\partial x} - \frac{\partial u}{\partial y}$ is the relative vorticity (equal to the vertical component of the curl of the horizontal wind speed), Θ is the potential temperature (cf. Equation 2.1) and p is the pressure (e.g., Pichler, 1997).

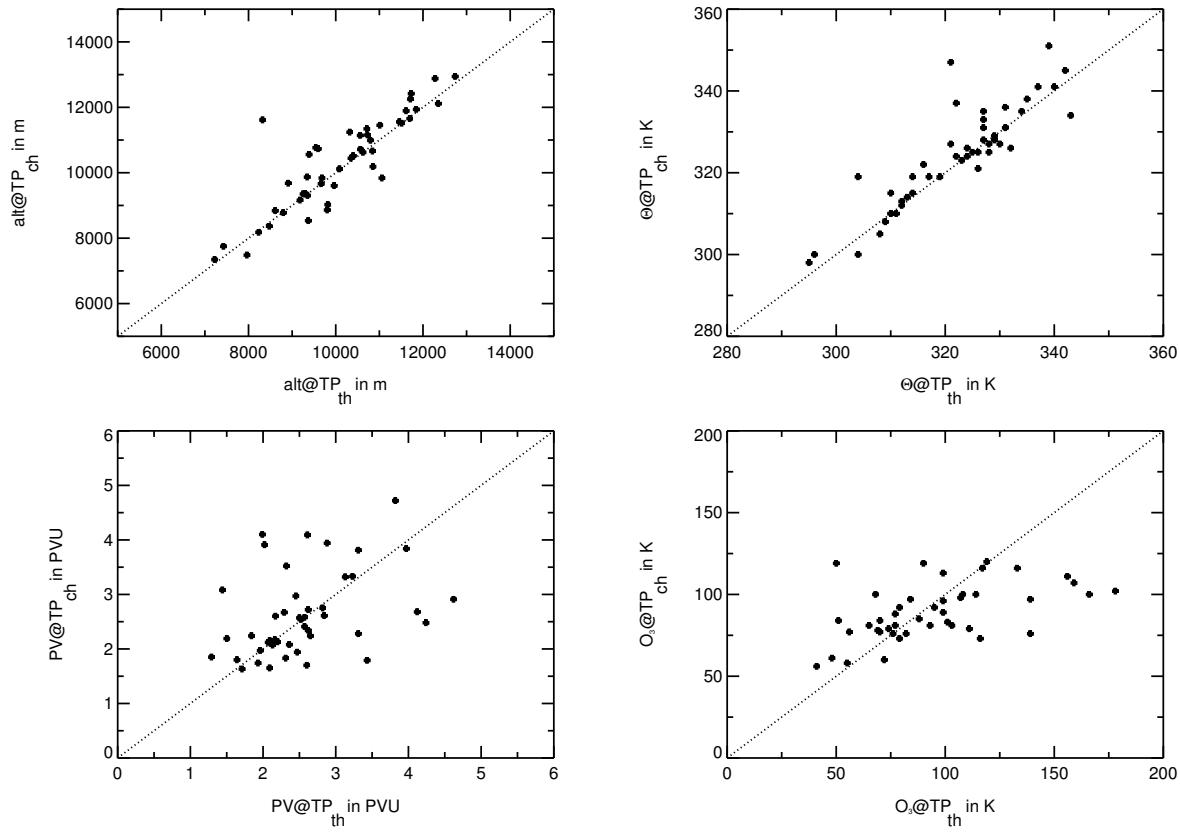

Figure 3.1.: Correlations between derived parameters at the chemical and thermal tropopause. Clockwise: correlations of altitude (alt), potential temperature (Θ), ozone mixing ratio (O_3), and potential vorticity (PV). The correlation coefficients are 0.87, 0.88, 0.45 and 0.39, respectively. The dotted lines indicate the perfect correlation.

of stratospheric O_3 into the troposphere (e.g., Danielsen, 1968; Browell et al., 1987). This finding is also represented by the similar correlation coefficients in Figure 3.1. For a comparison of the thermal and chemical tropopause definition and to estimate a threshold value for a dynamically defined extra-tropical tropopause, correlations for the four derived parameters as well as normalised frequency distributions of PV values at the identified thermal and chemical tropopause heights are shown in Figure 3.1 and Figure 3.2, respectively.

Altitude and potential temperature at different defined tropopause heights are rather well correlated with correlation coefficients of 0.87 and 0.88. In contrast to the results of Bethan et al. (1996), the chemical tropopause is located slightly above the thermal tropopause. The mean (median) of the differences are 452 m (238 m) and 4 K (3 K), respectively. The correlation of O_3 VMRs and PV values show no good correlation at all, illustrating the high gradients of both parameters near the tropopause (correlation coefficients 0.45 and 0.39, mean (median) 26 ppbv (14 ppbv) and 0.6 PVU (0.4 PVU), respectively). However, in the frequency distributions PV values at the derived thermal and chemical tropopause heights show nearly the same shape with a maximum frequency in the $2.0 - 2.5$ PVU range. Mean and median values for both definitions are also about 2.5 PVU. Considering the strong gradient of PV near the thermal and chemical tropopause, the vertical profile analyses of SPURT ascents

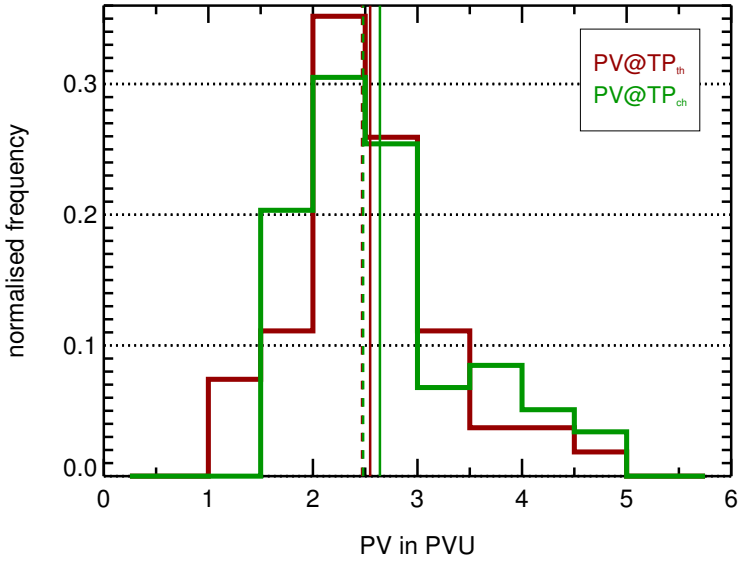

Figure 3.2.: Frequency distributions of potential vorticity at the thermal (red) and the chemical (green) tropopause as derived from SPURT ascents and descents where possible (cf. Table A-I for details). The vertical lines represent the mean (solid) and median (dashed) potential vorticity values at the derived thermal and chemical tropopause heights.

and descents suggest that a potential vorticity value of 2.0 PVU is a good proxy for a dynamical definition of the extra-tropical tropopause. Taking the value 2.0 PVU as the measure for the extra-tropical tropopause (and regarding the increase of PV with height) the dynamical tropopause is located slightly below the thermal tropopause which is in accordance with results from Hoerling et al. (1991) and Bethan et al. (1996).

3.2 Seasonal cycles of O_3 and H_2O

3.2.1 O_3 in the UT and LMS

Since ozone is a strong infrared absorber and due to O_3 photolysis, the radiative balance of the troposphere is largely sensitive to variability and changes in tropospheric ozone concentrations. In the troposphere about 10 % of the total amount of atmospheric ozone is present, whereas $\approx$ 90 % is enriched in the stratosphere (e.g., Lelieveld and Dentener, 2000). Owing to its high potential for participating in oxidation processes through the formation of hydroxyl radicals (OH) ozone increases with altitude and has also a strong gradient across the tropopause (cf. section 3.1). It was assumed that tropospheric ozone is controlled by cross-tropopause transport from the stratosphere into the troposphere (e.g., Regener, 1957; Danielsen, 1968). Despite that, breakdown of hydrocarbons and carbon monoxide can also cause episodes of photochemical *in situ* production of ozone in the troposphere, particularly in urban environments during summer. The build-up of ozone by photochemical oxidation of these species is thereby catalysed by nitrogen and hydrogen oxides (NO_x and HO_x) (e.g., Haagen-Smit and Fox, 1956; Crutzen, 1973; Chameides and Walker, 1973). In the literature, two aspects of tropospheric ozone origin are discussed: (i) ozone transport from the stratosphere (e.g., Levy et al., 1985) and (ii) *in situ* photochemistry (e.g., Crutzen, 1974; Fishman

et al., 1979). Some three-dimensional global chemical transport models (CTM, e.g., Müller and Brasseur, 1995; Levy et al., 1997; Wang et al., 1998b; Crutzen et al., 1999) account for both processes. However, in their results wide ranges of tropospheric ozone origin illustrate the involved uncertainties. Whereas both terms are globally approximately balanced, locally they may be very different (Lelieveld and Dentener, 2000). For an analysis of the stratospheric source of tropospheric ozone derived from the SPURT measurements it is referred to section 6.2.

The annual cycle of tropospheric ozone in unpolluted air shows a summer minimum and a winter maximum (Ayers et al., 1997), since, due to the prevailing photochemistry, low NO_x contents lead to net destruction of ozone. In contrast to these remote sites, there exists a number of regions that show a broad summer maximum in tropospheric ozone. The existence of such a maximum is often associated with the photochemical production (e.g., Logan, 1985). Ozone is thereby formed by reactions involving volatile organic compounds (VOC) and NO_x, driven by solar radiation. A lot of these regions are continental and influenced by pollution (e.g., Logan, 1989; Scheel et al., 1997). However, the appearance of a spring maximum in the ozone seasonal cycle in the Northern Hemisphere troposphere is heavily debated (cf. review of Monks, 2000).

In Figure 3.3 monthly mean ozone concentrations in different potential vorticity domains, characteristic for specific dynamic regions of the atmosphere, are shown as measured during the SPURT campaigns. Thereby, the data are binned for northbound (top, left), southbound (top, right) and all flights (bottom) separately. Since potential vorticity increases with height and latitude in the Northern Hemisphere, it is used here to split the data set into atmospheric subsets. As evidenced in section 3.1, a potential vorticity value of $2.0 - 2.5$ PVU is representative for the location of the extra-tropical tropopause during SPURT. Potential vorticity values < 2.0 PVU therefore denote the (upper) troposphere, values within the range $2.0 - 3.0$ PVU the tropopause region, and higher values reflect an increasing stratospheric character of the probed air.

Considering the complete data set the seasonal cycle of ozone shows a broad spring to summer maximum in the troposphere and a minimum during winter. This is consistent with Beekmann et al. (1994), who showed by balloon-borne Brewer-Mast sondes at Observatoire de Haute Provence (OHP) that the seasonal variation of tropospheric ozone is characterised by a large maximum during spring and summer. Furthermore, LIDAR and ozone sonde measurements from OHP within $1976 - 1995$ give evidence for a shift from a spring maximum to a spring/summer maximum in the free troposphere (Ancellet and Beekmann, 1997). Regarding the northbound and southbound flights during SPURT, the maximum in tropospheric ozone concentrations for higher latitudes occurs during late spring and is shifted to late sum-

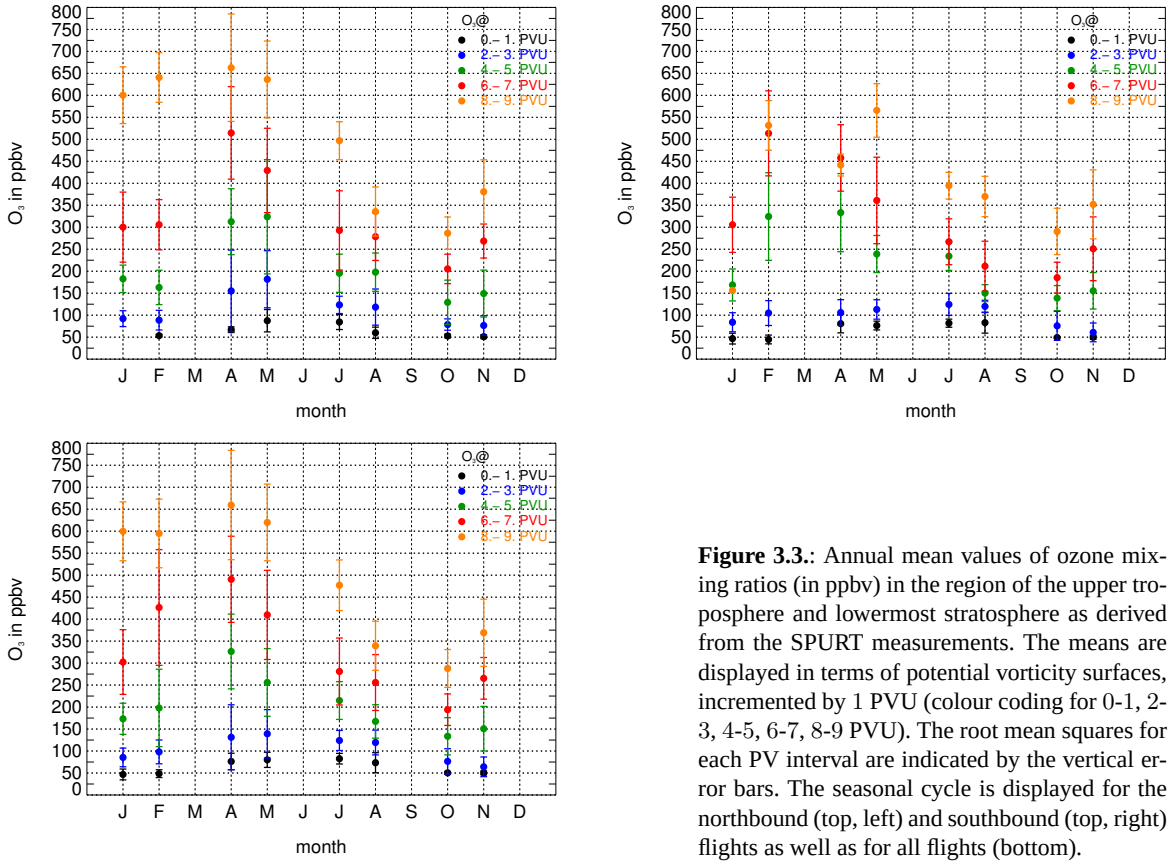

Figure 3.3.: Annual mean values of ozone mixing ratios (in ppbv) in the region of the upper troposphere and lowermost stratosphere as derived from the SPURT measurements. The means are displayed in terms of potential vorticity surfaces, incremented by 1 PVU (colour coding for 0-1, 2-3, 4-5, 6-7, 8-9 PVU). The root mean squares for each PV interval are indicated by the vertical error bars. The seasonal cycle is displayed for the northbound (top, left) and southbound (top, right) flights as well as for all flights (bottom).

mer further south. This is in agreement with results of Scheel et al. (1997) from low-altitude and mountain sites between $28 - 79°$N. Ozone precursors like NO_x, CO, and hydrocarbons at middle and higher latitudes accumulate in the free troposphere during winter and spring (e.g., 2-dimensional model studies by Hough, 1991). This may explain the slight shift towards spring observed during the northern flights. The observed maximum in ozone mixing ratios during summer is possibly a result of *in situ* photochemical production (e.g., Logan, 1985; Haynes and Shepherd, 2000) since photochemical activity is expected to be highest during this period (e.g., Liu et al., 1987) and thus in phase with the UV intensity, peaking in June (Beekmann et al., 1994).

For high potential vorticity values, i.e. in the lowermost stratosphere, a clear spring maximum and autumn minimum is evident with an amplitude of ≈ 400 ppbv ozone within the highest potential vorticity bin. This is apparent in all considered categories. The ozone build-up in this atmospheric region occurs during winter as a consequence of poleward and downward transport, since the lifetime of ozone is long with respect to chemical loss (e.g., Holton et al., 1995) and is largely controlled by dynamics (Logan, 1999). The observed spring maximum in the lowermost stratosphere over Europe is therefore owing to the downward advection of high ozone mixing ratios by the stratospheric winter/spring Brewer-Dobson circulation (e.g., Logan, 1985; Austin and Follows, 1991; Oltmans and Levy III, 1994; Logan, 1999; Haynes and Shepherd, 2000; Prados et al., 2003). Ozone concentrations fall off from March

to October with a maximum decrease rate within May to August. Much of this decrease is probably caused by the change in tropopause height and transport mechanisms (see also chapter 8), which leads to a decrease in the ozone content in this region. On the basis of observations of SAGE II (Stratospheric Aerosol and Gas Experiment II) aboard ERBS (Earth Radiation Budget Satellite), Pan et al. (1997) and Wang et al. (1998a) assumed that isentropic cross-tropopause inflow of tropospheric air into the lowermost stratosphere influences the seasonal cycle of ozone (and water vapour, cf. subsection 3.2.2) in that atmospheric region, especially during summer. A maximum of quasi-isentropic inflow into the lowermost stratosphere in summer was also identified in model studies by Chen (1995) (2-dimensional) and Eluszkiewicz (1996) (3-dimensional). Enhanced content of tropospheric air in September compared to May was identified by Ray et al. (1999) from balloon-borne CFC (chlorofluorocarbons) and water vapour measurements, which was also thought to be owing to quasi-isentropic in-mixing of tropospheric air. The seasonal cycle of ozone in the extratropics therefore differs between the upper troposphere and the lowermost stratosphere. The transition region between the troposphere and the stratosphere ($2.0-3.0$ PVU) is rather influenced by the troposphere. However, just above the tropopause ($4.0-5.0$ PVU) the stratospheric signal is already evident.

Comparing the mean ozone mixing ratios in the different potential vorticity ranges of the northbound and southbound flights the latitudinal ozone gradient is apparent. Whereas the tropospheric ozone concentrations are rather equal in amplitude, the northern stratospheric mixing ratios show to a large extent higher values than the southern. The higher mean ozone mixing ratios observed in February 2003 for the southbound flights compared to the northbound flights result from measurements within a broad stratospheric "streamer", expanding deep from high towards lower latitudes. Furthermore, the amplitudes of ozone mixing ratios increase from the troposphere to the stratosphere. The most prominent increase in ozone concentrations is apparent during winter and spring. This indicates, that the strongest ozone gradients across surfaces of potential vorticity exist during these seasons, whereas during summer and autumn the gradients are comparably weak. Since in Figure 3.3 rather dynamically equal air parcels are considered and potential vorticity exhibits a transport barrier, the lower ozone gradients through potential vorticity surfaces during summer and autumn suggest an intensified transport of tropospheric air into the lowermost stratosphere during these seasons (cf. also subsection 3.2.2 and chapter 8). Towards higher potential vorticity ranges (> 3.0 PVU), i.e. deeper in the lowermost stratosphere, tropospheric influence decreases which results in an increase in the slope (dO_3/dPV). The observed seasonal variation of the slope has a maximum of about $60-90$ ppbv/PVU in April and a minimum of $10-30$ ppbv/PVU in October. It is to note that the phase remains unaffected. The results are comparable with findings from Beekmann et al. (1994) and Zahn et al. (2004b).

3.2.2 H_2O in the UT and LMS

For the investigation of processes and atmospheric motions in the region of the upper troposphere and lowermost stratosphere water vapour is, as ozone, an adjuvant tracer (e.g., Appenzeller et al., 1996a). The transport of water vapour reflects also energy (latent heat) transport. Surface characteristics and temperature affect the distribution of water vapour making it highly variable in space and time. The tropical cold trap effect (dehydration of air entering the stratosphere) determines to the largest extent the annual cycle of water vapour in the lower stratosphere. Like a "tape recorder" (Mote et al., 1996) the water vapour signal propagates vertically over the equatorial region but is also latitudinally transported (e.g., McCormick et al., 1993; Hintsa et al., 1994; Boering et al., 1995; Rosenlof et al., 1997; Mote et al., 1998; Dessler, 1998; Jackson et al., 1998; Randel et al., 2001; Park et al., 2004). In the Northern Hemisphere stratosphere, the water content is beneath methane oxidation (e.g., Ackerman et al., 1979) and the dehydration mechanism strongly tributary on varying entry levels even at the mid-latitude tropopause. In contrast to the tropics, in the extra-tropics there are multiple pathways of how air is transported into the lowermost stratosphere. Many studies focus on mechanisms and evidence for transport processes across the extra-tropical tropopause into the LMS, be it of dynamic or radiative nature (e.g., Dessler et al., 1995; Poulida et al., 1996; Rosenlof et al., 1997; Zierl and Wirth, 1997; Hintsa et al., 1998; Fischer et al., 2003). For analyses of the SPURT measurements concerning these issues see also section 4.3 and section 5.1.

In Figure 3.4 the seasonal cycle of H_2O measured by the FISH instrument during SPURT is depicted in the same form as for ozone in Figure 3.3. Based on the annual cycle of tropopause temperatures (Hoinka, 1999), maximum water vapour mixing ratios in the UT/LMS are expected during summer, lowest during the winter months. The SPURT measurements show that in the troposphere ($0.0 - 1.0$ PVU) maximum H_2O mixing ratios are present during the summer months. However, during spring a secondary maximum is apparent. This feature pervades through the whole considered potential vorticity intervals and reflects the high variability of that trace gas in the probed atmospheric region. Anyhow, the tendency of higher VMRs during summer and lower ones during winter and also autumn is present. Across the tropopause the strong gradient in H_2O is evident. When considering northbound and southbound flights separately, the southern tropopause region is slightly dryer. This is probably due to the higher influence of the dryer sub-tropical regions (cf. section 5.2).

In the lowermost stratosphere (> 4.0 PVU) a more clear seasonal cycle in H_2O is apparent with a distinct maximum during summer and a minimum during autumn and winter. This is in agreement with previous *in situ* and remote observations (e.g., Mastenbrook and Oltmans,

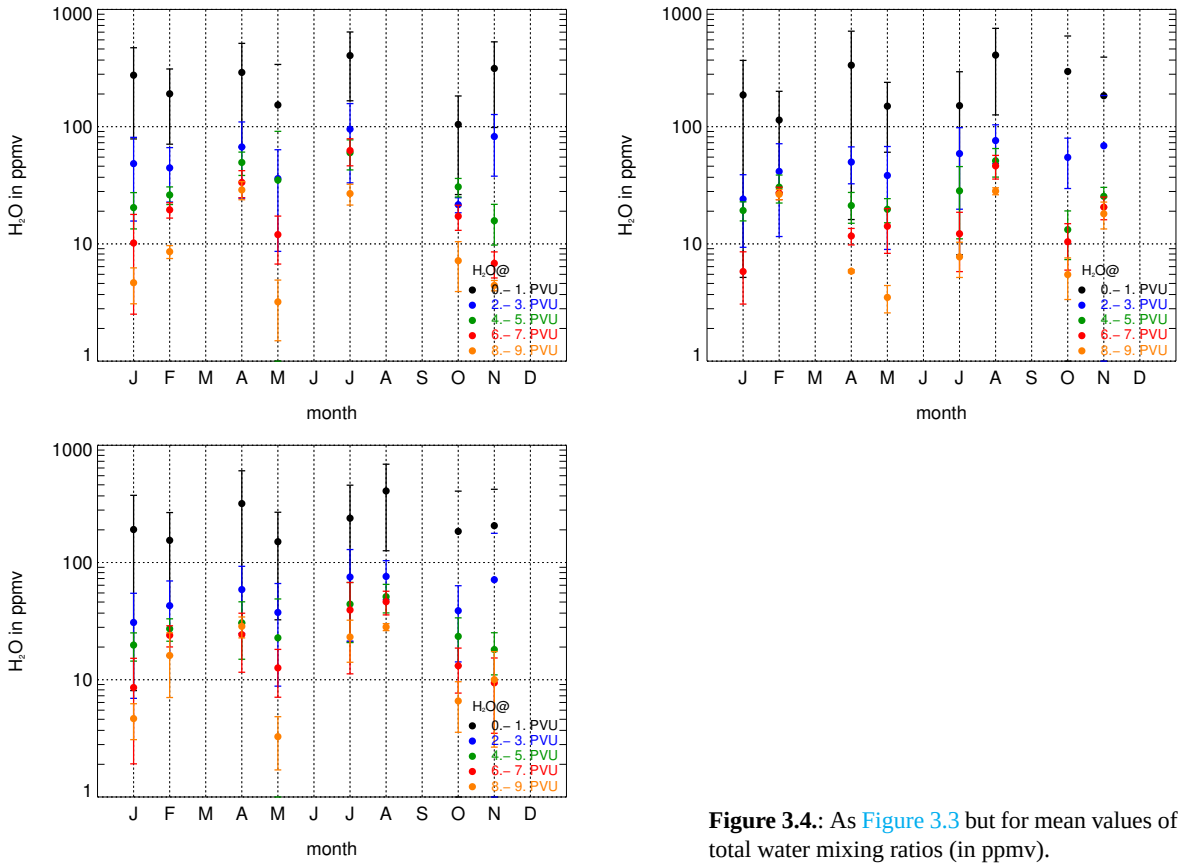

Figure 3.4.: As Figure 3.3 but for mean values of total water mixing ratios (in ppmv).

1983; Foot, 1984; Oltmans and Hofmann, 1995; Dessler et al., 1995; Pan et al., 1997; Stone et al., 2000). In contrast to the ozone distribution, with increasing altitude (potential vorticity) the mixing ratio as well as the amplitude of the annual cycle decreases (note the logarithmic ordinate). This indicates the more pronounced seasonal cycle in the lower lowermost stratosphere.

Air in the overworld is dehydrated as it is transported through the tropical cold trap. However, for a large extent of the performed campaigns H_2O VMRs are considerably enhanced compared to stratospheric background values of about $2-6$ ppmv (e.g., Brewer, 1949; Hintsa et al., 1994). In the highest considered potential vorticity range of $8.0-9.0$ PVU, mean VMRs in summer are about 30 ppmv. These concentrations are much higher than could solely be explained by entry of air into the lowermost stratosphere in the tropics (e.g., Foot, 1984; Nedoluha et al., 2002). Thus, values substantially greater than 6 ppmv evidence for transport mechanisms of air into the lowermost stratosphere across the extra-tropical tropopause, and this signature is carried deep into the lower stratospheric region.

Since H_2O is highly variable in space and time which is only slightly considered in Figure 3.4, the dynamically based coordinates of potential vorticity and potential temperature (Θ) (Hoskins, 1991) are used to put the measurements in the different seasons and years on a comparable basis. In this coordinate system seasonal variations of the tropopause height

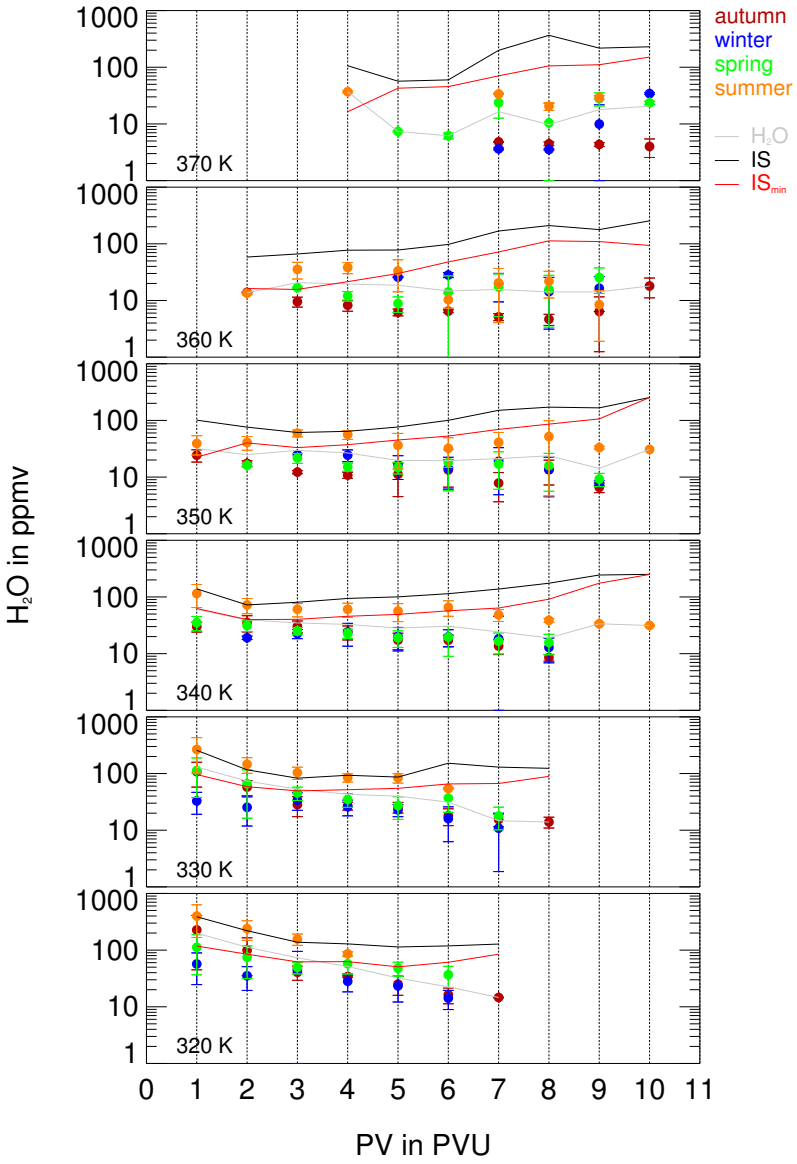

Figure 3.5.: Seasonal mean values of total water mixing ratios (in ppmv) in dependence of potential vorticity for different potential temperature intervals between 320 and 370 K (± 5 K) in the upper troposphere and lowermost stratosphere. Thereby, the data of the different SPURT measurement campaigns are summarised for each season. Potential vorticity is incremented in 1.0 PVU steps. The mean square root is plotted as error bars. Mean values for all campaigns of total water mixing ratios (H_2O), ice saturation mixing ratios (IS) and minimum ice saturation mixing ratios within the previous 10 days of the air parcels (IS_{min}) are given by the grey, black and red solid lines, respectively. The determination of IS_{min} is performed by trajectory calculations (cf. section 4.2).

are rather eliminated (e.g., Pan et al., 2000) and it ensures the computation of mean values of similar dynamically air parcels, restricted by the instruments' limitations (Stone et al., 2000). Additionally, trace gas variations on isentropic surfaces can be resolved. Seasonal mean values of H_2O as a function of potential vorticity ($1.0 - 10.0$ PVU ± 0.5 PVU) in different potential temperature bins ($320 - 370$ K ± 5 K) are displayed in Figure 3.5. The means of the autumn/winter and summer campaigns in each isentropic range should reflect the seasonal amplitude. For isentropes lower than 355 K this feature is given even through all considered potential vorticity bins. With increasing potential temperature and higher potential vorticity

values the mean H_2O concentrations as well as the seasonal amplitudes decrease monotonically. Hereby, it should be mentioned that less values in a certain Θ-PV-interval contribute considerably to this mean value (e.g., $4.5 - 6.5$ PVU within 370 ± 5 K). Without any influx from the troposphere, air on the highest isentropes considered would be very dry and exhibit only a minor seasonal cycle. The impact of troposphere-to-stratosphere transport (TST) in each potential temperature range could thus be estimated by considering deviations from $\approx 6 - 10$ ppmv. The decreasing variability in the seasonal amplitude reflects the decreasing tropospheric influence with deeper penetration into the lowermost stratosphere. Total water seems to be more uniformly distributed in higher Θ-PV-bins. Anyhow, in comparison with overworld abundances it is still considerably variable. Figure 3.5 suggests effective TST mechanisms (both adiabatic mixing and convective processes) and flux of water vapour into the lower lowermost stratosphere (although the tropospheric influence is apparent in the entire range examined). This is especially prominent during summer, in agreement with other recent studies (e.g., Ovarlez et al., 1999; Pan et al., 2000; Stone et al., 2000).

For each Θ-PV interval additionally the means for the total SPURT data set (in the following referred as annual means) of H_2O VMRs, ice saturation mixing ratios (IS) and minimum ice saturation mixing ratios within the previous 10 days (IS_{min}) is given. For the calculation of IS and IS_{min} it is referred to section 4.2. Seasonal variations as well as annual means in H_2O concentrations are still considerably large for different PV ranges, whereas above isentropes of 355 K the annual means vary only about 10 ppmv. Annual means of IS in each Θ-PV bin decrease with increasing PV on lower isentropes. On higher isentropes an increase through PV bins is apparent which is due to the increasing temperature with height in the lowermost stratosphere. It appears that the IS values (black solid line in Figure 3.5) are always higher than the annual mean H_2O VMRs (grey solid line). However, taking the temperature history of the air parcels during the previous 10 days into account (for details see section 4.2 and section 6.1) minimum values of IS during this period (red solid line) are often below the H_2O VMRs up to the $\approx 4.5 - 5.5$ PVU bin. The most frequent probed area during SPURT is the latitude range between 30 and $60°$N (cf. Figure 2.4). As proved in section 3.1, a value of about 2.0 PVU is representative for the extra-tropical tropopause. The comparison of the annual means of H_2O and IS_{min} shows that in particular in the tropopause region ($1.0 - 3.0$ PVU) IS_{min} values are widely below H_2O VMRs. Therefore, the extra-tropical tropopause seems to bear the potential to act, similar as in the tropics, as a cold trap. Although only annual means are considered here, it is evident that this investigated atmospheric region during SPURT is considerable often influenced by (super)saturation, also enhancing the probability for cirrus cloud formation (see section 6.1). When enlarging the 10 day history to 30 days this issue becomes more prominent.

Whereas the maximum in total water in the upper troposphere is approximately in phase with the ozone maximum, in the lowermost stratosphere it occurs about $2-3$ months later (prior) to the ozone maximum (minimum). A similar time lag was found by Pan et al. (1997) and Prados et al. (2003). Due to the large debate, especially concerning the often observed spring ozone maximum at some Northern Hemisphere stations, it is further to investigate to what extent the correlation and/or anti-correlation of both trace gases could be attributed to dynamics or to chemistry. Anyhow, the seasonal cycles subscript the influence of two competing processes in the region of the upper troposphere and the lowermost stratosphere: (i) subsidence of dry air from the overworld, which is primarily determined by the low tropical tropopause temperatures and transported by the large-scale Brewer-Dobson circulation (e.g., Holton et al., 1995), and (ii) direct transport of moister air of tropical, sub-tropical or mid-latitude origin across the extra-tropical tropopause (e.g., Dessler et al., 1995; Hintsa et al., 1998). As is apparent in Figure 3.4 and Figure 3.5, in contrast to the ozone VMRs, the seasonal variation of H_2O VMRs in the upper troposphere and the lower stratosphere are roughly in phase with each other. This issue of same seasonal variation is *a priori* not clear. Whereas much of the air in the lowermost stratosphere has probably been transported into the stratosphere by the former process it is likely that local vertical transport processes play a much larger role in determining water vapour VMRs in the lower lowermost stratosphere and upper troposphere.

3.3 Frequency distributions

In climatological mean values of atmospheric trace gases, e.g. for different atmospheric regions, no information about the shape and the range of the mixing ratio values of the considered trace gases is enclosed. Such information could be represented by frequency distributions. Due to the temperature lapse rate and the decrease in pressure, water vapour mixing ratios decrease exponentially with height from the troposphere up to the tropopause region. Calculated averages of measurements that span the transition region between the upper troposphere and the lowermost stratosphere, i.e. the tropopause region, will possibly be influenced by moister air from below the tropopause. Also O_3 shows a distinct gradient with a strong increase at the extra-tropical tropopause. To perform normalised frequency distributions of H_2O and O_3 measured during SPURT, for all seasons three different atmospheric regions are considered: the troposphere, the tropopause region, and the stratosphere. Potential vorticity is used to distinguish air primarily influenced by the troposphere or by the stratosphere, respectively. The detailed study of tropopause heights during all ascents and descents of the SPURT missions suggests 2.0 PVU to be a good proxy for the extra-tropical tropopause during SPURT. The PV criteria used in the frequency distributions for the extra-

tropical measurements in the three atmospheric compartments are PV< 1.0 for the (upper) troposphere, $1.0 \leq$PV≤ 3.0 defining the tropopause region, and PV> 3.0 representative for the lowermost stratosphere (values in PVU).

Frequency distributions for H_2O and O_3 of the three PV-intergraded atmospheric regions and for the total measurement region are displayed in Figure 3.6. For a distribution of a category with a total of N observations, the frequency, expressed in percent, for a definite trace gas range is equal to the number of occurrences within that range, normalised to the number of data points N within the respective category. For H_2O the bin size is set to 5 ppmv, for O_3 to 20 ppbv. The normalised frequency distributions display distinct characteristics and seasonal dependencies.

The tropospheric data category for H_2O (right column) is broadest in all seasons. In general, two maxima of frequencies are evident: one is located at lower mixing ratios around $20 - 60$ ppmv, the other one is placed at higher mixing ratio values. The latter is expectedly due to the moist (mid) troposphere. The enhanced maximum frequencies at lower mixing ratios are caused by measurements in the vicinity right below the dynamical tropopause, where profiles of H_2O show a strong decrease in mixing ratios. Note that the PV criteria for the tropospheric category is limited by PV< 1.0 PVU and one would anticipate high mixing ratios. However, for instance, near a tropopause fold there exists a rather vertical PV isopleth and tropospheric air and stratospheric air are close to each other, probably in a mixed state. In contrast to the distributions in the troposphere the stratospheric frequencies peak at lower H_2O VMRs near 10 ppmv during autumn, winter and spring and about 40 ppmv during the summer months. However, a stratospheric secondary maximum is present during almost all seasons (cf. also Figure 4.7). The shape of the distribution is consistent with the moister and more variable extra-tropical troposphere than the lowermost stratosphere. The resulting distributions for the tropospheric and the stratospheric regions are not very sensitive to small changes of the used PV criteria, whereas the distribution for the tropopause region reacts more sensitive to the choice of the upper PV limit. The structures of the frequency distributions for the tropopause region show intermediate curvatures between the tropospheric and stratospheric arrangements. However, the tails at high mixing ratios are more resembled by the tropospheric and the left sides by the stratospheric distributions. When considering all measurements, and in particular when increasing the lower PV limit for the stratospheric data points, these distributions are best reflected by the frequency distributions for the lowermost stratosphere. Anyhow, at low H_2O VMRs the left tails of the distributions of the tropopause region fall off very rapidly, in contrast to the stratospheric left tails. The amount of stratospheric measurements is also lowest during the summer months which is consistent with the seasonal change in altitude of the extra-tropical tropopause (lowest during winter, highest during summer) accompanied with the increasing mass of the troposphere during the

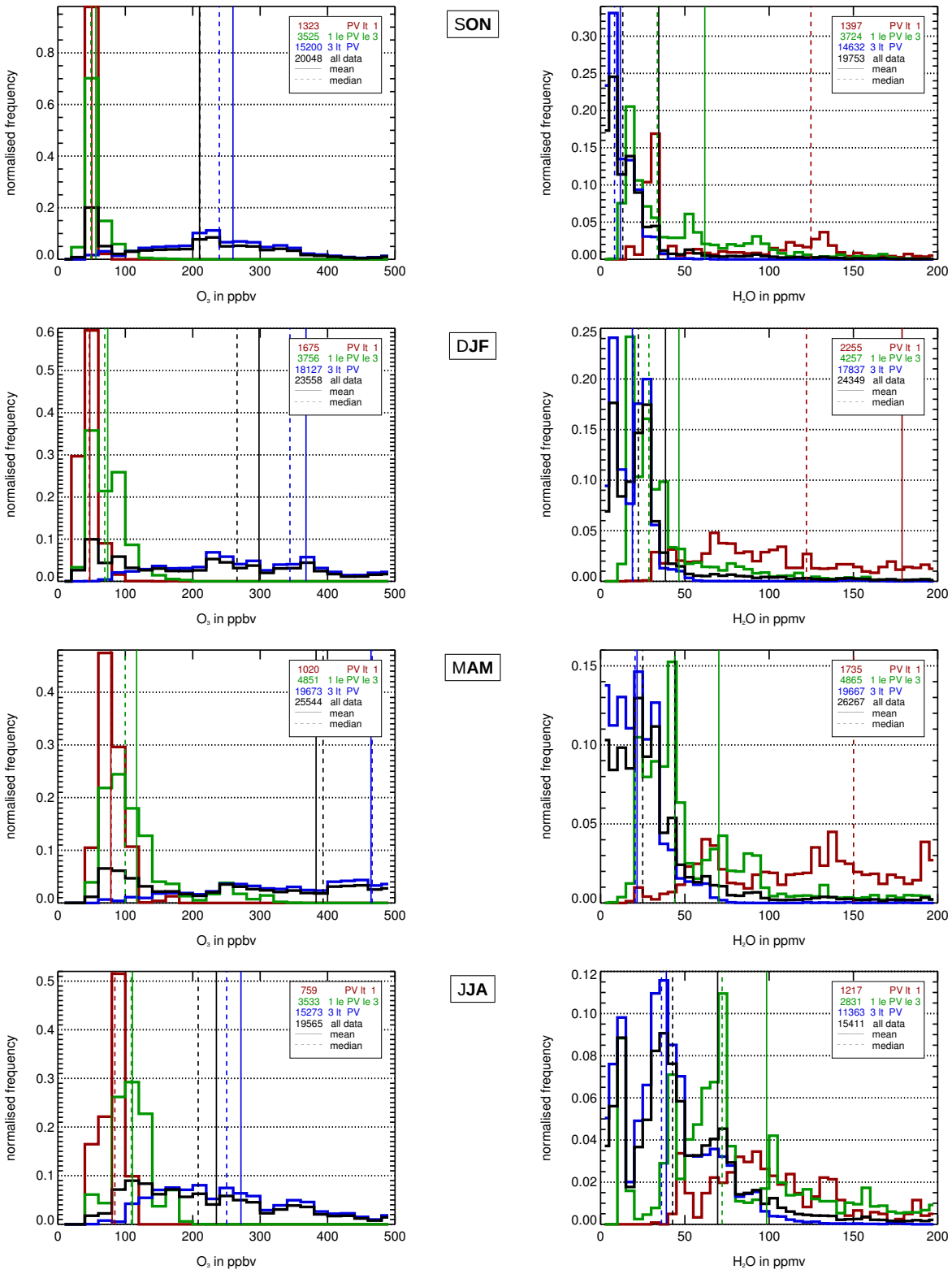

Figure 3.6.: Seasonal normalised frequency distributions for the mixing ratios of total water (right) and ozone (left) for all seasons as measured during the SPURT project (top to bottom: autumn, winter, spring, summer). The distributions are displayed for the three atmospheric regions: troposphere (red), tropopause region (green), and stratosphere (blue), separated according to the PV criteria PV$<$1, 1$\leq$PV$\leq$3, and 3$<$PV, respectively (values in PVU). Additionally, the frequency distributions of all measured data points are shown in black. Note the different ranges on the ordinates. The considered number of data points in the distributions is given in the upper right corner of each graph. Furthermore, for the three distinguished data categories as well as for all data points the vertical lines represent the mean (solid) and median (dashed) trace gas mixing ratios.

summer season (Appenzeller et al., 1996b).

For all the distributions there is a change in maximum frequencies from lower H_2O VMRs during autumn and winter to higher values during the summer season. Furthermore, the broadening of the distributions increases from autumn/winter to summer, as is also noticeable as a first guess from the different range of the ordinates. The displacement of the maximum frequencies towards higher H_2O VMRs as well as the widening spread of the distributions for the data points in the tropopause region and in the stratosphere towards summer do *a priori* not hint to extensive mass transport across the extra-tropical tropopause during that season. These issues rather suggest that such transport processes of water species are easier to manage (greater H_2O flux) and are more important and significant, especially for long-term transport. However, the lowermost stratosphere seems to be more influenced by the troposphere during summer than during winter which is in agreement with the discussed seasonal variability of water vapour in the lowermost stratosphere by e.g., Pan et al. (2000) (cf. also section 3.2).

The mean as well as the median of H_2O VMR values for the different data categories are also calculated. While the mean is an appropriate measure of the central tendency for roughly symmetric distributions, it is misleading when applied to skewed distributions since it can be greatly influenced by extremes. In contrast, the median is less sensitive to outliers and may be more informative and representative for skewed distributions. Caused by the very high H_2O VMR values during ascents and descents in the lower and middle troposphere and the strong water vapour gradient, this issue is prominent when determining these two measures for the tropospheric data. A large difference between the mean and the median is evident. For the tropopause region and the lowermost stratosphere values of the means and medians differ less due to the weaker H_2O gradient. All the medians tend towards moister values when approaching the summer months. The only factors that determine the water vapour content in the air are the availability of water and the amount of thermal energy. Thus, in summer more evaporation is more effective due to the higher amount of thermal energy.

Normalised frequency distributions for O_3 (left column in Figure 3.6) show similar results as the diagrams for H_2O. During all seasons the strong gradient of O_3 concentrations in the tropopause region arises in the pronounced decline on the right hand tails in the distributions of the troposphere and the tropopause region. The strong increase at O_3 VMRs below 50 ppbv is artificially caused by the measurement frequency, since the JOE instrument provides only accurate measurements below pressure levels of ≈ 400 hPa (cf. also Mottaghy, 2001). During autumn tropospheric O_3 VMRs appear to be more uniform. When approaching spring and summer the right hand tropospheric tails tend slightly towards higher O_3 VMRs, also the distribution broadens. Most variable tropospheric O_3 concentrations are present during spring but they are not highest. The often observed tropospheric spring maximum of

O_3 in some northern hemispheric stations (Monks, 2000, and references therein) is rather not observed by the SPURT measurements (see subsection 3.2.1). The seasonal cycle of tropospheric and stratospheric O_3 is also present in the distributions. Tropospheric O_3 is at minimum during winter and at maximum during summer, whereas the minimum of stratospheric O_3 concentrations is shifted towards autumn, the maximum towards spring. The change in maximum frequencies of O_3 VMRs in the stratosphere appears from spring (maximum around 450 ppbv) to summer (most frequent values around 200 ppbv). The tropopause region shows its broadest distribution during spring. During this season the influence of the large-scale downward motion is most prominent (Appenzeller et al., 1996b). Also the net ozone flux across the extra-tropical tropopause has a peak during spring to early summer, primarily effected by the outward O_3 flux of the lowermost stratosphere through the tropopause (Logan, 1999). A demonstrative feature is apparent when all measurements are considered in one distribution. Since there is almost a wave-like structure with two maximum frequencies around 80 ppbv and higher O_3 VMRs, nearly representing the tropospheric and stratospheric means, the distribution changes to a single maximum around 120 ppbv in the summer months with a strong (weak) decline towards lower (higher) mixing ratios. On the one hand, the probably enhanced photochemical *in situ* production of O_3 in the upper troposphere during summer is reflected, on the other hand, this indicates the stronger tropospheric influence during this season. The tropospheric impact is also present in the stratospheric distribution.

The seasonal O_3 cycles in the different atmospheric regions are reflected by the means and medians. Since the changes in O_3 concentration in the troposphere are not as pronounced as those for total water, means and medians are closer to each other in this atmospheric region. The difference between these quantities is largest in the stratosphere, due to the strong increase of O_3 with height there.

3.4 O_3 and H_2O in the view of different coordinates

The SPURT measurements covered a broad latitude range with different meteorological situations, often associated with small-scale phenomena (e.g., tropopause folds) and large-scale meridional advection of polar and/or sub-tropical and/or tropical air. The different dynamical impacts result in discontinuities and height changes in the tropopause location, particularly in the vicinity of regions with high wind velocities, the jet streams, in the literature often referred to as the region of the ”tropopause break”. In order to get a comprehensive insight into distribution, spreading/ranging, and variability of the measured trace gases in the SPURT region, 2-dimensional probability distribution functions (PDFs) were determined by using chemical, thermal, and dynamical coordinates, i.e. the trace gases total water (H_2O)

and ozone (O_3), pressure (p), temperature (T), potential temperature (Θ), distance to the local tropopause ($\triangle\Theta$), potential vorticity (PV), equivalent latitude (φ_e), as well as a natural relative coordinate, i.e. the wind speed difference to the jet stream maximum wind speeds ($\triangle$FF). The latter one is considered separately in chapter 8 concerning long-term simulation with the Jülich CLaMS (McKenna et al., 2002b,a) since the spatial distribution of the measurement data is too limited for this purpose and thus for an accurate statement.

3.4.1 Probability distribution functions

Trace gas mixing ratios as well as meteorological parameters, such as temperature, potential temperature, pressure, wind velocities, etc., were obtained directly from the *in situ* measurements aboard the Learjet 35A. Potential vorticity was calculated from Northern Hemisphere ECMWF analyses which are described on page 18 in subsection 2.1.4. After the change of the vertical coordinate in the analyses data from pressure to potential temperature, potential vorticity was computed upon isentropes using Equation 3.1. However, the diagnosis of PV from meteorological data fields is contracted with errors (e.g., Beekmann et al., 1994; Good and Pyle, 2004). The procedure of data assimilation will obviously remove observational errors (Hollingsworth and Lönneberg, 1989). Anyhow, the accuracy in calculating PV is sensitive to the horizontal and vertical resolution and, in particular, small-scale meteorological features like tropopause folds are hardly to be represented in detail in the meteorological analyses. In contrast, *in situ* measurements have a much larger resolution and can therefore resolve small-scale features. This has to be considered when correlating model derived quantities with *in situ* measurements.
Another used dynamical coordinate is equivalent latitude (φ_e) which can be inferred from potential vorticity fields on isentropes. For an illustrated discussion of this parameter see section 4.1.

Probability distribution functions serve as a tool to transform localised aircraft data to a more comprehensive view of the probed region. As an advantage of the probability distributions, all measurement data are considered, and averaging is minimised. Thus, outliers become more visible and the prominent structures and features are revealed (Ray et al., 2004). In Figure 3.7, 2-dimensional probability distribution functions of O_3 (left column) and H_2O (right column) as a function of the thermal vertical coordinate potential temperature for each annual season are depicted. Ozone is binned by 20 ppbv, H_2O by 2 ppmv, and potential temperature by 5 K. The tracer distributions are normalised to every bin of the thermal coordinate. This means, the colour coding reflects the probability in percent to measure a certain trace gas concentration at a certain potential temperature. Additionally, the mean in each Θ-bin

is represented by the solid coloured line. In the bottom chart in each column, all seasonal means as well as the medians (dashed lines) are displayed to better compare to each other.

High probabilities, reflected by the bluish shadings, are very scattered throughout the O_3 distributions and, although both parameters can widely be seen as a vertical coordinate, no clear correlation is apparent. There is no symmetry around the mean or median values and multiple modes can be noted. Generally, an increase of O_3 VMRs with increasing potential temperature (height) is present but the ranging and spreading of O_3 concentrations on levels with constant potential temperature, the isentropes, is considerably large, resulting in a funnel or wedge structure. However, the large scatter and spread in the O_3 distributions is expected, since the O_3 concentrations are largely dependent upon the location of the tropopause. The single flight missions extended over a large latitude range. Therefore, the variability of potential temperature at the tropopause location during each deployment along the flight path was sometimes considerably large. For instance, on a flight from Kiruna to Hohn on November 11, 2001, the tropopause was located at 296 K in the vicinity of Kiruna and at 324 K near the campaign base Hohn, which is a variation of 28 K (cf. Table A-I). However, also at higher isentropes, i.e., further away from the local tropopause, the spread in O_3 concentrations is very high.

The total water probability distributions show similar characteristics as those of O_3. The large variations of the tropopause location are transparent in the high amounts of H_2O concentrations below ≈ 340 K, where also in the means, and sometimes in the medians, at lower isentropes a strong kink is present. A more compact distribution is only present above ≈ 350 K, with the higher variability during the summer season (cf. subsection 3.2.2).
When shifting the mean H_2O mixing ratios by ≈ 20 K towards lower isentropes the shape of the mean line is quite similar to the mean line for the winter season. The SPURT measurements are mainly concentrated in atmospheric regions above isentropes of ≈ 320 K. Thus, a strongest tropospheric influence during summer, as already mentioned in the previous section 3.3, is in agreement with the seasonally integrated mass flux through TST by Sprenger and Wernli (2003, their figure 3.b).

Probability distribution functions of the trace gases during winter and spring are quite different from the distributions for the measurement data during summer and autumn. Whereas the former show a rather steep distribution with rising O_3 concentrations and increasing potential temperature, the latter are more flat or show a prominent wedge structure towards higher isentropes. The large variability of tracer mixing ratios, especially at higher isentropes (e.g., > 400 ppbv O_3 at 360 K during all seasons) and the occurrence of several high probabilities on single isentropes, indicate that quasi-isentropic mixing is rather weak (see also section 4.1).

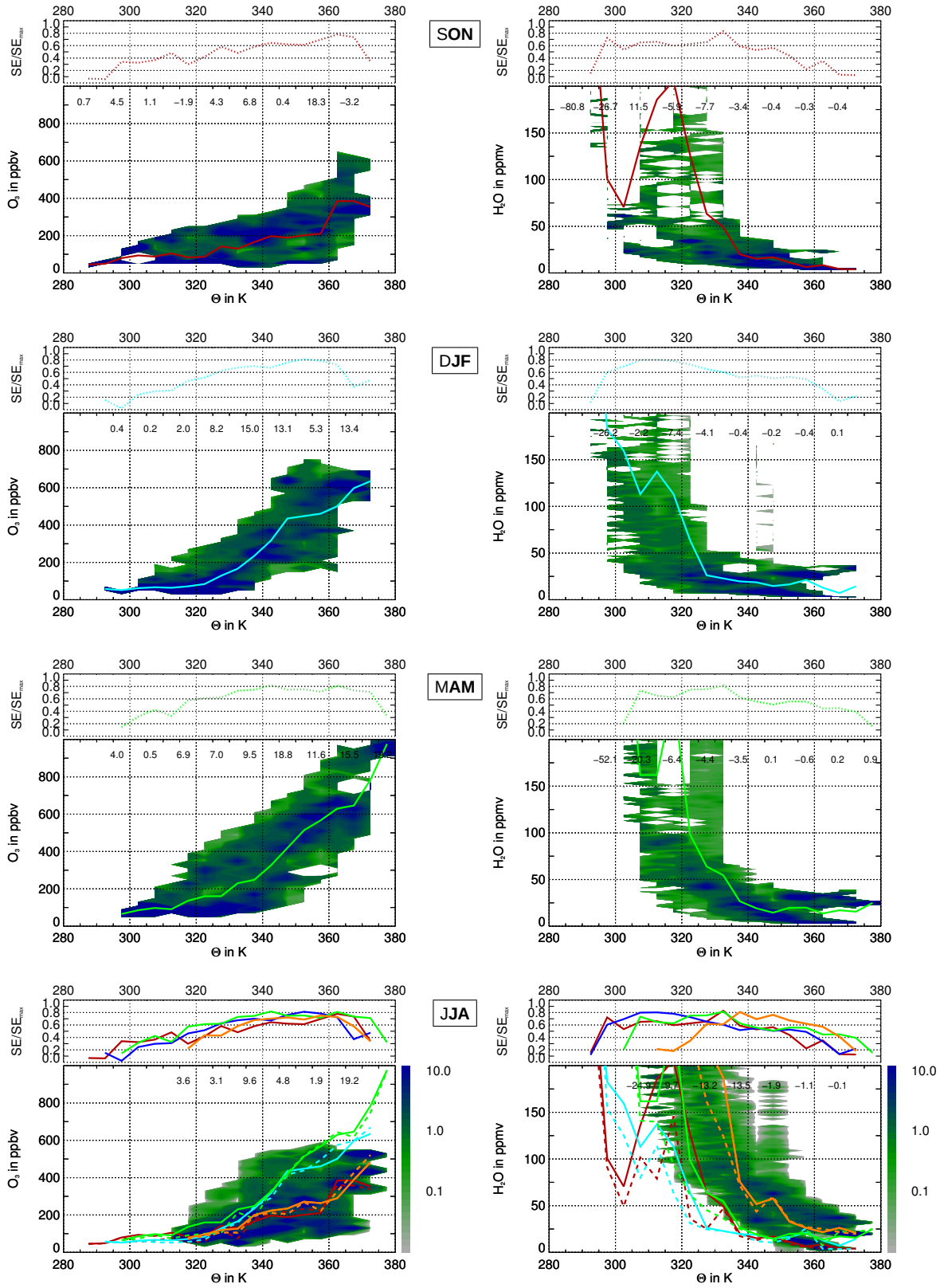

Figure 3.7.: Seasonal 2-dimensional probability distribution functions of ozone (left) and total water (right) as a function of the thermal coordinate potential temperature. The bin size is 20 ppbv for O_3, 2 ppmv for H_2O, and 5 K for Θ. The normalisation is performed to each Θ bin, i.e. the probability (colour coding) reflects the percentage of an observed tracer mixing ratio in a single Θ interval. In all panels the mean tracer mixing ratio in each particular Θ interval is given by the solid line. In the bottom plots, additionally, the derived means (solid lines) and medians (dashed lines) for each season are compared. In the top panel of each PDF the normalised mixing entropy in each Θ bin is displayed (see subsection 3.4.2), also seasonally compared in the bottom charts. From top to bottom: autumn, winter, spring, and summer.

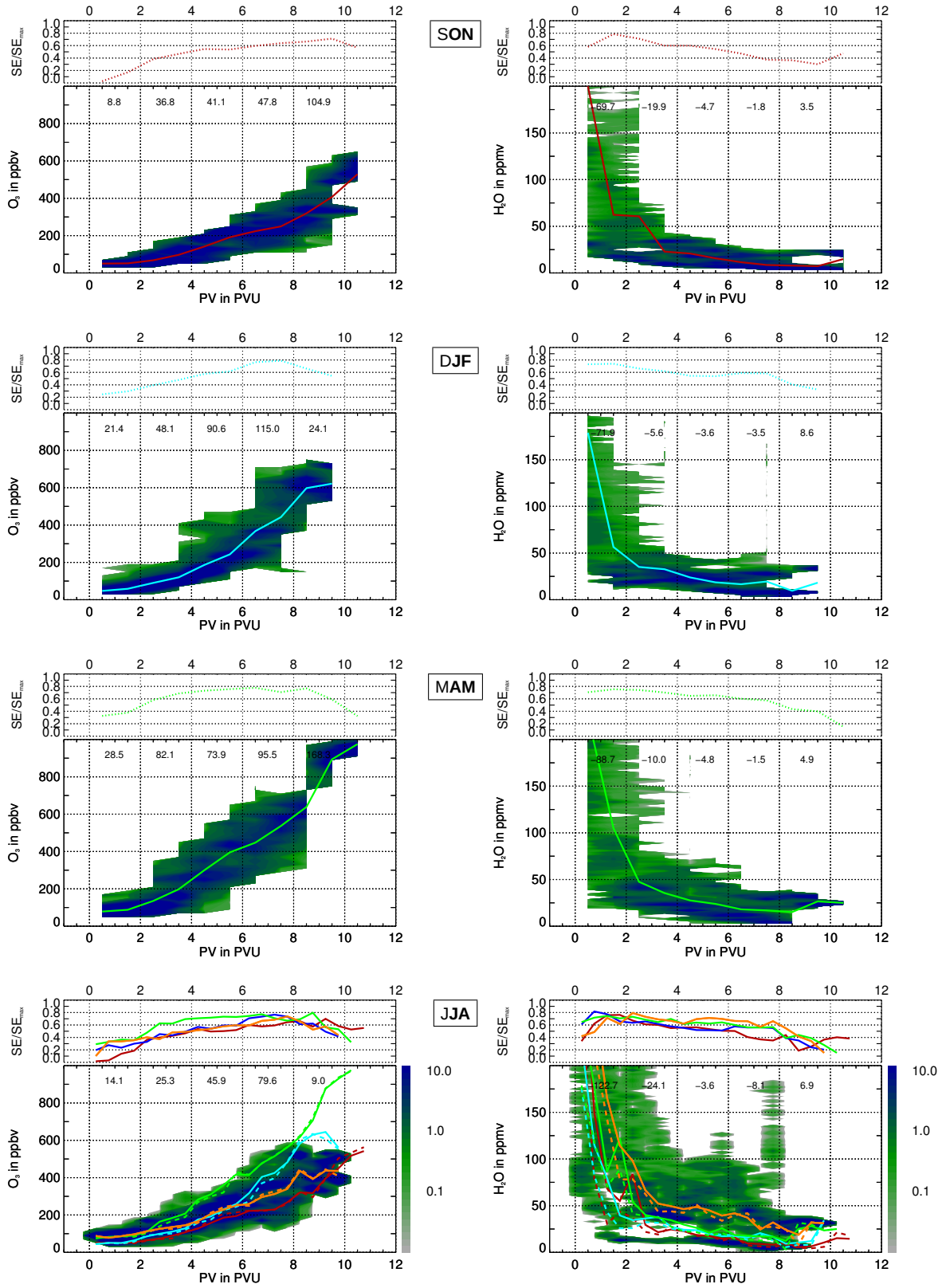

Figure 3.8.: 2-dimensional probability distribution functions of O_3 and H_2O as in Figure 3.7 but now for the dynamical coordinate potential vorticity. The bin size is 20 ppbv for ozone, 2 ppmv for total water, and 0.5 PVU for the dynamical coordinate.

The picture drawn on the basis of potential temperature changes significantly when shifting the thermal coordinate to a dynamic coordinate, namely PV. The corresponding tracer PDFs are shown in Figure 3.8 with PV incremented in 0.5 PVU steps. As is directly evident, O_3 is much more correlated with PV than with potential temperature, which is rather an accurate height or correlation parameter in the undisturbed stratosphere. The ranging of O_3 concentrations on surfaces of PV is considerably suppressed when compared to the spreading on isentropes. Even the wedge structure in the autumn and summer distributions with use of Θ is significantly reduced. The highest probabilities are mostly centred in the distributions and symmetrically arranged around the mean or median O_3 VMRs in every PV bin. In the 2-dimensional probability distribution functions additionally the tracer gradients in dependence from the coordinate are calculated for a doubled bin-size (except for PV where the gradients are given within 2.0 PVU intervals). The O_3/PV-gradients are $\approx 2-4$ times stronger in the $2.0-4.0$ PVU range than within the interval $0.0-2.0$ PVU. The means and medians show a slight kink in this range. This is once more an evidence that a value of 2.0 PVU is a good proxy for a dynamically defined extra-tropical tropopause during the SPURT missions. Of course, the gradient is weaker during summer which is due to the annual cycle of O_3 in the troposphere and in the lower stratosphere. A further issue in the PDFs is that the distinct seasonal cycles of O_3 in both atmospheric compartments, UT and LMS, are also present in the PDFs.
Considering the probability distributions for measured H_2O, the spreading is also reduced in the view of PV. The kink due to the varying location of the local tropopause in the potential temperature space is not present in the potential vorticity space. Also above $2.0-3.0$ PVU, i.e. the tropopause region, the variation of H_2O VMRs on PV surfaces is significantly reduced. As shown by the mean and medians, moreover the seasonal cycles of H_2O in the UT and LMS are reflected in the PDFs, with certainly higher mixing ratios during the summer months in the troposphere as well as in the lowermost stratosphere.

The tracer mixing ratios show a more compact distribution in a dynamical sense. In contrast to the spreading and distribution of several high probabilities on isentropic surfaces, Figure 3.8 reveals that tracer mixing ratios are more uniformly distributed and the probabilities vary less on PV surfaces. This indicates a more pronounced mixing state of trace gases on these surfaces rather than on isentropic surfaces.

A further coordinate system to look at the tracer distribution and their variability is a coordinate system centred at the tropopause. Unfortunately, there was no instrument aboard the Learjet 35A measuring the tropopause altitude. Anyhow, as shown in section 3.1, the extra-tropical tropopause during SPURT can be derived dynamically from a PV threshold value, i.e. 2.0 PVU. The distance from the local dynamical tropopause was therefore derived from the further described Northern Hemisphere ECMWF analyses by taking a certain PV sur-

face as the extra-tropical tropopause. Since the meteorological analyses were interpolated to isentropic surfaces, the actual distance of the aircraft's location to the local tropopause is denoted as $\triangle\Theta$ and is given in K. The tools for deriving $\triangle\Theta$ from ECMWF analyses were added to the `isentropic` package of CLaMS, developed in the recent years at the ICG-I. Thereby, two versions are implemented: one, called `add_dtp.f90`, works on the isentropic data set, the other, `add_dtp_isobar.f90`, works on isobaric levels. Both versions support the detection of tropopause fold locations as well as tropospheric injections into the stratosphere, if these features are resolved by the meteorological analyses. A short description of these tools was added to the documentation of the `isentropic` package of CLaMS.

To account for the strong gradient of PV in the tropopause region, several surfaces of potential vorticity were chosen as the dynamical extra-tropical tropopause ranging from 2.0 PVU to 4.0 PVU in 0.5 PVU steps. Through the different threshold values for the dynamical extra-tropical tropopause the character of the 2-dimensional probability distribution functions, i.e. location of high probabilities, spreading and tracer variability as well as the calculated tracer gradients, does not change seriously. Thus, for representativeness, only the distributions for the distance to the 2.0 PVU and 4.0 PVU surfaces are shown in Figure 3.9 and 3.10, respectively.
Both probability distribution functions with respect to the distance to a threshold value of PV look similar to those in the PV space. Anyhow, the use of $\triangle\Theta$ exhibits a slightly more compact shape, in particular for the campaigns in the winter and spring months (see also Table 3-I). Interpolation errors in the pure model derived quantity potential vorticity on a coarse grid are therefore larger compared to the coordinate $\triangle\Theta$ relative to the tropopause. Indeed, the latter is also partly derived from the meteorological analyses, but it also includes the *in situ* measurements of pressure and temperature, from which potential temperature is computed (Equation 2.1).

The fact that the PDFs in shape and distribution of probabilities in the view of PV and $\triangle\Theta$ look very similar suggests also an advanced mixing state of these trace gases on surfaces relative to the local tropopause. However, each air parcel in the atmosphere is labelled by its PV, controlling or restraining the parcels' range of motion. A relatively huge liberty of motion is given in regions of uniform potential vorticity (Sparling and Schoeberl, 1995). Thus, spatial gradients of PV might account for the dynamical affected trace gas distributions and not solely its absolute values. And this is exactly what the PDFs for different threshold values of PV for the dynamically defined extra-tropical tropopause show, since the shape and the spreading of distributions remain to the largest extent the same. This implies that the extra-tropical mixing-layer follows surfaces of PV or surfaces relative to the shape of the local tropopause rather than isentropic surfaces. This is consistent with the results from Hoor

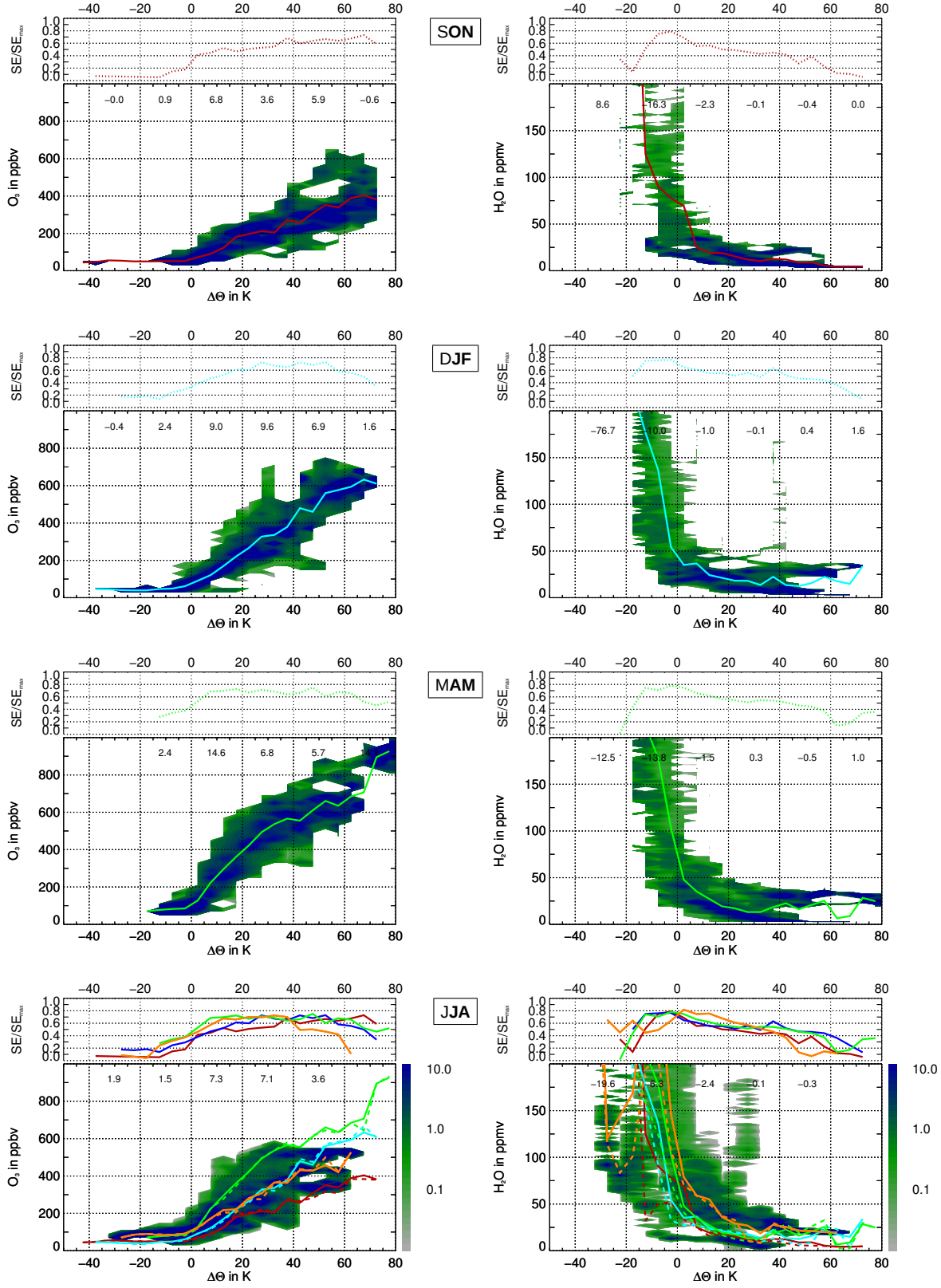

Figure 3.9.: 2-dimensional probability distribution functions of O_3 and H_2O as in Figure 3.7, but here as a function of $\triangle\Theta(2.0\ \mathrm{PVU})$, i.e. distance to the local tropopause, considered as the 2.0 PVU surface. The bin size is 20 ppbv for ozone, 2 ppmv for total water, and 5 K for $\triangle\Theta$.

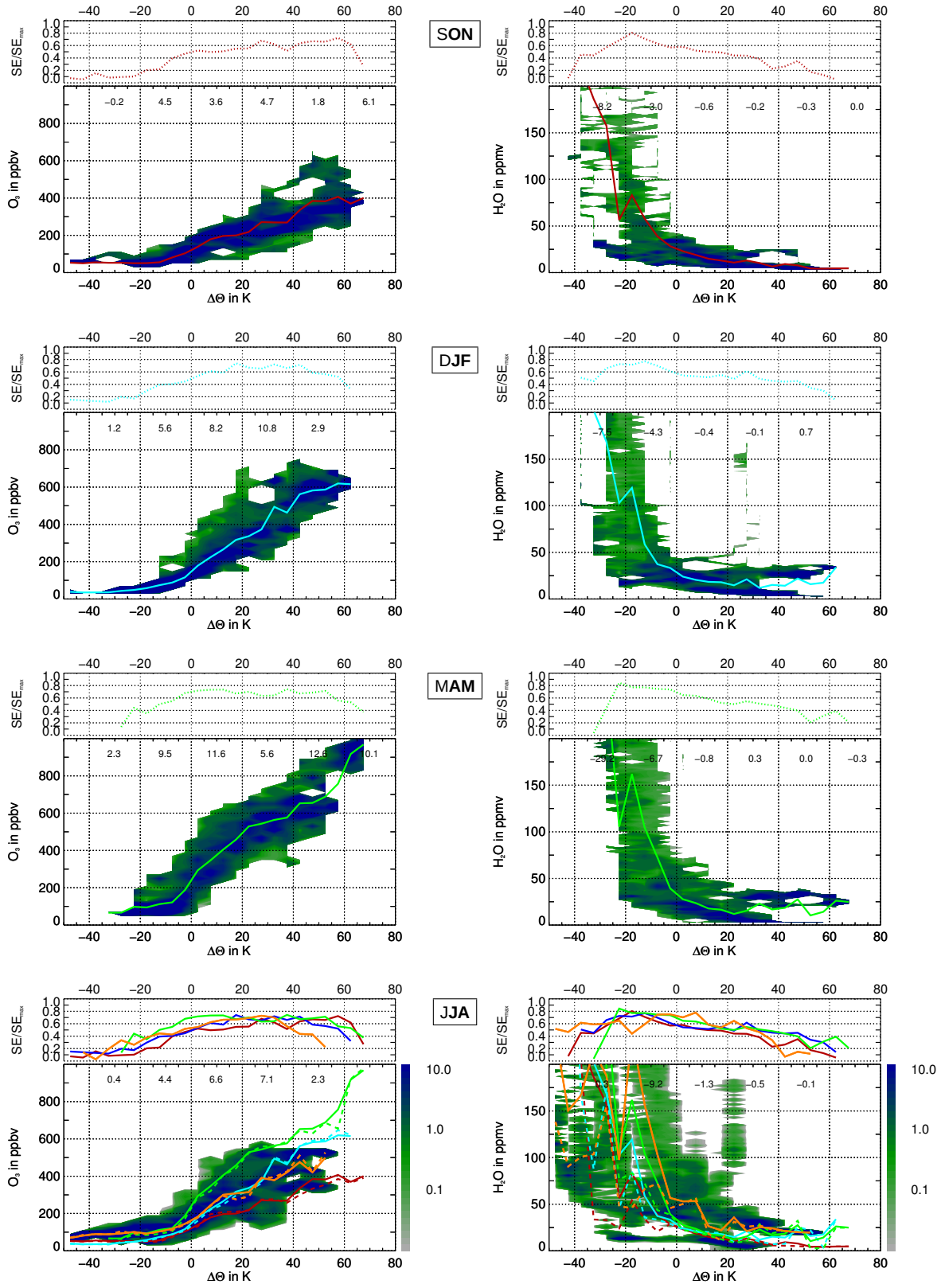

Figure 3.10.: 2-dimensional probability distribution functions of O_3 and H_2O as in Figure 3.7, but here as a function of $\triangle\Theta(4.0\ \text{PVU})$, i.e. distance to the local tropopause, considered as the 4.0 PVU surface. The bin size is 20 ppbv for ozone, 2 ppmv for total water, and 5 K for $\triangle\Theta$.

et al. (2004c). The implications related to this findings will be discussed in more detail in chapter 4.

The distributions for the other previously mentioned coordinates, such as meteorological parameters or equivalent latitude, show no such compact correlations as those before. Equivalent latitude, as a further dynamically significant coordinate, reveals an increase for the O_3 PDFs and an decrease for the H_2O distributions around $30°$N (not shown). However, the demonstrated range and spreading of trace gas mixing ratios in equivalent latitude bins is considerably large.

3.4.2 Mixing entropy

A useful measure for the tracer variability in the PDFs is, for instance, the entropy, which could in general be regarded as a measure for uncertainty. For a uni-modal PDF the characterisation is reliable given by the first and second moments, e.g. mean and variance, respectively. Using these moments, the PDF is described by a relation to a single reference value, like the mean. This is probably inaccurate for a multi-modal distribution, where there is no symmetry around the reference (Sparling, 2000). A measure for the information content in a PDF for a tracer μ provides Shannon's entropy which is given as

$$SE = -\sum_{i=1}^{N} p_i \cdot ln\, p_i, \tag{3.2}$$

with ln as the natural logarithm (e.g., Srikanth et al., 2000). It should be noted that SE is distinct from the thermodynamic entropy. Concerning a PDF with D total observed data points of tracer μ and N bins of width $\triangle\mu$, the fraction of observation in the i^{th} cell (p_i) is the number of observations within this cell (N_i) divided by D, and $\sum_{i=1}^{N} p_i = 1$. The information content is therefore solely dependent upon a given probability distribution and does not directly relate to the content or meaning of the underlying events, i.e. the quantity of the binned tracer. Only the probability of the occurring events is important, not the events themselves. SE is zero if the distribution has a maximum concentration, e.g. chemical homogeneity within one bin. For a uniform spatial distribution, i.e. $p_i = 1/N\ \forall i$, the considered tracer field has a maximum variability (any observed value can be placed in any one of the N bins) and the entropy is maximal ($SE = SE_{\text{max}} = ln\ N$). A maximum entropy implies indistinguishability of the air parcels. Moreover they have an unrestricted free range of motion. In reality, PV constrains the air parcels' range of motion (Sparling and Schoeberl, 1995). Thus, a maximum entropy value is not to expect.

The maximum entropy is dependent upon the number of bins. For a better comparison of different entropy values, a normalisation to the maximum entropy is performed, resulting in:

$$\frac{SE}{SE_{\text{max}}} = -\sum_{i=1}^{N} p_i \cdot \frac{ln\ p_i}{ln\ N} = -\sum_{i=1}^{N} p_i \cdot log_N\ p_i \quad \leq 1. \tag{3.3}$$

In all the 2-dimensional PDFs for O_3 the normalised mixing entropy values increase with height or distance to the tropopause. In the troposphere (i.e. low potential temperatures, PV values < 2 PVU, and negative values for $\triangle\Theta$) the normalised mixing entropy is considerably small, meaning only small-scale variability and low tracer variability. A low mixing entropy value indicates a rather homogeneous air mass. This seems a little bit strange, since a well-mixed state, as an equilibrium state, should have maximum entropy. However, the entropy here is considered in the "chemical space" in contrast to the "physical space" (Sparling, 2000). The 2-dimensional PDFs show highest entropy values in the tropopause region and in the lowermost stratosphere for H_2O and O_3, respectively. The corresponding tracer variability is maximal in these regions, implying the occurrence of different mixing states.
In all used different coordinates, normalised mixing entropy values show a reversed course for O_3 and H_2O. Total water mixing ratios are very variable in the troposphere, whereas ozone is more homogeneously distributed with respect to the considered bin size of the coordinate. Due to the strong gradient of both trace gases near or at the tropopause, normalised mixing entropy values increase for O_3 and decrease for H_2O. Therefore, at a PV value of ≈ 2 PVU ($\triangle\Theta = 0$ K for the distance to the 2.0 PVU surface) also a strong gradient in the mixing entropy is evident. During spring, the O_3 variability is highest in the lowermost stratosphere, probably due to the enhanced downward motion. Thus, the O_3 entropy values are maximal during this season. The same arises for the enhanced H_2O content and variability in the lowermost stratosphere during the summer months. The seasonal trace gas cycles are therefore also contained in the seasonal course of the mixing entropy.

3.5 Pearson's r and Spearman's ϱ

A measure of association between ordinal or continuous variables is Pearson's correlation coefficient r (product-moment coefficient). It reflects the degree of the linear relationship between two variables, say x and y, of size N ($1 \times N$ array). This functional correlation is defined as

$$r_{xy} = \frac{\sum_{i=1}^{N}(x_i - \bar{x})(y_i - \bar{y})}{\sqrt{\sum_{i=1}^{N}(x_i - \bar{x})^2}\sqrt{\sum_{i=1}^{N}(y_i - \bar{y})^2}}, \tag{3.4}$$

with $\bar{x}$ ($\bar{y}$) as the mean of the x_i's (y_i's). It can range from -1 to $+1$, inclusive, i.e. from a perfect negative to a perfect positive correlation, whereby $r = 0$ indicates that x and y are uncorrelated. For deciding, wether a correlation is significantly stronger than another, Pearson's r is not an accurate measure, since the individual distributions of x and y are not considered.

A more structural correlation provides Spearman's correlation coefficient ϱ. It is a nonparametric or rank correlation, i.e. a ranking measure for the relationship between two variables. The value of each x_i is replaced by the value of its rank, i.e. the smallest value of variable x is converted to rank 1, the highest to rank N. Thus, the x_i's are all distinct. For possible identical values of the x_i's, they are ranked by the mean of the ranks they would have if their values had been slightly different. The same applies for the y_i's. A high advantage of the rank correlation is that a nonparametric correlation is more robust than a linear correlation, in the same sort of sense that the median is more robust than the mean (Press et al., 1997). After converting the numbers to ranks the Spearman correlation coefficient is calculated according to Equation 3.4.

In Table 3-I both Pearson's and Spearman's correlation coefficients are shown for O_3 versus different parameters. Ozone does not show best correlations with potential temperature. As is directly evident from both coefficients, highest positive correlation coefficients appear when O_3 is correlated to potential vorticity and to the distance to the local tropopause. The coefficients are also high for almost all chosen threshold values of PV to define the local dynamical tropopause. Also the rather simple measure for the association between two parameters reveal the conclusion drawn from the 2-dimensional PDFs: tracer isopleths of O_3 seem to be orientated along surfaces of potential vorticity rather than along isentropes. The differences between r and ϱ for PV and the $\triangle\Theta$s are only small. However, correlation coefficients of O_3 with the other parameters are comparatively insignificant.

The correlation coefficients for total water and different parameters are listed in Table 3-II. When calculating Pearson's r, total water is best correlated with pressure. Both, p and H_2O decrease very rapid with height and they show a rather logarithmic decrease. Thus, the good correlation is to expect. Spearman's ϱ is independent of the mode or shape of the distribution, and it renders unnecessary to make assumptions on the functional relationship (Press et al., 1997). For this measure, H_2O shows high negative coefficients when correlated with Θ, $\triangle\Theta$ and PV. Correlations with the actual ice saturation (IS) mixing ratio and also with the minimum IS within the previous 5 and 10 days show very alternating coefficients and sometimes even almost no relationship.

Table 3-I: Pearson's r (top) and Spearman's rank ϱ (bottom) correlation coefficients for ozone versus potential temperature (Θ), potential vorticity (PV), distance to the local dynamically defined tropopause (i.e. 2.0, 2.5, 3.0, 3.5, 4.0 PVU surface, $\triangle\Theta_{2.0}$, $\triangle\Theta_{2.5}$, $\triangle\Theta_{3.0}$, $\triangle\Theta_{3.5}$, $\triangle\Theta_{4.0}$, respectively), pressure (p), temperature (T), horizontal wind velocity (FF), and equivalent latitude (φe). The correlation coefficients are given for the eight single SPURT campaigns IOP $1-8$). Best correlation coefficients (negative or positive) for each campaign are highlighted in red.

O_3	IOP1	IOP2	IOP3	IOP4	IOP5	IOP6	IOP7	IOP8
Θ	0.56	0.79	0.81	0.55	0.66	0.86	0.88	0.45
PV	**0.93**	0.88	0.90	**0.84**	0.87	0.87	0.92	**0.90**
$\triangle\Theta_{2.0}$	0.85	0.91	**0.92**	0.79	0.88	**0.93**	**0.93**	0.82
$\triangle\Theta_{2.5}$	0.85	**0.93**	**0.92**	0.80	**0.89**	0.92	**0.93**	0.83
$\triangle\Theta_{3.0}$	0.86	**0.93**	**0.92**	0.80	**0.89**	0.91	**0.93**	0.84
$\triangle\Theta_{3.5}$	0.86	0.92	**0.92**	0.81	**0.89**	0.91	**0.93**	0.85
$\triangle\Theta_{4.0}$	0.86	0.92	0.91	0.81	**0.89**	0.91	0.92	0.86
p	-0.27	-0.50	-0.28	-0.37	-0.43	-0.54	-0.71	-0.27
T	0.18	0.17	0.58	0.20	0.39	0.49	0.30	0.19
FF	-0.46	-0.26	-0.15	-0.37	-0.39	-0.30	-0.50	-0.36
φe	0.85	0.67	0.59	0.51	0.58	0.50	0.56	0.68

O_3	IOP1	IOP2	IOP3	IOP4	IOP5	IOP6	IOP7	IOP8
Θ	0.58	0.79	0.83	0.53	0.63	0.85	0.90	0.45
PV	**0.92**	0.93	0.92	**0.87**	**0.85**	0.88	0.92	**0.92**
$\triangle\Theta_{2.0}$	0.85	0.93	**0.95**	0.80	0.84	**0.91**	**0.93**	0.85
$\triangle\Theta_{2.5}$	0.85	**0.95**	**0.95**	0.80	0.84	**0.91**	**0.93**	0.88
$\triangle\Theta_{3.0}$	0.85	**0.95**	**0.95**	0.81	0.84	**0.91**	**0.93**	0.90
$\triangle\Theta_{3.5}$	0.86	**0.95**	0.94	0.83	**0.85**	**0.91**	**0.93**	0.91
$\triangle\Theta_{4.0}$	0.86	**0.95**	0.93	0.84	0.84	0.90	0.92	0.91
p	-0.13	-0.61	-0.18	-0.38	-0.38	-0.48	-0.78	-0.20
T	0.40	0.31	0.53	0.15	0.40	0.50	0.36	0.21
FF	-0.45	-0.28	-0.14	-0.44	-0.46	-0.25	-0.56	-0.41
φe	0.85	0.75	0.63	0.53	0.54	0.43	0.47	0.68

Table 3-II: As table Table 3-I but correlation coefficients computed for H_2O. Additionally, the ice saturation mixing ratio (IS) at the measurement time as well as the minimum IS during the previous 5 and 10 days (IS^5_{min} and IS^{10}_{min}, respectively) is considered.

H_2O	IOP1	IOP2	IOP3	IOP4	IOP5	IOP6	IOP7	IOP8
Θ	-0.60	-0.46	-0.55	-0.59	-0.40	-0.52	-0.43	-0.63
PV	-0.42	-0.48	-0.57	-0.46	-0.49	-0.58	-0.48	-0.52
$\triangle\Theta_{2.0}$	-0.43	-0.44	-0.51	-0.50	-0.45	-0.46	-0.38	-0.51
$\triangle\Theta_{2.5}$	-0.43	-0.45	-0.51	-0.48	-0.45	-0.46	-0.39	-0.50
$\triangle\Theta_{3.0}$	-0.44	-0.45	-0.50	-0.46	-0.45	-0.46	-0.39	-0.48
$\triangle\Theta_{3.5}$	-0.44	-0.45	-0.49	-0.45	-0.45	-0.47	-0.39	-0.47
$\triangle\Theta_{4.0}$	-0.44	-0.45	-0.49	-0.43	-0.44	-0.47	-0.40	-0.45
p	**0.73**	0.70	**0.73**	**0.80**	0.59	**0.74**	**0.65**	**0.74**
T	0.54	0.60	0.34	0.79	0.30	0.41	0.51	0.60
FF	0.04	0.08	0.14	-0.03	-0.00	0.35	0.07	0.12
φe	-0.16	-0.39	-0.43	-0.13	-0.36	-0.36	-0.29	-0.25
IS	0.61	0.64	0.50	0.67	**0.65**	0.39	0.49	0.49
IS^5_{min}	0.61	**0.74**	0.35	0.60	0.48	0.51	0.35	0.31
IS^{10}_{min}	0.62	0.73	0.36	0.59	0.57	0.62	0.37	0.41

H_2O	IOP1	IOP2	IOP3	IOP4	IOP5	IOP6	IOP7	IOP8
Θ	-0.74	**-0.87**	-0.89	**-0.91**	**-0.92**	-0.36	-0.60	**-0.86**
PV	-0.65	-0.85	-0.91	-0.64	-0.83	**-0.55**	-0.58	-0.60
$\triangle\Theta_{2.0}$	**-0.80**	**-0.87**	**-0.95**	-0.81	-0.90	-0.44	-0.56	-0.76
$\triangle\Theta_{2.5}$	**-0.80**	**-0.87**	**-0.95**	-0.79	-0.90	-0.44	-0.56	-0.75
$\triangle\Theta_{3.0}$	**-0.80**	**-0.87**	-0.94	-0.76	-0.90	-0.44	-0.56	-0.73
$\triangle\Theta_{3.5}$	-0.79	-0.86	-0.93	-0.71	-0.90	-0.44	-0.56	-0.71
$\triangle\Theta_{4.0}$	-0.79	-0.86	-0.92	-0.63	-0.90	-0.44	-0.56	-0.67
p	0.45	0.81	0.32	0.88	0.69	0.48	**0.67**	0.85
T	-0.06	0.01	-0.37	0.32	-0.45	0.26	0.22	0.56
FF	0.24	0.24	0.10	0.15	0.07	0.17	-0.05	0.08
φe	-0.33	-0.53	-0.59	0.06	-0.32	-0.45	-0.14	-0.05
IS	-0.16	-0.12	-0.43	0.08	-0.60	0.19	0.07	0.44
IS^5_{min}	-0.16	-0.18	-0.41	0.47	-0.58	-0.12	0.02	0.17
IS^{10}_{min}	-0.10	-0.23	-0.27	0.44	-0.50	0.15	0.03	0.16

3.6 Main results of this chapter

In the first part, the seasonal cycles of O_3 and H_2O in the upper troposphere and in the lowermost stratosphere have been analysed as measured during SPURT. Thereby, it was derived that the tropopause location, i.e. the noticeable boundary between the troposphere and the stratosphere, coincides quite well with the 2 PVU surface. Different analyses of the trace gas measurements reveal that the seasonal cycle of O_3 in the UT shows a spring to summer maximum, which is most probably affected by *in situ* photochemistry. In the LMS the seasonal O_3 cycle is shifted in phase by about $2-3$ months prior, exhibiting a distinct maximum during spring. This is the result of the large-scale downward transport of O_3-rich stratospheric air during the winter/spring Brewer-Dobson circulation.
In contrast to the O_3 seasonal cycle, H_2O shows no phase shift in the UT and LMS. Maximum H_2O mixing ratios were observed during the summer campaigns, whereas lowest H_2O VMRs were measured during autumn and winter.

In a second part of this chapter, the distribution, spreading, and variability of both trace gases were examined. Thereby, especially 2-dimensional probability distribution functions were used. Considering several chemical, thermal, and dynamical coordinates, the measured trace gases show most compact distributions and best correlations when related to potential vorticity and distance to the dynamically defined tropopause. Moreover, using various threshold values for the extra-tropical tropopause, the distributions show almost the same shape. This indicates that trace gas isopleths follow surfaces of PV or the shape of the tropopause.

Chapter 4

Seasonal variation of the extra-tropical mixing layer

4.1 Distributions in the Θ-φ_e space

When considering transport and mixing, potential temperature (Θ) has some advantages over altitude as a vertical coordinate, since transport and mixing tend to occur on isentropic levels rather than on isobaric levels. Furthermore, atmospheric motions can be investigated upon adiabates, levels of constant internal energy. Under adiabatic conditions, Ertel's potential vorticity is considered to be a conservative parameter in the lower stratosphere (LS) over a period of some days to weeks (Danielsen, 1990). Since PV increases monotonically in the Northern Hemisphere LS with altitude and geographical latitude, PV can be used as a transport tracer (Danielsen, 1968). The diagnosis of PV from meteorological data fields is contracted with errors (see subsection 3.4.1). However, although it is an appropriate parameter, but not an ideal one due to its limited conservation in the atmosphere (Good and Pyle, 2004), for each air parcel an equivalent latitude (φ_e) can be inferred from the PV distribution on isentropes (Butchart and Remsberg, 1986). After calculating the area that is enclosed by a PV contour on a hemisphere and transforming it to a circle of identical area centred at the pole, equivalent latitude is defined as the distance in degrees latitude from the equator to that circle. This has widely been used to indicate the edge of the polar vortex (Nash et al., 1996) and to estimate a parcel's average recent latitude (Strahan et al., 1999). It is to note that an equivalent latitude can not only be determined for PV, but also for any field μ that shows a mean monotonic decrease or increase with latitude on a given isentrope, as e.g. done for O_3 and H_2O by Esler et al. (2001). Thus, a unique relation between μ and φ_e arises on each isentrope. Equivalent latitude is thus defined by

$$\varphi_e = arcsin \frac{1 - A(\mu_q)}{2\pi r_e^2}, \tag{4.1}$$

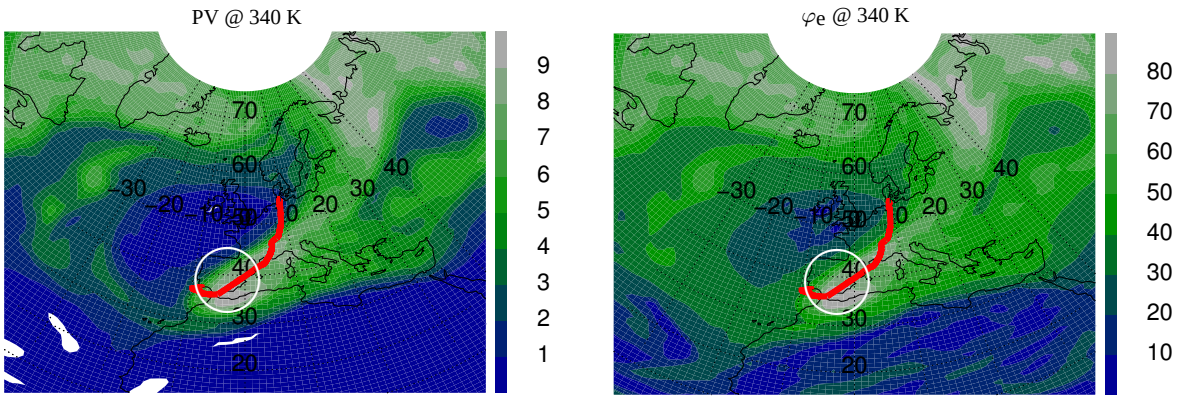

Figure 4.1.: Example (i) for advantages when using equivalent latitude instead of geographical latitude. Left: Potential vorticity (PV, colour coding in PVU) on the 340 K isentropic surface for the first SPURT mission on November 11, 2001. The flight path is displayed in red. Right: Same design but equivalent latitude (φ_e in °N) colour coded. For details concerning this mission see Hegglin et al. (2004).

where $A(\mu_q)$ is the area enclosed by the value μ_q on the considered isentrope and r_e is the Earth's radius (e.g., Sobel et al., 1997).

The use of equivalent latitude is especially favourable for deriving a tracer climatology since reversible large-amplitude wave motions are nearly smoothed out. For instance, polar air with high potential vorticity values encounters a large meridional displacement or filamentation (i.e. it is surrounded by air of different characteristic, say lower values of potential vorticity) from its originally high-latitude position deep into the mid-latitudes. Although this air now is located in the mid-latitudes the concept of equivalent latitude would move that air parcel to higher latitudes, due to its high potential vorticity values. This is illustrated in Figure 4.1 for the first SPURT mission on November 11, 2001. On the left hand side, the potential vorticity field on the 340 K isentrope is colour coded. The flight path is denoted in red. The aircraft crossed the stratospheric streamer with high potential vorticity values which was deeply elongated into middle and lower latitudes (down to Northern Africa, cf. also Thomas et al., 2003). The right chart shows the corresponding PV-derived field of equivalent latitude on the same isentrope. In the view of equivalent latitude, high-PV air is assigned to high equivalent latitudes, as schematically denoted by the white circle.

Another advantage of φ_e is the enhancement of information of airborne measurement data (e.g., Randel et al., 2001). During a flight mission air of different characteristic is sampled in a limited latitudinal area. This enlarges conspicuously when applying the concept of equivalent latitude. Exemplary, a height-latitude cross-section of the measured ozone distribution on the first flight of the SPURT campaigns is displayed in Figure 4.2. On the left hand side the distribution is displayed with respect to geographical latitude, and on the right the same measurement data is shown with the use of equivalent latitude. In the latter chart, the infor-

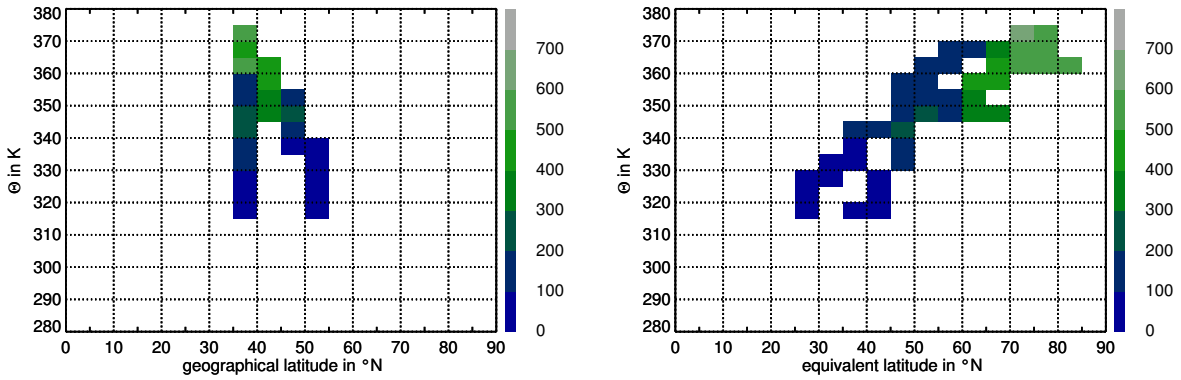

Figure 4.2.: Example (ii) for advantages when using equivalent latitude instead of geographical latitude. Left: Distribution of ozone measurements (O_3, colour coding in ppbv) on the first flight mission on November 11, 2001 in the potential temperature and geographical latitude (φ) space. Right: Same distribution with the use of equivalent latitude (φ_e).

mation content is considerable enhanced and the latitudinal range has increased by a factor of ≈ 3.

However, despite that also constraints to equivalent latitude arise. The important fine-scale variability cannot be resolved by the coarse resolution of meteorological data. Further, analysis data points in areas with sparse meteorological measurements for data assimilation and in the tropics can result in errors of equivalent latitude where it then is not viable (e.g., Strahan et al., 1999; Eyring et al., 2004).

Seasonal distributions of measured total water and ozone are depicted in Figure 4.3 in the space of potential temperature and equivalent latitude. Potential temperature is incremented by 5 K intervals, equivalent latitude by $5°$N. The black solid lines display the location of the (mean) iso-surfaces of potential vorticity (2, 4, 6, 8 and 10 PVU) in the established coordinate system. To define the extra-tropical local tropopause, the dynamical criterion of the 2 PVU surface is chosen (cf. section 3.1 and also Hoor et al., 2004c). Since the gradient of potential vorticity at the tropopause is very strong, the chosen value of 2 PVU is not very critical (Hoskins, 1991), except of course for quantifying mass fluxes through PV-surfaces (e.g., Bourqui, 2004). Additionally, a change to 3 or 4 PVU for the location of the extra-tropical tropopause does not effect the conclusions drawn in the following, which were also suggested from the results of the probability distribution functions in subsection 3.4.1 and the mixing entropy in subsection 3.4.2. The 2 PVU-surface in Figure 4.3 is therefore entitled as ”mean TP” (i.e. mean tropopause). The equivalent latitudes for each seasonal distribution were calculated from several ECMWF analyses according to the flight days included, which means also data from different years. The potential vorticity surfaces, in particular the lower ones, are hence *a priori* not uniquely defined in that potential temperature and equivalent latitude coordinate system. The lowest potential vorticity value of an isentrope in each analysis could obviously be different. This results in varying equivalent latitudes on the same

isentropes in different analyses. A slight spread of potential vorticity values in a grid cell of the given coordinate system is evident. To account for that issue the dashed black lines mark the maximal and minimal location of a 2 PVU value in each equivalent latitude bin.

In an overall view of Figure 4.3 the seasonal variation in the tropopause height and its exposure relative to isentropes is evident. Mean tropopause locations (mean variations) between $30°$N and $70°$N in autumn, winter, spring and summer are $297 - 346$ K (49 K), $289 - 337$ K (48 K), $300 - 343$ K (43 K), $315 - 354$ K (39 K), respectively. The location of the dynamical tropopause at lowest potential temperatures during winter implies the increasing mass of the Northern Hemisphere stratosphere and vice versa during summer (e.g., Appenzeller et al., 1996b). Additionally, the rising tropopause towards summer is an effect of the increasing temperatures. The variation in tropopause height between lower and higher latitudes is lowest during summer, exhibiting lowest gradients of potential vorticity on isentropic surfaces. This is accompanied with a weaker sub-tropical jet in summer and its northward propagation during this season. In winter and spring near $30°$N the surfaces of potential vorticity bulge upward with a strong vertical gradient, probably due to the location and the strength of the sub-tropical jet. All distributions show the strong gradient in total water and ozone across the tropopause which is present in the vertical as well as in the latitudinal direction. Three characteristic regions can be distinguished: the troposphere with high and variable total water (≈ 100 to above 1000 ppmv) and low ozone mixing ratios (≈ 100 ppbv), the lowermost stratosphere with low total water (in the mean < 20 ppmv) and high ozone (> 400 ppbv on average), and the tropopause region with intermediate tracer mixing ratios (cf. also Figure 3.6 and Table 4-I).

The strong mean gradient in total water at the local tropopause is to be expected since the water content of air (with the primary tropospheric water source) is widely controlled by temperature. Therefore, above the tropopause the total water variability decreases considerably and the latitudinal gradients are weaker. However, related to the stratospheric water content the variability is rather large.
Only 10% of the atmospheric ozone content is located in the troposphere (e.g., Lelieveld and Dentener, 2000). Due to its high potential for participating in oxidation processes, ozone increases with height and has also a strong gradient across the tropopause. Therefore, ozone has widely been used for a chemical tropopause definition (e.g., Bethan et al., 1996; Thouret et al., 1998; Talbot et al., 1999; Zahn et al., 2004a). The distributions of both total water and ozone mixing ratios clearly demonstrate the non-isentropic arrangement of the tracer isopleths which rather follow potential vorticity surfaces. Tracer mixing ratios in and several 10 K above the tropopause region form a layer which is strongly correlated to the shape of the tropopause and/or potential vorticity surfaces. These features are apparent in each season. Intermediate tracer concentrations indicate the region of the tropopause-following mixing

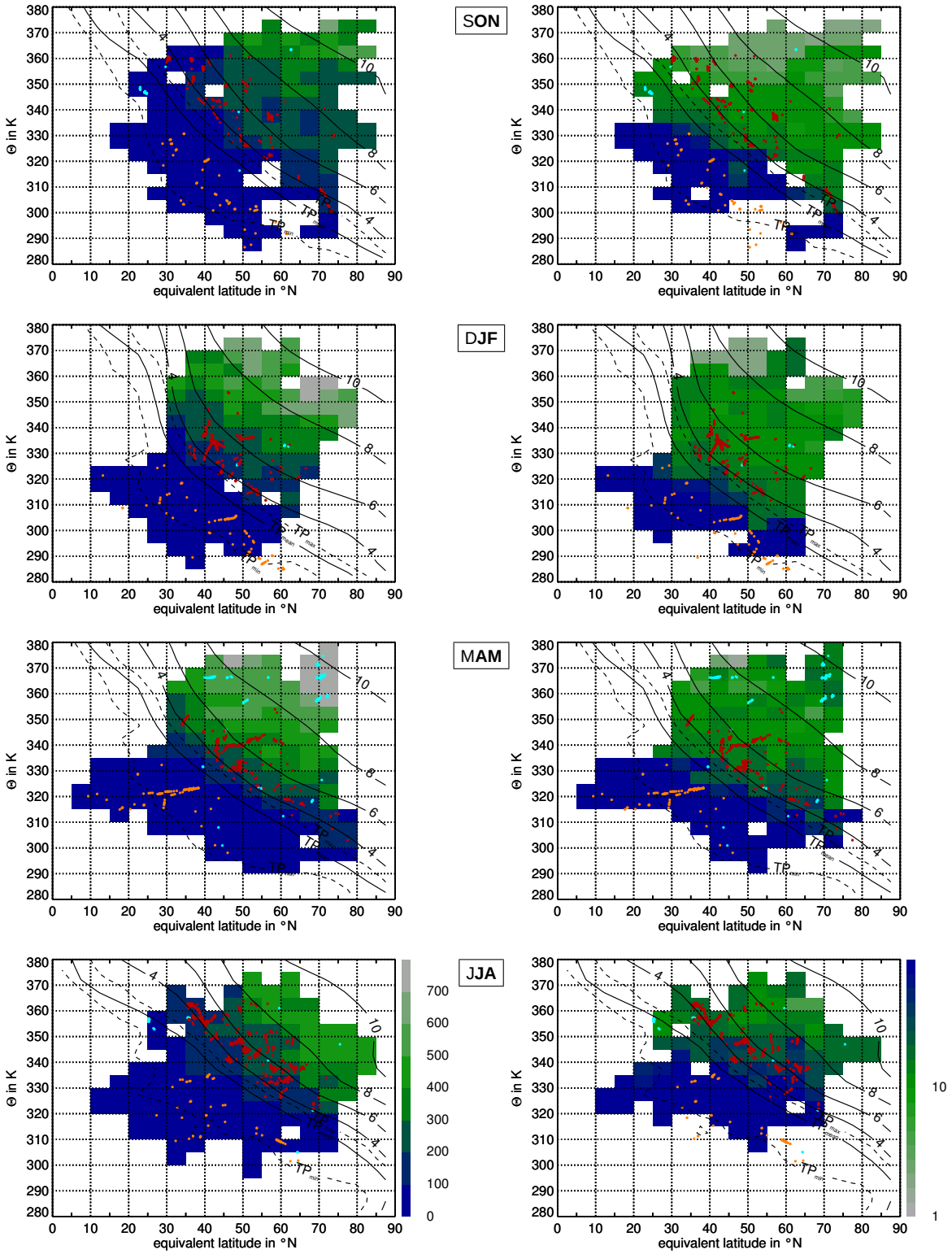

Figure 4.3.: Seasonal distributions of measured ozone (left) and total water (right) in the potential temperature and equivalent latitude space. Mixing ratios in ppbv and ppmv, respectively, are reflected by the colour coding bar placed at the right of the last chart in each column. The black solid lines display the mean PV iso-surfaces in the Θ-φ_e space from 2 to 10 PVU in 2 PVU increments. The dashed black lines reflect the maximal and minimal position of the dynamical tropopause (2.0 PVU) in each equivalent latitude bin (see text for remarks). Additionally, significant TST and STT trajectories (see section 4.2 for details) within the previous 10 days are displayed by the red and orange dots, respectively. Air parcels that travel quasi-isentropically (within a 5 K range) are reflected by the cyan dots. (Top to bottom: autumn, winter, spring, and summer.)

layer with the tropopause as its lower boundary. This is consistent with the findings from Hoor et al. (2004c), based upon CO measurements during SPURT. Total water shows less variability in the investigated area than ozone. At a distance of approximately $\triangle\Theta = 30-40$ K above the tropopause, compared to H_2O mixing ratios of the undisturbed lowermost stratosphere, total water is more variable in equivalent latitude regions between 50 and $85°$N. Further, H_2O VMRs are even as high as at about $10 - 20$ K above the tropopause. Those features with high ozone and significantly enhanced total water have also been detected during all seasons.

It is worth to note that several bins in the space of potential temperature and equivalent latitude at very high and low latitudes have been sampled only during a single flight so that the number of measurements there is low. Further, due to the larger variability of the H_2O data, the number of measurements or the limited spatial region is possibly too sparse to derive a definite and exact seasonal climatology of total water in the upper troposphere and lowermost stratosphere. A determination of a (more reliable) seasonal mean requires considerably more data. Especially, in the second half of SPURT primary higher total water mixing ratios have been observed in the lowermost stratosphere compared to the first 4 campaigns, highlighting the strong variability of total water in that atmospheric region.

4.2 Tracer and transport analyses with backward trajectories

4.2.1 Trajectory calculations and air parcel statistic

To quantify and identify transport across the tropopause by advection (and mixing) processes 10 day backward trajectories were calculated with the 3-dimensional trajectory module of the Chemical Lagrangian Model of the Stratosphere (CLaMS, McKenna et al., 2002b,a). The module was driven by the above described ECMWF analyses. Traditionally, to derive the isentropic vertical velocity ($\dot{\Theta}$ in K d^{-1}) for trajectory studies with CLaMS an extended Mocrette scheme (Mocrette, 1991) is applied. This works sufficiently in the stratosphere (Konopka, 2003, personal communication), but not necessarily in the troposphere and in the tropopause region since no cloud information is considered in CLaMS up to now. Since the measurements during SPURT had a maximum potential temperature of ≈ 380 K with most measurements below that level and rather in the vicinity of the tropopause region, the Mocrette scheme was not applied here. If alternatively the hybrid vertical velocity (ω) in the meteorological analysis is used and converted to its isentropic form, occasionally unrealistic strong differences in the vertical velocity of neighboured grid cells occur. Therefore,

before interpolating to the isentropic levels, the isentropic vertical velocity was calculated on isobars including temperature advection and local temperature change according to

$$\begin{aligned} \dot{\Theta} &= \mathrm{d}_t\Theta \overset{\text{(Equation 2.1)}}{=} \mathrm{d}_t \left[T \cdot \left(\frac{p}{p_0} \right)^{-\kappa} \right] \\ &= \frac{\Theta}{T} \cdot \left[\partial_t T + \mathbf{v} \bullet \nabla T \right] - \kappa \frac{\Theta}{p} \cdot \omega, \end{aligned} \tag{4.2}$$

which in K d^{-1} looks for an analysis data set like

$$\dot{\Theta}|_t = \left(\left. \frac{\Theta}{T} \right|_t \cdot \left[\frac{T|_{t-1} - T|_{t+1}}{2 \cdot TR} + \left. \begin{pmatrix} u \\ v \\ \omega \end{pmatrix} \right|_t \bullet \left. \begin{pmatrix} \partial_\lambda T \\ \partial_\varphi T \\ \partial_p T \end{pmatrix} \right|_t \right] - \kappa \left. \frac{\Theta}{p} \right|_t \cdot \omega|_t \right) \cdot DL. \tag{4.3}$$

Thereby, $\mathbf{v}$ is the wind vector with its horizontal components u and v in m s^{-1} and the vertical velocity ω in Pa s^{-1}, ∇T is the temperature gradient (horizontal deviations in λ and φ, vertical deviation in pressure p), DL is the length of day in s, TR is the time resolution of the analyses in s, $T|_{t-1}$ and $T|_{t+1}$ denote the temperature fields of the time slices before and after the considered "actual" ($|_t$) analysis data set. This is only slightly different from the approach performed by Norton (2001). However, the results of the applied scheme here tend to work sufficiently and are at least physically correct. This preprocessor named `add_thetadot_isobar.f90` for the ECMWF analyses is now also part of the `isentropic` package in CLaMS. For future studies with CLaMS in the extra-tropical tropopause region and in the tropics, a mixed scheme for the isentropic vertical velocity $\dot{\Theta}$ should be considered. A reasonable solution would be a weighted functional relation of the applied form in this study and of the Mocrette scheme, with a stronger weight of the former in the tropopause region and an increasing relevance of the latter in the stratosphere. An alternative for another vertical coordinate is the use of a generalised isentropic coordinate which is rather isobaric below the tropopause region and isentropic above (personal communication, Konopka, 2004; Günther, 2004). In the transition zone, troposphere – lowermost stratosphere, this hybrid coordinate (Mahowald et al., 2002) is changed smoothly from isobars to isentropes. However, stringent tests have to be taken into account for an "optimal" solution which are subject of recent work in the modelling group at the ICG-I.

To get a better insight into the character of the observed air parcels, in Table 4-I a simple statistic of the measurement data based upon the information of the calculated trajectories is presented. For each season the percentage of observed pure tropospheric (TRO), pure stratospheric (STR), and air parcels in between, denoted as the tropopause region (TPR), within which transient, quasi-reversible cross-tropopause flows are confined to (James et al., 2003a), are given. Furthermore, the corresponding mean and median ozone ($\overline{\mathrm{O_3}}$ and $\widetilde{\mathrm{O_3}}$), mean and median total water ($\overline{\mathrm{H_2O}}$ and $\widetilde{\mathrm{H_2O}}$) and mean and median ice saturation ($\overline{\mathrm{IS}}$ and

$\widetilde{\text{IS}}$) mixing ratio values are shown. Ice saturation (in ppmv) is obtained by applying the formula for ice saturation vapour pressure (in Pa) of Marti and Mauersberger (1993)

$$e_{\text{sat}} = 10^{\left(\frac{-2663.5}{T} + 12.537\right)} \tag{4.4}$$

and its conversion to ppmv (Wiederhold, 1997)

$$IS = 1.E6 \cdot \frac{e_{\text{sat}}}{p - e_{\text{sat}}}. \tag{4.5}$$

Temperature T in Equation 4.4 is in K, pressure p in Equation 4.5 is in Pa. Pure tropospheric air means parcels with potential vorticity values at the measurement time ≤ 1 PVU, pure stratospheric air denotes parcels with a potential vorticity ≥ 3 PVU. Additionally, a differentiation for sampling in three different equivalent latitude ranges ($0°$N$\leq \varphi_e \leq 30°$N, $30°$N$< \varphi_e < 60°$N, $60°$N$\leq \varphi_e \leq 90°$N) is regarded.

Table 4-I: Air parcel statistic with respect to different equivalent latitude ranges and three atmospheric regions (TRO≡troposphere, TPR≡tropopause region, STR≡stratosphere). Mean and median values for ozone ($\overline{O_3}$ and $\widetilde{O_3}$ in red), total water ($\overline{H_2O}$ and $\widetilde{H_2O}$ in blue) and ice saturation ($\overline{\text{IS}}$ and $\widetilde{\text{IS}}$ in green) mixing ratios are given in ppbv, ppmv and ppmv, respectively, mean and median potential vorticity values ($\overline{\text{PV}}$ and $\widetilde{\text{PV}}$ in black) are in PVU. Maximum values are displayed in bold, minimum values in italics.

		$0°\text{N} \leq \varphi_e \leq 30°\text{N}$				$30°\text{N} < \varphi_e < 60°\text{N}$				$60°\text{N} \leq \varphi_e \leq 90°\text{N}$			
		aut	**win**	**spr**	**sum**	**aut**	**win**	**spr**	**sum**	**aut**	**win**	**spr**	**sum**
	$\sum$	**2191.0**	1803.0	1433.0	*788.0*	*12952.0*	**23126.0**	22470.0	16085.0	**7351.0**	*2806.0*	4356.0	5011.0
	%	3.5	**6.5**	5.0	*2.6*	9.7	**10.1**	*7.3*	8.6	0.7	0.5	*0.2*	**1.2**
	$\overline{O_3}$	49.6	*46.8*	73.6	**74.4**	59.0	*55.2*	66.0	**74.9**	-	-	**73.6**	63.8
	$\widetilde{O_3}$	49.5	*46.5*	**80.1**	75.0	58.7	*55.0*	61.2	**73.6**	-	-	**74.1**	64.1
T	$\overline{H_2O}$	*142.9*	216.3	219.5	**248.5**	251.1	*134.8*	233.8	**300.8**	**668.8**	-	-	-
R	$\widetilde{H_2O}$	*32.5*	**176.9**	153.4	128.7	197.6	*95.9*	144.1	**242.4**	**667.8**	-	-	-
O	$\overline{\text{IS}}$	*346.4*	1253.6	2442.7	**2960.6**	3319.5	*2269.0*	4200.7	**4228.3**	3475.8	2060.2	*1871.2*	**8923.1**
	$\widetilde{\text{IS}}$	*97.5*	308.0	417.8	**814.8**	2381.1	*1275.5*	**3026.9**	1958.9	3292.8	2158.1	*1975.0*	**8736.9**
	$\overline{\text{PV}}$	**0.6**	*0.3*	*0.3*	0.4	***0.6***	***0.6***	***0.6***	***0.6***	**0.9**	*0.8*	*0.8*	*0.8*
	$\widetilde{\text{PV}}$	**0.6**	*0.3*	*0.3*	*0.3*	***0.6***	***0.6***	***0.6***	***0.6***	**0.9**	*0.8*	*0.8*	*0.8*
	%	**6.2**	-	<0.1	1.0	9.9	15.4	**16.4**	15.1	**2.2**	*0.4*	1.3	1.4
	$\overline{O_3}$	51.2	-	**96.3**	93.0	*63.1*	87.6	**120.8**	113.1	77.4	-	75.8	**83.5**
	$\widetilde{O_3}$	51.0	-	**96.3**	94.1	*54.0*	81.8	102.9	**110.0**	66.1	-	67.9	**84.6**
T	$\overline{H_2O}$	25.0	-	**62.2**	14.3	72.3	*44.1*	66.2	**99.1**	206.6	144.2	*142.7*	**256.6**
P	$\widetilde{H_2O}$	18.3	-	**83.9**	13.5	52.7	*28.3*	43.3	**72.7**	169.5	*116.6*	133.2	**204.5**
R	$\overline{\text{IS}}$	70.5	-	54.4	**74.5**	**195.1**	*66.6*	84.2	175.3	499.3	*213.5*	264.6	**1893.7**
	$\widetilde{\text{IS}}$	51.5	-	69.4	**71.8**	99.7	*41.4*	59.3	**150.3**	239.4	*180.6*	200.0	**1044.5**
	$\overline{\text{PV}}$	1.6	-	1.1	**1.8**	*1.9*	2.0	2.1	**2.2**	1.9	**2.0**	**2.0**	*1.8*
	$\widetilde{\text{PV}}$	1.4	-	1.1	**1.8**	*1.8*	1.9	2.1	**2.3**	*1.8*	**2.1**	**2.1**	1.9
	%	**<0.1**	-	-	-	*38.0*	**57.9**	55.8	49.7	**29.8**	*9.2*	13.9	20.2
	$\overline{O_3}$	-	-	-	-	*196.8*	379.0	**413.4**	247.8	*247.1*	**569.6**	560.6	320.4
	$\widetilde{O_3}$	-	-	-	-	*203.2*	384.0	**419.1**	236.3	*234.2*	**625.3**	538.9	325.4
S	$\overline{H_2O}$	**9.0**	-	-	-	*11.5*	20.0	20.3	**34.8**	*12.1*	12.2	27.0	**50.7**
T	$\widetilde{H_2O}$	**9.1**	-	-	-	*6.7*	20.8	18.7	**35.4**	10.4	*9.4*	24.7	**43.0**
R	$\overline{\text{IS}}$	**53.7**	-	-	-	**159.8**	*95.3*	146.0	154.0	193.4	*101.6*	**209.9**	203.5
	$\widetilde{\text{IS}}$	**54.3**	-	-	-	**150.4**	*73.4*	116.5	122.8	183.3	*109.6*	**196.1**	181.4
	$\overline{\text{PV}}$	**3.0**	-	-	-	**6.4**	6.3	6.1	*5.6*	**8.1**	7.7	7.7	*7.2*
	$\widetilde{\text{PV}}$	**3.1**	-	-	-	**6.9**	6.7	6.4	*5.5*	8.0	7.8	**8.1**	*7.6*

For equivalent latitudes between 60 and $90°$N rather no tropospheric information of the measured total water and ozone data points is present. This has the following reasons: (i) the tropopause is located at lower isentropes at higher equivalent latitudes (cf. Figure 4.3); (ii) the sampling strategy during SPURT with the base at Hohn ($54.31°$N/$9.53°$E, Germany) and the first flight leg with mostly potential vorticity values > 1 PVU, which is greater than the restriction for pure tropospheric air applied here; (iii) in Table 4-II only data points are considered where trace gas measurements of H_2O and O_3 are available (cf. remarks for trace gas

measurements on page 19); (iv) the mentioned restriction for deriving equivalent latitude and potential vorticity values. Accordant considerations should explain the sparse stratospheric data between $0°$N and $30°$N. In the following, one has to bear in mind these limitations.

The fact that the maximum in tropospheric sampling is located in winter, results primarily from a flight series from the basis in Northern Germany via Casablanca down to the Canary Islands in January 2002 with a longer measurement time in the troposphere and 4 more vertical profiles during the ascents and descents. This also explains the minimal stratospheric sampling in winter at high equivalent latitudes. The region between 30 and $60°$N is best captured by the measurements. With the given restrictions, in this range the expected sampling rates of minimum (maximum) tropospheric air in winter and spring when the tropopause is at lower levels (summer and autumn when the tropopause is at higher levels) and vice versa for stratospheric air appear. The sampling frequency within the tropopause region is rather comparable with that within the troposphere, albeit the number of measurements are slightly enhanced in the tropopause region.

Tropospheric O_3 is almost minimal during all seasons and in all data point categories. The clear peak in summer (probably due to enhanced photochemical O_3 production) and the minimum O_3 VMRs in winter are evident, whereas in the stratosphere the ozone minimum (maximum) occurs in autumn and summer (winter and spring). In the lowermost stratosphere the minima appear through the strong impact of tropospheric air entering the lowermost stratosphere quasi along isentropes during these seasons (Ray et al., 1999), thus lowering the O_3 content in this region (Logan et al., 1999; Logan, 1999). A main reason for the decrease in the O_3 content in the lowermost stratosphere from late spring to early autumn is caused by the increasing tropopause height with the maximum decrease in O_3 from May to June (Logan, 1999). The downward flux through the 380 K surface has a maximum during winter (Appenzeller et al., 1996b) and enhanced downwelling in the extra-tropics is also evident during that season (Ray et al., 1999). In times of the vortex break-up, typically in spring, vortex remnants can travel far into mid-latitudes (Strahan et al., 1999). These instances contribute to the trace gas composition of the lowermost stratosphere resulting in the observed build-up in O_3.The maximum O_3 VMRs were measured at high equivalent latitudes and high isentropes (cf. Figure 4.3). The seasonal amplitudes in ozone mixing ratios increase in all three considered regions from the troposphere to the stratosphere (cf. also Figure 3.3).
Total water is highly variable in the troposphere. This is, in particular, reflected by the values of the tropospheric means and medians which differ by tens of ppmv. As expected from the seasonal temperature variation, a tropospheric seasonal cycle in IS VMRs is present as well as H_2O appears to be maximal in summer and minimal during the winter months. Lowest stratospheric H_2O VMRs were measured in autumn and winter, highest are present in the summer season. The same arises for the tropopause region.

Although the sampling in the low and high equivalent latitude range is sometimes sparse for the tropospheric and stratospheric region, in general, beneath the vertical gradient also a latitudinal increase on isentropes of O_3 and H_2O VMRs from low to high equivalent latitudes is present.

4.2.2 Stratosphere-troposphere exchange

In the following, troposphere-to-stratosphere transport and stratosphere-to-troposphere transport are denoted by TST and STT, respectively, according to the nomenclature of e.g., Sprenger and Wernli (2003) and Bourqui (2004). When investigating TST and STT and their effects on e.g. chemistry and trace gas composition, it is important to take exchange depths and residence times of air parcels into account. This is only possible with a Lagrangian based model (Stohl et al., 2003a), like CLaMS. For instance, an air parcel crossed the tropopause and reentered its original atmospheric region after residing only for a short time in the atmospheric counterpart. This ”passing exchange” event obviously has, if ever, only weak or moderate impact on atmospheric chemistry and trace gas composition, since the time scale for re-/interaction with air of different characteristic is probably too small. Bi-directional stratosphere-troposphere exchange (STE) which is restricted close to the tropopause region also has no significant influence on the atmospheric region. James et al. (2003b) demonstrated with the Lagrangian particle dispersion model FLEXPART (Stohl et al., 1998) the high percentage of passing exchange of air parcels close to the tropopause. In contrast, air parcels with long residence times in an atmospheric region before the exchange carry, to a large extent, their characteristics into the ”new” atmospheric region, in particular, when they are involved in a deep intrusion. If they subsequently have a sufficiently long residence time in that atmospheric region, they possibly can mix with the surrounding air, thus affecting the chemical composition. In this context it is necessary to restrain the term ”mixing” which changes the properties and chemical composition of a particle while filamentation and stirring just change its shape (Wiggins, 1988). Real mixing can only occur by diffusion or chemical reactions.

The applied requirements for the detection of significant exchange events is schematically illustrated in Figure 4.4 for air parcels originating in the stratosphere. Only air parcels which spend a sufficiently long time in both the stratosphere (τ_s) and the troposphere (τ_t) before and after the exchange are considered. Additionally, the transition time (τ_{cross}) for exchange air parcels which travel several times to and fro the tropopause is limited. Here, for τ_s and τ_t 1 day, for τ_{cross} 12 hours is used. Furthermore, to diagnose STE by a change in potential vorticity, only air parcels with a potential vorticity ≥ 3 PVU (≤ 1 PVU) at the measurement time are considered as significant TST (STT). The use of threshold residence times re-

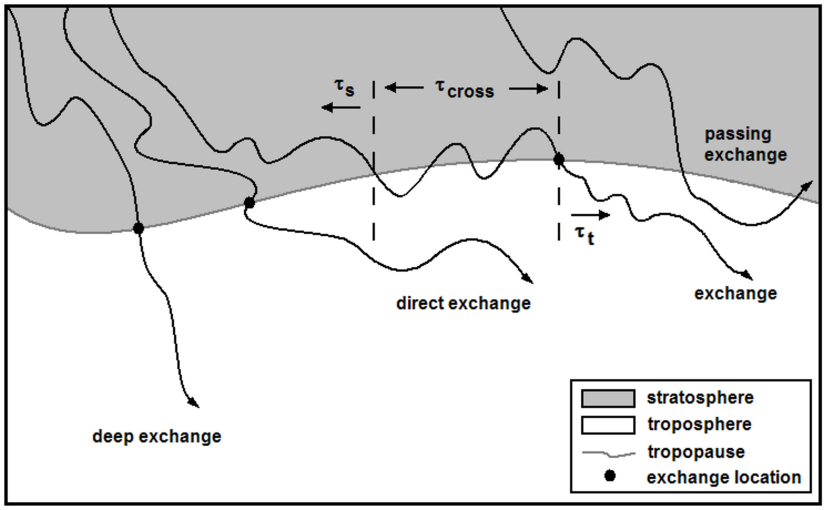

Figure 4.4.: Concept of applied trajectory requirements, exemplarily illustrated for trajectories originating in the stratosphere. An air parcel can be involved in an exchange event by crossing the local tropopause (i) directly, (ii) by a deep exchange event (where it penetrates deep into the troposphere (for STT) or stratosphere (for TST) within a short time interval) or (iii) by a shallow transition (where it crosses the local tropopause several times before residing in the "new" atmospheric compartment). An exchange event is considered as significant if the residence times in the respective atmospheric compartments before and after the exchange ($\tau_{s,t}$) is greater than 24 hours and a possibly time period with multiple tropopause crossings (τ_{cross}) is lower than 12 hours. A passing exchange, i.e. when a trajectory has crossed the tropopause but the residence time of the air parcel in the intruded atmospheric region is lower than $\tau_{s,t}$ and it reenters its originally atmospheric region, is not considered as significant.

moves effectively pseudo exchange events (Wernli and Bourqui, 2002; Bourqui, 2004), the required crossing of a certain potential vorticity region eliminates shallow exchange within the tropopause region (Stohl et al., 2001).

In Figure 4.3, additionally, the initialised locations of those 10 day backward trajectories which were involved into significant STE events are depicted. The dark red (orange) dots mark TST (STT) air parcels. It is evident that most TST occurs primarily within a belt of $\approx 20-25$ K (≈ 6.0 PVU) above the mean dynamical tropopause (2.0 PVU surface) with a maximum in summer of ≈ 30 K (≈ 7.0 PVU). A similar range was also given for the SPURT data by Hoor et al. (2004c), based upon 10 day backward trajectory calculations with the Lagrangian Analysis Tool (LAGRANTO, Wernli and Davies, 1997) and operational ECMWF T219L60 analyses data. When expanding the backward calculation time from 10 to 20 up to 30 days, the region in which most TST air parcels were detected enhances for the latter to $30-35$ K during summer and $40-55$ K during the other seasons (cf. Appendix A). Anyhow, for both Θ-ranges the potential vorticity value is nearly the same of about 8.0 PVU (see also section 4.3). A qualitative statement about the seasonality of STE could not be made by these trajectory data because the air parcels are initialised onto the distinct flight tracks which only cover a single line and not a (hemispheric) volume. Anyhow, the flight strategy and the performance is to the greatest possible extent unitary for all campaigns (cf. right panel in Figure 2.4). Therefore, some following remarks could be drawn.

The presented statistic in Table 4-I is extended to the backward trajectories. In Table 4-II the percentage and the mean tracer concentrations of air parcels which were involved into significant exchange events during their 10 day history are considered. Beneath the parameters in Table 4-I, the mean and median residence times in the accordant atmospheric compartments (denoted by LTPC, hours since the last significant tropopause crossing) as well as the numbers of tropopause crossings (NTPC) of air parcels are given for observations in the three equivalent latitude categories. For the regarded STE air parcels furthermore mean and median of the minimum and maximum values during the past 10 days for potential vorticity and IS VMR as well as the mean and median vertical distance to the tropopause (DTP) at the measurement time are represented. Hereby, the number of exchange air parcels for O_3 and H_2O differ. When considering trace gas values, only trajectories are included where data points of the respective trace gas exist. In Figure 4.3 (and also in Figure B.1 and Figure B.2) therefore, the number of STE air parcels can differ for the O_3 and H_2O charts.

As already mentioned at the end of section 1.2, even when using the information of the backward trajectories, statements related to winter, spring, summer, and autumn correspond to the months DJF, MAM, JJA, and SON, respectively.
Table 4-II reveals that TST was more frequent than STT throughout the year, but it is clear from Table 4-I that this high presence of TST compared to STT air parcels is largely determined by the higher sampling frequency in the stratosphere. Due to the restricted measurements at high equivalent latitudes, STT was predominantly observed at equivalent latitudes $< 60°$N. TST air parcels were detected more frequently in middle equivalent latitudes with decreasing frequency further poleward. A summer maximum in TST frequency is evident, a minimum is revealed for the winter and spring season. Also, the numbers of tropopause crossings of TST air parcels appear to be lower during autumn and summer. This is possibly the effect of convection during these seasons, when air parcels are raised rather directly into the LMS within convective cells. However, it is to emphasize that the mean values for NTPC are considerably higher than 1, indicating that an exchange event in the sense of significance applied here occurs mainly by several crossings of the 2.0 PVU surface before remaining in the entered atmospheric region. Given the significant requirements to the exchange air parcels and the sampling strategy, the summer maximum in TST is qualitatively in agreement with flux estimations for deep exchange by Sprenger and Wernli (2003, their figure 7.f) and cross-tropopause flux estimations with CLaMS by Günther et al. (2004). Due to the sparse sampling of tropospheric air involved in STT, no statement could be given about a seasonality of that transport. Although STT is an important factor, it seems to play a minor role for the O_3 budget of the upper troposphere than photochemical production, at least during the summer season. However, this statement is given a closer inspection in section 6.2.

Table 4-II: When considering significant STE-trajectories in the sense of Figure 4.4, additionally to the parameters given for the three atmospheric regions troposphere, tropopause region, and stratosphere in Table 4-I the mean and median values of the minimum and maximum values during the 10 day history is given for potential vorticity (PV) and ice saturation (IS). $\overline{\text{LTPC}}$, $\overline{\text{NTPC}}$ and $\overline{\text{DTP}}$ ($\widetilde{\text{LTPC}}$, $\widetilde{\text{NTPC}}$ and $\widetilde{\text{DTP}}$) denote the mean (median) number of tropopause crossings, the mean (median) time since the last tropopause crossing in hours and the mean (median) distance to the local tropopause in K. Maximum values are in bold, minimum in italics and are additionally highlighted for the measured trace gases ozone and total water and the ice saturation mixing ratios (red, blue, green, respectively).

		$0^\circ\text{N} \leq \varphi_e \leq 30^\circ\text{N}$				$30^\circ\text{N} < \varphi_e < 60^\circ\text{N}$				$60^\circ\text{N} \leq \varphi_e \leq 90^\circ\text{N}$			
		aut	**win**	**spr**	**sum**	**aut**	**win**	**spr**	**sum**	**aut**	**win**	**spr**	**sum**
	%	**<0.1**	-	-	-	2.5	2.0	*1.5*	**4.3**	0.8	*0.2*	0.7	**4.1**
	$\overline{\text{O}_3}$	-	-	-	-	*143.5*	193.8	**274.7**	167.5	*121.0*	138.1	141.2	**204.7**
	$\widetilde{\text{O}_3}$	-	-	-	-	*143.3*	170.7	**272.0**	163.3	133.5	139.0	*79.4*	**200.2**
	$\overline{\text{H}_2\text{O}}$	**9.0**	-	-	-	*16.4*	26.6	24.6	**49.6**	34.2	*15.9*	64.1	**81.3**
	$\widetilde{\text{H}_2\text{O}}$	**9.0**	-	-	-	*16.2*	21.9	21.4	**45.9**	25.4	*20.1*	58.6	**82.8**
	$\overline{\text{IS}}$	**53.1**	-	-	-	90.2	*52.6*	65.2	**119.5**	164.6	*68.9*	**180.4**	162.8
	$\widetilde{\text{IS}}$	**53.1**	-	-	-	69.8	*44.5*	49.9	**106.2**	161.2	*79.1*	**182.0**	172.2
	$\overline{\text{IS}^{\text{min}}_{\widetilde{10\text{d}}}}$	**11.2**	-	-	-	*26.7*	28.9	39.7	**50.6**	67.9	*35.1*	69.6	**83.0**
	$\widetilde{\text{IS}^{\text{min}}_{\widetilde{10\text{d}}}}$	**11.2**	-	-	-	*19.5*	29.2	35.2	**43.7**	59.8	*34.7*	64.0	**83.5**
	$\overline{\text{IS}^{\text{max}}_{\widetilde{10\text{d}}}}$	**169.5**	-	-	-	1438.3	1819.8	**3974.3**	*1066.0*	5279.2	3597.4	**10151.5**	*1972.0*
T	$\widetilde{\text{IS}^{\text{max}}_{\widetilde{10\text{d}}}}$	**169.5**	-	-	-	412.1	**1004.2**	652.4	*281.9*	1471.4	4590.0	**6921.2**	*413.5*
S	$\overline{\text{PV}}$	**3.1**	-	-	-	*4.4*	**4.7**	**4.7**	4.5	*4.1*	**6.0**	*4.1*	5.9
T	$\widetilde{\text{PV}}$	**3.1**	-	-	-	*4.0*	**4.8**	4.7	4.2	4.0	5.8	*3.7*	**6.1**
	$\overline{\text{PV}^{\text{min}}_{\widetilde{10\text{d}}}}$	**1.0**	-	-	-	*0.8*	1.1	0.9	**1.2**	1.0	*0.8*	0.9	**1.2**
	$\widetilde{\text{PV}^{\text{min}}_{\widetilde{10\text{d}}}}$	**1.0**	-	-	-	*0.7*	0.9	0.8	**1.1**	0.7	*0.4*	0.5	**1.3**
	$\overline{\text{PV}^{\text{max}}_{\widetilde{10\text{d}}}}$	**3.3**	-	-	-	*5.1*	5.3	**6.1**	5.4	**6.6**	6.3	*4.8*	6.5
	$\widetilde{\text{PV}^{\text{max}}_{\widetilde{10\text{d}}}}$	**3.3**	-	-	-	*4.7*	5.2	**6.0**	5.2	**7.0**	5.9	*3.9*	6.1
	$\overline{\text{LTPC}}$	**99.0**	-	-	-	89.1	93.2	*82.8*	**121.1**	*72.5*	**136.4**	95.6	103.9
	$\widetilde{\text{LTPC}}$	**99.0**	-	-	-	70.0	88.0	*58.0*	**109.0**	*64.0*	**98.0**	66.0	93.0
	$\overline{\text{NTPC}}$	**11.0**	-	-	-	*11.4*	**15.3**	12.7	12.1	*9.6*	**16.4**	12.4	12.1
	$\widetilde{\text{NTPC}}$	**11.0**	-	-	-	*9.0*	**11.0**	*9.0*	*9.0*	*5.0*	**13.0**	*5.0*	9.0
	$\overline{\text{DTP}}$	**11.2**	-	-	-	**19.9**	12.7	*10.9*	14.5	12.1	**22.6**	*10.7*	12.6
	$\widetilde{\text{DTP}}$	**11.2**	-	-	-	12.5	12.2	*10.7*	**14.3**	12.9	**20.6**	*9.3*	11.5
	%	*0.1*	0.6	**2.7**	*0.1*	**0.4**	*0.3*	*0.3*	**0.4**	0.1	**0.2**	-	0.1
	$\overline{\text{O}_3}$	-	41.6	62.1	**87.4**	59.0	*53.6*	61.4	**75.8**	-	-	-	-
	$\widetilde{\text{O}_3}$	-	41.9	55.9	**87.4**	56.8	*53.6*	56.4	**69.1**	-	-	-	-
	$\overline{\text{H}_2\text{O}}$	219.1	136.4	**299.5**	-	264.4	*131.1*	175.9	**343.7**	-	-	-	-
	$\widetilde{\text{H}_2\text{O}}$	251.2	101.3	**362.0**	-	291.4	*109.8*	172.5	**313.4**	-	-	-	-
	$\overline{\text{IS}}$	*633.8*	969.6	**1233.7**	995.4	2383.3	924.0	*416.7*	**2787.5**	3248.4	2181.5	-	**8144.5**
	$\widetilde{\text{IS}}$	951.8	473.4	*369.7*	**995.4**	**1514.2**	339.9	*191.0*	1199.5	3251.4	2193.9	-	**6316.8**
	$\overline{\text{IS}^{\text{min}}_{\widetilde{10\text{d}}}}$	*41.8*	52.5	53.0	**73.5**	53.6	*38.5*	63.6	**123.4**	44.3	91.3	-	**150.8**
	$\widetilde{\text{IS}^{\text{min}}_{\widetilde{10\text{d}}}}$	*43.0*	55.9	55.5	**73.5**	48.9	*34.3*	53.8	**122.1**	49.7	95.5	-	**142.4**
	$\overline{\text{IS}^{\text{max}}_{\widetilde{10\text{d}}}}$	4569.5	**6580.4**	4803.0	*995.4*	5156.6	*1703.6*	**5340.7**	3993.5	5134.8	2241.9	-	**8238.1**
S	$\widetilde{\text{IS}^{\text{max}}_{\widetilde{10\text{d}}}}$	**6512.1**	4305.6	4128.5	*995.4*	3142.2	*1124.5*	2609.8	**4314.5**	3251.4	2198.1	-	**6316.8**
T	$\overline{\text{PV}}$	**0.5**	*0.3*	0.4	*0.3*	*0.7*	*0.7*	**0.8**	*0.7*	**1.0**	0.8	-	0.7
T	$\widetilde{\text{PV}}$	**0.5**	*0.3*	*0.3*	*0.3*	*0.7*	*0.7*	**0.9**	*0.7*	**1.0**	0.8	-	0.7
	$\overline{\text{PV}^{\text{min}}_{\widetilde{10\text{d}}}}$	*<0.1*	0.1	0.2	**0.3**	0.4	**0.5**	*0.3*	**0.5**	**0.7**	0.5	-	0.6
	$\widetilde{\text{PV}^{\text{min}}_{\widetilde{10\text{d}}}}$	*0.1*	*0.1*	0.2	**0.3**	0.4	**0.6**	*0.3*	0.5	**0.8**	0.5	-	0.5
	$\overline{\text{PV}^{\text{max}}_{\widetilde{10\text{d}}}}$	5.6	*4.4*	4.9	**7.1**	5.5	*5.3*	*5.3*	**5.8**	4.9	4.0	-	**5.3**
	$\widetilde{\text{PV}^{\text{max}}_{\widetilde{10\text{d}}}}$	5.9	*4.3*	4.8	**7.1**	**5.6**	5.5	*4.8*	5.5	**4.9**	4.2	-	4.8
	$\overline{\text{LTPC}}$	158.0	**192.4**	121.0	*93.0*	**134.2**	82.2	*81.2*	133.5	70.2	**174.1**	-	151.0
	$\widetilde{\text{LTPC}}$	165.0	**197.0**	116.0	*93.0*	129.0	*45.0*	50.0	**132.0**	69.0	**168.0**	-	138.0
	$\overline{\text{NTPC}}$	20.5	*11.4*	16.7	**21.0**	12.2	15.3	**16.1**	*11.0*	8.0	**10.7**	-	10.2
	$\widetilde{\text{NTPC}}$	**30.0**	*6.0*	11.0	21.0	*9.0*	11.0	**14.0**	*9.0*	**9.0**	**9.0**	-	8.0
	$\overline{\text{DTP}}$	*-20.4*	-11.3	-12.2	**-8.7**	*-17.8*	-14.0	**-5.9**	-10.8	-34.5	-25.0	-	**-24.3**
	$\widetilde{\text{DTP}}$	*-14.7*	-11.6	-10.1	**-8.7**	*-14.4*	-9.8	**-4.5**	-10.4	-34.4	-25.0	-	**-14.2**

Obviously, air which was involved into exchange processes has O_3 VMRs in between pure tropospheric and pure stratospheric concentrations. Ozone mixing ratios of TST parcels are higher than mean concentrations in the tropopause region and lower than the mean for pure stratospheric air. In the LMS, TST air parcels give a clear signature in O_3 mixing ratios. In contrast, the signature of TST parcels in H_2O VMRs is not as distinct as in O_3. Total water mixing ratios of TST parcels are only slightly higher than stratospheric concentrations but significantly dryer than the tropopause region. Additionally, minimal IS VMRs and H_2O concentrations are more or less of equal amount (in the mean and median). The latter attribute

suggests that the water content of air crossing the dynamical tropopause is largely determined by temperature. This reflects the high potential for (super)saturation and for (cirrus) cloud formation combined or coupled with TST events (see section 6.1). Average minimum and maximum potential vorticity values during the 10 day history ($\overline{\mathrm{PV}^{\mathrm{min}}_{10\mathrm{d}}}$ and $\overline{\mathrm{PV}^{\mathrm{max}}_{10\mathrm{d}}}$) of almost all TST air parcels are between 1 PVU and 6 PVU, respectively. The mean and median values of the distance from the local tropopause ($\overline{\mathrm{DTP}}$ and $\widetilde{\mathrm{DTP}}$) lie between 10 and 20 K. They demonstrate that the vertical penetration of TST into the lowermost stratosphere seems to be deepest or rather highest above the tropopause during autumn and summer. Certainly, this should point to the maximal TST extent. However, the observed maximum frequency of TST does not *a priori* indicate that the TST extent into the lowermost stratosphere is indeed highest during these seasons. The slight "secondary maximum" of TST near 360 K, as was reported by Sprenger and Wernli (2003), is also apparent in Figure 4.3 at equivalent latitudes between $30°$N and $50°$N. This maximum of shallow TST, due to a higher tropopause and therefore a lower penetration depth, reduces to some extent the DTP values during these seasons. Anyhow, the DTP values for each season also include "deep" exchange events, i.e. air parcels which reach far into the lowermost stratosphere (e.g. more than 30 K above the dynamical tropopause) with potential vorticity values of 8.0 PVU or higher. Although they are not so frequent as shallower TST, when considering percentiles of $80 - 90$ % [1] instead of the mean and median (not shown), it is apparent that the TST extent reaches the maximum distance to the local tropopause during winter and spring. However, the PV value to which TST is traceable shows no clear maximum. These aspects will be discussed in the next section 4.3.

Air parcels involved into STT processes have commonly rather tropospheric tracer mixing ratios. It seems they lose their stratospheric character in a relative short time period probably as a result of their lower density and the higher turbulence in the troposphere. However, another possible reason could be an increased amount of wrong detected exchange events.

The above issues reveal interesting features. The higher O_3 values of TST compared to STT parcels are not necessarily conflicting. This could be justified by several reasons. Results of the Lagrangian "1-year climatology" of Wernli and Bourqui (2002) show that frequent positions of exchange air parcels in the vertical are located near or somewhat above the climatological tropopause for TST and some 150 hPa below for STT. Therefore, TST (STT) parcels just can exhibit near stratospheric (tropospheric) tracer concentrations. Also Vaughan and Timmis (1998) reported that O_3 VMRs of tropospheric intrusions have values above 100 ppbv. Concerning STT, James et al. (2003b) mentioned that exchanged air has a more recent origin in the tropopause region, which is the mixing layer, rather than in the stratosphere, resulting in less stratospheric character of the intruded air. This issue is

[1] indicating the range of DTP values in which $80 - 90$ % of TST air parcels fall into

also represented by the potential vorticity values in Table 4-II. Average maximum 10 day PV values of STT air parcels are about 5 PVU, i.e. they were not deep within the lowermost stratosphere during this time period. Minimal potential vorticity values in contrast do not exceed 0.5 PVU. Therefore, the identified STT particles show O_3 VMRs close to tropospheric values.

The main reason for the observed values of exchange particles could be mixing, which reduces differences in VMRs to the surrounding air. If STT particles travel below the 2.0 PVU surface there are only sparse observations of stratospheric O_3 VMRs > 100 ppbv (cf. also Stohl and Trickl, 1999; Stohl et al., 2001). Furthermore, computational errors, like interpolation over huge distances or coarse grids and raw time resolution, can cause inaccuracies in detecting exchange particles. However, due to the applied restrictions, the mêlée of air parcels in the tropopause region should be largely eliminated and trajectory errors should be limited.

The fact that TST (and due to the more turbulent troposphere obviously STT) is primarily aligned with mixing, appears also from a close look to correlations of H_2O and O_3. These correlations are displayed in Figure 4.7 in section 4.3 for the total measurement data set of each SPURT campaign. When solely considering STE parcels (not shown individually) only few particles occur on vertical branches at low H_2O VMRs (indicating stratospheric and/or sub-tropical and/or dehydrated air) and on horizontal branches at low ozone concentrations (reflecting tropospheric air). When displaying all measurements within 40 or even 50 K above the local tropopause (also not shown), the existence of a tropopause following mixing layer is indicated since the pure tropospheric and stratospheric branches of air are only sparsely equipped, whereas in the view of mixing line theory (Plumb and Ko, 1992; Waugh et al., 1997) the majority appears on these mixing lines, which are the results of irreversible mixing processes of tropospheric with stratospheric air. Thereby, the decline of tropospheric influence (reflected by H_2O VMRs) is evident by increasing distance to the tropopause. For further investigations of the extent of the mixing layer it is referred to section 4.3.

As is evident in Table 4-II the seasonal cycles of tracer mixing ratios of O_3 and H_2O in the stratosphere and troposphere are also present in the concentrations of TST and STT parcels, respectively, particularly in the best captured equivalent latitude range. Therefore, mixing is expected to contribute as the major factor for the observed concentrations of the exchange particles.

In Figure 4.3 STE air parcels identified through the crossing of the 2.0 PVU surface within the previous 10 days are depicted. When the tropopause defining potential vorticity surface is varied to 3.0 or 4.0 PVU and significant ”exchange air parcels” are detected in the same way as for the 2.0 PVU-surface, the distribution of STE around the corresponding potential vorticity surface does not change significantly. To get an impression of the upward and down-

ward components of transport, for the appropriate two SPURT campaigns in each season the percentages of air parcels which cross different definite threshold values of PV (thpv, varying from 0.5 PVU to 12.0 PVU in steps of 0.5 PVU) during the previous 10 and 30 days from below or from above are displayed in Figure 4.5. Additionally, the air parcels must fulfill the residence time criteria for the stratosphere and the troposphere ($\tau_{\mathrm{s,t,cross}} = 24$ h,24 h, 12 h, respectively, cf. page 60). Thereby, UWT denotes upward transport through the corresponding PV surface from below, DWT downward transport from above. To receive a more valuable information from the trajectories, which were initialised on the flight tracks and not in a 3-dimensional box, the calculated percentages are related to the number of air parcels above (for UWT) or below (for DWT) the corresponding PV threshold value at the measurement time. This will affect the given distribution of percentages, since with an increasing PV threshold value the number of air parcels (the footing), which potentially could be involved into UWT (DWT), decreases (increases). Anyhow, this procedure can suggest an estimation for potential transports.

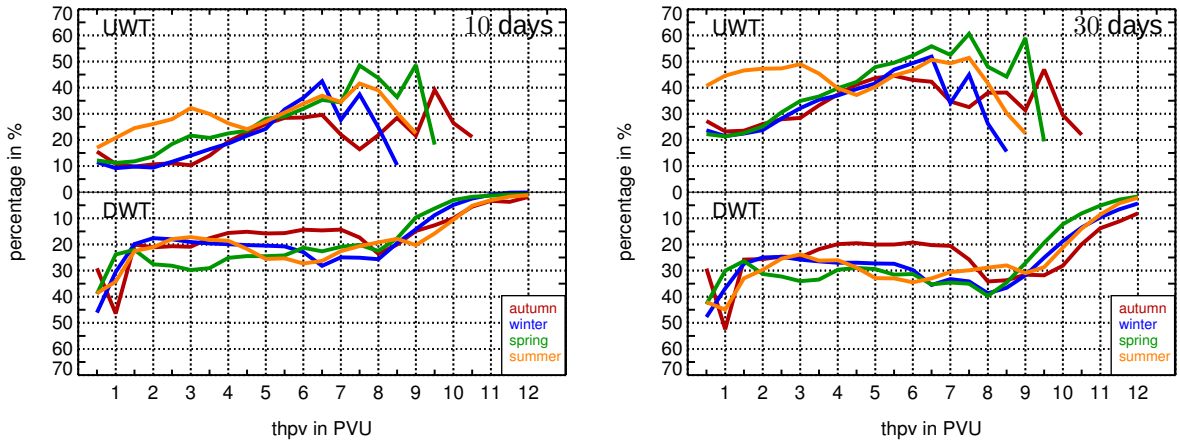

Figure 4.5.: Seasonal distribution of transport through different surfaces of potential vorticity. UWT (DWT) denote air parcels that cross the corresponding PV surface from below (above) during the previous 10 (left) and 30 (right) days. Each percentage for UWT (DWT) is based upon the whole set of air parcels with potential vorticity values at the measurement time greater (lower) than the corresponding threshold value of potential vorticity (thpv).

The distributions for observed DWT above the dynamical tropopause (2.0 PVU) seem to remain rather constant at $20 - 30$ % up to $8.0 - 9.0$ PVU. In contrast, the rates for upward transport increase in the mean from the tropopause (2.0 PVU) to higher PV values in all seasons. There is evidence for enhanced UWT up to $8.0 - 9.0$ PVU, except for winter with a limit at ≈ 8 PVU. The substantial increase for DWT within the range 12.0 PVU to 9.0 PVU and the decrease for UWT for PV threshold values $> 8.0 - 9.0$ PVU is most probably due to the lowering number of data points with increasing potential vorticity, i.e. the number of potential exchange air parcels, which could experience UWT or DWT, respectively, as mentioned recently. Further backward calculation in time enhance the percentages for both UWT and

DWT (cf. right chart in Figure 4.5). This is obviously owing to the higher potential for transport across PV surfaces with increasing backward calculation time. Anyhow, tropospheric influence is still present and noticeable at high potential vorticity surfaces and high isentropes. For an estimated upper limit of recent tropospheric influence it is referred to section 4.3.

To quantify quasi-isentropic transport, furthermore, air parcels that travel quasi-isentropically (within a 5 K range) during the last 10 days are displayed by the cyan dots in Figure 4.3. Quasi-isentropic transport within the considered previous days appears to be weak. This transport process seems to be more effective at high isentropes where transport rather takes place on photochemical time scales. However, air parcels which travelled quasi-isentropic during the considered backward calculation time reclined a distance of several 10 degrees in equivalent latitudes.

It is also interesting along which pathways TST occurs, i.e. where the exchange air parcels entered the lowermost stratosphere. The actual equivalent latitudes of TST particles versus the equivalent latitude at the last significant crossing of the dynamical tropopause is depicted in Figure 4.6 for 10 days (left) and 30 days (right) backward trajectory calculations. Hereby, once more a seasonal differentiation is performed (top to bottom: autumn, winter, spring, and summer). The colour coding represents the encountered difference in potential temperature between the actual value and the value at the last significant tropopause crossing ($\Theta|_{\text{act}} - \Theta|_{\text{LSTPC}}$). The potential vorticity value at the observation time is reflected by different symbols. Additionally, the bisecting line is depicted.

Considering the air parcels involved in TST during the previous 10 days, the data points are commonly located near the bisecting line but with an equivalent latitudinal difference of $\approx 20°$N. They indicate an entry position into the lowermost stratosphere at lower equivalent latitudes than the actual position. Only few particles entered the lowermost stratosphere at a higher than the actual equivalent latitude, but this difference is hardly greater than $10°$N. TST air parcels above the bisecting line have mainly positive Θ differences, since they likely entered the lowermost stratosphere at higher equivalent latitudes than their actual location (despite in situations with strong tropopause displacements). Only few parcels crossed the dynamical tropopause "locally", i.e. $\varphi\text{e}|_{\text{act}} \approx \varphi\text{e}|_{\text{LSTPC}}$, with a gain in Θ. Encountered differences in potential temperatures are mostly in the range between -5 K and 5 K (colour code). The occurrence of negative Θ differences implies also mean downward motion of TST air parcels.

For the 30 days backward trajectories the TST occurrence approximately doubles. Additionally, the mean downward transport becomes more apparent and the Θ differences enlarge. The exchange air parcels cross the 2.0 PVU surface at lower and middle equivalent latitudes and travel poleward. On this way they encounter gradients of potential vorticity and are

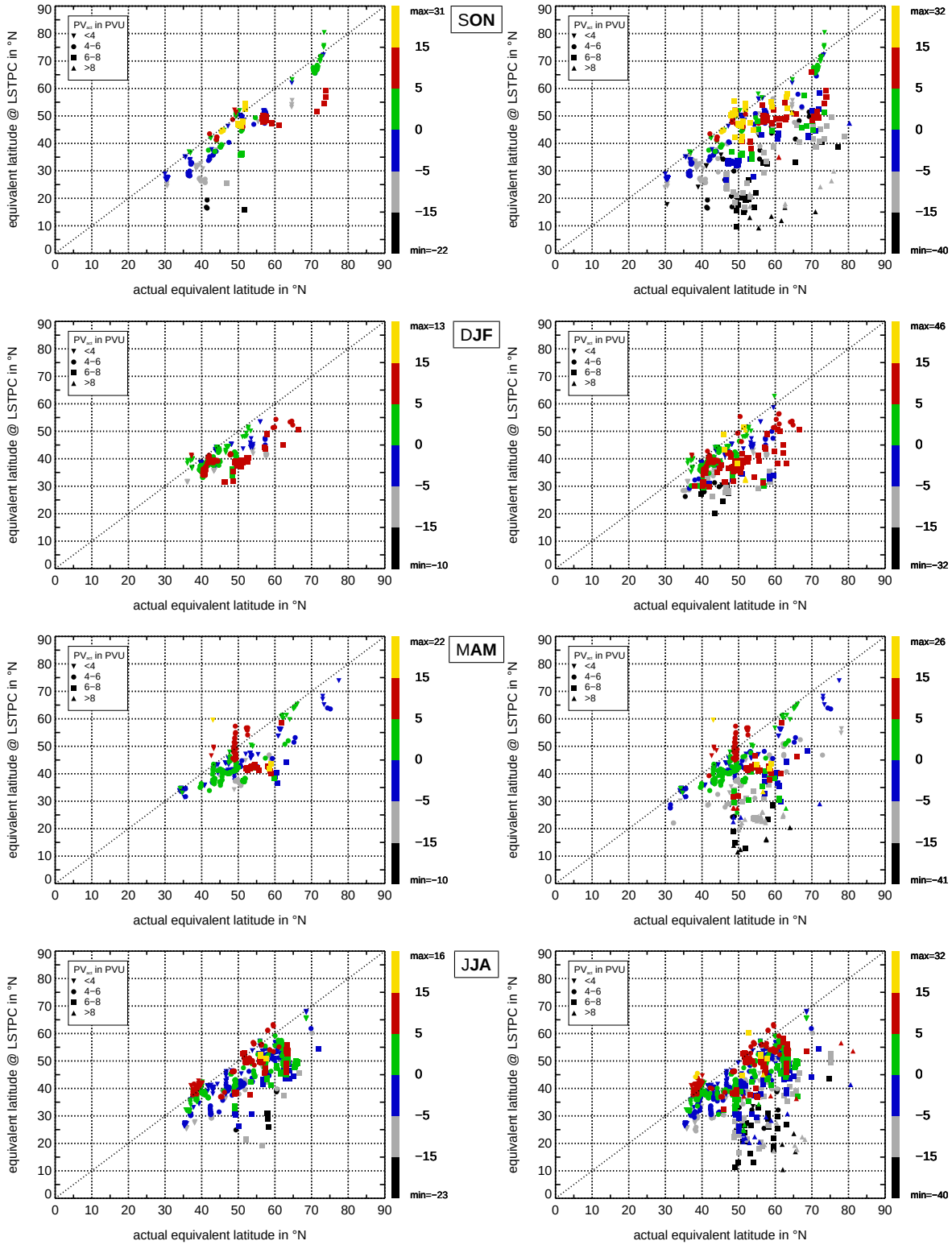

Figure 4.6.: Seasonal correlations of actual equivalent latitude, i.e. φ_e at the observation time (act), versus equivalent latitude at the last significant tropopause crossing (LSTPC) within the previous 10 (left) and 30 (right) days. The colour coding reflects the encountered differences in potential temperature in K, i.e. $\Theta|_{act} - \Theta|_{LSTPC}$. Thus, positive (negative) differences reflect encountered heating (cooling). The potential vorticity at the observation time (PV_{act}) is given as indicated in the upper left corner in each chart. Top to bottom: autumn, winter, spring, and summer.

"forced" to lower potential temperatures. Although extra-tropical TST is frequent (Vaughan and Timmis, 1998), it predominantly reaches not deeply into the stratosphere. This is prevented by the large-scale descent in the stratosphere (Holton et al., 1995).

The symbols for the actual values of potential vorticity show some kind of order. Air parcels crossing the dynamical tropopause at lower equivalent latitudes are now located at higher latitudes with a loss in potential temperature of > 20 K. Thereby, the PV value is the higher the larger the loss in Θ or the lower $\varphi_e|_{LSTPC}$.

Figure 4.6 moreover reveals seasonal differences in TST. The range of equivalent latitudes within which the observed TST parcels cross the dynamical tropopause as well as the transport over huge latitudinal distances show a minimum during the winter months. In contrast, clear maxima are evident during autumn and summer. This is possibly a result of the subtropical jet stream which acts as a transport barrier. In summer and autumn the strength of the jet stream is reduced allowing an enhancement of quasi-isentropic transport from low to high latitudes (cf. Figure 5.5 in section 5.2 and chapter 8). In combination with Figure 4.3 it appears that in the seasonal mean the 8 PVU surface remains relatively fixed in the Θ-φ_e space. In contrast, the densification of lower potential vorticity surfaces increases towards summer in the established coordinate system. This signifies that the vertical PV gradients across isentropes are in the mean strongest during summer and weakest during winter. For quasi-isentropic transport, however, the PV-gradients on isentropic surfaces are weakest during summer, since the slopes of PV iso-surfaces relative to the isentropes decrease towards summer. Thus, transport over large latitudinal differences is simplified or enhanced. This corroborates with the secondary maximum for TST at 360 K indicated by Sprenger and Wernli (2003, their figure 3.b) and with results from Hoor et al. (2004b). Based upon a new approach for a trace gas budget for the lowermost stratosphere Hoor et al. suggest a dominating tropically influenced tropospheric fraction with increasing distance from the mixing layer. This will contribute to the chemical composition of the lowermost stratosphere over Europe during winter and spring (summer and autumn) by about 35 % (55 %).

The high percentage of TST air parcels with Θ differences between -5 K and 5 K does *a priori* not imply predominant quasi-isentropic exchange between the troposphere and the stratosphere. The encountered maximal and minimal potential temperatures of those TST parcels reveal large differences which does not suggest merely quasi-isentropic transport.

For STT there is a general downward transport from higher towards lower equivalent latitudes. Anyhow, due to the sparse measurements in the pure troposphere, i.e. air with a potential vorticity < 2.0 PVU, in particular at high latitudes, no accurate statement could be drawn.

4.3 Estimation of an upper border for the extra-tropical mixing layer

In the previous section 4.2 the extent of troposphere-to-stratosphere transport was analysed with 3-dimensional backward trajectories based upon ECMWF winds. An estimation of an upper boundary for tropospheric influence in the lowermost stratosphere could also be derived from the trace gas measurements, especially from ozone and total water, during SPURT. Both trace gases show a strong gradient at the tropopause. The water vapour VMRs in the tropopause region covers about $2-3$ orders of magnitude, and the lowermost stratospheric ozone concentrations exceed those in the troposphere by a factor of 10. The high accuracy and sufficient time resolution of the *in situ* trace gas measurements also provide a prominent advantage for studying characteristics of the upper troposphere and lowermost stratosphere and processes confined to that region. Since total water is an indicator of small amounts of tropospheric air in the lowermost stratosphere and ozone has a much longer stratospheric lifetime than mixing processes (greater than 1 year in the lowermost stratosphere, Solomon et al., 1985), correlations between both trace gases can deliver some insight to how deep into the stratosphere tropospheric air could penetrate.

4.3.1 Extent of the extra-tropical mixing layer

4.3.1.1 Penetration of tropospheric air into the lowermost stratosphere in terms of O_3

Figure 4.7 shows the O_3:H_2O correlation for each of the eight single SPURT campaigns. Ozone could generally be regarded as a vertical coordinate due to monotonically growing mixing ratios with increasing height. Below the hygropause, above which methane oxidation starts to increase H_2O VMRs, H_2O and O_3 are in general anti-correlated. If the atmospheric compartments troposphere and stratosphere would not interact and mix with each other, the correlation would result in an ”L”-shape: (i) highly fluctuating total water in the troposphere and quasi-constant O_3 VMRs, in Figure 4.7 marked by the horizontal dashed line at 80 ppbv, a value supposed for the definition of the chemical tropopause (Bethan et al., 1996), and (ii) increasing O_3 values in the stratosphere with rather smooth fluctuations in water mixing ratios (denoted by the vertical dashed line at 5 ppmv, a value considered to be characteristic for the pure stratosphere).

In almost all of the O_3:H_2O correlations such an ”L”-shape appears with the vertical branch also at enhanced H_2O VMRs in the lowermost stratosphere of about $20-30$ ppmv. This feature is, for instance, very pronounced in the correlation of IOP 6. Anyhow, the discrete moist branch of high humidity at high O_3 in the correlation of IOP 1 was observed during the first SPURT mission on a southbound flight from Hohn (Germany) to Faro (Portugal).

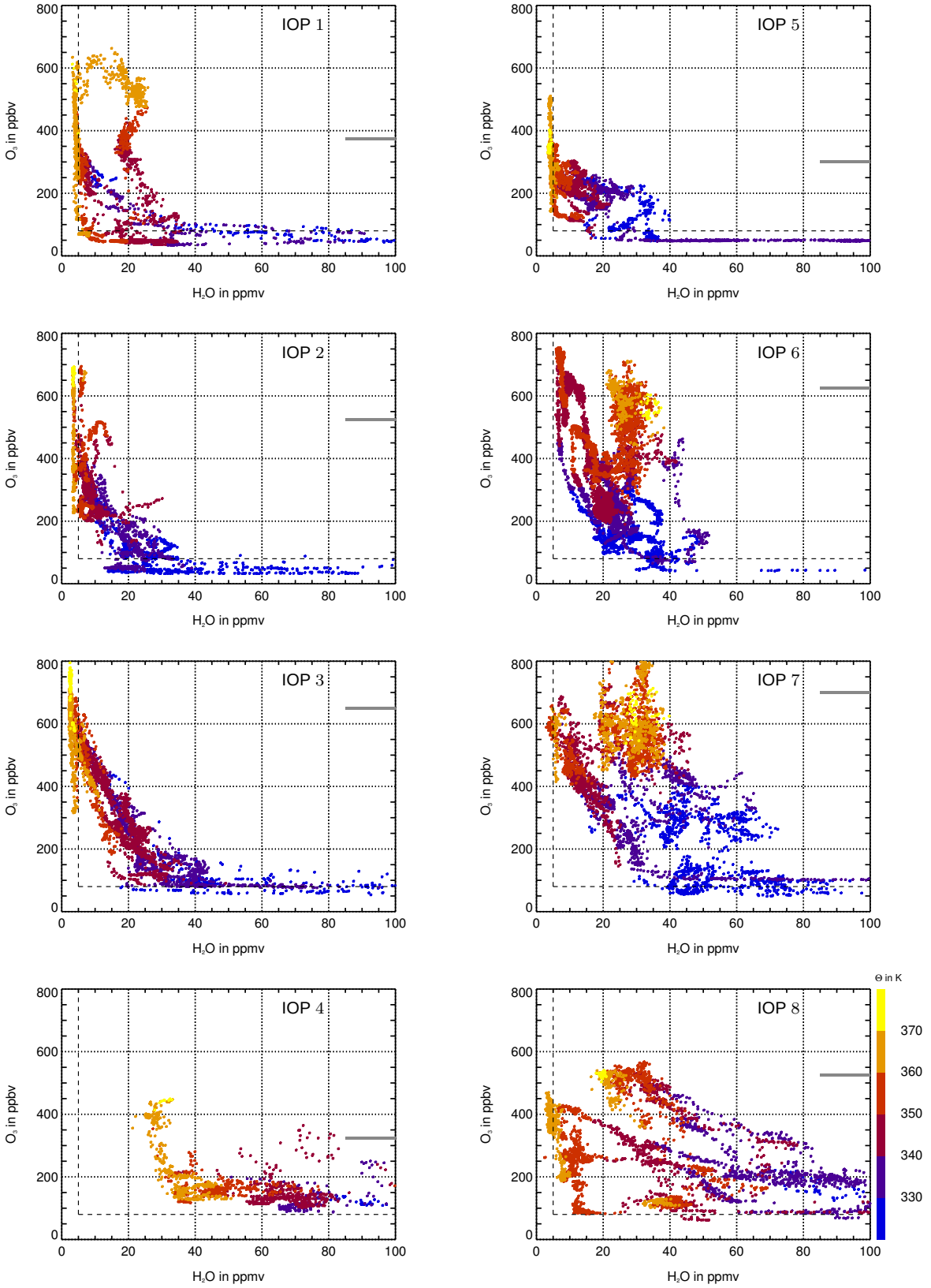

Figure 4.7.: Tracer correlations of ozone and total water for the eight SPURT campaigns IOP $1-8$. The horizontal grey bars at the right ordinate of each chart mark the ozone value to which tropospheric air (indicated by the total water mixing ratios) in the lowermost stratosphere is traceable. The colour coding, depicted at the right hand side of the chart in the bottom row, reflects the potential temperature in K for each data point. (From top to bottom: autumn, winter, spring, and summer. Left: IOP $1-4$; right: IOP $5-8$).

Model studies with CLaMS using the Reverse Domain Filling technique (RDF, see chapter 7) can not provide a suitable explanation for the measured enhanced H_2O VMRs in the lowermost stratosphere during a particular flight section. However, as indicated by Hegglin et al. (2004) the probed air was probably influenced by recent high reaching tropospheric injections during mid-latitude convective system events over middle Europe during that time period. Although convective events (Hauf et al., 1995; Poulida et al., 1996; Fischer et al., 2003) reaching sufficiently high into the lowermost stratosphere should occur frequently and effect the chemical composition and therefore the radiation budget of that atmospheric region, it will not be considered in the following discussion in this section, since the high total water content is probably of this special very recent origin. Anyhow, such high amounts of H_2O accompanied with high O_3 VMRs were discussed very recently by Dessler and Sherwood (2004) for the summer season.
All the correlations in Figure 4.7 reflect the nonuniform character of H_2O in the troposphere (wide spread) with a strong vertical gradient in the tropopause region (near 100 ppbv O_3). Towards higher O_3 VMRs – above ≈ 300 ppbv and ≈ 600 ppbv, depending on season (cf. subsection 3.2.1 and Table 4-III) – the H_2O distributions show a relative compact shape in contrast to the large deviations at low O_3 values due to varying tropospheric sources. The correlations indicate a dryer troposphere (and also lowermost stratosphere) during the autumn and winter months and an increasing tropospheric humidity from spring to summer (cf. also Table 4-I).

Considering bi-directional transport between the troposphere and the stratosphere trace gas concentrations between those of the pure reservoirs evolve due to mixing. Transport and subsequent mixing on time scales shorter than the lifetime of the trace gases result in mixing lines (Plumb and Ko, 1992; Waugh et al., 1997). This mixing line theory is a widely used tool to identify mixing processes in the stratosphere (e.g., Waugh et al., 1997; Plumb et al., 2000) and in the tropopause region (e.g., Bujok, 1998; Fischer et al., 2000; Beuermann, 2000; Hoor et al., 2002). From the mixing lines (for an extended analyses to derive H_2O entry values see section 5.2) an ozone value to which tropospheric air penetrates could be appraised. This is performed by taking the maximum (lowermost) stratospheric O_3 value at that point where the H_2O values are becoming more or less invariant on the corresponding flight to varying O_3. The variation of H_2O below these O_3 values is significant, which is caused by varying tropospheric sources and clouds in the vicinity of the tropopause.

The estimations of O_3 VMRs to which tropospheric influence is traceable are marked by the grey thick bars at the right ordinate of each correlation in Figure 4.7. Note that the derived O_3 values correspond not to the stratospheric H_2O background value but to tropospheric influence. Especially during the last campaigns (IOP $6-8$) a bimodal correlation of H_2O and O_3 in the lowermost stratosphere appears, nevertheless letting derive an ozone mixing ratio

above which a vertical branch (in both modes) establishes. A vertical branch at high potential temperatures in the correlations (i.e. varying O_3 concentrations with quasi-constant total water mixing ratios) could be indicative for chemically aged air (at rather higher potential temperatures) or dehydrated air. For instance, for IOP 6, in the correlation of carbon monoxide (CO) and O_3 (cf. figure 5 of Hoor et al., 2004c) two distinct covariances, i.e. change of slopes, occur, indicating air of different origin and history. The characteristic "kink" in the correlation of O_3 and CO by Hoor et al. (2004c) turns out at an ozone value of ≈ 380 ppbv with photochemically aged air above that value. Although total water mixing ratios reveal no "usual" stratospheric character, they appear in a vertical branch with primarily quasi-constant mixing ratios. This probed air could probably be affected by dehydration mechanisms which will be investigated in more detail in chapter 7. However, from the mixing lines a maximum O_3 value of ≈ 625 ppbv arises. The observation that the "kink" in O_3:CO correlations appears at lower O_3 values than in O_3:H_2O correlations is caused by the much stronger gradient through the tropopause for the latter compared to the more modest for the former. Additionally, the chemical lifetime of water in the stratosphere is probably much longer than that for carbon monoxide (e.g., Pfister et al., 2003). This makes water a more sensible tracer for small amounts of tropospheric air.

Table 4-III: Details on the deduction of seasonal tropospheric influence in the lowermost stratosphere. The functional relationship between measured ozone and ECMWF-derived potential vorticity, between ozone and the calculated distance to the local tropopause as well as the seasonal tropospheric penetration depths in terms of ozone (O_3^p), potential vorticity (PV^p) and distance to the local tropopause ($\triangle\Theta^p$) are given. Values in the polynomials are rounded up to two decimal places.

campaign	$O_3(PV)$ (cf. Figure 4.9 / 4.10)	$O_3(\triangle\Theta)$ (cf. Figure 4.11)	O_3^p	PV^p	$\triangle\Theta^p$
SPURT IOP1	$41.28+\ 1.50{\cdot}PV+\ 4.56{\cdot}PV^2$	$80.28+\ 4.71{\cdot}\triangle\Theta{+}0.01{\cdot}\triangle\Theta^2$	375	8.3	57.0
SPURT IOP2	$82.64-\ 34.11{\cdot}PV{+}10.52{\cdot}PV^2$	$81.11+\ 4.82{\cdot}\triangle\Theta{+}0.06{\cdot}\triangle\Theta^2$	525	8.3	54.4
SPURT IOP3	$66.80+\ 9.27{\cdot}PV+\ 6.99{\cdot}PV^2$	$128.29+\ 13.15{\cdot}\triangle\Theta{-}0.07{\cdot}\triangle\Theta^2$	650	8.5	56.6
SPURT IOP4	$117.53-\ 10.68{\cdot}PV+\ 3.91{\cdot}PV^2$	$111.94+\ 1.23{\cdot}\triangle\Theta{+}0.09{\cdot}\triangle\Theta^2$	325	8.8	42.7
SPURT IOP5	$34.21+\ 10.78{\cdot}PV+\ 2.20{\cdot}PV^2$	$76.49+\ 4.90{\cdot}\triangle\Theta{-}0.01{\cdot}\triangle\Theta^2$	300	8.8	52.4
SPURT IOP6	$22.80+\ 11.58{\cdot}PV+\ 6.79{\cdot}PV^2$	$82.15+\ 11.19{\cdot}\triangle\Theta{-}0.04{\cdot}\triangle\Theta^2$	625	8.5	62.4
SPURT IOP7	$44.66+\ 30.09{\cdot}PV+\ 5.46{\cdot}PV^2$	$149.23+\ 12.53{\cdot}\triangle\Theta{-}0.04{\cdot}\triangle\Theta^2$	700	8.5	53.4
SPURT IOP8	$82.13-\ 0.24{\cdot}PV+\ 5.56{\cdot}PV^2$	$141.52+\ 7.10{\cdot}\triangle\Theta{+}0.02{\cdot}\triangle\Theta^2$	525	9.0	47.9
POLSTAR 1997	$115.56-\ 9.67{\cdot}PV+\ 6.92{\cdot}PV^2$	$145.60+\ 5.75{\cdot}\triangle\Theta{+}0.02{\cdot}\triangle\Theta^2$	400	7.2	40.0
POLSTAR 1998	$104.42+\ 5.64{\cdot}PV+\ 4.97{\cdot}PV^2$	$153.71+\ 4.51{\cdot}\triangle\Theta{+}0.04{\cdot}\triangle\Theta^2$	400	7.2	40.6
STREAM 1996	$39.08+\ 24.93{\cdot}PV+\ 1.69{\cdot}PV^2$	$119.89+\ 6.58{\cdot}\triangle\Theta{-}0.03{\cdot}\triangle\Theta^2$	370	8.5	51.3
STREAM 1997	$68.78-\ 6.87{\cdot}PV+\ 7.28{\cdot}PV^2$	$114.68+\ 6.20{\cdot}\triangle\Theta{+}0.04{\cdot}\triangle\Theta^2$	500	8.2	48.1
STREAM 1998	$136.64-\ 48.12{\cdot}PV+\ 7.45{\cdot}PV^2$	$79.79+\ 1.08{\cdot}\triangle\Theta{+}0.13{\cdot}\triangle\Theta^2$	390	9.9	44.1

The estimated penetration depths from the O_3:H_2O correlations in terms of O_3 are summarised in Table 4-III for the eight SPURT campaigns. Additionally, penetration heights were derived from O_3:H_2O correlations from the Arctic campaigns POLSTAR (Polar Stratospheric Aerosol Experiment) $1997/98$ and STREAM (Stratosphere-Troposphere Experiments by Aircraft Measurements) 1997 (base station in Kiruna, Sweden) as well as from the mid-latitude STREAM $1996/98$ campaigns (base stations in Shannon, Ireland, and Timmins, On-

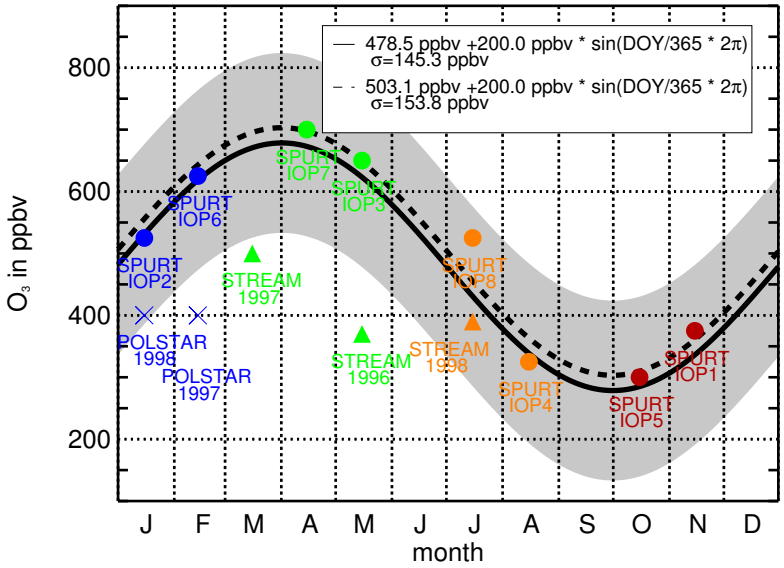

Figure 4.8.: Penetration heights of sensible tropospheric influence in the lowermost stratosphere in terms of ozone as a function of time. The ozone mixing ratios were derived from O_3:H_2O correlations obtained during the eight SPURT campaigns between November 2001 and July 2003 (see grey bar in each charts of Figure 4.7) as well as during the POLSTAR $1997/98$ and STREAM $1996/97/98$ campaigns (cf. Figure C.1 and Figure C.2 in Appendix C). For the SPURT data as well as for all considered mid-latitude campaigns (i.e. SPURT IOP $1-8$ and STREAM $1996/98$) sinusoidal curves are approximated to the penetrations depths (dashed and solid line, respectively).

tario, Canada). These correlations are displayed in Figure C.1 and Figure C.2 in Appendix C. They all let anticipate a limit for tropospheric affection in O_3 with a definite strong sinusoidal annual cycle which is graphically illustrated in Figure 4.8.

For the mid-latitude campaigns STREAM $1996/98$ and SPURT IOP$1-8$ and separately only for the SPURT data sinusoidal curves (black solid and dashed line, respectively) were fitted to the O_3 penetration values and are given explicitly in the upper right corner in Figure 4.8. Both POLSTAR campaigns and the STREAM 1997 campaign were not included into the fitting process for the reason that these are pure polar/artic campaigns. The computed sine curve matches the SPURT data quite well which is possibly due to the even geographical sampling region of these campaigns. However, the grey sinusoidal shading illustrates a varying amplitude about the standard deviation of the fitted O_3 penetration values for the selected SPURT and STREAM data ($1\sigma = 145.3$ ppbv) which roughly matches also the excluded arctic campaigns. The penetration value of O_3 for the STREAM 1996 campaign does not fall into the 1σ scatter range which is probably caused by too low O_3 data (Schiller, 2004, personal communication). The picture drawn here is in qualitative agreement with results from Zahn et al. (2004b, their figure 5) who used a constant CO VMR of 38 ppbv (i.e. their annual mean CO concentration at $8.0-9.0$ PVU) as a representative for the upper border of the mixing layer. From the O_3:CO correlations (mixing lines) for the CARIBIC data, Zahn et al. (2004b) derived a corresponding seasonal O_3 VMR at that CO level. However, the deduced estima-

tions from the STREAM $1996/98$ and SPURT data sets show a higher annual mean in O_3 of ≈ 480 ppbv in contrast to 360 ppbv for the CARIBIC data. Additionally, their annual cycle is shifted about one month. This is probably the effect of the different measurement regions. The CARIBIC data analysed by Zahn et al. (2004b) was taken in the region above the Indian Ocean, Southern Africa and the Caribbean whereas the SPURT data was sampled over the European area (cf. Figure 2.4). Thus, the difference occurs most likely to the varying latitudinal (e.g., Logan (1999) or subsection 3.2.1) and longitudinal (e.g., Appenzeller et al., 2000; Fusco and Logan, 2003) distribution of O_3 VMRs.

4.3.1.2 Penetration of tropospheric air into the lowermost stratosphere in terms of PV

The penetration of tropospheric air into the lowermost stratosphere increases from autumn ($O_3 \approx 300$ ppbv) to mid spring ($O_3 \approx 650$ ppbv), and thus establishes a seasonal cycle. Higher ozone mixing ratios are present during the winter and spring season, lower values during late summer and autumn with an amplitude of ≈ 480 (or ≈ 500) ppbv.
The cycle of penetration depths in terms of ozone is highly correlated with the seasonality of that trace gas in the lowermost stratosphere, with e.g. its maximum during spring (see subsection 3.2.1). Therefore, to reconceive the information of penetration depths of tropospheric air into the lowermost stratosphere from another point of view, it has to be transformed into another quantity. For an estimation of the mixing layer extent into the LMS the quasi-conserved quantity potential vorticity is used. From the availability of meteorological analyses (here ECMWF analyses), a distribution of PV, which is a nearly conservative quantity on timescales of a few weeks, could be derived. Potential vorticity is obtained by spatial and temporal interpolation to the flight tracks as mentioned earlier in subsection 3.4.1. The well-established correlation of ozone and potential vorticity in the lowermost stratosphere states the feasibility to express the ozone penetration depths in terms of PV.
Figure 4.9 shows the correlations of measured ozone and model derived PV for the total SPURT data set. As an additional information, measured total water is displayed by the grey shading. On an iso-surface of potential vorticity a broad spectrum of ozone (and total water) measurements could be noted (refer to subsection 3.4.1). This appears since the *in situ* measurements register large and small-scale variations. The used time resolution of measured data is 5 s which, by an average flight velocity of about 200 m s^{-1}, results in a horizontal distance of ≈ 1 km. In contrast, the derived PV values are restricted to the resolution of the meteorological analysis data, which here is about a factor of $11 - 12$ coarser than that of the measurement data. For each set of data points of the eight SPURT campaigns a 2^{nd} order polynomial is fitted. The approximated polynomials are depicted by the solid coloured lines in Figure 4.9 (red, blue, green and orange corresponding to autumn, winter, spring, and summer, respectively).

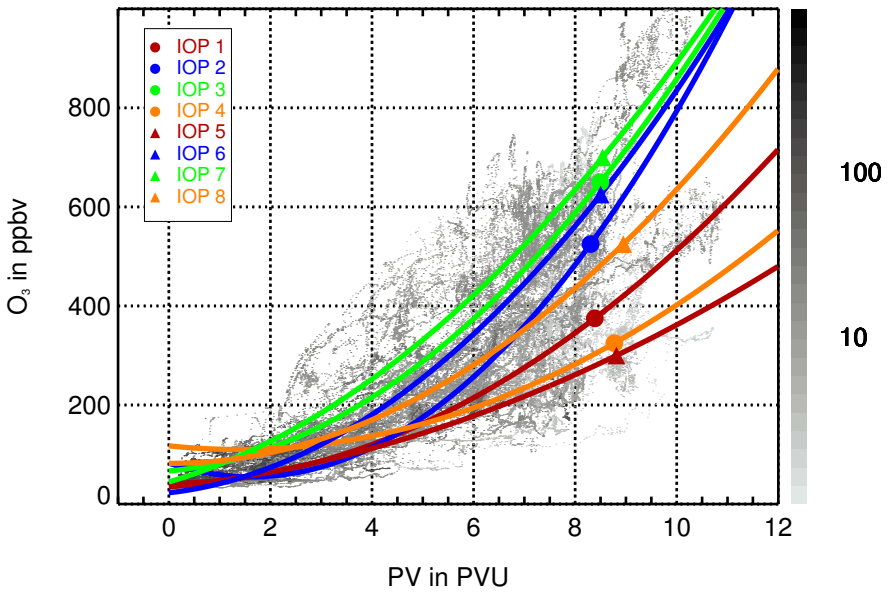

Figure 4.9.: Measured ozone versus spatially and temporarily interpolated potential vorticity from ECMWF analyses with measured total water as grey shading (in ppmv). For each campaign a cubic curve is fitted and colour coded: autumn (dark red), spring (green), winter (blue), and summer (orange). The functional relationship for each polynomial is given in Table 4-III.

At least three features arise from Figure 4.9. First, for ozone lower than ≈ 100 ppbv there is no large deviation between the polynomials. From a potential vorticity value of about 2.0 PVU on these curves begin to diverge with increasing PV. This feature is, of course, also evident in the 2-dimensional probability distribution functions in subsection 3.4.1, leading to the result that a PV value of ≈ 2.0 PVU seems to be satisfying for the extra-tropical dynamical tropopause definition during SPURT. Second, ozone in the troposphere is lowest during winter and highest during summer, whereas stratospheric ozone is at maximum during spring and winter. This was also derived from subsection 3.4.1 for seasonal data. Additionally, the polynomial for the single winter and spring campaigns differ less than those for the missions in summer and autumn. However, the third feature is illustrated by the coloured filled circles and triangles on each fitted curve, corresponding to the conducted SPURT campaign. They mark the ozone mixing ratio to which tropospheric air penetrates, received from the O_3:H_2O correlations in Figure 4.7. These points (ozone mixing ratios) reside in a narrow PV range of about 8.5 ± 0.5 PVU. Details concerning the approximated curves as well as the tropospheric penetration depths in terms of O_3 (O_3^p) and PV (PV^p) are listed in Table 4-III.

For the POLSTAR and STREAM campaigns, the transformation of ozone penetration depths of tropospheric influence to potential vorticity is displayed in Figure 4.10. Also here, at least for the STREAM $1996/97$ campaigns, a PV value of 8.5 ± 0.5 PVU establishes. The assumption of the too low ozone data for the STREAM 1996 campaign is supported by the O_3:PV correlation. For the two SPURT spring (and winter) campaigns, the 2^{nd} order polynomials

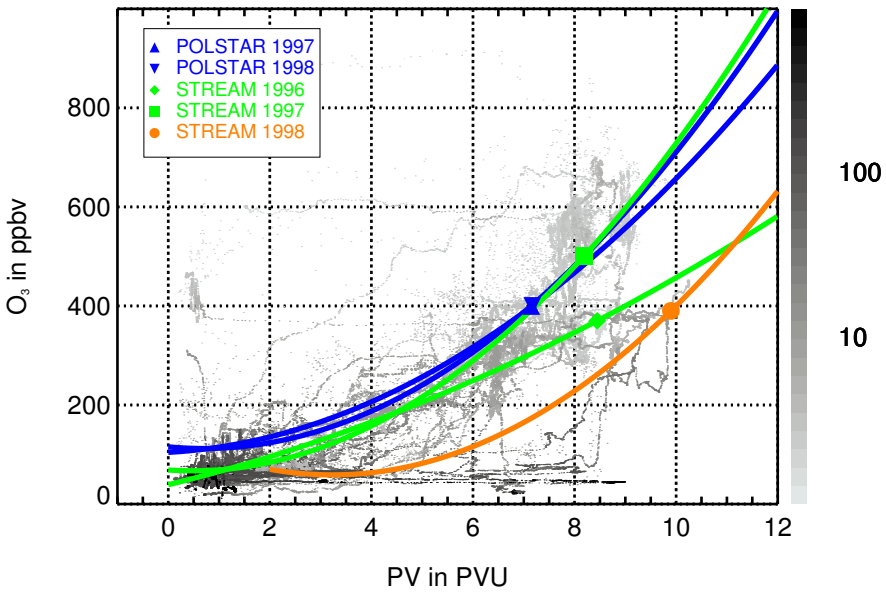

Figure 4.10.: As Figure 4.9 but for the POLSTAR and STREAM campaigns. The functional relationship for each polynomial is also given in Table 4-III.

show not much deviation in contrast to the fits for both STREAM spring campaigns. Due to the compact distributions during that season (cf. Figure 3.8 in subsection 3.4.1) a comparison of all spring polynomials portend to a negative offset for the O_3 measurements during STREAM 1996. This would lead to an enhanced tropospheric penetration value in O_3. Anyhow, due to the then steeper polynomial with increasing PV the higher value for $O_3{}^p$ would probably not change the derived value for PV^p significantly.

For the pure arctic POLSTAR campaigns the transformation results in a penetration depth of about 7.2 PVU. The latter finding is consistent with Pfister et al. (2003) who received nearly the identic feature for the arctic lowermost stratosphere during winter and early spring with a PV value for tropospheric influence of ≈ 7.5 PVU. The transformation for the STREAM 1998 penetration depth results in a PV value of about 10.0 PVU. However, whereas the other considered polar and mid-latitude campaigns were conducted near the European area, this campaign was performed in Canada with the base station at Timmins, Ontario. Atmospheric conditions, e.g. orographically or convectively induced, in this region differ from those above Europe in almost all seasons. For instance, this issue is also present in the analysis of parameters at the tropopause, which were derived from Northern Hemisphere ECMWF analyses and are discussed in section 5.2. Therefore, also the extent of tropospheric air into the lowermost stratosphere could be variable there. Unfortunately, no further data within the STREAM 1998 region or other Northern Hemisphere mid-latitude regions, especially for all seasons, were analysed this way so far to investigate that item in more detail.

Anyhow, although tropospheric air penetrates to higher ozone mixing ratios with progressing season from autumn to spring the according PV value does not change seriously. The SPURT data represents a substantial contribution. It captures the mid-latitudes and covers all seasons. Thus, this study goes far beyond that of Pfister et al. (2003).
Whereas the mean ozone mixing ratio in the seasonal cycle of tropospheric influence in the lowermost stratosphere of the considered CARIBIC and SPURT data set are quite different, the chosen PV range for deriving a stratospheric CO concentration by Zahn et al. (2004b) and the derived PV range from the SPURT correlations are about the same. The implication for the extra-tropical mixing layer – where ascending tropospheric air and descending stratospheric air mix – is that this layer, or at least the well mixed part, has its lower border at the tropopause and its upper border at around 8.5 ± 0.5 PVU, almost independent on season. Although extra-tropical TST seems to be most frequent during summer (and autumn) when the derived PV values show a slight maximum, the vertical extension in terms of PV is quite constant throughout the year, suggesting a very weak annual cycle. The upper part of the mixing layer is, in particular seen in combination with Figure 4.6 for summer (and autumn), highly controlled and influenced by tropospheric air entering the lowermost stratosphere at higher potential temperatures at lower latitudes. To this, also the reduced strength of the sub-tropical jet stream barrier will contribute (see chapter 8).

Although during several SPURT campaigns – especially during the second half of SPURT – total water amounts are uncommonly enhanced combined with high ozone mixing ratios, the estimated upper border for the extra-tropical mixing layer remains at the same PV level. Anyhow, that does not mean that above 8.5 ± 0.5 PVU water vapour mixing ratios must be lower than $\approx 5 - 8$ ppmv as indicative for an unperturbed (lower) stratosphere. The water content can likely be enhanced since it is primary dependent on the temperature history and where the air entered the stratosphere. Mixing ratios above 10 ppmv exclude the tropics or sub-tropics as the entering region, due to the cold tropopause temperatures there, but rather imply the middle and higher latitudes (cf. section 5.2). However, high reaching events, as observed during the first SPURT mission (Hegglin et al., 2004), could have large derogation and impact on chemistry, radiation, and particularly cloud formation in the lowermost stratosphere (cf. section 6.1). Furthermore, once water vapour has entered the stratosphere it could remain more or less unchanged for a substantial long time period, due to the higher temperatures there.

4.3.2 Isentropic depth of the extra-tropical mixing layer

Another approach for transforming the derived penetration heights in ozone of tropospheric influence into the lowermost stratosphere to a more geometric quantity is to correlate ozone

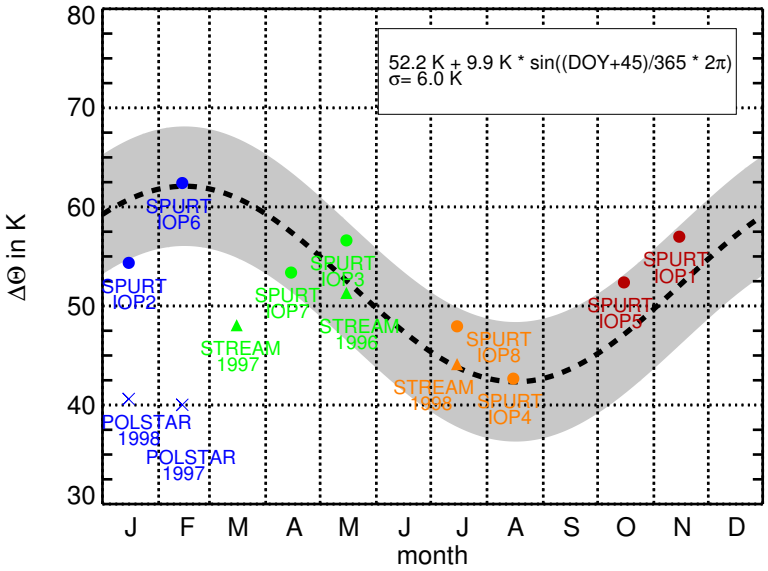

Figure 4.11.: Distance from the local tropopause (2.0 PVU surface) up to which tropospheric influence is traceable in the lowermost stratosphere. The values for $\triangle\Theta$p were received from functional relationships between PV and $\triangle\Theta$ (see Table 4-III) for the considered POLSTAR, STREAM and SPURT campaigns by inserting the corresponding $O_3{}^p$ value and solving the quadratic equation.

with the distance to the local tropopause ($\triangle\Theta$) instead of PV. The extraction of $\triangle\Theta$ was already introduced in subsection 3.4.1 on page 43. Alike for the O_3:PV correlations, the best fit relating both parameters is a 2^{nd} order polynomial. For each SPURT, POLSTAR and STREAM campaign the resulting fits relating $\triangle\Theta$ and O_3, are listed in Table 4-III. Inserting the respective O_3 penetration height and solving the corresponding quadratic equation for $\triangle\Theta$ results in varying values ($\triangle\Theta^p$) given in the last right hand column in Table 4-III. However, in contrast to the derived values of PV^p, the distances from the local tropopause exhibit a seasonal cycle. This issue is graphically depicted in Figure 4.11. Hereby, a sine curve (given in the upper right corner, dashed line) with a 1σ scatter range (grey shading) is fitted to the $\triangle\Theta^p$ for the mid-latitude campaigns, i.e. SPURT IOP$1-8$, STREAM 1996 and 1998. All these derived penetration depths fall within the 1σ range. As is apparent, the distance to the local tropopause, up to which "recent" tropospheric influence is traceable in the lowermost stratosphere, is highest during winter and lowest during the summer season. The mean in the seasonal cycle of $\triangle\Theta^p$ is ≈ 50 K. The traceable tropospheric influence reaches well within the lowermost stratosphere, with a peak-to-peak amplitude of about 20 K.

There are several studies concerning stratosphere-troposphere exchange and the mixing layer. Year-round STE below an isentropic surface of 340 K was inferred from model studies by Chen (1995) and Eluszkiewicz (1996) as well as from meteorological analyses by Dethof et al. (2000), suggesting stronger extra-tropical TST during summer. In contrast, from ozone sondes and satellite data Rood et al. (2000) derived stronger cross-tropopause mixing dur-

ing winter and spring. Seo and Bowman (2001) analysed global-scale cross-tropopause air parcel exchange on isentropes and found greatest transport during autumn and winter.
Based upon CO and O_3 measurements during STREAM 1997 and 1998 Hoor et al. (2002) suggested an isentropic depth of the mixing layer of about 20 K during winter and 40 K during summer. Accessorily, from CO analyses for the SPURT campaigns, Hoor et al. (2004c) concluded that TST and subsequent mixing with extra-tropical tropospheric air influences the region 20 K above the tropopause during all seasons, except 30 K during summer, on time scales of days to weeks. Concerning the mixing layer extent, in contrast to the results of Hoor et al. (2002) and Hoor et al. (2004c), the analysis shown here seems to result in a conflict. On the one hand, the mid-latitude isentropic thickness (i.e. $\triangle\Theta$) of the mixing layer shows a maximum during winter and a minimum during summer. On the other hand, the corresponding depth (i.e. PV^p) is much higher. The second item is probably caused by the consideration of the different trace gases CO and H_2O, the latter species being a more sensitive indicator of small amounts of tropospheric air in the stratosphere.

To qualitatively explain the seasonal cycle of the isentropic depth of the extra-tropical mixing layer, some aspects can be considered:
(i) Reiter (1975) presented quantitative estimates for STE processes. The yearly mass transport of one hemispheric stratosphere through the tropopause was thereby estimated to 20 % for large-scale eddies in the vicinity of the jet stream regions and to 10 % for the seasonal variation of the tropopause height. The two processes are seasonally dependent. During the winter and spring season the enhanced storm activity, breaking Rossby waves and baroclinic instabilities are strengthened at the jet stream level. Strongest wave-induced forces occur in the Northern Hemisphere winter season. The exchange rate is also a maximum during that season (Holton et al., 1995). Thus, quasi-horizontal transport of tropospheric air into the stratosphere is possible strongest during this period (Pfister et al., 2003). Further, Wernli and Bourqui (2002) gave evidence for generally greater (lower) cross-tropopause mass fluxes during winter (summer). Enhanced STE will possibly lead to a promoted potential for mixing processes on small scales. In equatorward breaking Rossby waves high PV stratospheric air extends further south, in poleward breaking events upper tropospheric air is transported northward (e.g., Thorncroft et al., 1993; Hood et al., 1999). In such events a net exchange of tropospheric and stratospheric air is established due to the connection of the sub-tropical upper troposphere with the extra-tropical lowermost stratosphere.
(ii) As illustrated in the Θ-φ_e coordinate system, during winter and spring between 30 and $50°$N mean surfaces of potential vorticity strongly start to bulge upward towards lower latitudes evoked by the decreasing Coriolis parameter and by the strong sub-tropical jet. Hence, the jet stream regions are often referred to as ”tropopause breaks”. A huge gradient of mean PV surfaces on isentropes is present in that region. In contrast, the PV gradient across isen-

tropes is weak. Therefore, a distance from a certain PV surface could therefore be very large. For instance, an air parcel with a PV value of 4.0 PVU appears not to be deep in the stratosphere, traced by its PV character. However, the distance to the dynamically defined local tropopause (e.g. 2.0 PVU) results in a large value. This should also contribute to the observed annual cycle of $\triangle\Theta$ with the maximum during winter.

(iii) On the contrary, the slope between iso-surfaces of PV and potential temperature is lowest during the summer season. Therefore, during that season there is an additional transport path for STE, due to a weaker sub-tropical jet stream barrier, which allows more likely quasi-isentropic transport at higher potential temperatures between the sub-tropics/tropics and the extra-tropics (see chapter 8). This leads to a mixing layer up to $360 - 370$ K (or 40 K above the tropopause). However, meridional displacements over large distances and Rossby wave breaking events are severely reduced compared to winter.

(iv) The extra-tropical tropopause is located at lower isentropes during winter than during summer. Tropopause height estimations derived from the SPURT data in the Θ-φ_e space are given in section 4.1 on page 54. Surfaces of PV above $\approx 8.0 - 9.0$ PVU in the mid-latitudes are rather fixed in that coordinate system and the distance from that surface to the tropopause between winter and summer is ≈ 20 K. This is in quantitative agreement with the peak-to-peak amplitude in the course of $\triangle\Theta^p$. Thus, under the restriction of a "fixed" upper border a variation of the tropopause alone could possibly explain the derived seasonal cycle in isentropic depth of the mixing layer.

(v) As previously noted and illustrated in Figure 5.5 in section 5.2, the annual course of the sub-tropical jet stream strength (maximum horizontal wind velocities during winter, weakened by the monsoon circulations during summer) is in phase with the seasonal cycle of the distance from the local tropopause given in Figure 4.11. However, the jet stream appears not as a closed band and, for instance, one permeable gap is located in the North Atlantic area. In their "1-year climatology of cross-tropopause exchange in the extratropical Northern Hemisphere" Wernli and Bourqui (2002) showed that in particular during winter, the Pacific and Atlantic storm tracks are preferred regions of STE. For instance, biases in observations due to preferential locations of dynamical features are therefore potentially important. An analysis by Beekmann et al. (1997) concerning tropopause fold occurrence gave also evidence for maximum folding activity in Europe.

(vi) The polar regions are highly affected by diabatically descending aged stratospheric air from the overworld during winter. Thereby, the upper isentropic boundary of the mixing layer declines with increasing latitude (cf. derived isentropic depths for both POLSTAR campaigns and STREAM 1997).

Even though the derived penetration depths in terms of ozone ($O_3{}^p$) during summer were estimated too low, the seasonal cycle of the isentropic depth of the extra-tropical mixing layer

above the tropopause would not change seriously. The thickness of the mixing layer ($\triangle\Theta$) shows a definite seasonal course. The extent of this layer into the lowermost stratosphere (PV^p), however, undergoes, if ever, only a weak seasonal cycle. Anyhow, the chemical composition of the lowermost stratosphere, inclusive the mixing layer, will undergo a strong seasonal cycle.
Although two consecutive years of SPURT measurements in the same geographical region as well as POLSTAR and STREAM campaigns are included, the obtained extent of the extra-tropical mixing layer could be (i) variable from year to year and (ii) of different character in other geographical regions. Therefore, the presented results can in the first instance only held for the European area and have to be supplemented by additional year-round data covering different geographical regions.

4.4 Main results of this chapter

In this chapter the O_3 and H_2O measurements during SPURT have been analysed with use of $10 - 30$ day backward trajectory calculations. The main outcomes are summarised as follows:
The trace gas measurements were investigated in the potential temperature and equivalent latitude space, a coordinate system, which is especially favourable for climatological distributions. Three regions could be identified: the troposphere, the stratosphere and a region with intermediate trace gas mixing ratios between the both atmospheric compartments. The latter is termed as the extra-tropical mixing layer. Therein, tracer isopleths follow surfaces of potential vorticity and/or the shape of the local tropopause, which was already suggested in subsection 3.4.1.

Taking information from backward trajectory calculations, statistics of troposphere-to-stratosphere (TST) and stratosphere-to-troposphere transport (STT) were performed. Thereby, only significant exchange air parcels were considered (cf. Figure 4.4). As is evident in the statistics, TST air parcels carry tropospheric O_3 signatures into the stratosphere, whereas the H_2O VMRs of TST air parcels are rather stratospheric. Since H_2O is involved in heterogeneous processes this suggests freeze-drying of the air on its way into the lowermost stratosphere.
Identified STT air parcels seem to loose their stratospheric character within a very short time period, which is possibly caused by the higher turbulence in the troposphere.

Furthermore, the trajectories suggest that the well mixed lower part of the extra-tropical mixing layer is highly influenced by recent mixing events, whereas quasi-isentropic transport is more effective on higher isentropes.

Using correlations of O_3 and H_2O and the corresponding mixing lines, the upper border of the extra-tropical mixing layer was estimated to $\approx 8-9$ PVU, independent on season. The tropopause as the lower boundary is located at $2-3$ PVU. Thereby, the time since the last tropopause crossing of TST air parcels increases most likely along the mixing lines towards the stratospheric end members. In contrast to the quasi-constant extent of the mixing layer into the LMS, its isentropic depth shows a seasonal dependence with a maximum thickness during winter and a minimum during summer. The seeming conflict with results from CO measurements during SPURT by Hoor et al. (2004c), who suggest a maximum depth during summer, is most probably affected by the different characteristics of the considered trace gases CO and H_2O.

Chapter 5

H_2O and parameters at the tropopause

Compared to the known seasonal cycle of the large-scale downward circulation and the boundary conditions of water vapour in the overworld, the transport processes across the lower boundary of the (lowermost) stratosphere, in particular at the extra-tropical tropopause, are only poorly known (Pan et al., 1997). For climatological aspects the distribution of water vapour at the tropopause is fundamental for e.g. calculations of present climate and its sensitivity to varying greenhouse gases (Hoinka, 1999). In section 5.1 H_2O entry values ($\mu^{e}_{H_2O}$) at the tropopause are estimated from *in situ* measurements during the POLSTAR $1997/98$, STREAM $1996/97/98$ and SPURT campaigns. The term entry value denotes the H_2O mixing ratio which possibly can enter the lowermost stratosphere, derived from O_3:H_2O mixing lines. Due to the good seasonal coverage, continuous performance and data availability of the SPURT measurements, the entry values can be derived for all seasons.

In addition, perennial data sets provide an exquisite footing for describing a climatology of e.g. meteorological parameters at the tropopause without gap. However, model analyses can only provide an approaching representation of the real atmosphere. In order to estimate the stratospheric-tropospheric exchange of water continuously and globally, section 5.2 shows an almost ”2-year climatology” around the SPURT time period (August 10, 2001, to July 11, 2003) of parameters at the tropopause. The episodical and regional SPURT measurements, which are restricted to the European sector, will be set into the context of this climatology on the global scale.

5.1 H_2O entry values derived from *in situ* measurements

The H_2O VMR of air parcels entering the stratosphere at potential temperatures $> 370 - 380$ K is changed by two processes: (i) freeze-drying at the very cold tropical tropopause and (ii) gradual methane oxidation in the stratosphere (Nedoluha et al., 2002). The former shows a strong seasonal dependence (the "tropical tape recorder", Mote et al., 1996). The latter will gradually increase H_2O VMRs in the stratosphere. Beyond, the H_2O content in the Northern Hemisphere stratosphere is also determined by some limited dehydration in the winter Arctic vortex (Herman et al., 2002). A comprehensive study of H_2O measurements from a large number of independent instruments reveals an H_2O entry level VMR of about $\approx 3.0 - 4.1$ ppmv into the stratosphere during $1990 - 1999$ (SPARC, 2000, table 2.4., and references therein). Thus, the highest potential water, i.e. $2\times CH_4+H_2O$, results in a VMR of $\approx 6.4 - 7.5$ ppmv. Air masses with greater VMRs are not expected to have entered the stratosphere via passing the tropical tropopause. The extra-tropical tropopause is significantly warmer than the tropical tropopause during the entire year (cf. Figure 5.6). Thus, H_2O VMRs at the extra-tropical tropopause are much higher (cf. Figure D.4), allowing the intrusion of moister air into the lowermost stratosphere. In contrast, the extra-tropical tropopause is located at much lower potential temperatures than the tropical tropopause (cf. Figure D.3). To reach higher potential temperatures in the extra-tropics, the intruded air has to be involved in cross-isentropic transport. To establish this transport, both potential temperature and potential vorticity have to be built up. High reaching convective events in the extra-tropics (e.g., Hauf et al., 1995; Poulida et al., 1996; Fischer et al., 2003; Wang, 2003, 2004b,a) can establish this transport mechanism. Additionally, there is evidence for equatorward transport with sufficient potential to convey high and mid-latitude air into the rising regions at lower latitudes. Bypassing the tropical cold trap, such transport can bring huge amounts of H_2O into the (lowermost) stratosphere (Richard et al., 2003). Both events with their significance and long-term changes can contribute to the observed change in stratospheric H_2O (Oltmans et al., 2000; Rosenlof et al., 2001). Anyhow, the dryness of the stratosphere at first indicates that in the extra-tropics transport of tropospheric air into the overworld is very restricted.

As mentioned in subsection 4.3.1, in the absence of STE processes, the correlation of O_3 as a stratospheric tracer and H_2O as a tropospheric tracer would result in an "L"-shape. High O_3 VMRs are associated with low H_2O VMRs, and vice versa. In reality, in the tropopause layer and in the mixing layer above the tropopause H_2O VMRs of several tens of ppmv are observed, indicating tropospheric influence. From the *in situ* measurements H_2O entry values at the tropopause in the presence of TST ($\mu^{e}_{H_2O}$) can be estimated by the tropospheric end members of the mixing lines in the O_3:H_2O correlations. This is done by an extrapolation to the point of intersection with a chosen tropospheric O_3 value. Here, the tropopause is

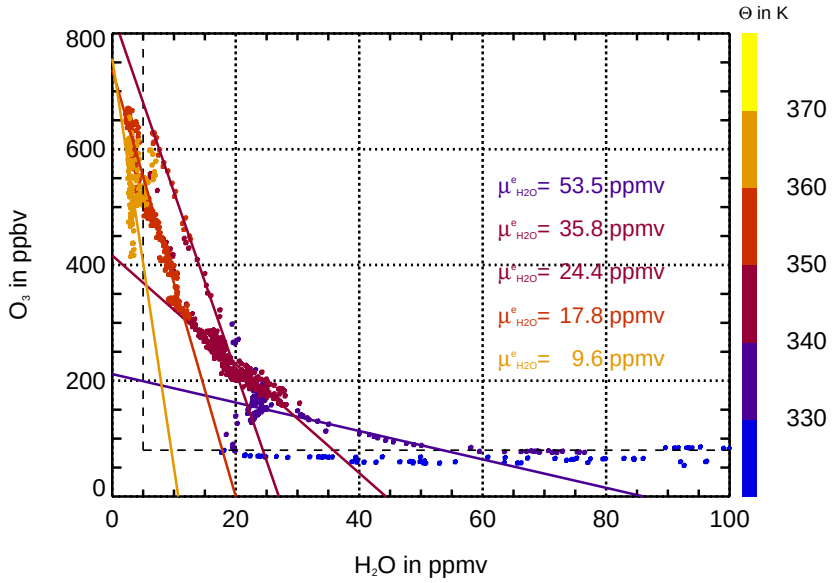

Figure 5.1.: Example correlation of ozone and total water for deriving the H_2O entry values ($\mu^{e}_{H_2O}$) at the tropopause, possibly entering the (lowermost) stratosphere. The single entry values are estimated from the tropospheric end members of the mixing lines for different potential temperature ranges. The tropopause is taken as the ozone level of 80 ppbv. Shown is the O_3:H_2O correlation for May 16, 2002, for the SPURT flight mission from Jerez (Spain) to the main base station Hohn (Germany).

approximated by an O_3 VMR of 80 ppbv (Bethan et al., 1996), denoted by the horizontal dashed line in the O_3:H_2O correlations (see Figure 4.7 and Figure 5.1). For deriving the entry values, a seasonal variation of O_3 at the tropopause, which is identifiable in Figure 3.3, was not considered. This is justifiable since (i) mixing lines for lower potential temperatures (< 340 K) are anyway highly variable, due to the different and varying tropospheric sources, and (ii) a change in the chosen O_3 value for the tropopause by $\approx 10 - 20$ ppbv has only little effect on $\mu^{e}_{H_2O}$, as the slope of mixing lines for higher potential temperatures (> 360 K) is very large (see Figure 5.1). To account for different height regimes, the mixing lines in the O_3:H_2O correlations (cf. Figure 4.7) were derived for different potential temperature ranges.

Whereas the chemical lifetime of O_3 in the exchange layer is on the order of months (WMO, 1990), H_2O is strongly coupled to temperature and thus highly variable. Dehydration processes can remove high amounts of H_2O within hours or days by condensation with subsequent sedimentation. In contrast, evaporation of water and/or ice particles can (re)hydrate the air. Sedimentation with subsequent evaporation (re)hydrates subjacent air. Intrusion of particles to higher regions, e.g. in a cumulonimbus during high reaching convection (Vömel et al., 1995) and/or by so called ”jumping cirrus” during such events (Wang, 2004b,a), can humidify air at higher altitudes. Thus, the mixing layer is a composite of several different mixing processes, indicated by a number of mixing lines.

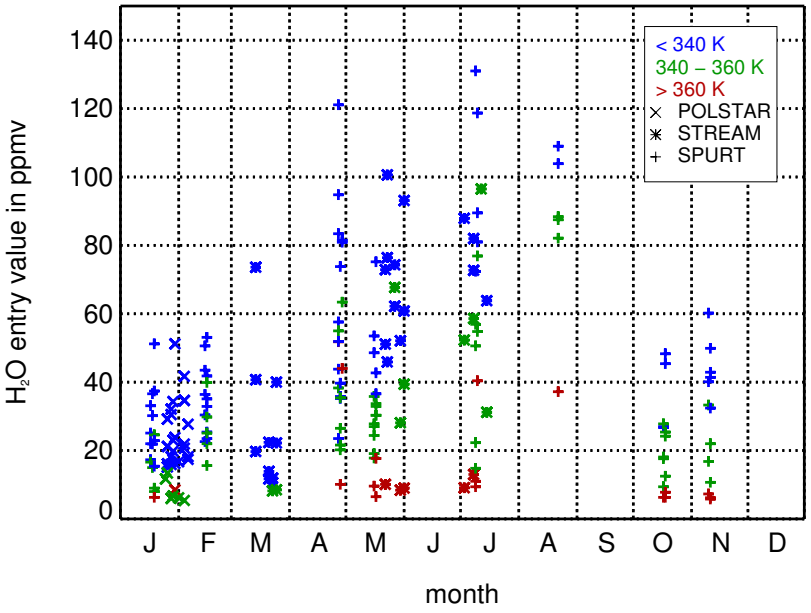

Figure 5.2.: Seasonal cycle of H_2O entry values ($\mu^{e}_{H_2O}$) at the tropopause. The single $\mu^{e}_{H_2O}$ were derived from the tropospheric end members of the mixing lines in the O_3:H_2O correlations. Thereby, POLSTAR $1997/98$ (crosses), STREAM $1996/97/98$ (asterisks) and SPURT (plus signs) missions are considered. Additionally, three potential temperature ranges are distinguished: < 340 K (blue), $340 - 360$ K (green), and > 360 K (red).

For facility of inspection, in Figure 4.7 no derived mixing lines are displayed. In lieu thereof Table E-I shows the tropospheric H_2O and stratospheric O_3 end members as well as the considered data points for each derived mixing line. The values are given for the SPURT flights as well as for missions during the POLSTAR $1997/98$ and STREAM $1996/97/98$ campaigns. Exemplary, a correlation with the estimated mixing lines for different potential temperature ranges is depicted in Figure 5.1. The shallowest mixing line is the result of exchange of tropospheric air with an H_2O VMR of ≈ 53 ppmv and air of stratospheric character with an O_3 VMR of ≈ 200 ppbv. Mixing of dry tropospheric air with ≈ 10 ppmv and stratospheric O_3 rich air of ≈ 400 ppbv forms the steepest mixing line. With increasing potential temperature the slope of the mixing lines increases and the derived $\mu^{e}_{H_2O}$ decreases.

The H_2O entry value for each identified mixing line is depicted in seasonal dependence in Figure 5.2 for three potential temperature ranges: < 340 K (tropopause region), $340 - 360$ K (well ventilated mixing layer) and > 360 K (upper lowermost stratosphere). A distinct seasonal cycle of $\mu^{e}_{H_2O}$ at the tropopause can be identified with an explicit maximum during late spring and summer, and a minimum during the winter months. During autumn and winter the mixing layer is relatively dry. The seasonal variation of the trace gas composition of the two mixing reservoirs troposphere and stratosphere shifts the mixing lines towards higher H_2O VMRs during summer compared to autumn and winter. The H_2O entry at higher isentropes (> 340 K) is significantly reduced compared to lower isentropes. The lowest considered po-

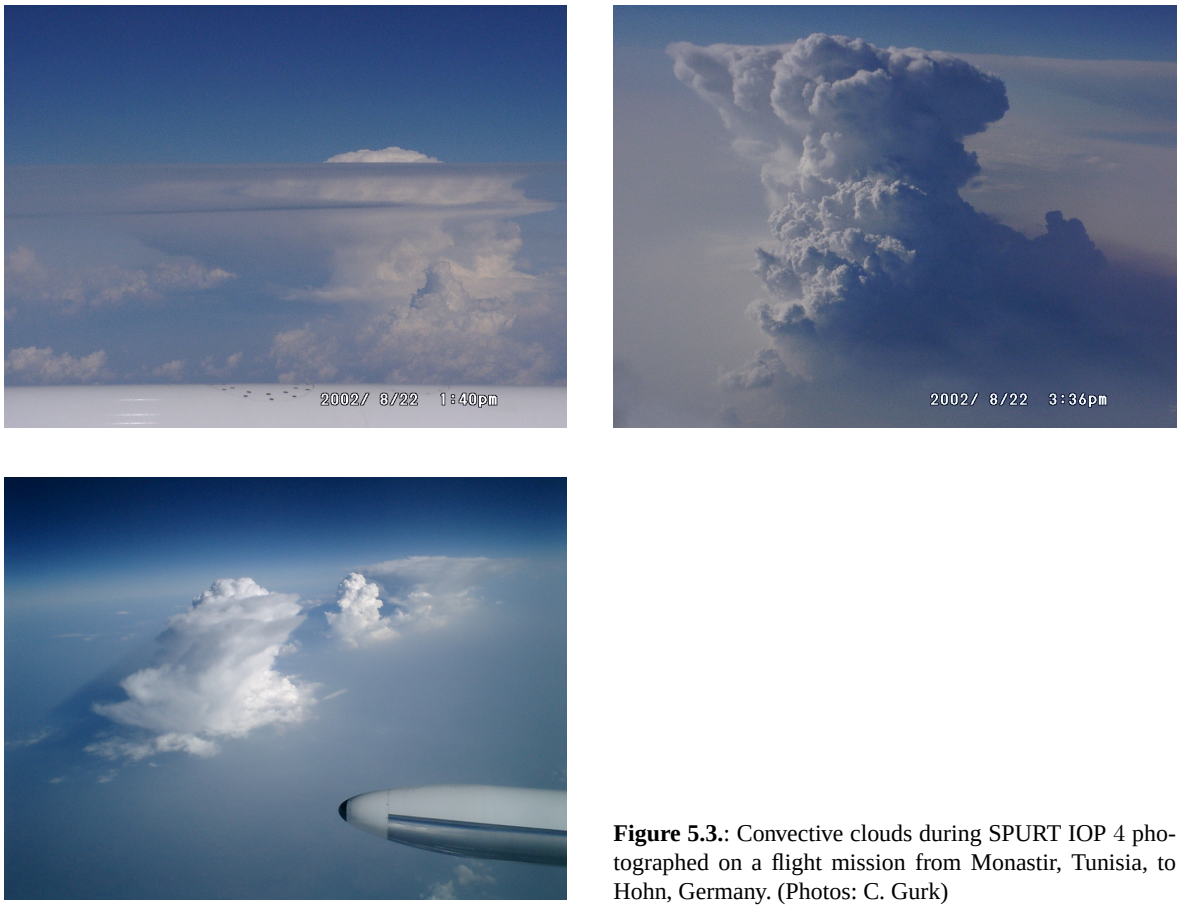

Figure 5.3.: Convective clouds during SPURT IOP 4 photographed on a flight mission from Monastir, Tunisia, to Hohn, Germany. (Photos: C. Gurk)

tential temperature range is influenced by a number of mixing lines with different tropospheric end members. As mentioned before, this is due to the high tropospheric coupling with varying extra-tropical tropospheric sources and the higher amount of turbulence in that region. In contrast to the explicit extra-tropical tropospheric coupling at lower isentropes, $\mu^{e}_{H_2O}$ VMRs lower than ≈ 10 ppmv above 360 K apply for lower latitudes as the entering region. However, the highest Θ region considered also reveals significantly enhanced $\mu^{e}_{H_2O}$ VMRs. These are not present during winter but primarily during the summer months. During both SPURT summer campaigns (IOP 4 in August 2002 and IOP 8 in July 2003) the aircraft crossed regions with convective activity and cumulonimbus (see Figure 5.3). As mentioned earlier, the latter can significantly contribute to an enhancement of H_2O VMRs, even at higher levels in the lowermost stratosphere.

The seasonality and the latitudinal dependence of $\mu^{e}_{H_2O}$ can principally have two reasons: (i) an undergoing change of tropopause temperatures, which effects a differing level of freeze-drying, and (ii) varying intensity in TST processes. The variation with season and potential temperature is qualitatively in agreement with the variability of humidity in the exchange layer. This strongly indicates that temperature limits the amount of H_2O entering the (lowermost) stratosphere.

Measured H_2O VMRs versus equivalent latitude (obtained along trajectory pathways) at the last significant tropopause crossing (LSTPC, cf. Figure 4.4) is displayed in Figure 5.4, seasonally separated (left) as well as colour coded with measured ozone (right). Low equivalent latitudes at the last significant crossing of the 2.0 PVU surface are commonly associated with high O_3 and low H_2O VMRs. These locations are additionally combined with high potential temperatures (> 370 K), exposing lower latitudes (sub-tropics/tropics) as the entering region. O_3 VMRs of TST particles are higher during spring and lowest during summer (cf. Table 4-II). Between 30 and $50°$N, the scatterplot shows a curved pattern towards higher H_2O VMRs. Additionally, most TST is identified within this range. In fact, this is the region of the sub-tropical jet stream. A geographical distribution of the identified TST locations for the SPURT measurements reveals a great coincidence with regions of high horizontal wind velocities (cf. Figure 5.5), in particular with the North Atlantic and Pacific storm track regions. In the summer season, the Mediterranean area appears as an additional preferred TST region.

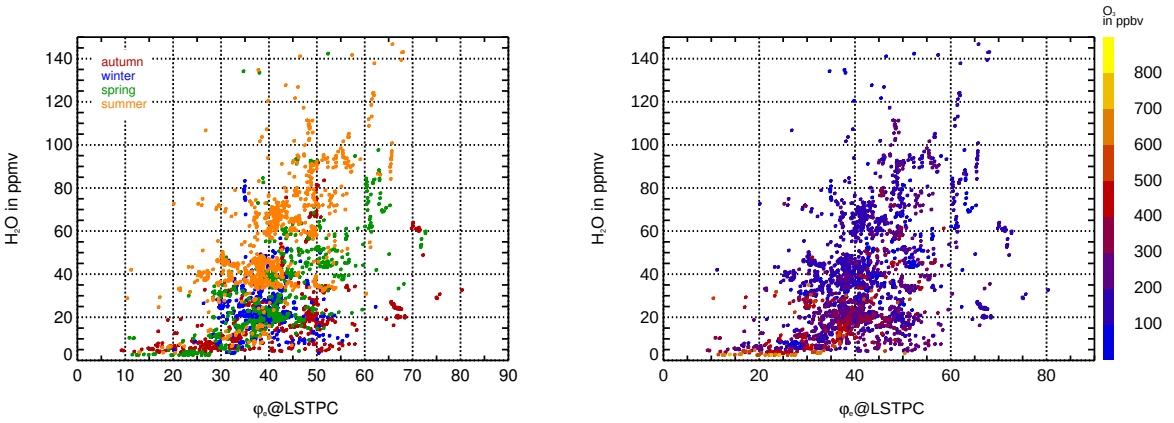

Figure 5.4.: Measured total water versus equivalent latitude at the last significant tropopause crossing (LSTPC, cf. Figure 4.4). The tropopause is chosen as the 2.0 PVU surface. The scatterplot is shown in a seasonal dependence (left: autumn, winter, spring, and summer colour coded with dark red, blue, green, and orange, respectively) as well as colour coded with measured ozone (right).

The seasonally separated scatter plot shows the shift of the curved pattern to higher H_2O VMRs with progressing season towards the summer months. During summer, TST processes can convey higher amounts of H_2O into the lowermost stratosphere. This is valid for the whole summer hemisphere, as tropopause temperatures are highest during that season (cf. Figure 5.6).

The H_2O entry across the tropopause is significantly reduced at higher potential temperatures (lower equivalent latitudes). Thus, the region around the polar jet is a more fertile source for H_2O in the lower stratosphere than its sub-tropical counterpart. However, up to now it is unclear if a variability in frequency and intensity of TST processes will contribute to the observed pattern.

5.2 Meteorological parameters at the tropopause derived from ECMWF analyses

The following study of parameters at the tropopause is based upon Northern Hemisphere ECMWF analyses data in the form described on page 18 in subsection 3.4.1. The time period considered covers the temporal frame of the SPURT campaigns from August 10, 2001, to July 11, 2003, i.e. 701 days, representing an almost "2-year climatology". The tropopause location was evaluated by applying the dynamical tropopause definition for various PV threshold values. Parameters at the tropopause were determined by interpolating the parameter values in each vertical grid profile to the respective threshold PV value for the dynamical tropopause. The dynamical tropopause definition is only valid in the extra-tropics. Surfaces of potential vorticity strongly bulge upwards and tend to be rather vertical near the equator. Additionally, the Coriolis parameter changes its algebraic sign at the equator. Therefore, if the threshold PV value below a latitude of $20°$N is located at a potential temperature greater than 380 K (a mean value for the tropical tropopause) the thermal tropopause definition (cf. page 21) is applied. The tropical tropopause parameter is then defined by its value at the lowest isentropic level where the lapse rate definition is valid. In the used isentropic form of the analyses data this is almost everywhere the level of the cold point tropopause, except within the deep tropics, as mentioned by Highwood and Hoskins (1998), where the lowermost stratosphere is close to being isothermal. Furthermore, the time resolution of the analyses data set was 6 hours (i.e. 00, 06, 12, 18 UTC, resulting in a total of 2804 analysis data files). However, for deriving the "climatology" only calculated daily means were considered. The mean of a parameter ξ at the tropopause for the whole considered time period was computed according to

$$\widehat{\xi(\lambda,\varphi)} = \frac{1}{N}\sum_{i=1}^{N}\overline{\xi_i(\lambda,\varphi)}, \tag{5.1}$$

with N as the number of considered days, λ and φ as the geographical longitude and latitude, and $\overline{\xi_i(\lambda,\varphi)}$ as the daily mean at the tropopause of the i^{th} data file. In the following, the seasonal distribution for the tropopause parameters pressure (p), geopotential height (GPH), horizontal wind velocity (FF), potential temperature (Θ) and temperature (T), specific humidity (SH), and ice saturation mixing ratio (IS) are shown for a threshold PV value of 2.0 PVU.

Pressure, geopotential height and horizontal wind velocity

As known from usual weather charts convergence zones of isobars or isohypses indicate regions of high wind velocities, i.e. the jet stream is correlated with strong gradients in tropopause pressure and/or height. Strong horizontal gradients reflect high horizontal wind

velocities and vice versa (cf. e.g., Hoinka, 1999). In Figure 5.5 the horizontal wind velocity for the considered time period at the tropopause (2.0 PVU) is depicted as seasonal means (clockwise: SON, DJF, JJA, MAM). The corresponding average fields of pressure and geopotential height at the tropopause are shown in Appendix D, Figure D.1 and Figure D.2, respectively. During DJF the jet stream at the tropopause is strongest in the West Pacific with mean wind velocities of about 65 m s^{-1}. A second pronounced jet stream region during winter is placed to the east of the orographically induced planetary wave trough over North America. High jet stream intensities are also present in the "climatology" above the Arabian peninsula. Towards the summer season (JJA) the jet stream moves northward. Additionally, mean tropopause horizontal wind velocities weaken about a factor of 2 (down to 30 m s^{-1} in the West Pacific and over North America and 15 m s^{-1} over Arabia. A pronounced feature is apparent above the Indian region and China. Whereas during winter the jet stream is very strong over China, during JJA the jet stream is shifted further north and the Indian region is affected by the easterly winds. A study towards the seasonal dependence of cross-tropopause tracer transport upon the sub-tropical jet stream intensity is performed in chapter 8.

In concordance with Highwood and Hoskins (1998), mean tropical tropopause pressures during JJA are higher than during Northern Hemispheric winter. Thereby, the lowest pressure levels occur near the region of the Asian monsoon. Additionally, meridional and zonal variations in tropopause height and temperature (see below) reflect the jet stream structure.

Reid and Gage (1981) showed on the basis of radiosonde data that tropopause heights over large tropical areas are lowest during Northern Hemisphere summer and highest during winter. Figure D.2 reflects that finding. Within the considered time period mean tropopause heights in the tropics range from 16 km during JJA to 17 km during DJF. At high latitudes tropopause heights are about 8 km (7 km) during summer (spring). From the tropics towards the pole tropopause heights decrease monotonically with weak meridional gradients between $0-20°$N and $50-90°$N. The meridional gradients are pronounced in the mid-latitudes, especially during DJF and MAM, and particularly over Northern India, China, Japan, and the West Pacific region. During summer the meridional gradients are weakest. The seasonal variation of the gradients is largest in the West Pacific.

The distributions imply that the SPURT region is strongly coupled to the large-scale dynamics. The jet stream strength during winter and spring with the combined increase in Rossby wave breaking events drives the Brewer-Dobson circulation. This leads to enhanced downward transport in the extra-tropics. Thus, the meridional gradient in tropopause height is stronger during that season. Additionally, the SPURT sector is within or downstream a preferred wave breaking zone, i.e. the North Atlantic region. Thus, pollutants from the high emission regions as North America can affect the atmospheric chemical composition, in

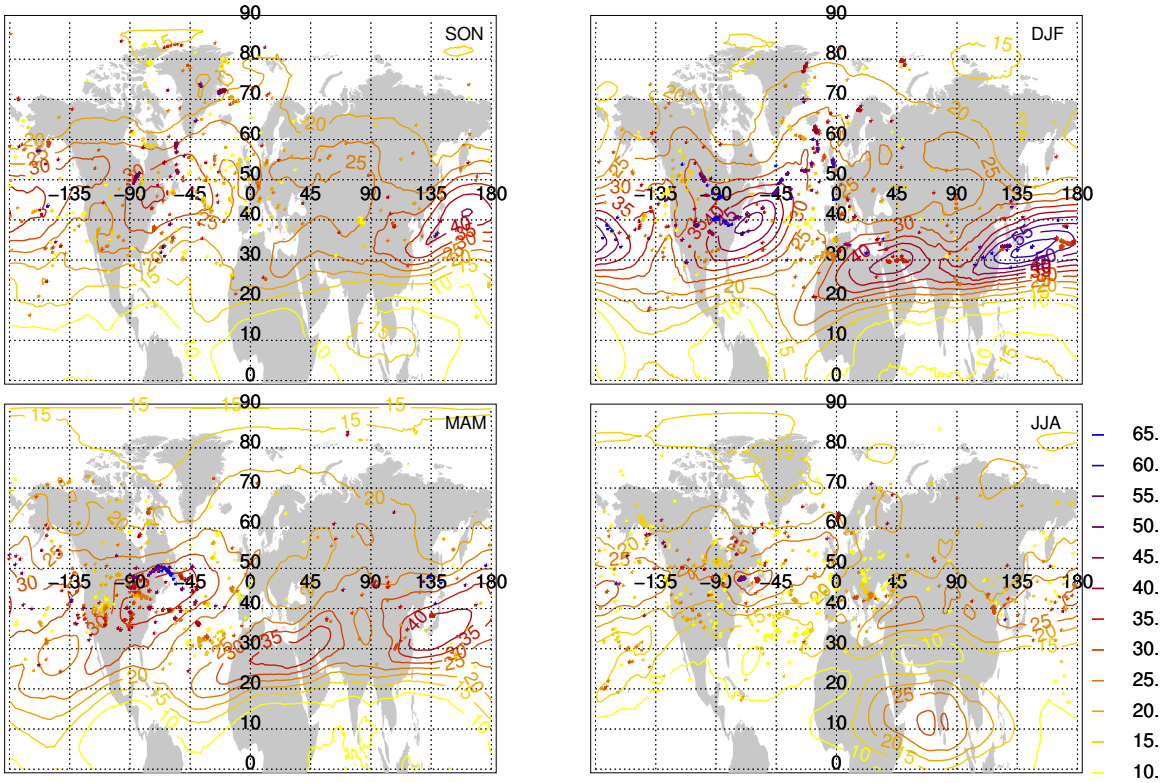

Figure 5.5.: Contour fields: horizontal wind velocity FF at the tropopause defined by the 2.0 PVU surface (colour coded in m s^{-1}). Additionally, locations of last significant tropopause crossings of identified TST trajectories are displayed with FF at the exchange location (same colour coding). Clockwise: autumn, winter, summer, and spring.

particular above Europe. However, during summer the jet stream wind velocities are weaker, reducing the barrier for quasi-isentropic transport between the troposphere and the stratosphere (see also chapter 8).

Potential temperature and temperature

Seasonal mean distributions of potential temperature and temperature at the tropopause are shown in Appendix D (Figure D.3 and Figure 5.6, respectively). Tropopause potential temperatures in the tropics are highest during winter and vice versa during summer. The opposite is valid for the polar regions. Tropical tropopause temperatures are ≈ 196 K during JJA and $190 - 192$ K during DJF (cf. also Highwood and Hoskins, 1998). They occur over the western and central Pacific Ocean. As pointed out by Highwood and Hoskins (1998), the temperature distribution suggests that the tropopause is at high altitudes and very cold in the region of the Asian monsoon. Thus, it may have prominent importance in STE. The temperature distributions are well correlated with those of the tropopause height and pressure shown in Figure D.2 and Figure D.1, respectively. Strongest meridional temperature gradients are located at the jet stream core, which is located at the northern side of the strong concentrations of isohypses.

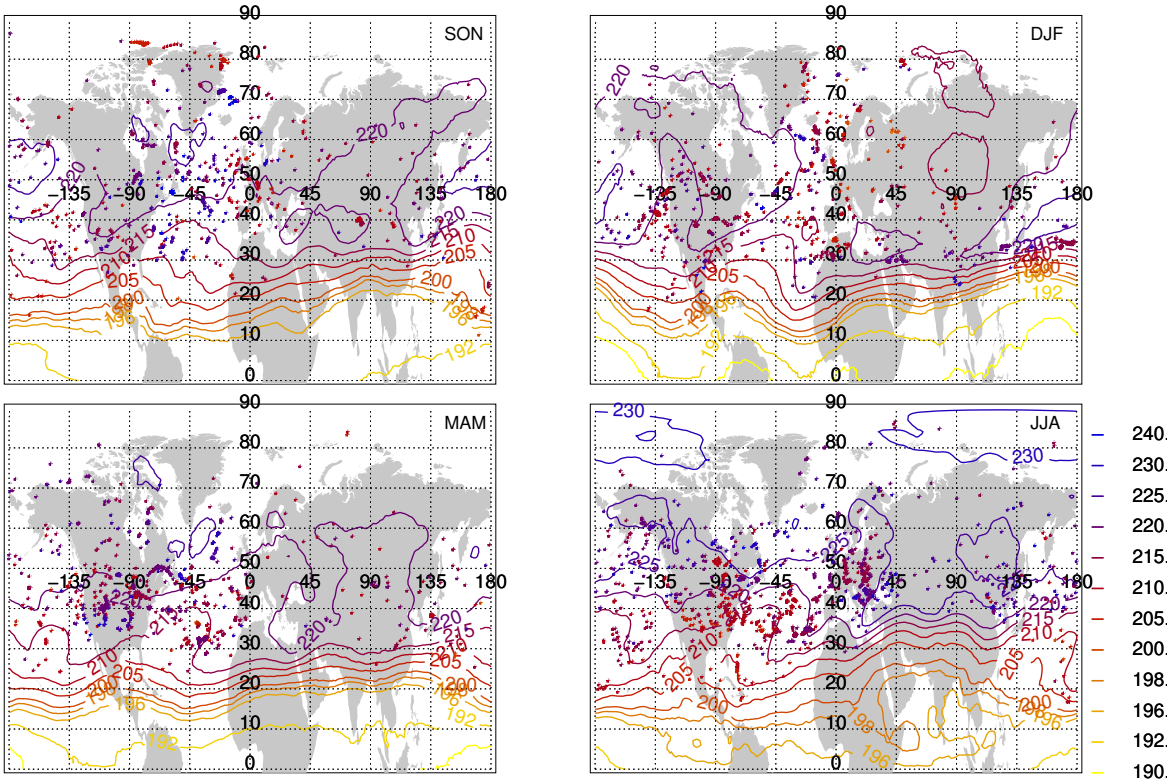

Figure 5.6.: Contour fields: temperature T at the tropopause defined by the 2.0 PVU surface (colour coded in K). Additionally, locations of last significant tropopause crossings of identified TST trajectories are displayed with T at the exchange location (same colour coding). Clockwise: autumn, winter, summer, and spring.

Nagurny (1998) analysed data from observations and measurements during 1954 and 1991 at "Russian North Pole drifting stations". Thereby, tropopause temperatures at the lower (upper) tropopause bound were around 210 K (212 K) in January, in July the temperatures were about 225 K (233 K). This is in accordance with the derived "climatological" mean tropopause temperatures shown here. The annual temperature amplitude is in the range of about $15 - 20$ K, which is strongly caused by radiation, i.e. polar night and day.

Specific Humidity and ice saturation mixing ratio

Figure 5.7 shows the ECMWF derived averaged specific humidity at the tropopause. In the ECMWF analyses dehydration processes are considered. In case of relative humidities above 100 % in the stratosphere, the H_2O content is reduced to the ice saturation mixing ratio (Simmons et al., 1999). For a better comparison with the H_2O *in situ* measurements during SPURT (and also POLSTAR and STREAM), specific humidity, given in g kg^{-1}, is translated to the volume mixing ratio ppmv. The conversion arises from the ratio of the mole weights of air (29 g mol^{-1}) and water (18 g mol^{-1}).

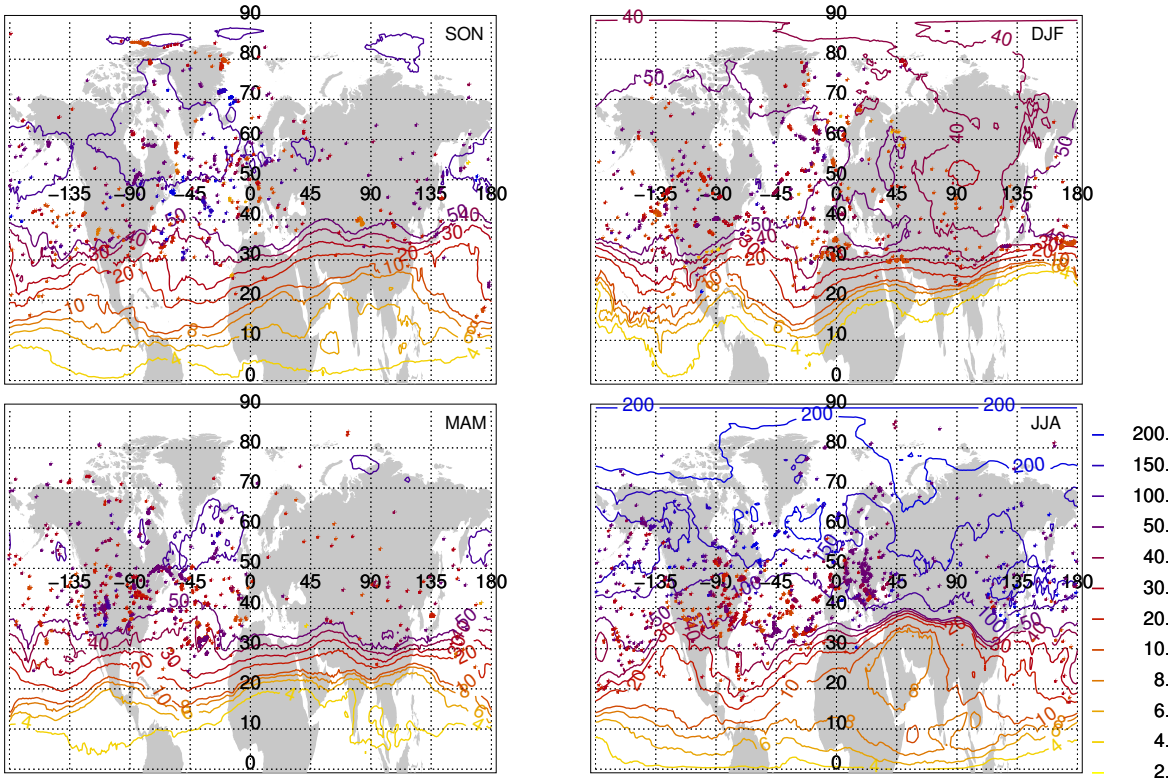

Figure 5.7.: Contour fields: specific humidity SH at the tropopause defined by the 2.0 PVU surface (colour coded in ppmv). Additionally, locations of last significant tropopause crossings of identified TST trajectories are displayed with SH at the exchange location (same colour coding). Clockwise: autumn, winter, summer, and spring.

Lowest tropopause SH mixing ratios appear in the tropics. The gradually poleward increase is apparent in all seasons. From MAM towards JJA a moistening of the tropopause region is evident (cf. also Simmons et al., 1999), whereas towards SON H_2O at the tropopause decreases significantly. The latter is also shown by the SPURT data (e.g., Figure 3.6). Combined with low pressures and temperatures very low VMRs occur in conjunction with deep convection. Especially over the equatorial Western Pacific, Indian Ocean and Northern South America low SH VMRs are evident during DJF, which correspond approximately to the stratospheric ”fountain” regions nominated by Newell and Gould-Steward (1981). The extreme cold tropopause during DJF in the vicinity of the Western Pacific convection results in extremely low ice saturation mixing ratios, thus giving potential for dehydration of the air on its way to the stratosphere. Mixing ratios for the same regions during JJA are obviously higher.

In the Northern Hemisphere summer months over the Western to Central Pacific and near the east coast of North America, seasonal mixing ratios have maximum values ranging from ≈ 50 to ≈ 170 ppmv, in accordance with Stone et al. (2000). These moist regions in the extra-tropics coincide with enhanced convective cloud amount owing to baroclinic waves activity along storm tracks (Hu and Liu, 1998). Thus more H_2O is transported upward to the tropopause.

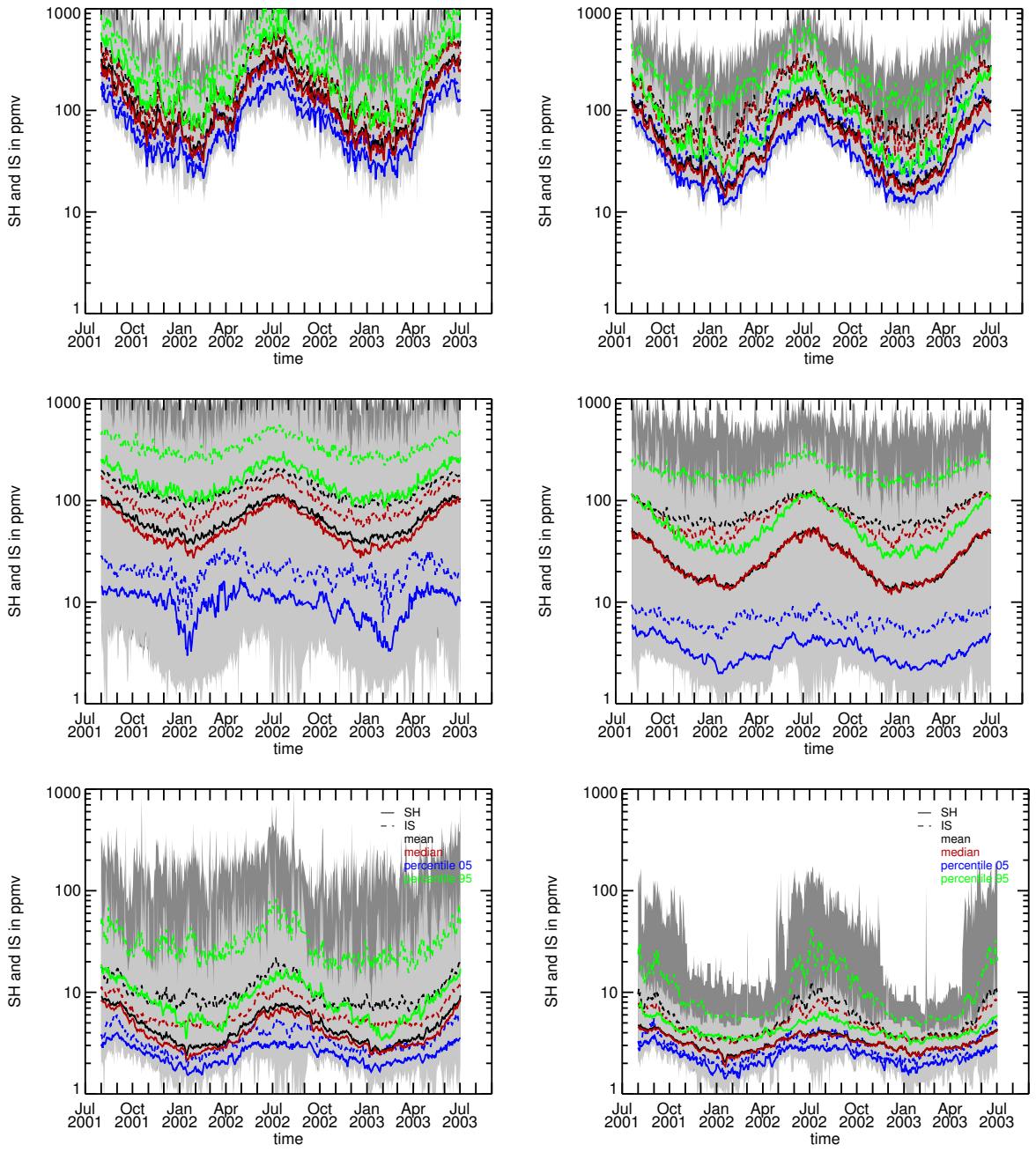

Figure 5.8.: Seasonal cycle of daily mean specific humidity (SH, solid lines) and ice saturation (IS, dashed lines) mixing ratio at the tropopause derived from ECMWF analyses between August 10, 2001, and July 11, 2003. In the extra-tropics, the tropopause is dynamically defined by the 2.0 PVU (left) and 4.0 PVU (right) surface. The mixing ratios are given in ppmv for three equivalent latitude ranges: polar ($71-90^\circ$N, top), sub-tropics/mid-latitudes ($21-70^\circ$N, middle) and tropics ($0-20^\circ$N, bottom). For both quantities, the mean, median as well as the 5 % and 95 % percentiles are given. The light (dark) grey shading reflects the range within which derived tropopause values for SH (IS) fall into.

For a better impression and to emphasize the variability of humidity in the tropopause region, in Figure 5.8 the seasonal cycle of Northern Hemisphere ECMWF derived specific humidity and ice saturation mixing ratio (cf. Equation 4.5) interpolated to the 2.0 and 4.0 PVU surface are displayed. Thereby, a differentiation for the polar regions ($71-90^\circ$N), the mid-latitudes and sub-tropics ($21-70^\circ$N) as well as for the tropics ($0-20^\circ$N) is performed. As is evident, the annual cycle of tropical tropopause temperatures has an impact on the H_2O content in

the lower stratosphere (e.g. Newell and Gould-Steward, 1981). Whereas during winter mean values at the tropical tropopause are about $2-3$ ppmv, during summer they are elevated to about $7-8$ ppmv.

The seasonal cycles for the extra-tropics show the same course with a maximum during JJA and a minimum during DJF. The polar tropopause is relatively humid during summer and dry during winter. The largest seasonal variations appear in the region considered for the sub-tropics/mid-latitudes. This is mainly effectuated by the strong meridional H_2O gradient between $20°$N and $40°$N (cf. Figure 5.7).
The seasonal variation with a minimum during the winter months could be explained by at least two potential causes: (i) annual variations of tropopause temperatures are combined with variations in ice saturation mixing ratios, thus potentially decreasing H_2O during winter; (ii) descent of stratospheric air during winter may also contribute to the decrease.

Due to the hemispheric illustration, to consider uncertainties concerning the dynamical tropopause definition, a change from 2.0 PVU to 4.0 PVU leads to a decrease in mixing ratios of ≈ 50 %. Anyhow, the seasonal variation remains about the same. This is in qualitative agreement with the seasonal cycle of H_2O at the tropopause measured by Polar Ozone and Aerosol Measurement (POAM) III (Nedoluha et al., 2002, their figure 4). Additionally, the seasonal course of entry values shown in Figure 5.2 is comparable with the annual cycle of specific humidity at the tropopause derived from ECMWF analyses during the SPURT time period. Thereby, the distinguished three potential temperature regimes can be widely compared with the three latitudinal regions considered in Figure 5.8.

In the shown hemispheric distributions of parameters at the tropopause, additionally, the locations of the last significant tropopause crossings of SPURT TST trajectories are given. The trajectories are colour coded according to the respective parameter value. Note, that the mean contour field is not representative for TST. Thus, the colour coding of TST parcels can differ significantly from the surrounding mean background field. Anyhow, in DJF the northern parts of the mid-latitude storm tracks are characterised by enhanced TST activity. The southern parts of North America and Canada are year-round preferred TST regions. During summer the eastern Mediterranean area shows enhanced TST. The preferred TST in these regions is possibly evoked by the high frequency of warm conveyor belts (Wernli and Davies, 1997), which are associated with extra-tropical cyclones (Stohl, 2001; Eckardt et al., 2004). Thus, areas like the Eastern United States are important for the chemical composition of the UT/LMS. These high emission regions are a source for rapid transport into the (lowermost) stratosphere (Stohl et al., 2003b).
The identified locations of TST regions for the SPURT data can not supply a hemispheric distribution of TST patterns. The trajectories were initialised on the flight tracks during SPURT

in the European area (cf. Figure 2.4). Anyhow, the identified locations are qualitatively in agreement with the "1-year climatology" of TST in the extra-tropical Northern Hemisphere by Wernli and Bourqui (2002).

5.3 Main results of this chapter

The emphasis in this chapter was led on the seasonality of H_2O entry values into the lowermost stratosphere. Using O_3:H_2O correlations, the entry values were derived from the end members of mixing lines at the tropopause, resulting in a seasonal cycle with a distinct maximum during summer. Thereby, the H_2O entry values decrease towards higher isentropes, which is in accordance with an entry location of the air into the LMS at lower latitudes, i.e. in the sub-tropics/tropics.

A quasi "2-year climatology" of H_2O and parameters at the tropopause covering the SPURT time period was performed to set the episodical and regional SPURT measurements into the climatological context on the global scale. The SPURT sector is strongly coupled to the large-scale dynamics. In particular, it is located in a preferred wave breaking zone, and the atmospheric composition is thus possibly influenced by air origination from high emission regions as North America.
The derived H_2O entry values from the SPURT measurements are consistent with values for specific humidity and ice saturation at the tropopause obtained from the performed ECMWF climatology. This implies that the H_2O entry value is strongly dependent on tropopause temperatures, which is addressed im more detail in the following chapter 6.

Chapter 6

Impact of stratosphere-troposphere exchange

6.1 Freeze-drying at the extra-tropical tropopause

The well collocated SPURT measurements, their high accuracy and the fine sampling scale allow a detailed study of saturation in the probed air masses or during their recent history. In this section, the emphasis is led on saturation and/or supersaturation during the SPURT campaigns and how often and where (super)saturation occurs in the UT/LMS. Clouds are composed primarily of water-ice particles. Thus, observation of ice saturation should be concomitant with clouds. However, for a cirrus cloud formation, significant (super)saturation may be required, depending on the freezing process (homogeneous or heterogeneous, Mangold, 2004, and references therein). Thus, supersaturation in the upper troposphere can be understood as an effect of nucleation barrier (Jensen et al., 1998). To investigate (super)saturation/dehydration processes, measurements of total water, i.e. water in the gas and condensed phase, are desirable (Schiller et al., 2002). Since FISH measures total water, also cirrus regions are captured by the measurements. Together with the temperature and pressure measurements aboard the Learjet 35A, the FISH data can be used to study (super)saturation of the probed air masses. Beneath the determination of the occurrence frequency of ice saturation, the vertical extent of saturated regions can be derived.

For each SPURT 5 s data point the corresponding PV value has been determined which allows for a classification with respect to its relative location to the tropopause. Thereby, the tropopause is chosen as the 2.0 PVU surface. For the whole SPURT data set the left chart in Figure 6.1 shows a scatterplot of the ECMWF derived potential vorticity at the location of

the measurement with observed relative humidity with respect to ice (RH_{ice}). Thereby, RH_{ice} was calculated according to

$$RH_{ice} = \frac{e_{H_2O}}{e_{sat}}, \tag{6.1}$$

where

$$e_{H_2O} = \frac{p \cdot [H_2O]}{1.E6 + [H_2O]} \tag{6.2}$$

with pressure p and $[H_2O]$ as the measured total water in ppmv; e_{sat} is given by Equation 4.4 on page 58. The colour coding represents the minimum PV during the previous 10 days, obtained from 10 day backward trajectory calculations with CLaMS. As long as the measured H_2O is less than the ice saturation VMR (calculated according to Equation 4.5 on page 58), it is assumed to sample in a cloud free region. Otherwise, particles entering the inlet must cause the difference. Thus, the FISH measurements have to be corrected for anisokinetic sampling (Schiller et al., 1999). The according scatterplot for the corrected FISH signal is given in the right chart in Figure 6.1.

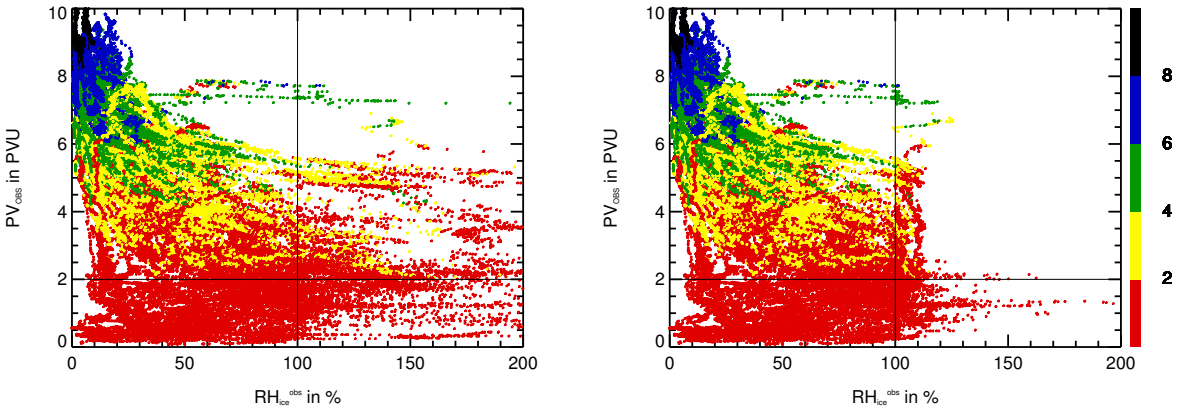

Figure 6.1.: Interpolated potential vorticity (PV) at the observation time versus observed relative humidity with respect to ice (left, RH_{ice}) and versus RH_{ice}, corrected for anisokinetic sampling. The colour coding of each chart reflects the minimum potential vorticity of the air parcels during their 10 day history.

In this analysis, saturation is assumed at RH_{ice}=100 %. Saturation and supersaturation includes both sampled water and ice particles. As can be identified, in several cases saturation and supersaturation were observed during the measurements, up to PV values of > 5 PVU. This is clearly within the lowermost stratosphere. In a special case, RH_{ice}values > 100 % were observed even up to ≈ 8 PVU, with minimum PV values of about $4 - 6$ PVU. This case is given a closer look with an RDF study in chapter 7. As is to expect from the temperature profile with minimum temperatures near the tropopause, immediately in the vicinity of the tropopause the majority of supersaturation is present. This is also concordant with e.g. Winker and Vaughan (1994), who showed from LIDAR data that cirrus cloud layers are found most often near the tropopause. Maximum ice supersaturations above the tropopause, although rarely, range up to ≈ 60 %. This is in the order of observed RH_{ice} in cirrus clouds in

the Northern Hemisphere (cf. Ovarlez et al., 2002). Anyhow, the most interesting feature is the occurrence of (super)saturation even above the tropopause.

The application of backward trajectories informs about the origin of the single air parcels and how deep it penetrates into the stratosphere. The colour bar scaling is the same as the vertical extension of the ordinate. Thus, the particles which, in the mean, gain PV during the previous 10 days can easily be identified by the colour change in the respective PV range. All red marked air parcels above the actual PV value of 2.0 PVU (black horizontal line) have at least once been in the troposphere, i.e. < 2.0 PVU, during their 10 day history. Saturated and supersaturated air parcels at and above the tropopause mostly have their origin in the troposphere. This indicates that episodes of TST are frequently combined with humidity anomalies in the tropopause region, in particular with condensation and thus with freeze-drying. Cirrus clouds have a high potential of effective drying of air masses, in particular for those transported into the stratosphere. Cold temperatures give potential for cloud formation, and thus for removing water out of atmospheric regions, where radiative active trace gases as H_2O have a disproportional effect on the radiation budget of the Earth (Jensen et al., 1996a,b). Moreover, if these clouds are injected into a relatively dry environment they are likely to moisten this part of the atmosphere, leading to higher H_2O in the stratosphere.

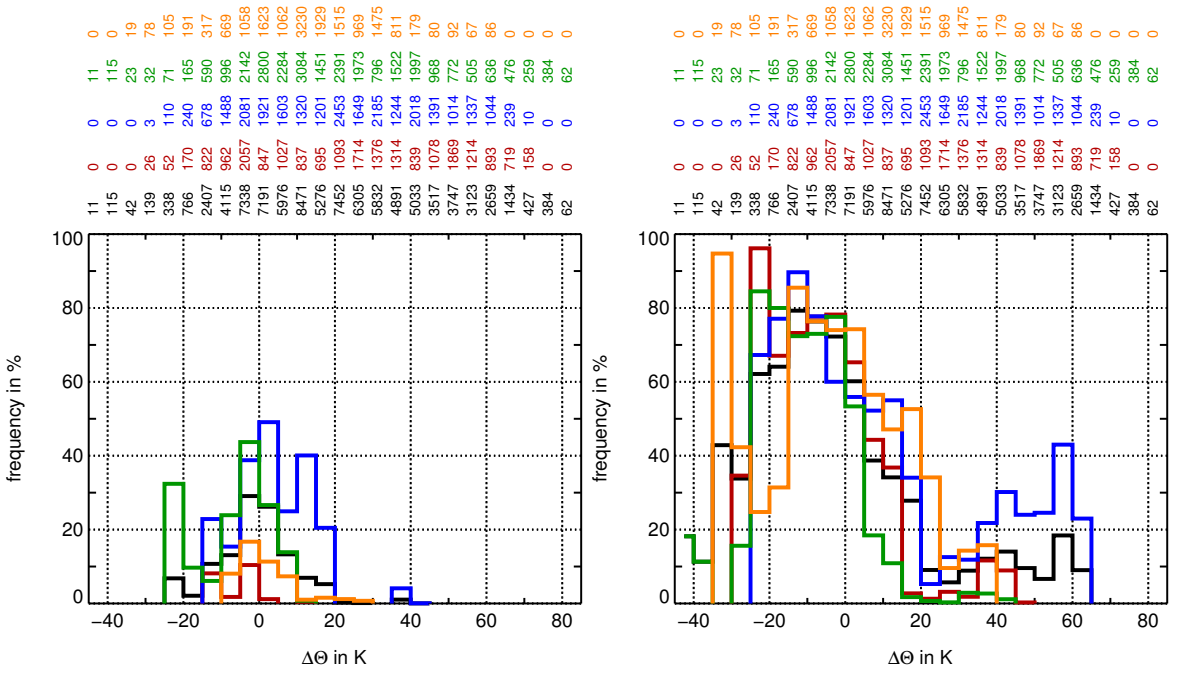

Figure 6.2.: Occurrence frequencies of observed ice (super)saturation relative to the local tropopause ($\triangle\Theta = 0$ K) (left) and potential for (super)saturation within the last 10 days (right). The frequencies are binned by steps in $\triangle\Theta$ of 5 K and normalised to the total number of observations in each bin. Thus the occurrence frequency is given in %. The distributions are shown for the total SPURT measurements (black) as well as separated by season: autumn (dark red), winter (blue), spring (green), and summer (orange). The corresponding amount of considered data points in each bin is given at the top of the plot (same colour coding).

On the left side of Figure 6.2 the normalised occurrence frequency of RH_{ice} above 100 % is shown for the total SPURT measurements (black) with relation to the local tropopause. The distance to the tropopause is expressed by $\triangle\Theta$ relative to the 2.0 PVU surface and is incremented by 5 K. Additionally, the distributions are given for each season (autumn, winter, spring, and summer in dark red, blue, green and orange, respectively). Hereby, the total number of observations in each $\triangle\Theta$-bin for the seasonal and total data is given above the corresponding bin at the top. The ratio of (super)saturated data points to the total number of data points in each $\triangle\Theta$-bin defines the frequency of cloud occurrence, given in percent. With increasing values of $\triangle\Theta$ below the tropopause the occurrence frequency of RH_{ice} increases. It peaks slightly below the tropopause. Above the tropopause, an abrupt decrease in frequency to a few percent is evident within the first 20 K. Further in the lowermost stratosphere there is no evidence of saturation, expect for some single cases during some winter missions around 35 K. With increasing altitude the H_2O VMRs decrease and there is a sharp gradient of H_2O in the tropopause region (cf. e.g., Figure 3.9). Additionally, the temperature usually remains constant or increases in the vicinity and above the tropopause. Thus, the potential for saturation is further decreased. In the stratosphere, observation of cirrus clouds have been reported only just above the tropopause and mostly in the tropics (e.g., Jensen et al., 1996b; Beyerle et al., 1998). Although ice saturation seems to be rare in the mid-latitude lowermost stratosphere more than 20 K above the tropopause, the SPURT data provide evidence for the existence of stratospheric cirrus clouds, in contrast to results from ER-2 missions analysed by Smith et al. (2001).

The temperature history of each trajectory in conjunction with the corresponding H_2O measurement informs about a potential for cloud formation or experienced (super)saturation/dehydration within the past 10 days. Whether or not an air parcel encountered (super)saturation conditions within the previous 10 days can be derived from the temperature history of the backward trajectories, assuming a constant H_2O VMR of the air parcels within that time period. However, there are limitations for trajectory calculations based on large scale analyses. Turbulent mixing and lateral mixing by inertia-gravity waves (Danielsen, 1993) are not considered. Furthermore, small-scale gravity waves can significantly affect temperature (Gary, 1989). The latter is important for considering cloud formation, since the relation between ice saturation and temperature is exponential (cf. Equation 4.4). Small temperature variations can significantly change ice saturation. To estimate at least the uncertainty of the ECMWF temperatures, a comparison of measured and ECMWF derived temperatures, interpolated to the single SPURT flight tracks in each season, is shown in Figure 6.3. Owing to the large temperature gradients in the troposphere and tropopause region, errors are much larger there than errors in the stratosphere. Therefore, only data points above the 2.0 PVU surface are considered. Obviously, the fine scale structures captured by the mea-

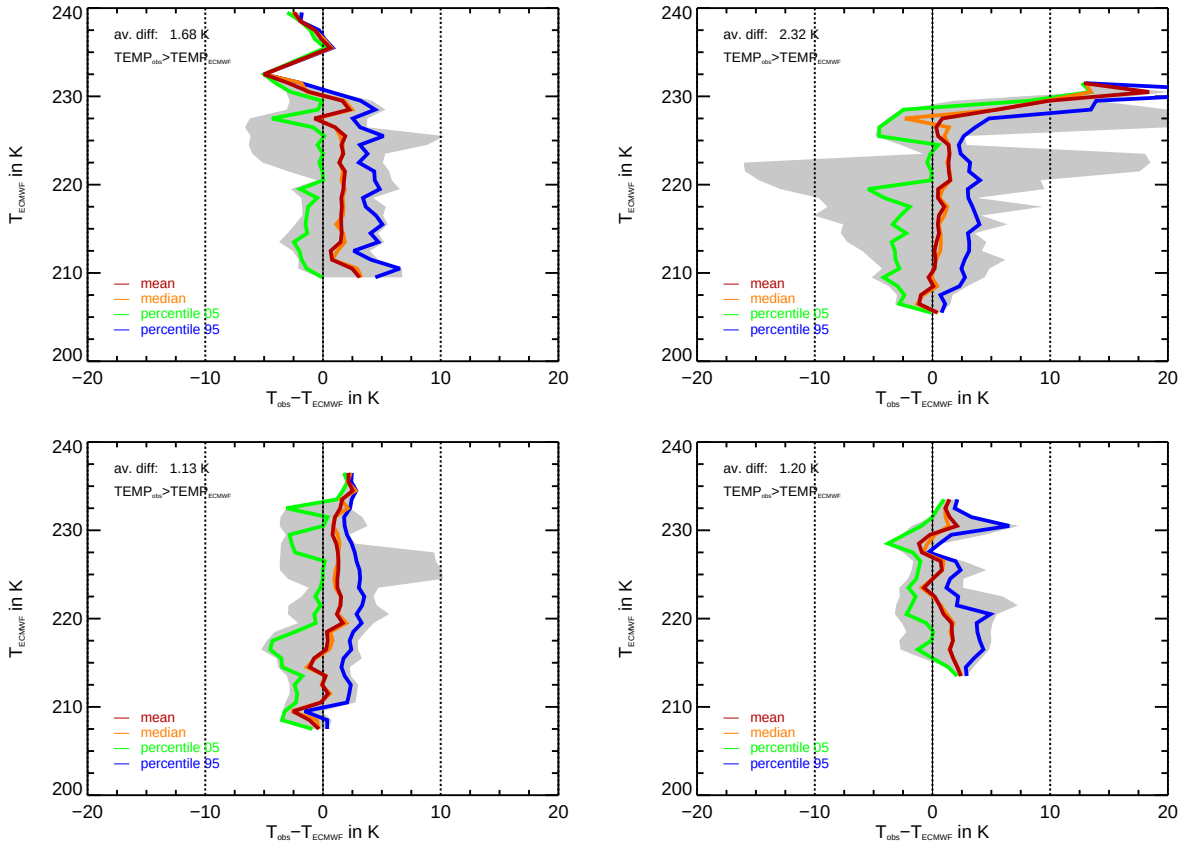

Figure 6.3.: ECMWF derived temperatures above the 2.0 PVU surface versus temperature difference of measurements and the model. The comparisons are given for the SPURT missions in each season (clockwise: missions during autumn, winter, summer, and spring).

surements can not be reflected by the ECMWF analyses. However, measured temperatures were always slightly higher with a maximum average difference during the winter missions of ≈ 2.3 K. In mid- and high-latitudes, variations of the polar front jet stream along with the developing storms cause enhanced temperature variations (Shapiro et al., 1980). However, mean temperature differences between measurements and model during the other missions were definitely below 2 K. Thus, the temperature history of the backward trajectories is assumed to be satisfying to account for evidence of prior saturation conditions.

In Figure 6.4 the maximum temperature difference which the trajectories encountered during the previous 10 days is displayed with respect to their location relative to the local tropopause ($\triangle\Theta$) at the measurement time. The highest temperature differences were experienced by those particles, which are now located close to the tropopause.

Considering the temperature history along the trajectories, there is a serious increase in the likelihood for (super)saturation. The reason is that with increasing backward time the likelihood for colder temperatures increases. This is represented by the scatterplot in Figure 6.5, showing PV at the measurement time versus maximum encountered RH_{ice} during the last 10 days. To quantify the degree of saturation occurrence and its seasonal variation,

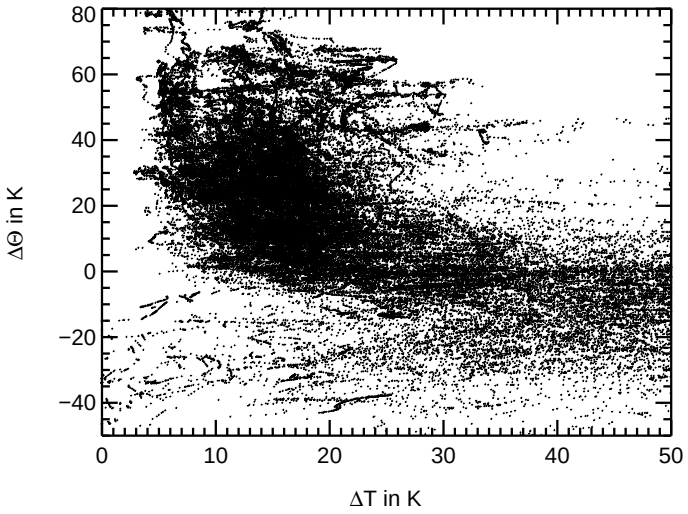

Figure 6.4.: Maximum encountered temperature differences of air parcels during their 10 day history ($\triangle T$) relative to the observed distance to the tropopause ($\triangle \Theta$).

frequency distributions of encountered $RH_{ice} > 100$ % during the calculated backward time is displayed in the right chart in Figure 6.2. The likelihood for occurrence of (super)saturation is > 50 % within 20 K below the tropopause and shows a peak there for all seasons. Above the tropopause, the saturation potential is still considerably large but it decreases abruptly within the next 20 K. There is rather no evidence for encountered saturation higher than 10 K above the tropopause during spring. However, for the other seasons, a slight secondary maximum around $30 - 40$ K is evident. For the wintertime measurements, especially for northbound flights during IOP 6 (cf. chapter 7), more than 20 % of air parcels, even up to 60 K above the tropopause, encountered saturation conditions. The potential for cloud formation in the lowermost stratosphere is highest during this period, in agreement with results of ER-2 data from Murphy et al. (1990).

A prominent feature is apparent in the autumn distributions. At the measurement time (left chart in Figure 6.2) very few saturation events were observed and only slightly below the tropopause. In contrast, taking the temperature history in account (right chart in Figure 6.2), the potential for encountered (super)saturation increases significantly. This suggest an efficient drying of the air during that season (see also Figure 9.1 in section 9.1).

The backward trajectories show evidence of prior (super)saturation, even well within the lowermost stratosphere. This indicates the important issue that temperature near the extra-tropical tropopause has the potential to limit transport of H_2O into the lowermost stratosphere, similar to the freeze-out of H_2O at the tropical ”cold trap”.

Although saturation and supersaturation do occur, air near the extra-tropical tropopause is, on average, undersaturated. There is no need for cloud formation if saturation or supersaturation is present. Anyhow, it is obvious that the H_2O distribution is influenced by the potential for forming clouds. Further, the occurrence of RH_{ice} values up to 150 % implies cloud formation, but possibly only for a short time, depending on temperature. Thus sedimentation could be reduced and this would limit freeze-drying.

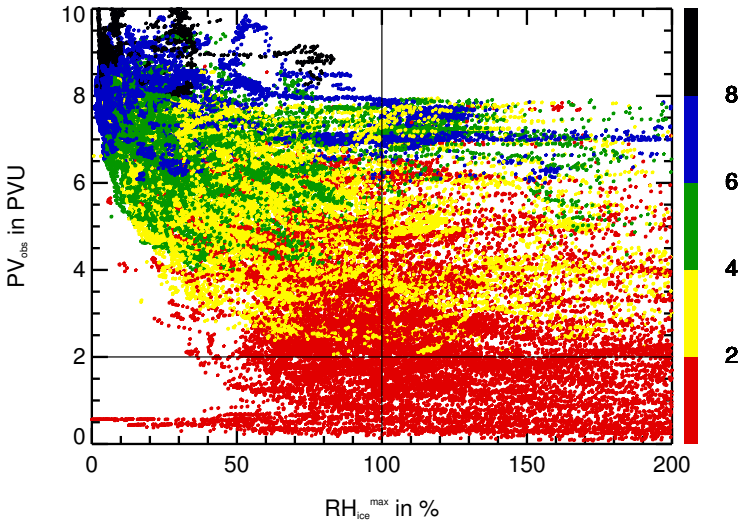

Figure 6.5.: As Figure 6.1, but for the maximum encountered RH_{ice} during the 10 day history, corrected for anisokinetic sampling.

6.2 Ozone transport into the troposphere

In the previous section 6.1 the focus was on the implication of TST for cloud formation in the tropopause region and in the lowermost stratosphere. Here, the effect of STT on the O_3 seasonal cycle in the upper troposphere will be addressed. On the one hand, changes in tropospheric O_3 concentrations influence the radiative balance of the troposphere, as O_3 is a strong infrared absorber. On the other hand, as O_3 photolysis is the principal source of OH radicals, also photochemical cycles are affected (Beekmann et al., 1994). Thus, tropospheric climate is sensitive to O_3 perturbations in that region (Ramaswamy et al., 1992).

Cut-off lows are combined with STT (e.g., Bamber et al., 1984; Price and Vaughan, 1993; Ancellet et al., 1994). Within stratospheric intrusions, air often descents down to the middle troposphere (e.g., Ancellet et al., 1991; Stohl and Trickl, 1999) and can even reach the surface (Davies and Schuepach, 1994). Concerning the discussed spring time O_3 maximum (see review by Monks, 2000), some studies suggest that the annual variation of STT might be the major contributing factor (Oltmans, 1981; Levy et al., 1985). From O_3 soundings over Uccle, Belgium, Van Haver et al. (1996) inferred a maximum O_3 exchange rate in tropospheric fold events during spring. These events have the potential to transport O_3 down into the free troposphere (Beekmann et al., 1997; Elbern et al., 1997). The seasonal variation of STT intensity by tropopause folds for the Northern Hemisphere was estimated by Danielsen and Mohnen (1977), showing a maximum in April and a minimum in October. During spring the tropopause altitude increases, which entrains stratospheric air into the troposphere (Reiter, 1975; Appenzeller et al., 1996b). In contrast, there are studies, concluding that there are no preferred STT events during the spring season (e.g., Price and Vaughan, 1992). Thus, a spring maximum should be caused by the strength of such events rather than by their frequency (Monks, 2000).

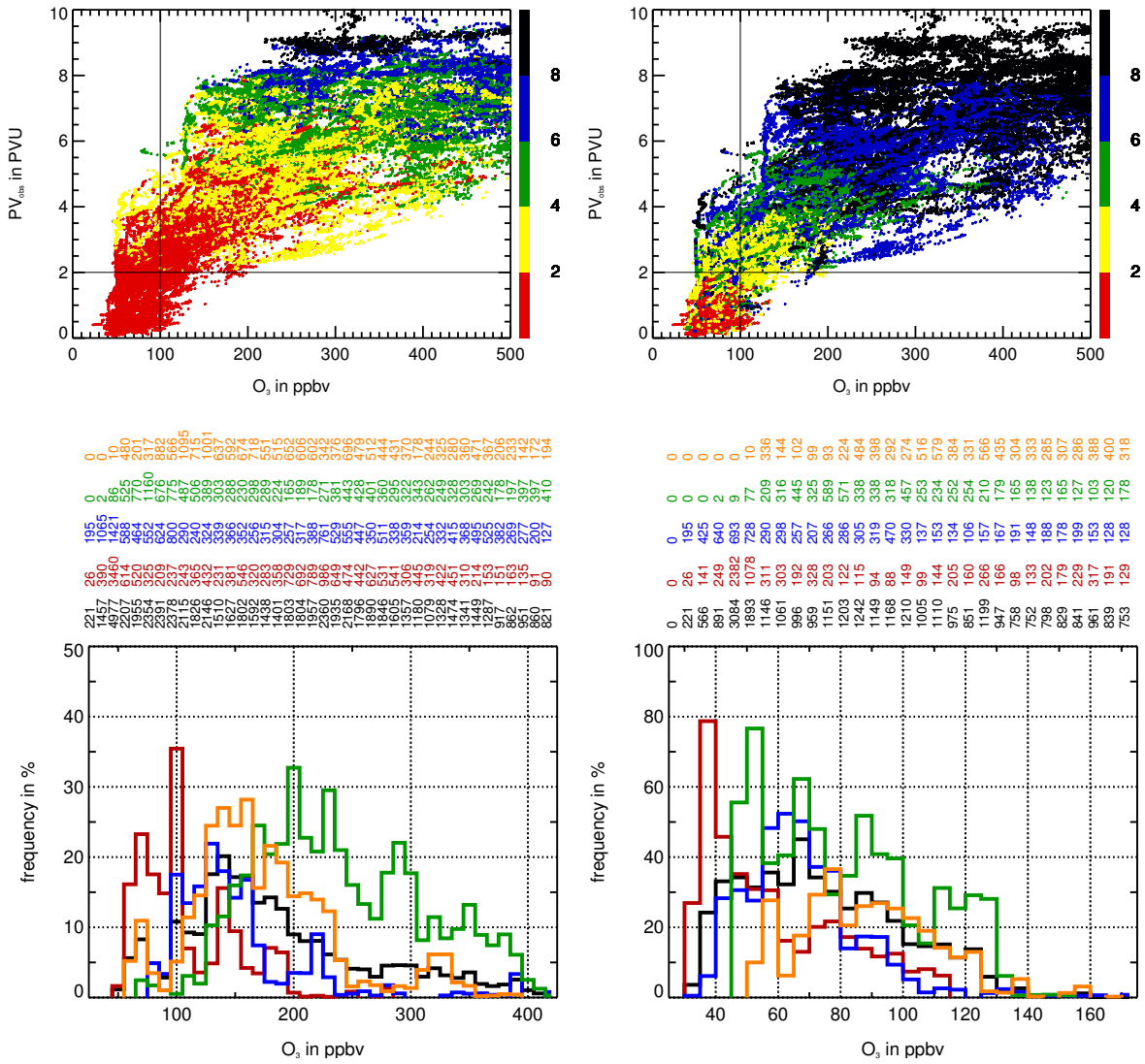

Figure 6.6.: Top: Potential vorticity versus measured ozone, colour coded with the minimum (left) and maximum (right) potential vorticity during the past 10 days.
Bottom: Seasonal frequency distributions of identified TST (left) and STT (right) parcels during the previous 10 days as a function of O_3. The frequencies, given in %, for the TST (STT) trajectories are binned by O_3 steps of 10 ppbv (5 ppbv). The normalisation is performed to the total number of observations in each bin, given at the top. The distributions are shown for the total SPURT measurements (black) as well as separated by season: autumn (dark red), winter (blue), spring (green), and summer (orange).

In the top left chart of Figure 6.6 a scatterplot of ECMWF derived PV at the observation time with measured O_3 is shown. The colour coding represents the minimum PV during the previous 10 days. The bottom left chart shows the corresponding frequency distributions of those trajectories, which were involved into TST processes during this time period. The distributions are shown for seasonal missions as well as for the total SPURT measurements. Hereby, O_3 is binned in steps of 10 ppbv. TST particles show the lowest O_3 VMRs during the autumn missions. In contrast, during spring, highest and frequent O_3 VMRs up to > 400 ppbv of identified TST particles are present. O_3 reveals the most rapid increase with altitude during spring. Thus, within TST events, tropospheric air can mix with highest O_3 values (Pfister

et al., 2003) during that season. For the summer missions, TST particles also show relatively high O_3 VMRs, indicating that photochemically produced O_3 in the troposphere can also contribute significantly to the O_3 budget of the lowermost stratosphere (Lelieveld and Dentener, 2000).

The right column in Figure 6.6, shows the analog pictures for STT. In the corresponding frequency distributions, an air parcel with an actual PV < 2.0 PVU and a maximum PV within the previous 10 days > 2.0 PVU is considered as an STT parcel. The O_3 intervals are here set to 5 ppbv. The highest occurrence frequencies are evident for the spring season. Maximum frequencies of > 70 % are around $50 - 55$ ppbv O_3 for that season. Even up to 130 ppbv considerable STT frequencies can be identified. Thus, a contribution of STT to tropospheric O_3 seems to play a major role during spring in the investigated region. Also during summer, STT parcels show occurrence frequencies of $10 - 20$ % up to 125 ppbv O_3. Anyhow, the maximum in tropospheric O_3 seems to be rather the effect of photochemical *in situ* production than transport from the stratosphere.

Another approach to assess the impact of STE to the O_3 cycle provide the correlation coefficients (cf. section 3.5). Both ozone and potential vorticity are tracers for stratospheric air. Ozone concentrations in the stratosphere are much higher than in the troposphere. Thus, inflow of stratospheric air into the troposphere results in strong positive correlations between those parameters (e.g., Danielsen, 1968; Browell et al., 1987). However, for time scales larger than some days, potential vorticity is not a perfect identifier for stratospheric air penetrating the troposphere (Beekmann et al., 1994).

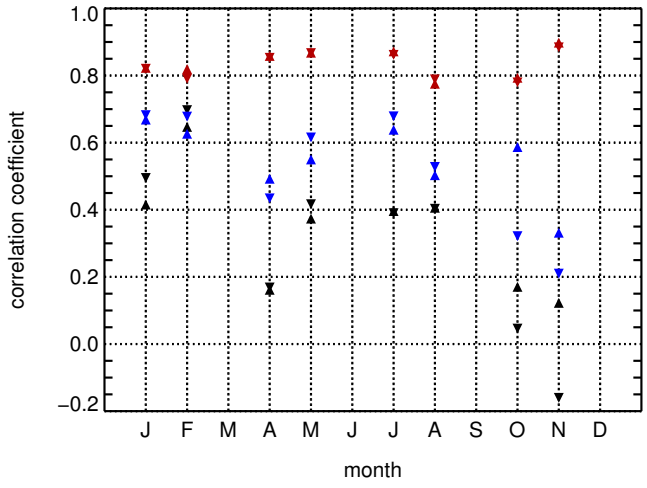

Figure 6.7.: Seasonal variation of Pearson's (▲) und Spearman's (▼) correlation coefficient for ozone versus potential vorticity for three different regions: < 2.0 PVU (black, troposphere), $1.0 - 3.0$ PVU (blue, tropopause region), > 3.0 PVU (red, lowermost stratosphere).

Figure 6.7 shows the seasonal variation of Pearson and Spearman correlation coefficients for O_3 versus PV. Thereby, three different regions as characterised by their potential vorticity are considered: < 2.0 PVU (troposphere), $1.0 - 3.0$ PVU (tropopause region), > 3.0 PVU (lowermost stratosphere). Both correlation coefficients show a strong seasonal variation in the

troposphere and tropopause region with a maximum in February and a minimum in November. With deeper penetration into the lowermost stratosphere the correlation increases, indicating a decreasing influence of tropospheric air. The higher tropospheric correlation coefficients for the winter measurements suggest downward transport of stratospheric air into the troposphere.
A secondary maximum for the correlation coefficients in the tropopause region and in the lowermost stratosphere is apparent in July. Due to the seasonal cycle of O_3 in the troposphere the enhanced positive correlation coefficients in July suggest in-mixing of photochemically produced ozone-rich tropospheric air.

6.3 Main results of this chapter

In this chapter the impact of troposphere-to-stratosphere (TST) and stratosphere-to-troposphere transport (STT) on the chemical composition of the lowermost stratosphere and upper troposphere, respectively, was investigated. During the SPURT project H_2O was measured as the sum of vapour and vaporised ice, which is desirable to study (super)saturation and/or dehydration processes. On several research flights regions of saturated and supersaturated air were crossed, even well within the lowermost stratosphere. However, (super)saturation was primarily observed within ± 20 K around the local tropopause.

In conjunction with backward trajectory calculations the occurrence frequency of encountered (super)saturation in the air parcels' recent history was estimated. With longer backward calculation time the potential for experienced saturation and supersaturation increases. Moreover, it turned out that also air parcels, which were probed deep within the LMS, were involved in saturation processes. Most of the air parcels, which encountered (super)saturation in their recent history, originate from the troposphere. This indicates that TST is widely combined with saturation events and thus with freeze-drying. A special flight, during which a saturation region was crossed for ≈ 1 hour, is analysed in more detail in the following chapter 7.
On the research flights during the autumn SPURT campaigns (super)saturated air was observed very rarely. However, taking the temperature history into account, the occurrence frequency of encountered (super)saturation is considerably large. This suggests an efficient drying of the air during this season (cf. also section 9.1).

In a second part the impact of STT on tropospheric O_3 was investigated. Thereby, using O_3 measurements during SPURT and information of the performed trajectory calculations, it was shown that the observed high tropospheric O_3 mixing ratios during spring are likely to be affected by a contribution of stratospheric O_3 due to STT.

The pure tropospheric measurements are, unfortunately, too sparse to investigate the effect of STT to tropospheric O_3 in more detail. Therefore, the considerations in section 6.2 can not give significant information related to this process. Anyhow, in the Northern Hemisphere, photochemistry is more strongly enhanced by man-made emissions of O_3 precursors (Lelieveld and Dentener, 2000). Thus, STT should contribute more significantly to the seasonal tropospheric O_3 cycle at background locations.

Chapter 7

Reverse domain filling - a case study

In connection with the observed high saturation even well within the lowermost stratosphere during the winter campaign IOP 6 (see section 6.1), a special flight during this campaign is analysed here in more detail. This northbound flight took place on February 16, 2003, from the base station Hohn, Germany, to Tromsø, Sweden. After an analysis of the meteorological conditions and an interpretation of time series of measured and model derived parameters, the measurements will be analysed with a Lagrangian technique. A common method to identify and investigate transport processes in the tropopause region is the RDF technique (Reverse Domain Filling). This technique is based upon meteorological data and has the intention to reproduce meso- and small-scale structures, which could not be resolved by these meteorological analyses. In addition, TST or STT can be identified.

7.1 Meteorological analysis by ECMWF data

Around the middle of February 2003, a stable Omega-situation developed in the upper air, i.e. a situation, where the upper level high pressure takes the shape of the Greek letter Ω. This is a normally stable and persistent, thus blocking, meteorological condition. This high pressure system, called Helga, ranged over all tropospheric altitudes up to the stratosphere. It was the guiding centre for the European weather pattern. The western upper air flow succeeds north above Northern Europe. Atlantic troughs of low pressure had no chance against the stronghold. They were driven far north. Their clouds only reached the Iberian peninsula and western Island. Then they were transported clockwise around the high pressure system until they reached Finland and Russia. Consequently, there were dry and cold conditions in central Europe. On the northern flank of Helga the inward flow of mild maritime air from the Norwegian Sea continued, whereas on the southern flank cold winter conditions prevailed. At the eastern flank of the high pressure system a cold upper low pressure zone, even well

developed at the 500 hPa surface, travelled from Russia to Austria. Due to the high pressure system above the North Sea, the tropopause was therefore relatively high in the whole flight area. On Sunday, February 16, 2003, a conspicuous tropospheric streamer with an anchor like structure developed, ranging from Portugal to Spitsbergen. This streamer broke in the course.

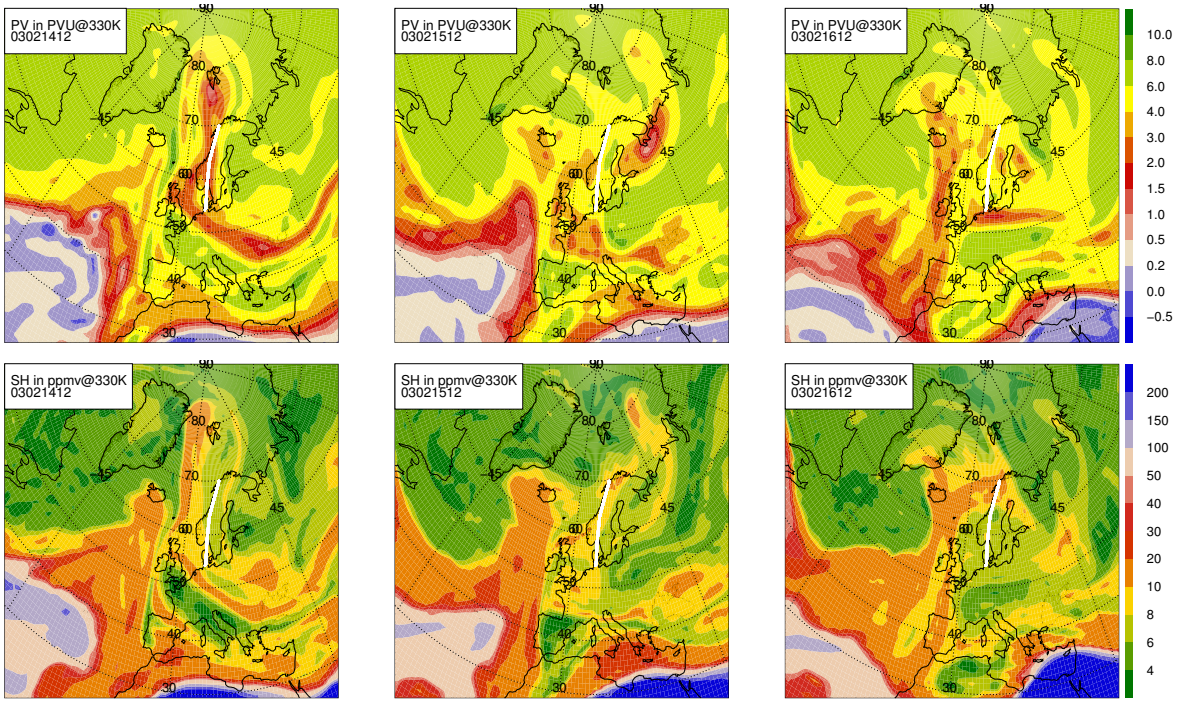

Figure 7.1.: Meteorological ECMWF analyses of potential vorticity (top) and specific humidity (bottom) on the 330 K isentrope on February $14-16$, 2003, at $12{:}00$ UTC (left to right), both colour coded. The flight path for the first mission on February 16, 2003, is marked by the white line.

The mean flight level during the first mission on February 16, 2003, corresponds approximately to an isentrope of 330 K. In Figure 7.1 ECMWF analyses of potential vorticity (top, in PVU) and specific humidity (bottom, in ppmv) are displayed on that isentropic level for February $14-16$, $12{:}00$ UTC, respectively. Thereby, the flight track is displayed by the white line.

In both parameter fields the northward encroachment of the tropospheric streamer is evident. Within this flow, tropospheric air, poor in O_3 and rich in H_2O, is transported deep to high latitudes.

7.2 Interpretation of time series

By virtue of the meteorological situation the first SPURT mission on February 16, 2003, was planned to go from the aircraft's basis Hohn, Germany, to Tromsø, Sweden. The flight

duration was supposed to be relatively short in order to operate a further northbound flight up to $83°$N at the same day to sample air with low N_2O, high age and high equivalent latitudes. Thus, the flight path was directly along the Norwegian coast.

Figure 7.2 shows time series of several parameters, measured during this flight. In the top panel, avionic data for temperature ($T + 100$ K, orange), pressure (p, black) and potential temperature[1] (Θ, red) are shown. The dark grey and black shadings reflect the temperature range, the air parcels encountered during the previous 5 and 10 days, respectively. Additionally, the location of the local tropopause is given ($\Theta - \triangle\Theta$, dark green). The middle panel represents the trace gas measurements of the FISH and JOE instrument, operated by the ICG-I of the Research Centre Jülich. The measured FISH signal (H_2O_{OBS}) is displayed in magenta, to anisokinetic sampling corrected total water (H_2O) is overlayed in dark blue. The green line reflects the ice saturation (IS) mixing ratio, determined according to Equation 4.5. Specific humidity (SH), derived from the ECMWF analyses, is given in light blue. Again, the dark grey and black shadings reflect the encountered SH range of the air parcels during the previous 5 and 10 days, respectively. Measured O_3 is given in dark red (right ordinate). In the bottom plot, potential vorticity (PV, black line) with the maximum and minimum PV of the air parcels during the previous 5 and 10 days is also reflected by the dark grey and black shading, respectively. The tropopause (2.0 PVU surface, 80 ppbv O_3) is marked by the dashed horizontal line. Additionally, the O_3 measurements are given once more in this panel.
The shown local tropopause, i.e. 2.0 PVU surface, as well as SH_{ECMWF} and PV were derived from the ECMWF analyses by temporal and spatial interpolation to the flight track.

The flight profile of this mission reflects the SPURT strategy. There were three flight legs at rather constant pressure, marked by 1, 2, 3 in Figure 7.2, respectively: one leg slightly above the tropopause, a second at an higher altitude and the climb to maximum altitude at the end of the mission. The pressure levels correspond approximately to the 320 K, 330 K and 350 K isentropes, although the variation in potential temperature on the first pressure level is considerably large.
The trace gas time series of H_2O (inverted logarithmic scale) and O_3 show large- and small-scale structures. Take-off and landing can also be easily identified by the large H_2O VMRs and variations. *In situ* measurements of O_3 in combination with the pressure data show that the strong rises in O_3 coincide with the climbs to the next higher flight level. Despite the constant flight leg there are regions of relative strong variations in O_3. The decrease in O_3 VMRs at about $08{:}50$–$09{:}10$ UTC results from a considerable decrease in potential temperature. The incursions in O_3 indicate the sampling of air with more tropospheric character. Since O_3 is highly correlated to PV, the interpolated time series for PV reflects the large-scale structures in the O_3 measurements. Even some small-scale structures are represented by the PV data.

[1] calculated according to Equation 2.1 from the pressure and temperature measurements aboard the Learjet 35A

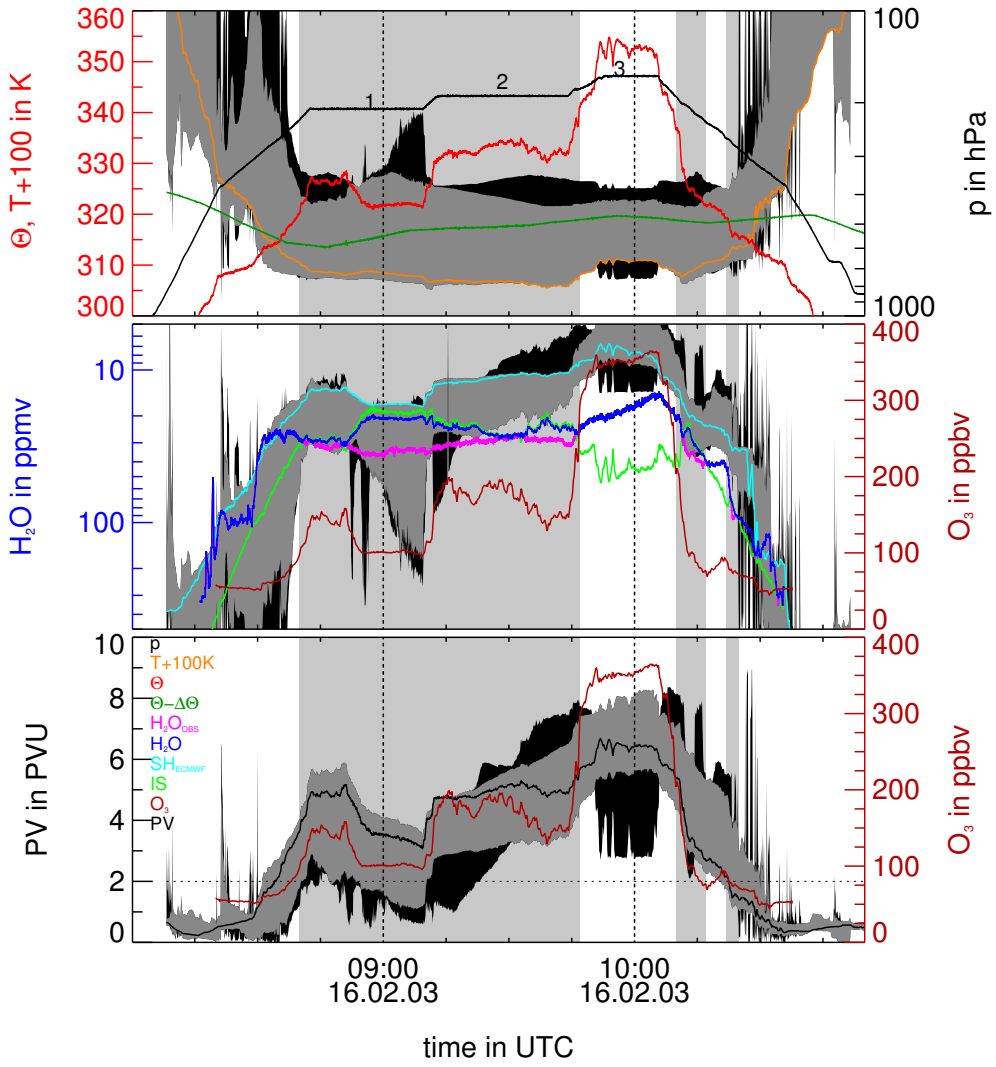

Figure 7.2.: Time series of parameters for the first SPURT mission on February 16, 2003. See text for details.

The minimum PV values for air parcels probed during 08:50–09:10 UTC show a very recent tropospheric origin of less than 5 days and thus also lower O_3 VMRs.

As is evident, during this flight the FISH signal (H_2O_{OBS}) was several times larger than the ice saturation mixing ratio (marked by the light grey vertical bars in Figure 7.2). It is to expect that during these time periods the measurements took place in clouds, e.g. altocumuli, thin cirrus. Thus, the FISH data is corrected to anisokinetic sampling (Schiller et al., 1999), resulting in the H_2O data (blue). Necessarily, the corrected data resemble the shape of IS during these times. The difference between H_2O_{OBS} and H_2O is up to $10 - 15$ ppmv. Since the FISH inlet is heated, supercooled drops or ice particles should be vaporised. In the presence of such particles, therefore spikes should be visible in the FISH signal. However, there is no evidence for particles in the measurements during this flight. Especially within the ice saturation time period 08:40–10:17 UTC, the measured FISH data H_2O_{OBS} is rather constant compared to other parameters like Θ or O_3. Thus, there is *a priori* no need for an anisokinetic

correction of the FISH signal. Unfortunately, there is no documentation of the environment outside the aircraft available, caused by enhanced intense instrumental support during this flight. Anyhow, during this period the aircraft probably flew above the lower bank of clouds, associated with the prominent high pressure system above the North Sea. If there were very small more or less homogeneously distributed particles or water droplets like in fog at the flight altitude, there is no reason to expect spikes in the FISH signal.

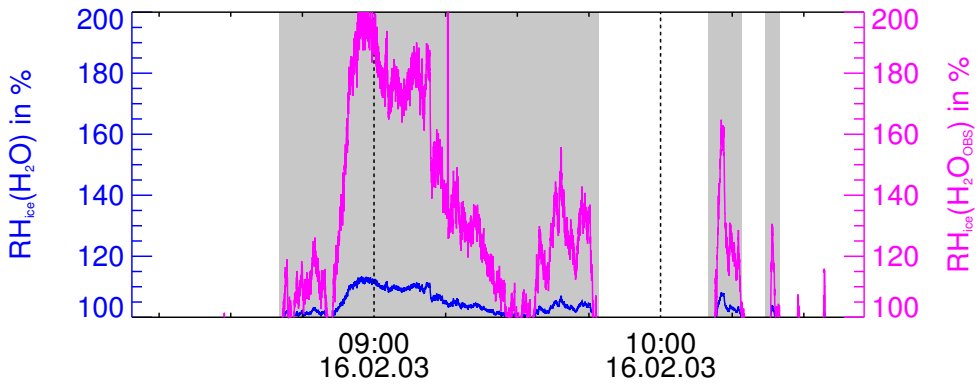

Figure 7.3.: Relative humidities with respect to ice for the observed FISH signal (magenta) and for the to anisokinetic sampling corrected H_2O (blue), measured during the first SPURT mission on February 16, 2003.

In Figure 7.3 the relative humidities with respect to ice for the uncorrected ($RH_{ice}(H_2O_{OBS})$, magenta) and to anisokinetic sampling corrected ($RH_{ice}(H_2O_{corr})$, blue) FISH signals are displayed. The $RH_{ice}(H_2O_{OBS})$ values show a strong increase from ≈ 110 % at $08{:}45$ UTC up to ≈ 200 % around $08{:}55$ UTC. They then decrease towards 180 % between $09{:}00$–$09{:}12$ UTC and drop down to ≈ 100 % around $09{:}30$ UTC before they increase again to ≈ 140 % around $09{:}45$ UTC. The temperatures within this time period were between 205 and 210 K. Relating to Koop et al. (2000), at this temperatures ice particles should be present. However, with decreasing particle size the relative humidity for ice nucleation increases. Hence, values of $RH_{ice}(H_2O_{OBS})$ suggest the presence of very small ice particles. Another aspect which evidences for very small particles arises from the enhancement factor, in particular from the aspiration efficiency (see Krämer and Afchine, 2004). The used enhancement factor applied to the FISH data during SPURT is 7.9. However, the aspiration efficiency is dependent upon the particle size and U/U_0, i.e. the ratio of the flow velocity inside the inlet and the velocity of the free flow. Probably, the applied factor is too large, thus reducing the corrected H_2O mixing ratios and reducing or obliterating cirrus structures, i.e. spikes. This is a very interesting flight, which will be investigated in more detail in future work.

In the absence of dehydration and hydration processes, specific humidity is a conservative quantity. In the ECMWF data, dehydration processes are considered. In the occurrence of ice saturation, SH is set to the ice saturation mixing ratio (Simmons et al., 1999). During take-off, H_2O and interpolated SH_{ECMWF} agree very well within the resolution limitations of

the ECMWF analyses. Within $08{:}50$–$09{:}10$ UTC SH_{ECMWF} approximates IS. This conforms with the region influenced by recent TST. Air parcels sampled during this time show a high water content and low PV within their considered history.
Since O_3 is a stratospheric and H_2O a tropospheric tracer, the signals should be anti-correlated. For the model-derived SH_{ECMWF} and measured O_3 this is true during the entire flight (note the inverted H_2O-axis). However, during the time periods which indicate ice saturation, the corrected H_2O correlates with the observed O_3. In the absence of ice saturation, H_2O and O_3 show the expected anti-correlation. However, the uncorrected FISH signal shows the expected anti-correlation, albeit the response to varying O_3 is very weak.

7.3 3-dimensional RDF calculations

High resolution *in situ* measurements are only available for a distinct region. In contrast, meteorological analyses are globally available. They usually have a horizontal resolution of $\approx 0.5° - 2.5°$, i.e. a grid distance of $\approx 50 - 250$ km. Thus, only large- and meso-scale processes are captured by these analyses. This deficit can be diminished by model techniques. On the basis of meteorological winds, transport of air parcels can be calculated to generate fine scale structures, which are not present in the prior analyses. The CAS (Contour Advection with Surgery, Dritschel, 1989; Waugh and Plumb, 1994) and the RDF (Reverse Domain Filling, e.g., Sutton, 1994; Schoeberl and Newman, 1995; Beuermann et al., 2002) technique are commonly used. During exchange of air masses often sub-synoptic structures (laminae, filaments) develop, which can be reproduced by these techniques (e.g., Fairlie et al., 1997). The RDF technique provides an efficient method for the reconstruction of advection processes with relatively low computational costs. However, a direct consideration of mixing between air parcels is not included. In this section 7.3 the RDF technique will be applied for an analysis of the first flight mission on February 16, 2003.

The RDF technique used here is based upon the calculation of 3-dimensional backward trajectories to a specified time in the past. Thereby for each measurement data point, a trajectory was initialised on a vertical curtain ($280 - 400$ K in steps of 1 K) along the flight path. Using the meteorological data sets (isentropic ECMWF analyses), the dynamics is only driven by wind deformation. Assuming tracer conservation, the past time values are mapped forward in time to the initial parcel positions, i.e. the parameter values at the initial times are replaced by the corresponding values of the air parcels in the past. This procedure results in a high resolution tracer field in the area of interest. For a quasi-conserved quantity, the mapped values are correlated to corresponding tracer measurements, e.g. model PV and measured O_3. However, the quality or accordance of measurements and reconstructed tracer fields is dependent upon the trajectory length (Bujok, 1998). On the one hand, a short

trajectory length would not generate sufficient fine scale structures. On the other hand, the trajectory length is restricted by physical and numerical effects (Beuermann, 2000). Thus, a too large trajectory length could produce excessive fine scale structures.

Figure 7.4 shows the RDF results for the potential vorticity field. In the top panel, the ECMWF derived PV, interpolated in space and time to the flight track curtain, is displayed as the background field. The tropopause (2.0 PVU surface) is given by the black thick solid line. Additionally, pressure contours are shown by the dashed thin black lines. Further, the ozone measurements, reflected by the colour coded dots, are overlayed onto the flight height in potential temperature. The magenta and blue lines correspond to the measured FISH signal and to the to anisokinetic sampling corrected total water, both given in ppmv (inverted logarithmic right ordinate). The following panels reflect the advected PV field from 12, 24, 48, 120, 180 and 240 hours before the measurements. In the reconstructed PV fields, the green dots mark those air parcels which were involved in TST, i.e. they were at least once in the troposphere (< 2.0 PVU) within the considered backward time period.
An enhancement of the trajectory length produces pronounced fine scale structures and strong gradients. This is especially evident in the advected PV fields within $08{:}15$–$08{:}35$ UTC and generally below 2.0 PVU. For a trajectory length greater than 120 h the advected PV field in the troposphere is not representative. This indicates the enhanced turbulence and mixing in the troposphere in contrast to the rather stirring and filamentation processes in the stratosphere.

The advected PV field for a trajectory length of 12 h shows that the slight dropping in O_3 VMR at the end of the first flight leg (around $09{:}10$ UTC, see Figure 7.2 for more details in O_3) could be explained by very recent TST (green dots), thus reducing the O_3 VMR there. The cross section for the 240 h advected PV shows TST events for the whole region crossed during the first flight leg as well as during the first part of the next higher flight altitude. The advected PV fields expose that the region of observed ice saturation was also mostly associated with conspicuous TST. Within the first half of the flight, encountered TST is enhanced with an increasing trajectory length. Tropospheric intrusions up to > 350 K are identifiable. In contrast, in the second part of the flight no significant TST is evident. Anyhow, when climbing to the maximum altitude, there is a slight peak with a following drop in O_3, which does not correspond to the variations in potential temperature (see Figure 7.2 for more details in O_3). The run of the O_3 VMR can be explained by RDF for a trajectory length of 180 h or better 240 h. The advected PV field shows a tongue of low PV within the region crossed at the highest flight level, indicating that the region is influenced by air which originated near the tropopause. However, the recent stratospheric character prevails and also the total water mixing ratios there are the lowest measured during the entire flight ($12 - 13$ ppmv).

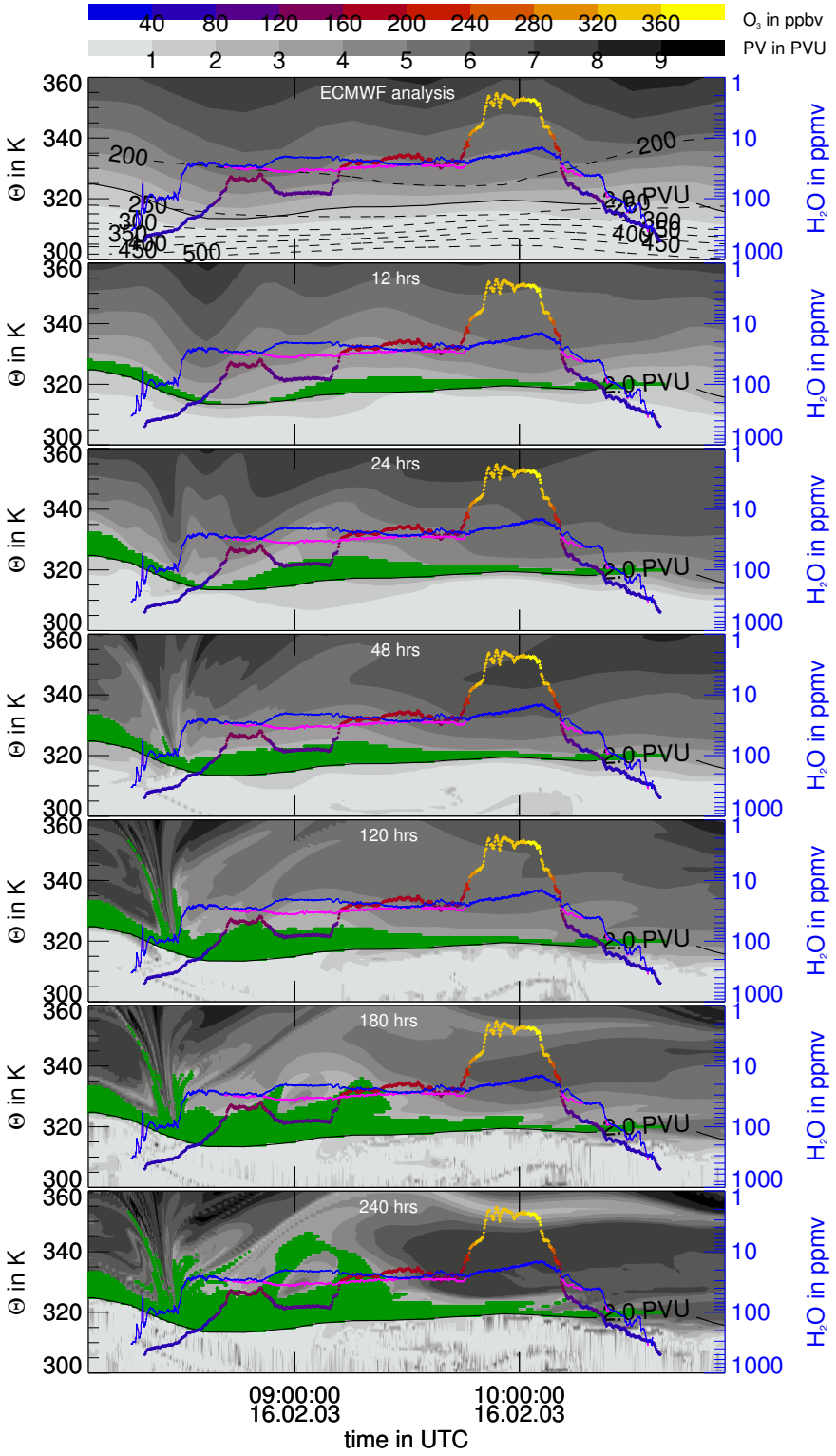

Figure 7.4.: Vertical cross sections of potential vorticity and with the RDF technique reconstructed potential vorticity fields (grey coding) along the synoptic flight track for the mission on February 16, 2003. Top to bottom: PV field of the ECMWF analyses, advected PV fields for backward trajectory lengths of 12, 24, 48, 120, 180 and 240 hours, respectively. The flight height in potential temperature is shown together with measurements of O_3 reflected by the colour coding. The magenta and blue lines correspond to the measured FISH signal and to anisokinetic sampling corrected H_2O, respectively. The black thick solid line in all cross sections denotes the tropopause (2.0 PVU surface) at the measurement time. Green dots in the reconstructed PV fields mark those trajectories, which were at least once in the troposphere ($<$ 2.0 PVU) within the corresponding calculated backward time. Additionally, pressure contours are depicted in the ECMWF field by the dashed thin black lines.

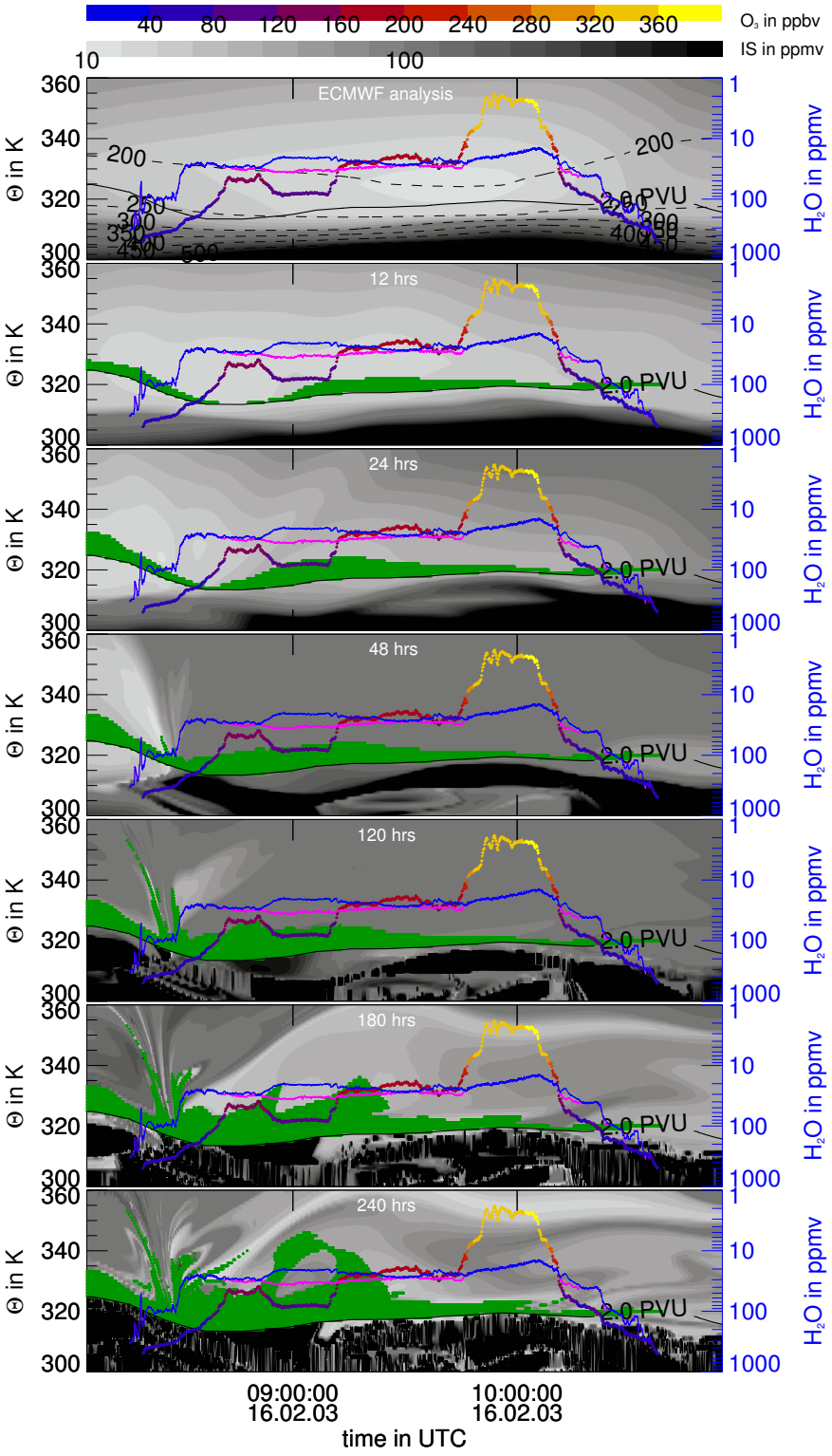

Figure 7.5.: As Figure 7.4 but for the ice saturation mixing ratio in ppmv.

As mentioned earlier, specific humidity is a conserved quantity in the absence of dehydration and hydration processes. Since the difference between measured H_2O and SH_{ECMWF} is considerably large (see Figure 7.2), instead cross sections of analysed and advected ice saturation mixing ratios are shown in Figure 7.5 for the same trajectory lengths as for the PV field, i.e. for 12, 24, 48, 120, 180 and 240 hours. Reconstructed fields of ice saturation are a valuable addendum for PV, giving more information about the possible water content. The strong gradient of IS across the tropopause is evident. 5 days prior to the flight, air parcels in the regions crossed by the aircraft show ice saturation mixing ratios > 40 ppmv. 240 hours before the measurements there were regions with lower IS VMRs, but never lower than 25 ppmv. Only about 24 hours before the flight a significant cooling of the region sampled on the first and second flight level between $310 - 340$ K is apparent. Thus there was a high potential for ice saturation and therewith for dehydration, only 24 hours prior to the observation.

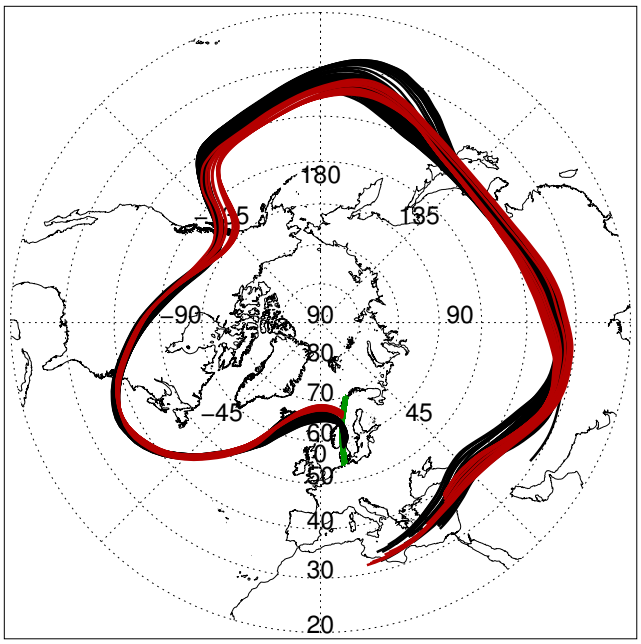

Figure 7.6.: Pathways of 10 day backward trajectories for two flight segments during the first mission on February 16, 2003. The black (red) coloured lines reflect the pathways of trajectories initialised between $08{:}45$–$09{:}45$ UTC ($09{:}55$–$10{:}10$ UTC) on February 16, 2003. The flight track is marked by the green line.

For a closer look to the 10 day history of the air parcels, the focus is now on trajectories initialised on the flight track between $08{:}45$–$09{:}45$ UTC and $09{:}55$–$10{:}10$ UTC on February 16, 2003. These correspond to the ice saturation region with the quasi-constant FISH signal and to the highest flight level. Figure 7.6 displays the pathways of these trajectories. Although the initial potential temperatures of the trajectories of the two flight segments range from 320 to 355 K (see Figure 7.7), the geographical spread is very small. At both flight levels, the trajectories remain relative close to each other and form a compact band. Thus, considerable mixing during the previous 10 days is not expected.

To consider the history of parameters, Figure 7.7 shows the values for several parameters during the past 10 days. In contrast to the compact band, the potential vorticity values of

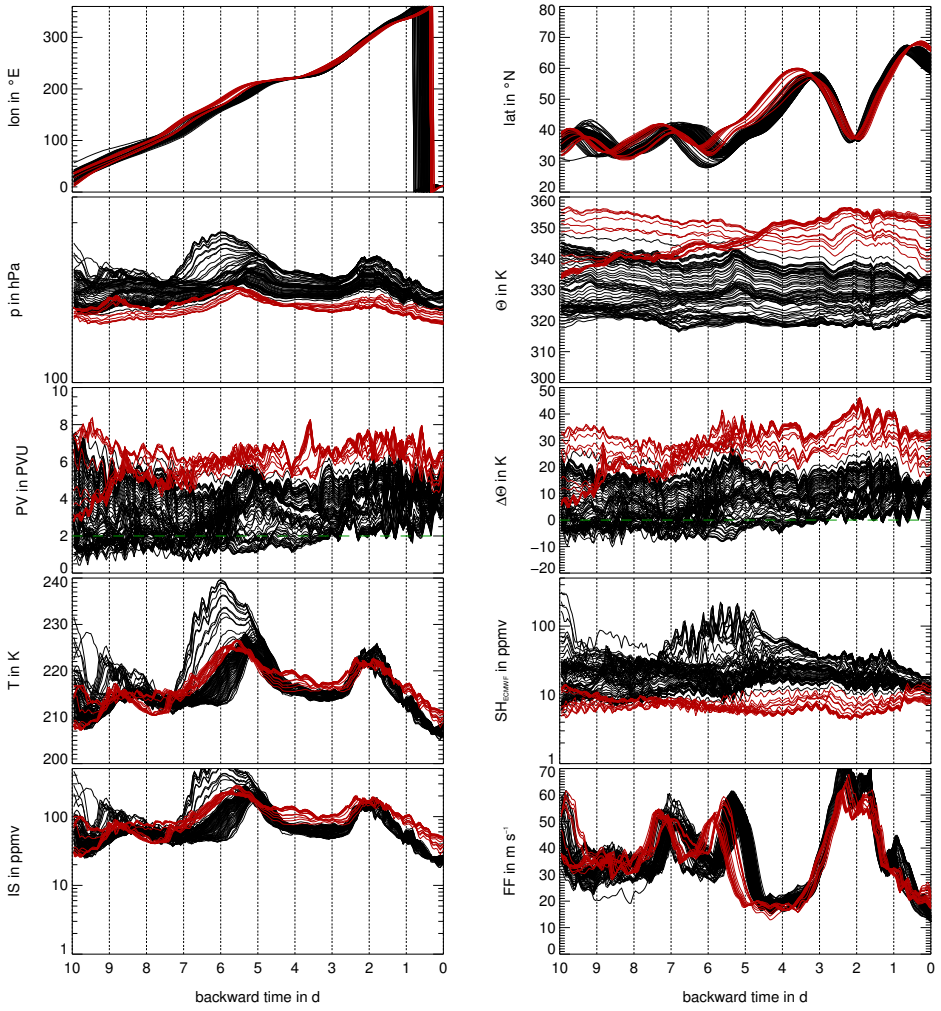

Figure 7.7.: 10 day history of parameters for the two flight segments during the first mission on February 16, 2003. The black (red) lines reflect the parameter values of trajectories initialised between 08:45–09:45 UTC (09:55–10:10 UTC) on February 16, 2003. From left to right and top to bottom: geographical longitude and latitude, pressure, potential temperature, potential vorticity, distance to the local tropopause (2.0 PVU) temperature, specific humidity of the ECMWF analyses, ice saturation mixing ratio, and horizontal wind velocity. The dashed green lines in the PV and $\triangle\Theta$ charts reflect the tropopause location.

the trajectories cover a broad range between ≈ 0.0 and 8.0 PVU. Several particles were influenced by the troposphere, indicated by PV values < 2.0 PVU. Also for the highest flight level, some air parcels show an origin near the troposphere within the considered time period. This is interesting since sinking and raising air parcels show nearly the same horizontal pathways. These air parcels correspond to the first part of the highest flight level, where the tropospheric influence is noticeable in O_3. Additionally, this is also evident in the RDF reconstructed PV field for $180 - 240$ h prior to the observation. However, at the observation time they show a maximum distance from the local tropopause of ≈ 45 K, i.e. well within the lowermost stratosphere.

History values for pressure, temperature, ice saturation and horizontal wind velocity show also only a reduced spread. They all show the same relative course, a double-wave structure with maximum values about 5 and 2 days prior to the observation and minimum values

about 3 days before and at the measurement time. Approximately 5 days prior to the observation, a strong decrease in mean horizontal wind velocity (FF) from ≈ 55 to ≈ 20 m s^{-1} corresponds to a loss in temperature from 225 to 215 K, thus causing a decrease in ice saturation from ≈ 200 to ≈ 60 ppmv. Also specific humidity is reduced in the ECMWF analyses, ranging from ≈ 5 to ≈ 40 ppmv. During the next 2 days a considerable increase in FF, T and IS to ≈ 60 m s^{-1}, ≈ 222 K and ≈ 130 ppmv is evident. In contrast, SH shows no significant change. Two days before the observation, again the horizontal wind velocity decreases significantly to less than 20 m s^{-1}. Also the air temperature cools off to ≈ 210 K, resulting in a reduction of IS to ≈ 20 ppmv. This double-wave structure is excited when the trajectories approach western North America. Due to the orographically induced planetary wave trough over North America the trajectories are transported further south, reaching the minimum latitude ≈ 2 days before the flight combined with maximum horizontal wind velocities. Then they were transported to higher latitudes where the air is significantly cooled. The minimum temperatures were encountered ≈ 12 hours prior to the measurements. Within the previous 10 days the considered air parcels have undergone severe temperature variations. If particles have formed, the time for sedimentation and therewith dehydration of the air was possibly too short. Subsequent increase in temperature could therefore cause rehydration. In addition, few hours prior to the observation there is a slight tendency to increasing temperatures at the lower flight levels. Thus, in the region with the quasi-constant uncorrected H_2O mixing ratio of $\approx 25 - 30$ ppmv, spikes in the FISH-signal are not necessarily expected.

This case study emphasises once more that TST is combined with freeze-drying and thus with high potential for saturation/supersaturation and cirrus cloud formation in the lowermost stratosphere. Beside, it should be mentioned that long-term simulation over 2 years with CLaMS by Günther et al. (2004) are in very good agreement with the total water measurements by FISH, which were not corrected to anisokinetic sampling. The simulation included a parametrisation of the formation, evaporation and sedimentation of cirrus particles. If a particle encounters ice supersaturation of > 30 % the water content was reduced to an ice saturation of 130 % (cf. section 9.1).

Chapter 8

Long-term simulation with CLaMS - jet streams as a transport barrier

Stratosphere-troposphere exchange in the vicinity of jet stream regions has dynamical, chemical and radiative impact on the UT/LMS. The jet stream regions generally divide the tropical upper troposphere from the extra-tropical lower stratosphere. Thus, the regions of strong wind velocities in the tropopause region, as the sub-tropical or polar jet stream, are often referred to as ”tropopause breaks”. Changes in tropopause height and variations are considerably large within a relative small latitudinal distance. The sub-tropical jet stream undergoes a pronounced seasonal cycle in the Northern Hemisphere. Its latitudinal position is $\approx 30°$N during winter, whereas it is shifted further north to $\approx 45°$N during the summer season (cf. e.g., FF at the 2.0 PVU surface in Figure 5.5). Additionally, the horizontal wind velocities during the summer months are reduced by a factor of 2 compared to those during winter. The polar jet is located further north at around 60 °N. Whereas the orientation of the sub-tropical jet is rather zonal the polar jet stream pattern is more meandering. Additionally, the sub-tropical jet has a huge persistence and strength compared to the polar jet. The latter is mainly associated with the upper level wave patterns, i.e. Rossby waves. However, in some cases, when either of the jet streams is zonally strongly distorted, both can fall together or even merge.

Isentropic surfaces cross the jet stream. This allows quasi-horizontal adiabatic STE along isentropes. However, the maximum jet stream wind velocities are characterised by large horizontal and vertical wind shear. In particular, the strong gradients of potential vorticity at the cyclonic shear side of such a wind band can form an effective barrier for quasi-horizontal transport and reduce large-scale exchange of air through the jet. Anyhow, for instance, Vaughan and Timmis (1998) and Postal and Hitchman (1999) showed that Rossby wave activity most often results in stirring and quasi-horizontal exchange. Thereby, frequently small

filaments and laminae develop (Appenzeller et al., 1996a), which involve exchange and mixing in the sense of the scale cascade (Haynes and Anglade, 1997).

Ozone, with a lifetime longer than several months in the upper troposphere and lowermost stratosphere, is an appropriate tracer to characterise the variability and features of transport and dynamics. The objective here is to investigate the tracer variability of O_3 in the jet stream regions and its relation to the transport barrier effect (Haynes and Shuckburgh, 2000), i.e. how transport and mixing is hindered or enabled by dynamics. Thereby, a natural coordinate centred at the jet maximum wind speeds is applied.

8.1 CLaMS simulation - configuration of the model

Sensitive and high resolution *in situ* measurements are highly valuable for process studies and model comparisons. The SPURT data set provides detailed information about the UT/LMS region. However, despite the unique seasonal and geographical coverage of the European area, there are too few flights crossing the sub-tropical or polar jet stream immediately. To investigate tracer variability in the jet stream regions, thus the Jülich CLaMS (McKenna et al., 2002b) was used to generate sufficient amount of data. Thereby, the CLaMS initialisation and boundary conditions were determined using the SPURT observations (see section 4.1) and the HALOE climatology. The initialisation for ozone during the summer season in the potential temperature and equivalent latitude space is shown in Figure 8.1.

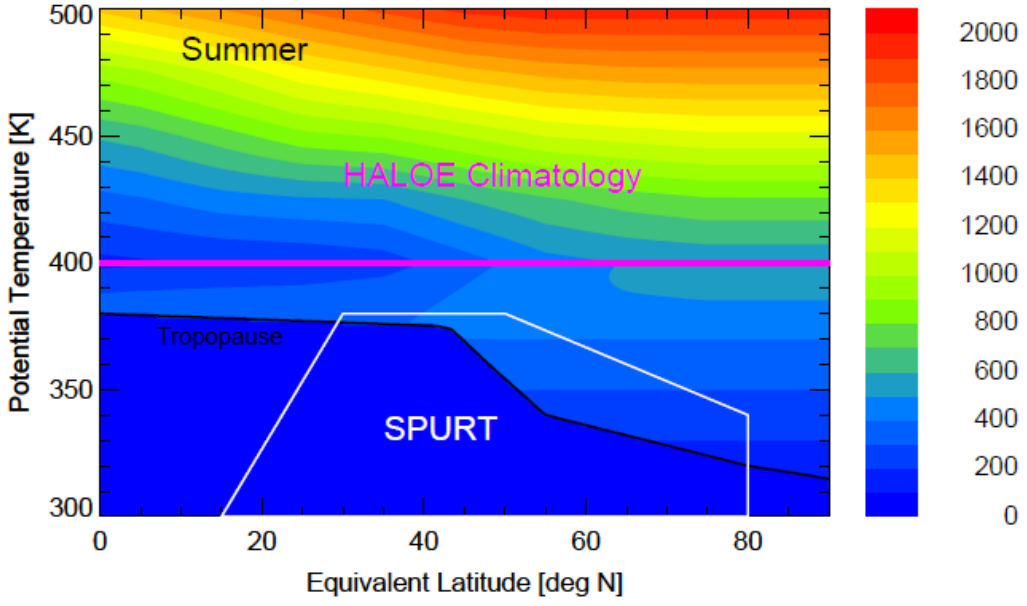

Figure 8.1.: CLaMS initialisation of ozone in the potential temperature and equivalent latitude space for a simulation period August 1, 2001, to August 31, 2002, with optimised mixing. (Courtesy of Paul Konopka, ICG-I)

On short time scales ($\approx$ 2 weeks) transport is established by isentropic and reversible transport processes as filamentation, whereas on seasonal time scales mixing and cross-isentropic velocities are predominant. Thus, the pure transport simulation between $290 < \Theta < 500$ K was performed for a time period during SPURT, from August 1, 2001, to August 31, 2002, inclusive. The resolution was set to 100 km in the horizontal and to 400 m in the vertical. Within CLaMS, mixing is driven by the horizontal strain and by the vertical shear. The mixing itself is thereby determined through a controlled interaction between nearest neighbours of air parcels by using the dynamically adaptive grid after each advection step $\triangle t$. This provides a controlled mass exchange between air parcels, which is coupled to the atmospheric dynamics. The mixing intensity is thereby controlled by the critical Lyapunov exponent λ_c and $\triangle t$ (for details, see McKenna et al., 2002a; Konopka et al., 2003). For the simulation an optimised mixing is used, i.e. $\lambda_c \triangle t = 1.5$. The meteorological wind fields were taken from ECMWF, whereby the cross-isentropic velocities, i.e. $\dot{\Theta}$, were obtained from a radiation module (no clouds and no convection) based upon the Mocrette scheme (Mocrette, 1991). Results show that the observed structures in O_3 are reliable resolved by the CLaMS simulation (Konopka et al., 2004a). Fine-scale structures and meteorological phenomena are also rendered sufficiently. Thus the simulation should provide an accurate data set to investigate the seasonal climatology of ozone and its variability near the jet stream.

8.2 Jet maximum wind velocities - a natural coordinate centre

Strong horizontal gradients of PV are in general related to the jet stream regions. As mentioned above, the tropical troposphere is divided from the extra-tropical lower stratosphere at the jet stream locations which should thus roughly coincide with the tropopause location (see Figure 8.2). In order to investigate the spatial structure and trace gas variability relative to the direction of the mean planetary wave structure, i.e. the mean flow, it seems appropriate not to use PV rather than a certain relative coordinate: the isentropic wind speed difference to the jet stream maximum, hereafter nominated as $\triangle$FF. Due to the wind speed difference, the coordinate is centred at the maximum jet stream wind velocity, establishing a natural coordinate system. The computation of the wind speed difference was performed in several steps. First of all, regions of high horizontal wind velocities have to be diagnosed in the ECMWF analyses. The precision of the jet detection is limited to the temporal and spatial resolution of the meteorological analysis data. Thereby, regions with high horizontal wind velocities were determined on each isentropic level (from 290 K to 500 K in 10 K steps) and then filtered to derive the grid points with the maximum wind speeds. The method even allows to identify meandering jet stream regions with sufficient accuracy. An example result of the applied jet detection algorithm is depicted in Figure 8.2.

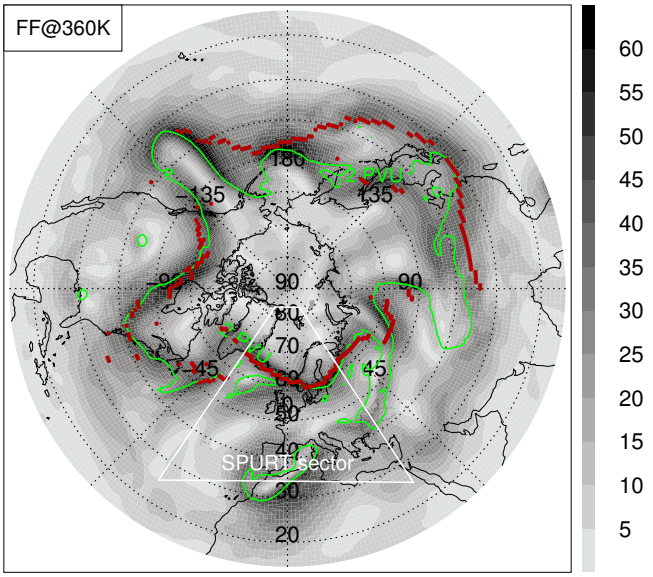

Figure 8.2.: Example result for detection of regions with high horizontal wind velocities (FF) on the 360 K isentrope on November 11, 2001, 12:00 UTC. The grey shading reflects horizontal wind velocities, red dots mark diagnosed jet stream grid points, restricted to the resolution of the ECMWF data. The potential vorticity contour 2.0 PVU is given by the green line. It roughly coincides with the detected jet stream grid points. The white frame marks the SPURT sector.

Once the jet stream grid points are identified, several parameters at each grid point are available, in particular the jet wind direction. In a next step, for every air parcel in the simulation the nearest jet grid points on the model isentropes below and above the considered air parcel's isentrope are identified. The jet wind speeds are then interpolated to the corresponding air parcel's isentrope. Thereafter, $\triangle$FF is calculated by subtracting the horizontal wind velocity at the air parcel's location from this jet maximum wind speed. By definition, this difference is positive. With the information of the jet wind direction it is possible to decide wether an air parcel is located at the cyclonic or anticyclonic side of the jet stream. To distinguish air parcels at opposite sides of the jet stream, the wind speed differences related to the cyclonic side are assigned to negative $\triangle$FF. The method for calculating $\triangle$FF is illustrated in Figure 8.3.

The jet maximum wind speed in this coordinate system is defined as the maximum at each isentrope. Thus there is no single maximum jet wind speed but rather a range of different values in Θ. The coordinate system only depends on the difference and not the absolute wind speed values. The identified jet stream locations obviously show gaps and leaps since the regions of high wind speeds do not appear as a closed band (cf. Figure 8.2). This affects the calculation of $\triangle$FF and air parcels can occasionally be assigned to a wrong jet side. However, the number of these critical identified jet grid points is rather sparse.

8.3 Seasonal characteristics of the jet stream strength

As mentioned earlier, observed structures during SPURT are sufficiently resolved by the CLaMS simulation. It is therefore assumed that the CLaMS results provide a reliable data set to investigate the seasonal variation and spatial structure of O_3 with relation to the maximum

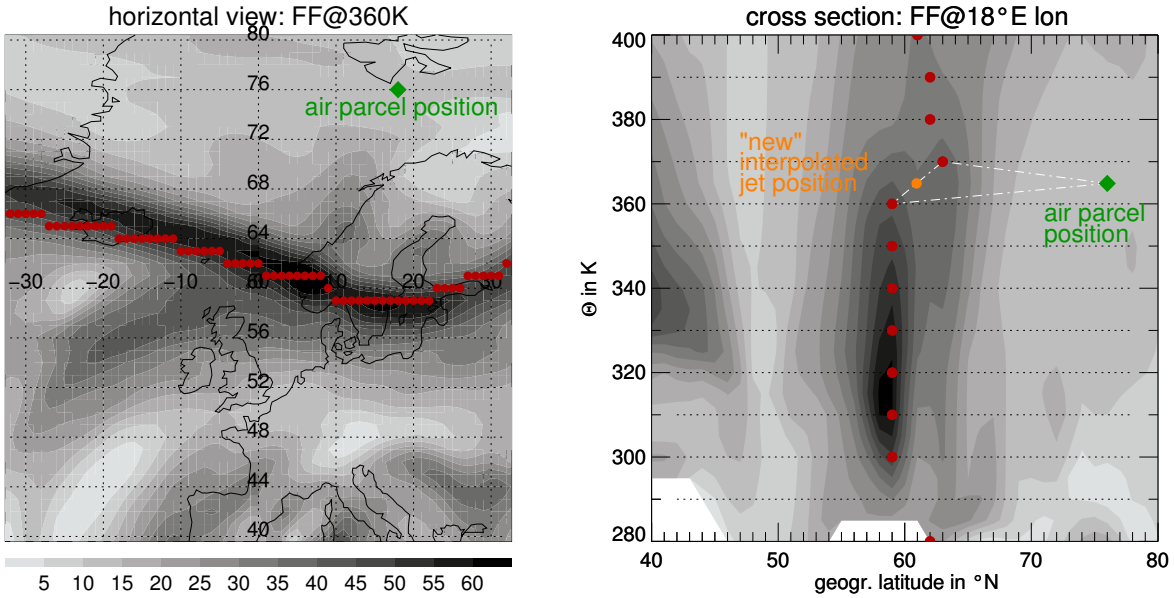

Figure 8.3.: Sketch for determining the wind speed difference to the jet stream maximum wind speeds. The left chart shows exemplary the horizontal distribution of ECMWF horizontal wind velocities in the SPURT sector on the 360 K isentrope on November 11, 2001, 12:00 UTC. Thereby, the green diamond reflects an arbitrary air parcel position with known parameters, among the horizontal wind velocity. The red dots mark the ECMWF grid points with diagnosed high horizontal wind speeds. In the right chart, a latitudinal isentropic cross section of FF along 18°E for the same time is shown. Thereby, once again the arbitrary air parcel position as well as the jet stream grid points are given, now in the vertical. The orange point denotes the "new" to the air parcel's isentrope interpolated jet stream wind velocity. The wind speed difference is then calculated by subtracting the wind speed at the air parcel's location from this "new" jet stream wind velocity.

jet wind velocities. In subsection 3.4.1 2-dimensional PDFs were used to summarise the total SPURT data. An important advantage of using this technique is that errors in the jet detection and relation of air parcels to a jet side can not significantly change the statistics and thus the shape of the PDFs (cf. also Konopka et al., 2004b). Due to the large data set and the advantages of the PDFs once more this tool is applied here. Although the CLaMS simulation provides sufficient, approximately equally distributed, data for the whole Northern Hemisphere, only air parcels in the SPURT sector are considered here, i.e. $40°$W$-40°$E and $25-85°$N.

Seasonal PDFs of wind speed at the air parcels' locations relative to the maximum wind speeds give a summary of the jet stream structure. The distributions are displayed in Figure 8.4 and Figure 8.5 for SON, DJF and MAM, JJA, respectively. The FF distributions reflect furthermore the quality and accuracy of the applied method to set air parcels in relation to the jet stream. The PDFs are displayed in the same manner as in subsection 3.4.1. The bin size is set to 2 m s^{-1} for FF and $\triangle$FF. Thereby, a normalisation is performed to each $\triangle$FF bin. Thus, the probability reflects the occurrence frequency of a definite range of FF at a particular location within the corresponding wind speed difference interval. Due to the varying mean tropopause height with latitude, the PDFs are computed separately for three potential temperature intervals: $300-330$ K, $330-360$ K, $360-390$ K. The mean and me-

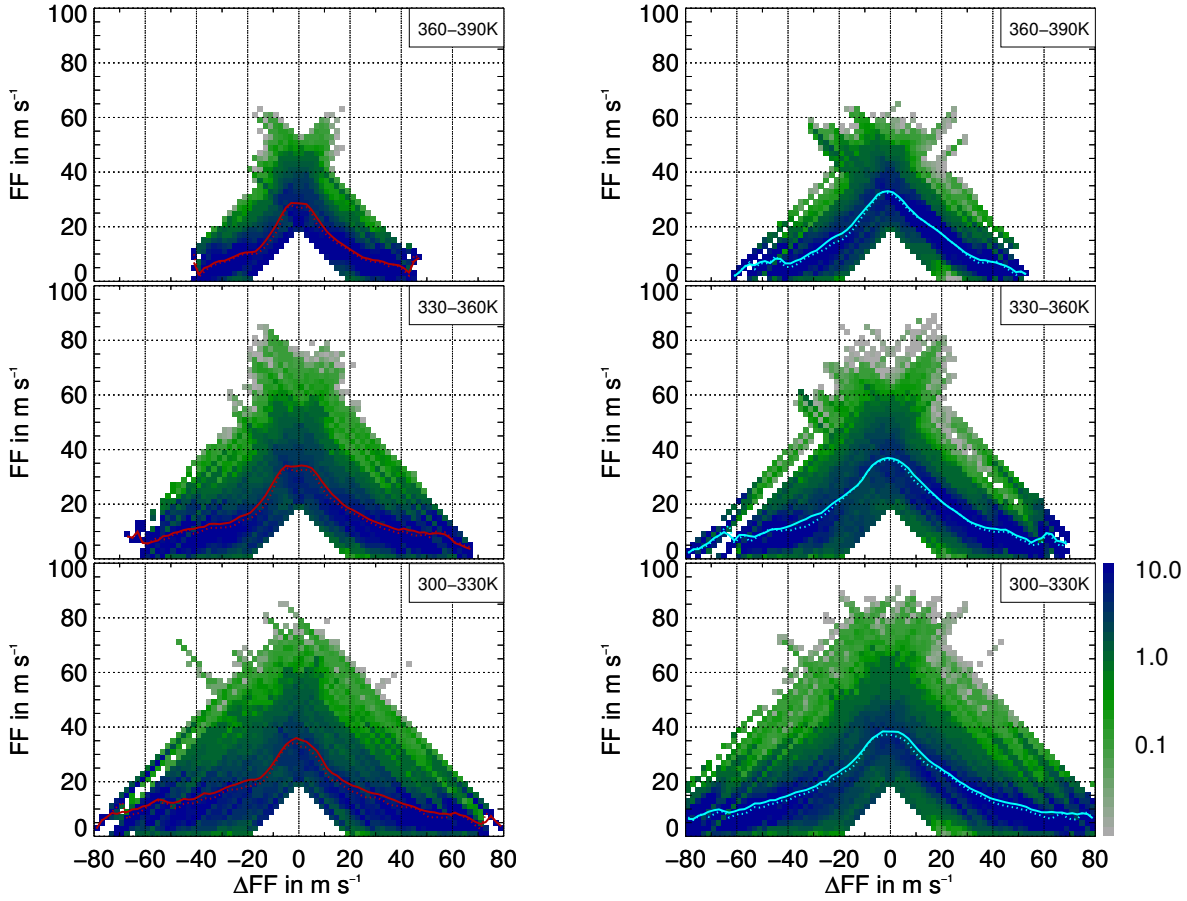

Figure 8.4.: Seasonal 2-dimensional probability distribution functions of wind speed at the air parcels' locations as a function of the relative coordinate wind speed difference to the jet stream maximum wind speed. The bin size is 2 m s^{-1} for FF as well as for the coordinate $\triangle$FF. The normalisation is performed to each $\triangle$FF bin. The PDFs are shown in the same manner as in subsection 3.4.1. Further, the PDFs are limited to the SPURT sector, i.e. $40°$W$-40°$E and $25° - 85°$N. Due to the latitudinal variation of tropopause height, the 2-dimensional PDFs are shown for three potential temperature ranges: $300 - 330$ K (bottom), $330 - 360$ K (middle), $360 - 390$ K (top). In the left panel distributions for autumn are displayed, the right panel shows the winter PDFs. The mean and median FF in each $\triangle$FF interval is given by the solid and dashed line, respectively.

dian FF in each $\triangle$FF interval is given for each Θ range and each season by the solid and dashed lines, respectively. In the summer PDFs, additionally the means for all seasons in the corresponding Θ range are given.

The PDFs generally show the expected symmetric shape of a hat. Highest wind velocities should, by definition of $\triangle$FF, be present near the jet core and fall off with increasing wind speed difference. Thereby, the tails should decrease in the same amount as the wind speed difference. The open white triangle at $\triangle$FF$= 0$ m s^{-1}, i.e. the jet core, is due to a chosen minimum threshold wind velocity for detecting jet stream regions, which is set to 20 m s^{-1}. However, near the jet core the contours show an attached slight cross pattern at the highest wind speeds. This is an effect resulting from cases where the jet occasionally is split into two (or more) branches of high wind velocities, separated by several degrees in latitude. Thus, an air parcel can be related to a jet grid point, which is nearest but has not the highest

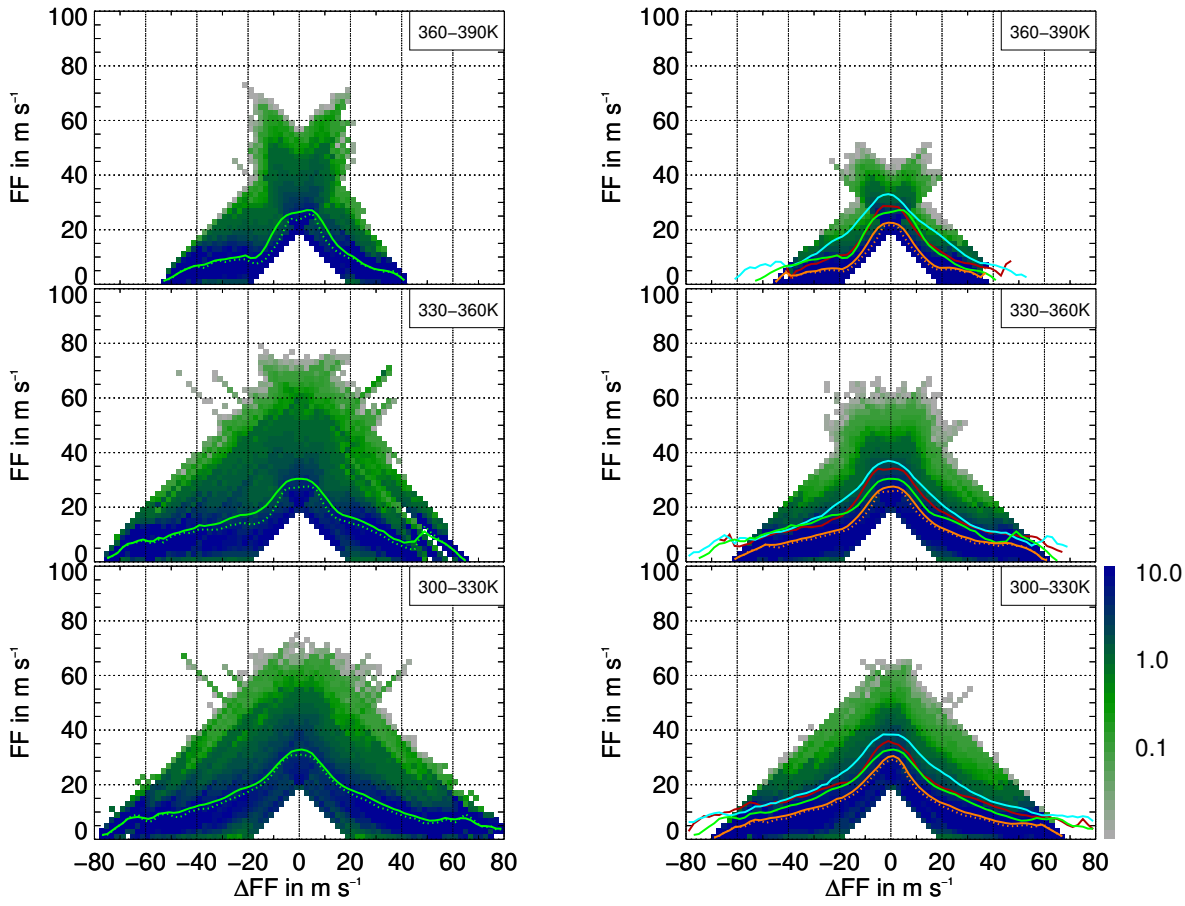

Figure 8.5.: As Figure 8.4 but for the spring (left) and summer (right) season. Additionally, in the summer PDFs, mean FFs during this season are compared to the means during the other seasons.

wind velocity. The consequence of this jet detection problem could be reduced or nearly inhibited by simplifying the calculation in that way to use only one maximum jet wind speed at each longitude (Ray, 2004a, personal communication). In situations where the jet splits into a northern and southern branch being both nearly equal in strength (e.g., within $5 - 10$ m s^{-1}), always the northern branch could be taken to define the jet maximum winds and locations. The choice of the northern branch is reliable since the O_3 gradients are always strongest across the northern branch and so this seems to be the most significant ”barrier” to O_3 transport (Ray, 2004b, personal communication). However, there are certainly different methods to apply (e.g., use of the Nash criterion, Nash et al., 1996) and ways to do the calculation. The one considered here is to take the difference in wind speed between the air parcel’s location and the closest location to the jet maximum on the air parcel’s isentrope, regardless of longitude. This allows to identify a meandering jet with a retrograde part but also produces the discussed branching problem. Despite that uncertainty in the jet detection, the shapes of the PDFs indicate a sufficient quality of the applied method. Thus, this should not gradually affect the O_3 gradient across the jet core (cf. section 8.4).

The mean strength of the jet stream is apparent in the mean wind velocities at the jet core. During the winter jet stream wind speeds are at maximum. In contrast, the jet stream strength is significantly reduced during the summer season. This is evident in all considered potential temperature ranges. A further feature in the PDFs is the decrease in jet stream wind speeds with increasing potential temperature range. However, regarding only the maximum wind speeds at the jet core in the $360 - 390$ K range the change is most prominent in the decrease between spring and summer. This could probably partly be linked to the onset of the summer circulation in the northern hemisphere stratosphere. From spring to summer the westerly winter circulation above the North pole turns into the easterly summer circulation, usually around the beginning of July (Piani and Norton, 2002), thus retarding the wind strength. Anyhow, also in the $330 - 360$ K range the decrease in maximum jet wind speeds is pronounced compared to the other seasons. The decreasing westerly wind strength during summer is the result of the decreasing temperature difference between low and high latitudes, thus lowering the thermal wind.

8.4 Seasonal climatology and variability of model derived O_3 in the SPURT sector related to the jet stream

The objective here is to get insight into the spatial structure and variability of O_3 relative to the regions of the jet stream. Therefore, PDFs of O_3 as a function of wind speed difference to the maximum jet wind speed for SON, DJF and MAM, JJA are shown in Figure 8.6 and in Figure 8.7, respectively. Hereby, the bin size is set to 20 ppbv for O_3 and to 2 m s^{-1} for $\triangle$FF. The normalisation is performed for each $\triangle$FF bin. Since ozone has a relative strong vertical gradient, the PDFs are computed separately in the same three potential temperature intervals as the wind speed PDFs in the previous section 8.3. Once more, in the summer PDFs the means are compared with those of the other seasons.

The seasonal mean data will obviously average a large range of locations relative to the centre of high wind velocities. Generally, due to the latitudinal O_3 distribution, mean and median O_3 VMRs increase with increasing distance to the jet and are maximal at the cyclonic side. Towards the anticyclonic jet side a considerable decrease is evident in the means and medians. Also the PDF contours in all seasons and Θ ranges show a sloped pattern from high to low O_3 VMRs across the jet core. Furthermore, the vertical O_3 gradient is also evident in all PDFs. With increasing potential temperature the occurrence probabilities of higher O_3 VMRs increase. However, there are several seasonal contrasts and features in the distributions.

The winter distribution in the highest considered Θ range shows two regions with high occurrence probabilities. One is located at the cyclonic jet side at $600 - 750$ ppbv and negativ $\triangle$FFs between -40 and -60 m s^{-1}, far away from the jet core. The other area appears at the anticyclonic side at O_3 VMRs between 250 and 350 ppbv and extends from the jet core to $\triangle$FF≈ 40 m s^{-1}. This feature is more pronounced during spring. In contrast to the winter PDF, during spring also in the $330 - 360$ K range this bimodal shape is evident. Due to the vertical O_3 gradient the most probable O_3 VMRs in this Θ region are slightly reduced compared to the highest Θ range. These contours reflect the large-scale downward motion of stratospheric air (e.g., Pan et al., 1997; Logan, 1999; Prados et al., 2003). In the course of winter and early spring descending O_3-rich stratospheric air accumulates in the lower and lowermost stratosphere. This leads to a strong contrast between polar O_3-rich air at the cyclonic jet side and comparable O_3-poor air at the tropospheric anticyclonic side. Both regimes are definitely separated. Even in the lowest Θ regime, which partly contains tropospheric air also at the cyclonic shear side, the separation is noticeable. During winter and still during spring the jet stream wind velocities are obviously high enough to effectively inhibit quasi-horizontal cross-tropopause transport through the jet core. The disjunction is most pronounced during the spring.

In the $330 - 360$ K range the winter PDFs show regions of higher probabilities of O_3 VMRs between $300 - 400$ ppbv at the cyclonic as well as at the anticyclonic side $\approx 20 - 40$ m s^{-1} from the jet core. This feature seems to reflect enhanced cross-tropopause interactions. Since the wave activity is most prominent during that season, the observed contours are probably the result of poleward and equatorward Rossby wave breaking. Such events occur predominantly in a jet exit region (e.g., Ray et al., 2004), leading to filamentation and laminae, which have high potential to subsequently mix with the surrounding air in the sense of the scale cascade (Haynes and Anglade, 1997). However, the North Atlantic sector, and thus the SPURT sector, is such a preferred region.

The summer PDFs indicate the decreasing capacity of the jet to separate the mentioned segregated regions of high and low O_3 at the cyclonic and anticyclonic jet side, respectively. The mean O_3 gradients across the jet core are very strong during winter and spring, especially in the highest Θ region. During summer the gradients are significantly reduced, indicating an increasing amount of quasi-horizontal cross-tropopause transport and mixing. Moreover, compared to the other seasons the jet strength is considerably lowered during summer. The lack of high jet stream wind velocities and thus absence of strong shear at the jet flanks as well as subsequent strong meandering of the jet simplifies quasi-isentropic transport between lower and higher latitudes.

O_3 VMRs during DJF and MAM as well as during JJA and SON show comparable mean values in the $360 - 390$ K region. In the lower Θ ranges the differences between the mean O_3

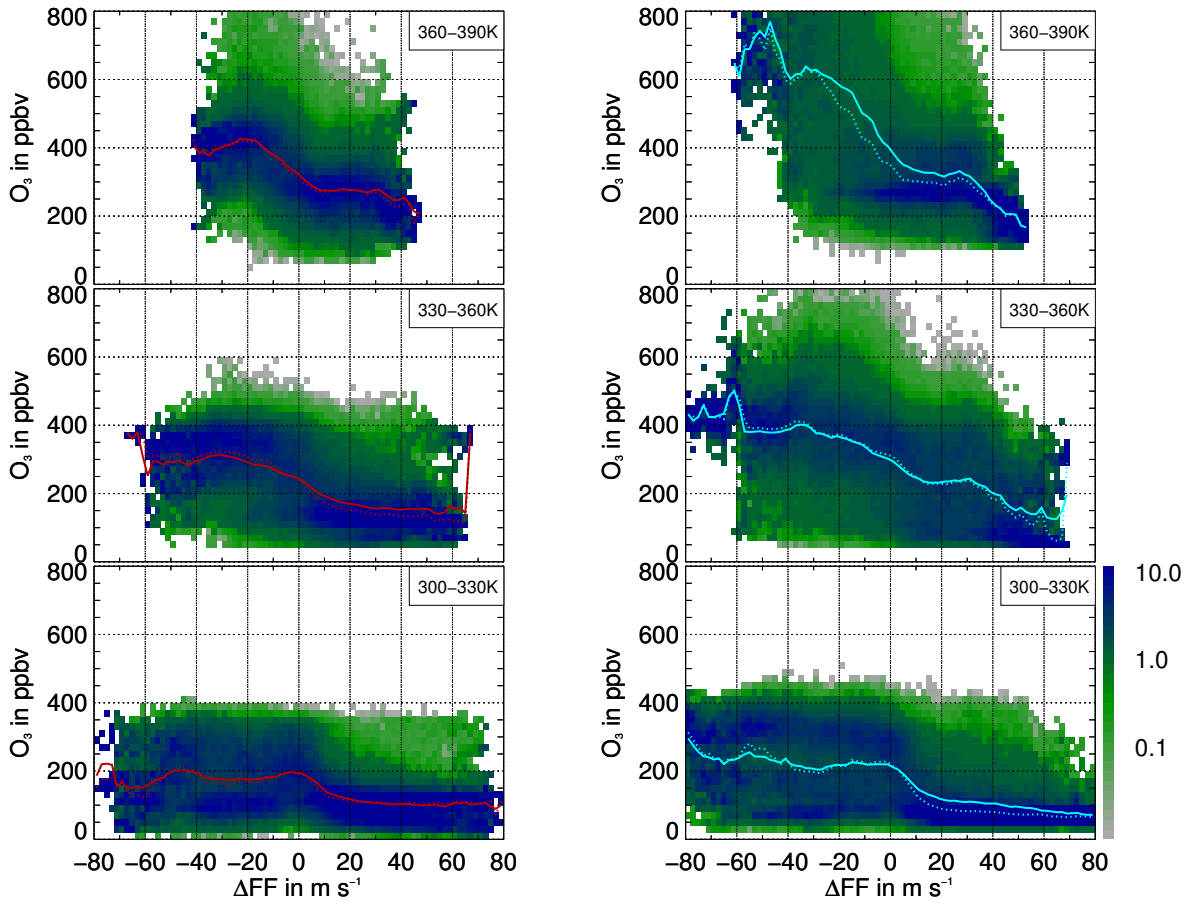

Figure 8.6.: Seasonal 2-dimensional probability distribution functions as a function of ozone and wind speed difference. The bin size is 20 ppbv for O_3 and 2 m s^{-1} for the coordinate. Due to the vertical gradient in O_3 the PDFs are performed for the same three different potential temperature regimes as in Figure 8.4.

values are evident, especially for summer and autumn. Also the summer and autumn PDFs show distinct structures. During autumn, the contours are symmetrically distributed around the mean with a smooth decrease to higher and lower O_3 values. Additionally, the spread of O_3 in each $\triangle$FF bin is minimised compared to the other seasons. A weaker gradient near the highest wind velocities across the jet core implies an elevated mixing state of the stratospheric tracer in the UT/LMS region, i.e. transport and mixing from the troposphere to the stratosphere across the jet. Indeed, jet stream wind velocities increase during SON and are even higher in the mean compared to their spring means (cf. Figure 8.6 and Figure 8.7). However, the O_3 gradient through the jet core is weakest during autumn. The strength of the jet hence does not affect the tracer gradient importantly. This could be explained by considering the actual O_3 source for the extra-tropical lowermost stratosphere, which can build up O_3 gradients across the jet. Diabatic transport of O_3 into the lower stratosphere onsets first in autumn and winter and convective transport from the troposphere is not resolved in CLaMS. Thus, the O_3 gradient across the jet core can not be stronger than during summer. Rather the seasonal integral effect of enhanced quasi-horizontal transport during summer becomes apparent. This lasts until the onset of the polar winter circulation, within which stratospheric

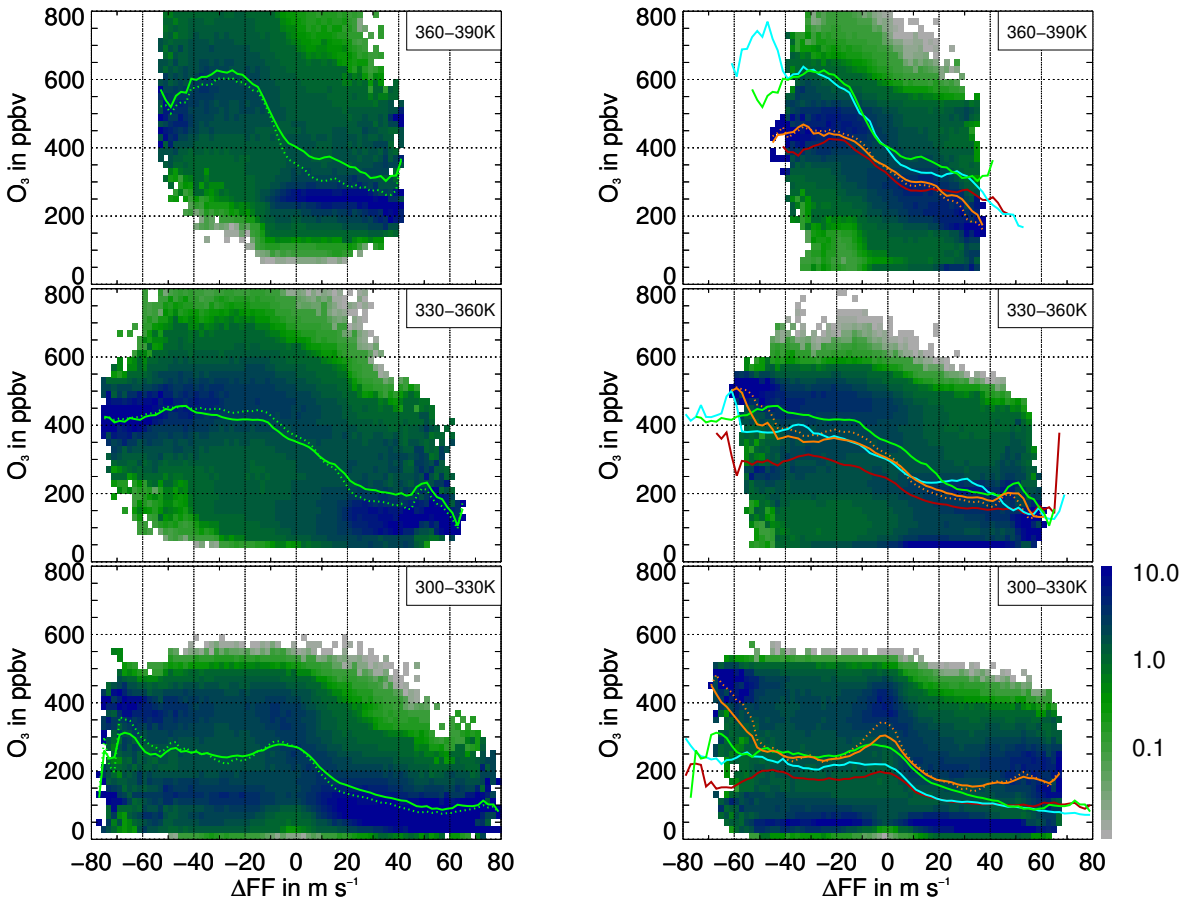

Figure 8.7.: As Figure 8.6 but for the spring and summer season. Thereby, also here mean values of O_3 during summer are compared to the means during the other seasons.

air is transported downward into the UT/LMS region. This leads to a pool of O_3-rich air at the cyclonic shear side of the jet. Further increase in jet stream wind speeds enhances the PV gradient. Thus quasi-horizontal transport between lower and higher latitudes is inhibited more efficiently, resulting in an increased O_3 gradient across the jet core.

Since the considered SPURT sector is a preferred region of wave breaking, O_3 gradients across the jet core can be weaker compared to other geographical areas as the North Pacific regions. Particularly between $135 - 180°$E the jet stream is zonally rather undisturbed (cf. Figure 5.5), possibly constituting a more effective barrier to quasi-horizontal transport. Thus, an important factor should also be the variability of the jet upstream to the considered sector (Ray et al., 2004). However, the distributions shown here are generally in agreement with a distinct transport barrier near the location of the steepest tropopause in winter (Haynes and Shuckburgh, 2000) and a maximum of cross-tropopause exchange during summer (Chen, 1995). From an analysis of tracer *in situ* measurements in the lower stratosphere Ray et al. (1999) showed definite reduced in-mixing of tropospheric air near the 360 K isentrope during spring and much larger tropospheric contributions in September.

8.5 Seasonal characteristics of zonal jet stream asymmetry

Differences in the O_3 PDFs can be significantly affected by the zonal asymmetry of the jet stream. In order to investigate the zonal jet distortion, in Figure 8.8 normalised seasonal frequency distributions of latitudinal positions of the detected jet stream grid points are displayed. Thereby, the three potential temperature regions are considered separately.

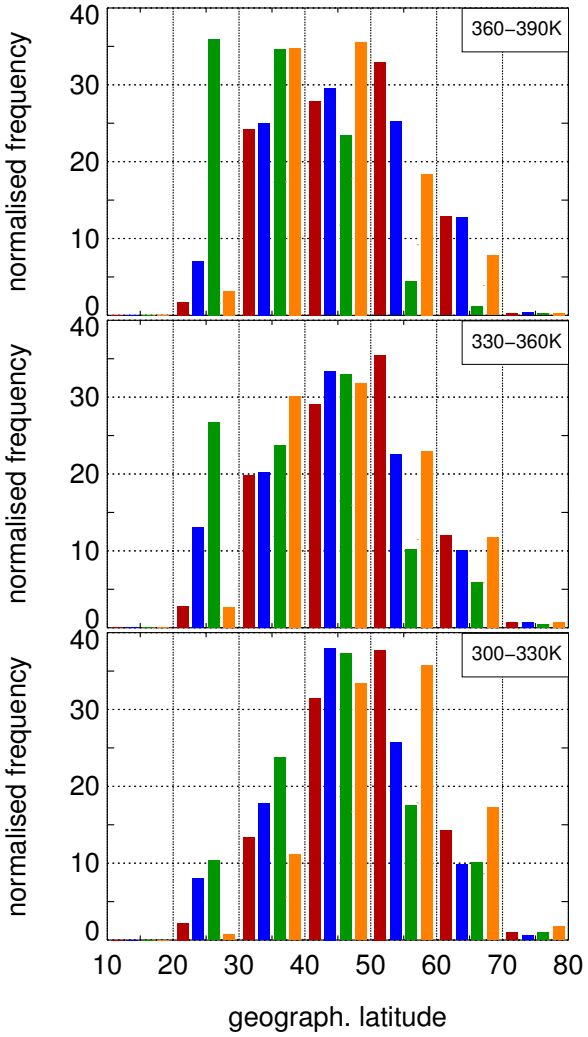

Figure 8.8.: Seasonal normalised frequency distributions of latitudinal jet stream positions in the SPURT sector, derived from ECMWF analyses from August 1, 2001, to August 31, 2002. Geographical latitude is binned by 10°N. Again a vertical separation in three potential temperature ranges is performed. Autumn, winter, spring, and summer are reflected by the dark red, blue, green, and orange colours, respectively.

Generally, the shape of the envelope of all seasonal frequency distributions shows a bell shape with maximal occurrence frequencies within $40 - 50$°N. Anyhow, the jet stream seems to be slightly shifted towards lower latitudes with increasing potential temperature. This implies the adaption of the vertical jet axis to the isentropic PV gradients. The frequency distribution for the winter season is similar to the one for spring. Except in the highest considered potential temperature region, a distinct displacement to $20 - 30$°N during spring appears.

Maximal occurrence frequencies are > 35 %. The summer distributions reflect the poleward shift of the jet stream (cf. also Figure 5.5). Due to the rather Gaussian distribution during winter and, for the both lower Θ regions also during spring, the jet stream seems to be zonally more distorted during DJF and MAM. During these seasons, enhanced wave activity and wave breaking is apparent, as mentioned earlier. This is also reflected in the winter O_3 PDFs in Figure 8.6.

8.6 Results of the simulation and conclusions

The derived O_3 climatology during the SPURT project was used for a long-term simulation with the Jülich CLaMS model to characterise features of transport and dynamics. Thereby, the O_3 variability relative to the main flow direction of the planetary wave pattern and its relation to the transport barrier effect was investigated, using a coordinate centred at the jet maximum wind speeds. The simulation, which was purely based upon advection, shows that the O_3 distribution is strongly linked to the strength of the jet stream, which acts as a transport barrier. High wind velocities reduce deep large-scale quasi-isentropic transport between the troposphere and the stratosphere during winter and spring, whereas during summer this transport pathway is enhanced owing to a weaker transport barrier.

The findings are also in accordance with the SPURT measurements of $SF6$, a tracer used to determine the mean age of air in the UT/LMS. Bönisch (2004) and Engel et al. (2004) derived from lag time studies that the oldest air was sampled during the spring campaigns. Within the summer, young tropospheric air enters the lowermost stratosphere. Due to the integral effect, the consequences of this transport process is most noticeable at the end of each period, i.e. during spring and autumn. This is also evident in the probability distribution functions of O_3 and $\triangle$FF shown here. However, *in situ* measurements of H_2O during the SPURT campaigns show already very low VMRs in autumn (see chapter 3). Therefore, it is most likely that the younger air origins from the sub-tropics/tropics.

The mean O_3 values in the PDFs obviously also reflect the seasonal cycle of that trace gas in the lowermost stratosphere (cf. subsection 3.2.1). In the lowest considered potential temperature region, which occasionally lies partly in the troposphere, mean O_3 VMRs during spring and summer at the cyclonic side are of comparable amount. This implies that the stratospheric influence extents deep into the lowermost stratosphere to the tropopause region. Thus, the importance of STT and its possible impact on tropospheric O_3 is underlined once more, as was already mentioned in section 6.2.

Chapter 9

Conclusions and outlook

9.1 Synopsis and what we have learned from O_3 and H_2O measurements during SPURT

In the experimental part of this thesis, high resolution airborne *in situ* measurements of ozone and total water in the upper troposphere and lowermost stratosphere (UT/LMS) have been performed with great success within the BMBF supported AFO 2000 project SPURT (cf. chapter 2). At the ICG-I of the Research Centre Jülich, in the recent years specific instruments were developed or modified for implementation on research aircraft. In the frame of the SPURT project, I was responsible for the FISH (Zöger et al., 1999) and the JOE (Mottaghy, 2001) instruments, measuring total water and ozone, respectively. Using a Learjet 35A, a total of 8 extensive airborne campaigns, evenly distributed over all seasons, were conducted between November 2001 and July 2003. Beside the H_2O and O_3 trace gases, several chemical species in the UT/LMS with different lifetimes, sources and sinks have been investigated in the European sector between 20 and $80°$N. During the whole SPURT period there were only few data losses. Thus, the achieved high amount of H_2O and O_3 data during SPURT reflects the equipment dependability of the FISH and the JOE instrument as well as the quality of the associated service and maintenance.

Until today, the SPURT project provides the unique continuous and high qualitative data set of high resolution *in situ* measurements of several trace gases in the UT/LMS region in the European sector. The large amount of information offers a vast quantity of potentialities and options for data analyses and investigations of scientific problems. In this thesis, the H_2O and O_3 SPURT data were analysed using several statistical perspectives and interpretations by diagnostics, facilitating a comprehensive overview of the seasonal trace gas distribution and variability in the UT and LMS. The obtained results are summarised in the following.

The seasonal cycle of O_3 is distinct in the upper troposphere and in the lowermost stratosphere. Up to the tropopause, which was analysed to correspond largely to the 2 PVU surface for the SPURT measurements, a winter minimum and a broad spring to summer O_3 maximum is evident in the data. The latter is most probably the result of *in situ* photochemistry during these seasons.

In the lowermost stratosphere a more prominent seasonal cycle in O_3 is apparent. Compared to the O_3 seasonal cycle in the UT, the maximum of O_3 in the LMS is shifted in phase by about $2-3$ months earlier. In the upper part of the LMS, a pronounced O_3 maximum is established during spring, whereas the lower part of the LMS still contains large contributions of rather O_3-poor tropospheric air during winter and early spring. Only around April the O_3 maximum is also established in the lower part. This is the effect of the large-scale stratospheric winter/spring Brewer-Dobson circulation. Induced by breaking Rossby waves and strong diabatic subsidence (the downward control principle, Haynes et al., 1991) aged and O_3-rich stratospheric air is transported downward into the LMS (e.g., Austin and Follows, 1991; Beekmann et al., 1994; Logan, 1999). Thus, during spring a contribution of stratospheric O_3 due to stratosphere-to-troposphere transport (STT) is likely to affect tropospheric ozone. Performed calculations with the trajectory module of the Jülich CLaMS model indicate that the higher tropospheric O_3 mixing ratios already in spring can partly be related to STT (cf. section 6.2).

The O_3 minimum in the whole lowermost stratosphere appears during autumn. Using a natural coordinate system centred at the jet stream core, this minimum was shown to be the result of an integral effect. During summer and autumn the stratospheric downward transport is significantly reduced. Moreover, the extra-tropical tropopause is more permeable to deep large-scale quasi-isentropic transport than during winter and spring. This is owing to the weakening potential vorticity gradients along isentropes crossing the tropopause (a decreasing transport barrier effect, Haynes and Shuckburgh, 2000). Thus, enhanced quasi-isentropic transport allows an elevated mixing state of tropospheric and stratospheric air in the UT/LMS region (cf. chapter 8).

In contrast to the O_3 seasonal cycles in the UT and LMS, there is no phase shift observed in the H_2O data. Highest H_2O mixing ratios were observed during summer close to the tropopause in the UT as well as in the LMS. Driest seasons were found to be autumn and winter. The reason for this seasonality is twofold. First, since H_2O is strongly influenced by heterogeneous processes, it follows the temperature variation at the tropopause, i.e. the air is widely freeze-dried during its transport into the LMS. Second, whereas – as mentioned above – downward transport of dry air from the overworld into the LMS is dominant during winter, the barrier for quasi-isentropic transport of moist air over the tropopause deep into the LMS is weak during summer.

These two reasons for the seasonal H_2O cycle were analysed more precisely. The H_2O entry value into the LMS is strongly coupled to the seasonal cycle and variability of tropopause temperatures. Estimated H_2O entry values at the tropopause show a distinct seasonal cycle at all latitudes (cf. chapter 5). As in the tropical cold trap the air is also freeze-dried at the extra-tropical tropopause on its way into the LMS. However, substantial (super)saturation was observed during some research flights even above 6 PVU, i.e. well within the LMS. Due to the participation in heterogeneous processes the highly variable H_2O is widely traceable to temperatures the air parcels suffered during troposphere-to-stratosphere transport (TST). Using the information content of backward trajectory calculations, the SPURT data indicates significant potential for and occurrence of (super)saturation and cirrus cloud formation in and even above the tropopause region. This underlines the relevance of dehydration and hydration processes on chemistry and climate in the UT/LMS (cf. section 6.1). Furthermore, an RDF case study using fields of potential vorticity and ice saturation was performed, which highlights once more the impact of TST and combined freeze-drying on the atmospheric H_2O composition (cf. chapter 7).
Due to the strong downwelling in the extra-tropics during winter, transport of H_2O-poor overworld air into the LMS is enhanced, which leads to the observed H_2O minimum during that season. The measured low H_2O mixing ratios in the LMS already in autumn suggest an efficient drying of the air during that season on its way into the LMS. Thereby, the air most probably originates from the (sub-)tropics. The transport from the (sub-)tropics is in accordance with lag time studies by Bönisch (2004) and Engel et al. (2004) using the SPURT data. They revealed the youngest tropospheric air in the LMS during summer and autumn. The efficient drying during autumn is furthermore supported by long-term simulations of water vapour with the Jülich CLaMS by Günther et al. (2004) covering the SPURT time period. In these simulations the seasonal distribution of H_2O, determined by the large-scale transport processes as described above, could be qualitatively reproduced as measured during SPURT. In combination with a quasi-inert tropospheric tracer, cross-tropopause transport of moist air from the (sub-)tropics deep into the LMS is apparent during summer. Thereby, our results indicate highest ice water content in the tropopause region extending from the tropics up to high equivalent latitudes, especially during autumn (see Figure 9.1).

Further emphasis in this thesis was led on the investigation of processes in the transition region between the troposphere and the stratosphere. Using different reference coordinates, it was shown that both trace gases O_3 and H_2O are best correlated and reveal the most compact distributions when related to potential vorticity and/or distance to the local tropopause. Thereby, especially 2-dimensional probability distribution functions have been used as a powerful tool to visualise the seasonal as well as the high spatial and temporal trace gas variability. Application of different PV threshold values for the extra-tropical

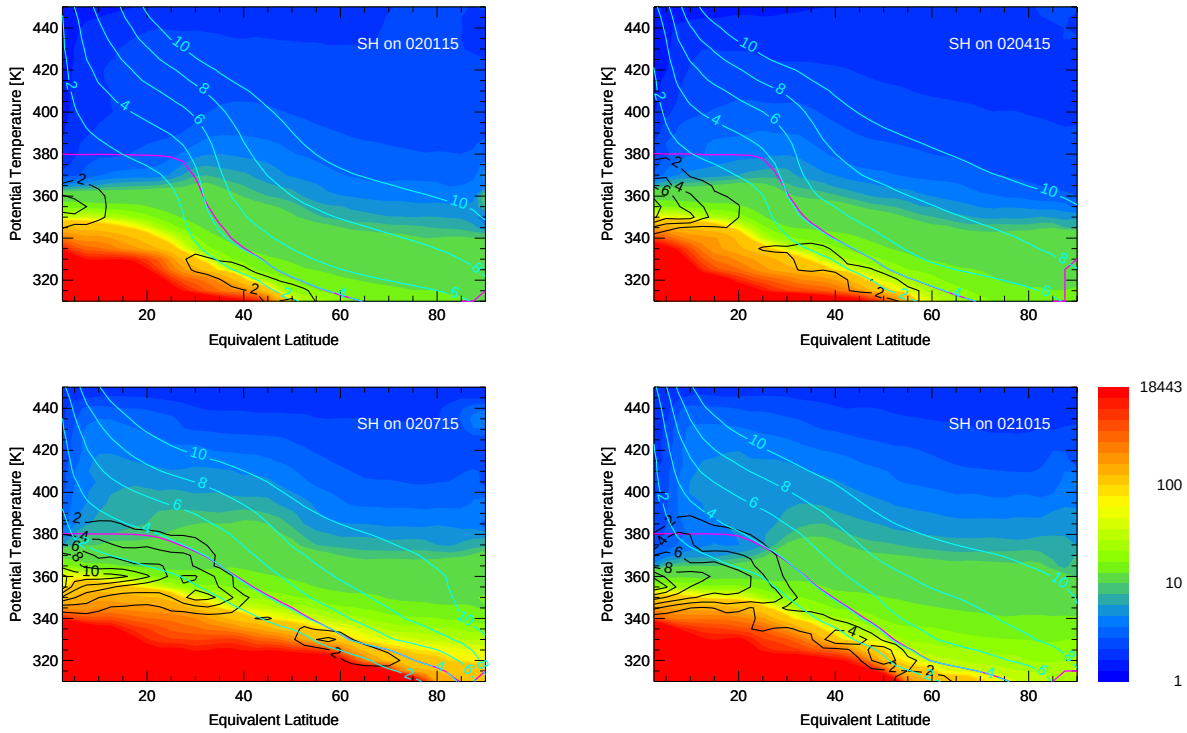

Figure 9.1.: Results from long-term simulations for the Northern Hemisphere by Günther et al. (2004). Shown are seasonal equivalent zonal means of specific humidity (SH, colour coded in ppmv) together with ice water content (black contours). In all charts, the dynamical tropopause, defined by the 4.0 PVU surface in the extra-tropics and by 380 K for $\varphi_e < 20°$N, is indicated by the magenta line. Additionally, potential vorticity surfaces of 2, 4, 6, 8, and 10 PVU are reflected by the cyan contours. Clockwise: snapshot on 15 th of January, April, October, and July, 2002. During winter the Brewer-Dobson circulation characterises the UT/LMS with strong upwelling in the tropics, poleward transport in the stratosphere and downwelling in the polar regions. Stratospheric air is advected into the troposphere below the sub-tropical jet core with subsequent mixing. This leads to an enhanced meridional tracer gradient. A very dry tropical tropopause is evident due to the coldest temperatures there during winter. Also H_2O mixing ratios at the extra-tropical LMS are low. With the decreasing transport barrier during summer tropospheric influence in the LMS is enhanced, leading to a moistening of the LMS. (Courtesy of G. Günther)

tropopause exhibit the alignment of tracer isopleths to potential vorticity surfaces rather than their orientation along isentropes (cf. chapter 3). This is supported by tracer distributions in the potential temperature and equivalent latitude space, a coordinate system which is especially favourable for climatological aspects. Within this reference frame, an extra-tropical tropopause exchange layer exhibiting trace gas signatures characteristic for a mixture of tropospheric and stratospheric air could be identified. This year-round mixing layer follows the shape of the tropopause and/or PV surfaces and ranges several $10°$ poleward in equivalent latitude and several 10 K above the tropopause in potential temperature (cf. section 4.1). The observed arrangement of tracer isopleths is in accordance with results from James et al. (2003a), who showed that layers of air of similar mean age are a function of distance to the tropopause.

The O_3 and H_2O measurements during SPURT provide evidence for a significant amount of troposphere-to-stratosphere transport and thus a strong coupling of the mixing layer to the

troposphere. The extra-tropical tropopause mixing layer is not the result of an instantaneous meteorological situation at the tropopause and is not formed by individual mixing events. It is rather composed by the superposition of many cross-tropopause mixing events on different time scales. Back trajectory calculations for the SPURT measurements show evidence for cross-tropopause transport into this layer within time scales on the order of weeks. However, within the LMS the influence of troposphere-to-stratosphere transport and subsequent mixing decrease with increasing distance to the local tropopause in both vertical and horizontal direction (cf. section 4.2).
From tracer-tracer correlations the upper bound of the mixing layer was estimated to $8-9$ PVU, independent on season. Thereby, the extra-tropical tropopause itself as the lower boundary is located at $2-3$ PVU. In contrast to its extension into the LMS, the isentropic depth of the mixing layer varies significantly with season, exhibiting a distinct winter maximum and a summer minimum. Hoor et al. (2004c) derived similar results from CO measurements during SPURT. They estimated a maximal isentropic depth of the mixing layer during summer and vice versa during winter. However, the seeming conflict arises from the different chemical characteristics and the behaviour of both trace gases H_2O and CO. Additionally, the sensitivity of the deduced value, up to which recent tropospheric influence is detectable, should contribute to that difference (cf. section 4.3).

Compared to previous mid- and high-latitude campaigns, even beyond the mixing layer enhanced H_2O mixing ratios higher than the stratospheric background of $4-8$ ppmv have been detected during all seasons and especially during summer. This is indicative for significant tropospheric contributions via extra-tropical pathways. Transport on the order of a few weeks from the troposphere deep into the LMS is not supported by backward trajectory calculations. However, once in the LMS an air parcel can maintain its water vapour signature on long time scales due to the relative warm temperatures there. As mentioned above, Lagrangian long-term simulations with the Jülich CLaMS by Günther et al. (2004) could reproduce the observed tropospheric influence. Thereby, the enhanced H_2O even beyond the mixing layer originates from transport processes on longer time scales. However, above all, the H_2O measurements during SPURT imply that the lower stratosphere may be moister than usually expected.

9.2 Outlook

The work presented here exposes some responses to the central objectives of the SPURT project. Several queries are still outstanding, which sometimes could only hardly be addressed here due to insufficient amount of measurement data in some atmospheric regions. Nevertheless, this thesis demonstrates the high worthiness of the performed aircraft mea-

surements with the innovative concept of campaign performance. The unique and high resolution SPURT data set of high quality provides an excellent basis for process studies. Especially, dedicated case studies should be performed to investigate transport and mixing processes in order to reveal details of the underlying processes.
A wide choice of scientific challenges can be considered by the high resolution data set. For instance, it would be interesting to investigate exchange between the upper troposphere and the lowermost stratosphere by using the technique of unified scale invariance (e.g., Tuck et al., 2003b,a). All scales participate in atmospheric dynamics, however, significant impact to the chemical composition of atmospheric regions can arise by substantial contributions from relatively infrequent but intense events. Especially for total water, an analyses of scale invariance and implications for a conservative cascade of energy from the largest to the smallest scales should be discussed.
A further related interesting topic is the finding that the lowermost stratosphere appears to be moister than usually expected. Also the seasonality of the mixing layer and the underlying processes need more investigation. However, the SPURT measurements took place in the European sector which has specific characteristics, for instance, it is a preferred wave breaking zone. Thus, a compilation of *in situ* measurements at other geographical regions should be considered. Anyhow, for an exact resolution of details and small-scale structures in the atmosphere observations with even higher time resolution are desirable.

As it was shown in this thesis, the SPURT data provides a powerful and valuable tool in connection with Lagrangian studies to analyse exchange processes. Further, the trace gas climatologies obtained during SPURT demonstrate a high value for implementation in models, from which substantial outcomes can be inferred. Based upon measurements (e.g., Hintsa et al., 1998; Ray et al., 1999; Hoor et al., 2004b) as well as Lagrangian transport models (e.g., Dethof et al., 2000; Wernli and Bourqui, 2002; Sprenger and Wernli, 2003), numerous studies have been performed to investigate mass and trace gas fluxes across the tropopause into the troposphere and the stratosphere as well as through the 380 K surface (e.g., Appenzeller et al., 1996b; Schoeberl, 2004). It was shown that the trace gas composition of the UT/LMS undergoes a pronounced seasonal variability. However, concerning the exchange fluxes, a key factor of pure advective transport calculations with models is the vertical velocity. In Lagrangian models which operate on isentropic levels, as the Jülich CLaMS, appropriate solutions for the vertical velocity have to be found to reveal high accuracy within the simulations, especially in the tropics. There is currently extensive work at the ICG-I on a ”new” vertical coordinate in CLaMS. This coordinate uses pressure surfaces as well as isentropes, which merge continuously near the tropopause region (cf. Mahowald et al., 2002). Thus, with this coordinate accurate quantification of stratosphere-troposphere exchange processes can potentially be performed with high accuracy, even in the tropics.

Saturation/supersaturation processes and cirrus cloud formation are also challenging issues to study in more detail. The distribution of H_2O is yet simulated in CLaMS considering transport, phase changes and sedimentation of ice particles using a simplified module. As it was adverted in section 9.1, accurate and promising results have been obtained. However, this module could be improved, for instance by considering aerosols and heterogeneous freezing processes.

During SPURT it was not possible to obtain *in situ* data in the region above 380 K, i.e. the overworld. That region is strongly coupled to the tropics (the tropically controlled transition region, Rosenlof et al., 1997). It is in particular of interest, how dynamics and chemistry act on the tracer budget of the mixing layer and the lowermost stratosphere, and especially how their seasonality contributes to the stratospheric (overworld) ”background”. The approved new research aircraft HALO (high altitude and long range research aircraft) will be able to operate in this atmospheric region. Combined with the successful and effective campaign concept, whose power has been demonstrated by the SPURT project and the results of this thesis, future measurements will be able to deepen the understanding of atmospheric processes and to answer open questions, especially the feedback from a changing climate.

Appendix A

Thermal and chemical tropopause heights during SPURT ascents and descents

Table A-I: Altitude, potential temperature, ozone mixing ratio and potential vorticity at the lapse rate (TP_{th}, definition after WMO, 1986a) and chemical (TP_{ch}, definition after Bethan et al., 1996) tropopause. Values are in m, K, ppbv and PVU, respectively.

		@TP_{th}				@TP_{ch}			
IOP/mission season	**ascent location descent location**	**alt**	**Θ**	**O_3**	**PV**	**alt**	**Θ**	**O_3**	**PV**
1/1	Hohn	-	-	-	-	11265	341	55	2.97
autumn	Faro	9250	327	95	2.20	9350	328	92	2.13
1/2	Faro	8321	321	72	2.16	11613	347	60	2.17
autumn	Hohn	11044	334	91	1.49	-	-	-	-
1/3	Hohn	9595	322	50	1.99	10734	337	119	4.10
autumn	Kiruna	7221	295	76	2.07	7346	298	76	2.12
1/4	Kiruna	7424	296	51	2.45	7749	300	84	2.97
autumn	Hohn	10398	324	55	2.13	10517	326	58	2.07
2/1	Hohn	-	-	-	-	-	-	-	-
winter	Casablanca	10565	322	48	2.57	10714	324	61	2.58
2/2	Casablanca	-	-	-	-	11331	332	63	3.45
winter	Gran Canaria	-	-	-	-	11335	336	131	4.22
2/3	Gran Canaria	10559	327	79	2.88	11140	331	92	3.94
winter	Lisbon	11727	331	41	2.17	12419	336	56	2.60
2/4	Lisbon	-	-	-	-	-	-	-	-
winter	Hohn	11710	327	70	1.50	12251	335	84	2.19
2/5	Hohn	9150	315	-	2.80	-	-	-	-
winter	Tromsø	9386	304	-	2.02	10558	319	128	3.91
2/6	Tromsø	9994	310	-	2.95	-	-	-	-
winter	Hohn	8440	303	-	2.45	-	-	-	-
3/1	Hohn	-	-	-	-	11338	330	119	2.96
spring	Jerez	12736	342	99	1.96	12942	345	113	1.97
3/2	Jerez	10726	334	77	3.31	11154	335	88	3.81
spring	Hohn	11845	331	82	2.62	11936	331	76	2.34
3/3	Hohn	9815	328	204	4.12	9026	325	81	2.68
spring	Tromsø	7962	304	116	2.60	7481	300	73	1.70
3/4	Tromsø	8910	314	74	3.82	9678	319	79	4.72
spring	Hohn	12275	339	176	2.29	12879	351	239	2.67
4/1	Hohn	10851	330	139	4.62	10187	327	97	2.91
summer	Monastir	10711	337	90	1.29	11343	341	119	1.85
4/2	Monastir	-	-	-	-	11376	340	129	1.82
summer	Hohn	11057	332	156	3.43	9837	326	111	1.79
4/3	Hohn	10085	325	88	2.50	10116	325	85	2.57
summer	Keflavik	9179	319	103	3.97	9162	319	81	3.84

continued on next page

Table A-I continued from previous page

		@TP$_{th}$				@TP$_{ch}$			
IOP/mission season	**ascent location descent location**	**alt**	**Θ**	**O_3**	**PV**	**alt**	**Θ**	**O_3**	**PV**
4/4	Keflavik	7995	317	-	2.65	-	-	-	-
summer	Hohn	10841	329	166	2.31	10661	328	100	1.83
5/1	Hohn	8230	310	114	2.10	8178	310	100	2.11
autumn	Seville	-	-	-	-	12829	349	123	4.64
5/2	Seville	-	-	-	-	-	-	-	-
autumn	Hohn	9350	310	111	2.57	9303	310	79	2.41
5/3	Hohn	9343	310	65	2.32	9867	315	81	3.52
autumn	Keflavik	11008	321	56	1.84	11451	327	77	2.24
5/4	Keflavik	-	-	-	-	-	-	-	-
autumn	Hohn	-	-	-	-	-	-	-	-
6/1	Hohn	-	-	-	-	11293	326	84	2.09
winter	Faro	12350	343	212	2.65	12112	334	91	2.24
6/2	Faro	9241	322	-	3.35	-	-	-	-
winter	Hohn	9681	312	69	2.52	9838	313	78	2.54
6/3	Hohn	10319	316	68	2.61	11240	322	100	4.09
winter	Tromsø	11695	326	99	3.23	11655	325	96	3.33
6/4	Tromsø	9677	312	-	2.23	-	-	-	-
winter	Longyearbyen	9369	308	139	3.31	8535	305	76	2.28
6/5	Longyearbyen	10348	314	70	3.13	10443	315	77	3.32
winter	Hohn	10795	317	77	2.09	10990	319	81	2.15
7/1	Hohn	8610	313	99	2.62	8840	314	89	2.72
spring	Kiruna	9663	312	79	2.84	9664	312	73	2.61
7/2	Kiruna	8796	309	107	2.82	8779	308	98	2.75
spring	Hohn	8474	311	133	2.09	8363	310	116	1.65
7/3	Hohn	-	-	-	-	10817	326	92	2.14
spring	Lisbon	11611	335	119	1.64	11892	338	120	1.80
7/4	Lisbon	-	-	-	-	-	-	-	-
spring	Hohn	11511	329	101	2.36	11512	329	83	2.08
6/5	Hohn	-	-	-	-	9464	320	93	2.25
spring	Hohn	10622	324	108	1.93	10622	324	100	1.74
8/1	Hohn	9296	323	93	2.12	9369	323	81	2.14
summer	Faro	-	-	-	-	12684	357	120	2.60
8/2	Faro	-	-	-	-	10987	342	97	1.84
summer	Hohn	9540	327	84	1.44	10765	333	97	3.08
8/3	Hohn	-	-	-	-	10824	336	123	2.52
summer	Tromsø	9803	326	159	4.24	8861	321	107	2.48
8/4	Tromsø	9961	328	178	2.47	9604	327	102	1.94
summer	Hohn	11458	340	117	1.71	11556	341	116	1.63

Appendix B

Extension of trajectory analyses

This addendum contains the trajectory statistics for the 20 and 30 day backward calculations discussed in section 4.2. Additionally, the tracer distributions in the Θ-φ_e space with initial trajectory locations are included (cf. section 4.1). It is to annotate that the meteorological boundary data used here for the backward trajectory calculations only cover the Northern Hemisphere within a vertical domain between 280 and 400 K. Due to the 3-dimensional winds initialised trajectories can leave the domain at the top or bottom or can be advected from the Southern Hemisphere. When leaving the domain, information of the origin and characteristics of those trajectories could not be obtained for the full time period.

In general, for an enhanced backward calculation time the frequency of STE increases. Also the distance from the tropopause increases for TST and STT. This is to expect, since an increased calculation time enhances the trajectories' potential to originate from the deeper troposphere or stratosphere. In comparison to the 10 day calculations, TST O_3 VMRs are slightly enhanced. This is probably due to the potential for a longer residence time in the stratosphere, hence the result of the greater potential for participating in mixing processes. STT O_3 concentrations remain about the same presumably because of the higher turbulence in the troposphere. H_2O VMRs of TST and STT trajectories show no significant variability. An increased backward calculation time has no large effect on the stratospheric H_2O content since it is largely limited by its entry value at the tropopause, i.e. controlled by tropopause temperatures. Certainly, the entry values have a geographical dependence with dryer air at lower and moister air at higher latitudes (cf. Hoinka, 1999, and Figure 5.7 in section 5.2). With increasing backward time H_2O VMRs for TST parcels slightly decrease. This is in accordance with the results based on Figure 4.6, i.e. the higher the backward time the lower φ_e of the last significant tropopause crossing and thus the dryer the exchanged air. Once in the LMS H_2O VMRs are only controlled by temperature (and methane oxidation in the higher stratosphere).

In contrast to the 10 day backward trajectory calculations, there are also mean minimal IS VMRs ratio values of TST trajectories lower than their H_2O VMRs. This suggests that the extra-tropical tropopause acts, similarly as in the tropics, as a ”cold trap”, determining the H_2O content during transport into the LMS. Anyhow, since these data are only mean values also during the previous 10 days there is a high potential for (super)saturation (cf. section 6.1). Thereby, possibly small particles could form which were transported within the updraft into the LMS where they experienced a warming event, thus (re)hydrating the air.

B.1 20 day backward trajectories

Table B-I: Same as Table 4-II but for 20 day backward trajectories.

		$0^\circ N \leq \varphi_e \leq 30^\circ N$				$30^\circ N < \varphi_e < 60^\circ N$				$60^\circ N \leq \varphi_e \leq 90^\circ N$			
		aut	**win**	**spr**	**sum**	**aut**	**win**	**spr**	**sum**	**aut**	**win**	**spr**	**sum**
	%	**0.1**	-	-	-	3.5	2.6	*1.8*	**5.6**	1.4	*0.5*	1.2	**5.0**
	$\overline{O_3}$	-	-	-	-	*149.6*	204.9	**292.8**	179.3	181.5	*157.8*	**221.4**	219.9
	$\widetilde{O_3}$	-	-	-	-	*144.4*	215.6	**282.2**	166.1	186.0	*154.4*	200.4	**201.3**
	$\overline{H_2O}$	**9.0**	-	-	-	*15.2*	26.2	24.0	**46.9**	26.2	*13.0*	50.2	**79.2**
	$\widetilde{H_2O}$	**9.1**	-	-	-	*11.2*	21.8	21.3	**44.8**	22.8	*11.5*	51.4	**78.8**
	$\overline{IS}$	**53.7**	-	-	-	94.2	*56.4*	80.3	**121.3**	159.2	*65.4*	**178.2**	170.0
	$\widetilde{IS}$	**54.3**	-	-	-	85.6	*45.2*	53.6	**107.3**	160.9	*58.3*	**179.1**	172.3
	$\overline{IS^{min}_{10d}}$	**5.2**	-	-	-	23.8	*23.1*	35.8	**35.9**	57.6	*31.4*	51.3	**69.0**
	$\widetilde{IS^{min}_{10d}}$	**6.5**	-	-	-	*20.0*	21.4	**33.3**	26.2	52.4	*35.1*	51.8	**68.7**
	$\overline{IS^{max}_{10d}}$	**200.0**	-	-	-	*3670.2*	6155.6	**8259.5**	5038.9	**9161.1**	*4121.1*	8447.0	6535.9
T	$\widetilde{IS^{max}_{10d}}$	**214.6**	-	-	-	*510.2*	1942.9	**2007.9**	871.6	**10528.9**	*1587.2*	1823.0	1691.9
S	$\overline{PV}$	**3.0**	-	-	-	**4.9**	**4.9**	**4.9**	*4.7*	5.3	**6.2**	*4.9*	6.1
T	$\widetilde{PV}$	**3.1**	-	-	-	4.6	**4.8**	4.7	*4.5*	*4.3*	6.0	4.5	**6.1**
	$\overline{PV^{min}_{10d}}$	**0.3**	-	-	-	0.5	*0.4*	**0.6**	**0.6**	*0.7*	*0.7*	**0.8**	*0.7*
	$\widetilde{PV^{min}_{10d}}$	**0.8**	-	-	-	0.3	*0.2*	**0.4**	**0.4**	**0.5**	**0.5**	**0.5**	*0.4*
	$\overline{PV^{max}_{10d}}$	**3.3**	-	-	-	*5.8*	5.9	**6.6**	6.0	**7.2**	7.0	*5.8*	6.9
	$\widetilde{PV^{max}_{10d}}$	**3.3**	-	-	-	**6.4**	*5.6*	**6.4**	*5.6*	7.1	**7.4**	*5.9*	6.5
	$\overline{LTPC}$	**194.5**	-	-	-	155.0	146.2	*127.9*	**165.9**	177.5	**270.4**	177.8	*144.6*
	$\widetilde{LTPC}$	**290.0**	-	-	-	87.0	127.0	*68.0*	**137.0**	164.0	**358.0**	188.0	*109.0*
	$\overline{NTPC}$	**12.0**	-	-	-	10.9	**14.1**	12.2	*10.8*	*9.4*	11.8	**13.0**	11.6
	$\widetilde{NTPC}$	**13.0**	-	-	-	**9.0**	**9.0**	8.0	*7.0*	*5.0*	**10.0**	9.0	9.0
	$\overline{DTP}$	**10.9**	-	-	-	**21.4**	15.5	*13.2*	16.0	17.6	**24.8**	14.5	*13.9*
	$\widetilde{DTP}$	**11.2**	-	-	-	**19.1**	12.9	*11.3*	15.0	14.5	**24.2**	*10.6*	11.8
	%	0.7	2.9	**3.0**	*0.4*	**0.6**	0.4	*0.3*	**0.6**	0.1	**0.3**	-	0.2
	$\overline{O_3}$	47.5	*44.9*	61.8	**73.3**	59.5	*53.9*	60.5	**74.3**	-	-	-	-
	$\widetilde{O_3}$	47.5	*44.0*	55.9	**71.0**	57.6	*53.7*	56.4	**68.0**	-	-	-	-
	$\overline{H_2O}$	308.6	*193.0*	289.4	**537.9**	259.7	*137.9*	172.8	**378.3**	-	-	-	-
	$\widetilde{H_2O}$	308.1	*216.0*	355.3	**537.9**	286.3	*105.7*	148.3	**334.4**	-	-	-	-
	$\overline{IS}$	*619.9*	687.1	**1538.7**	855.6	2627.5	986.8	*511.1*	**3709.4**	3221.7	2176.9	-	**8658.3**
	$\widetilde{IS}$	*454.4*	**888.2**	456.0	800.3	1527.6	434.4	*193.7*	**2296.5**	3245.4	2193.9	-	**8518.9**
	$\overline{IS^{min}_{10d}}$	79.4	*30.2*	41.5	**103.9**	50.0	*31.1*	49.5	**92.3**	47.6	73.3	-	**146.2**
	$\widetilde{IS^{min}_{10d}}$	83.1	*32.8*	38.0	**111.2**	42.6	*27.5*	50.7	**92.5**	49.7	85.6	-	**150.0**
	$\overline{IS^{max}_{10d}}$	5945.7	**11565.5**	7657.6	*4989.4*	6744.3	*3906.5*	**9859.5**	7394.7	5820.8	7018.9	-	**9721.6**
S	$\widetilde{IS^{max}_{10d}}$	5064.1	**12268.5**	5796.9	*2151.6*	5489.4	*3204.2*	4446.8	**5916.6**	3251.4	2676.4	-	**11659.3**
T	$\overline{PV}$	**0.4**	**0.4**	**0.4**	*0.3*	*0.6*	0.7	**0.8**	0.7	**0.9**	0.8	-	0.8
T	$\widetilde{PV}$	**0.4**	*0.3*	*0.3*	*0.3*	*0.6*	0.7	**0.8**	0.7	**1.0**	0.8	-	0.8
	$\overline{PV^{min}_{10d}}$	*<0.1*	0.1	0.2	**0.3**	*0.3*	**0.4**	*0.3*	**0.4**	**0.6**	0.4	-	0.4
	$\widetilde{PV^{min}_{10d}}$	*-0.1*	0.1	0.2	**0.3**	*0.3*	**0.4**	*0.3*	**0.4**	**0.8**	0.4	-	0.4
	$\overline{PV^{max}_{10d}}$	6.9	5.7	*5.6*	**7.9**	**6.5**	*5.8*	*5.8*	6.1	**6.0**	4.9	-	5.4
	$\widetilde{PV^{max}_{10d}}$	**7.6**	5.5	*5.3*	7.1	**6.4**	5.6	*5.1*	5.9	**6.5**	4.5	-	5.2
	$\overline{LTPC}$	**329.8**	322.2	*144.2*	253.0	185.9	149.2	*104.8*	**218.6**	115.0	195.2	-	**288.2**
	$\widetilde{LTPC}$	**345.0**	323.0	*131.0*	253.0	170.0	96.0	*90.0*	**183.0**	69.0	168.0	-	**313.0**
	$\overline{NTPC}$	*8.7*	**17.0**	15.7	10.7	11.9	14.2	**15.2**	*11.2*	9.4	10.2	-	**13.3**
	$\widetilde{NTPC}$	*5.0*	**16.0**	10.0	7.0	*9.0*	11.0	**13.0**	*9.0*	9.0	9.0	-	**13.0**
	$\overline{DTP}$	*-19.2*	-11.4	-12.9	**-9.8**	*-19.1*	-14.5	**-6.5**	-12.8	-33.5	-25.0	-	**-24.3**
	$\widetilde{DTP}$	*-19.6*	-13.4	-10.7	**-8.7**	*-15.9*	-10.9	**-4.5**	-11.0	-34.4	-25.0	-	**-18.3**

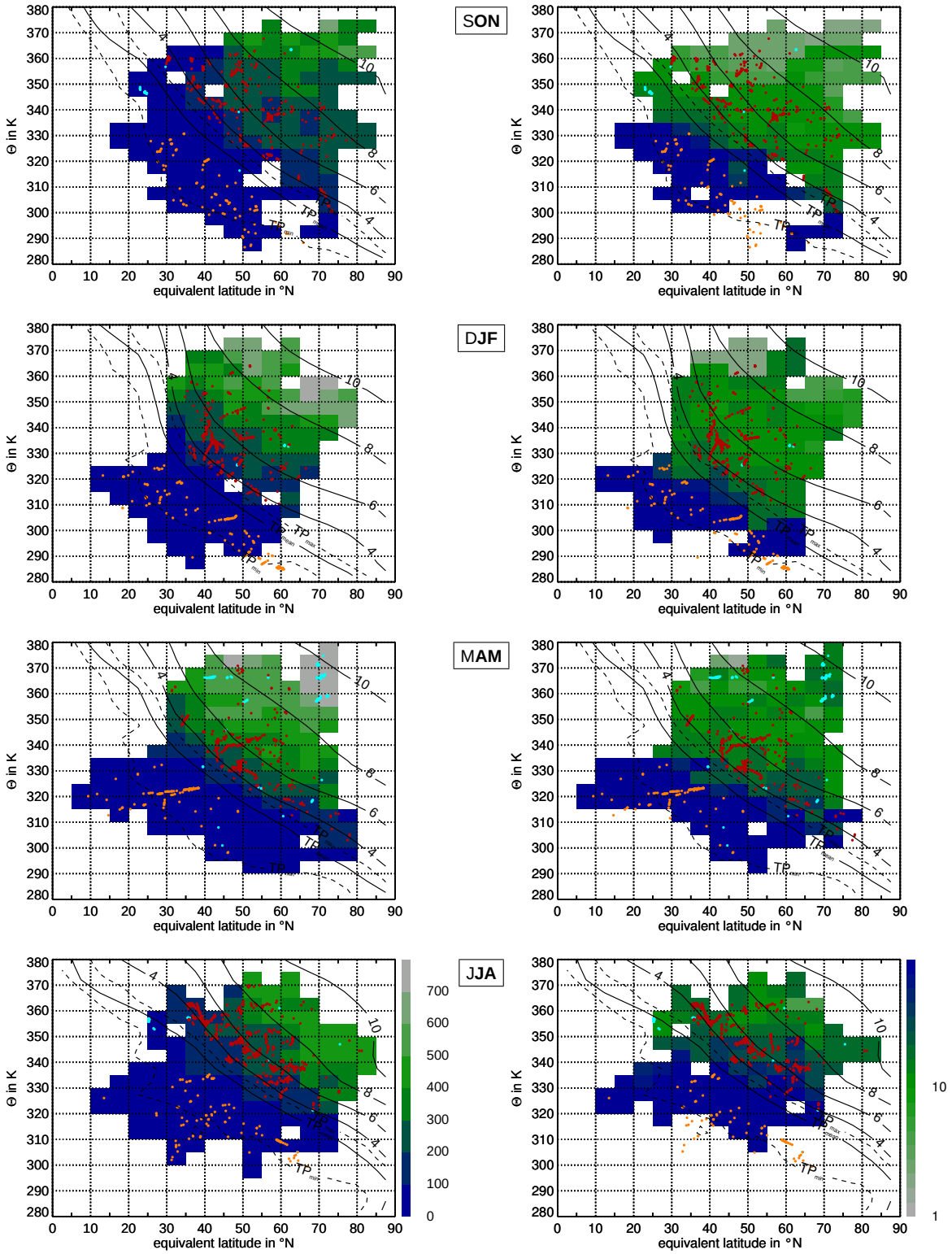

Figure B.1.: As Figure 4.3 but with significant STE trajectories within the previous 20 days.

B.2 30 day backward trajectories

Table B-II: Same as Table 4-II but for 30 day backward trajectories.

		$0°N \leq \varphi_e \leq 30°N$				$30°N < \varphi_e < 60°N$				$60°N \leq \varphi_e \leq 90°N$			
		aut	**win**	**spr**	**sum**	**aut**	**win**	**spr**	**sum**	**aut**	**win**	**spr**	**sum**
	%	**0.1**	-	-	-	4.0	2.7	*2.0*	**5.8**	1.8	*0.5*	1.4	**5.2**
	$\overline{O_3}$	-	-	-	-	*154.5*	207.9	**309.9**	183.3	199.4	*157.8*	**246.1**	225.7
	$\widetilde{O_3}$	-	-	-	-	*145.3*	218.6	**289.4**	167.1	210.9	*154.4*	**236.7**	202.2
	$\overline{H_2O}$	**9.0**	-	-	-	*14.5*	26.2	22.1	**46.9**	22.2	*12.8*	45.0	**78.2**
	$\widetilde{H_2O}$	**9.1**	-	-	-	*9.2*	21.8	20.8	**44.7**	19.2	*11.5*	50.9	**78.6**
	$\overline{IS}$	**53.7**	-	-	-	96.3	*57.2*	102.3	**123.2**	165.4	*67.7*	**180.6**	171.0
	$\widetilde{IS}$	**54.3**	-	-	-	85.6	*45.9*	55.3	**107.5**	166.3	*58.3*	**178.4**	172.3
	$\overline{IS^{min}_{10d}}$	**4.9**	-	-	-	*19.5*	20.5	28.8	**31.5**	49.5	*27.7*	41.7	**58.8**
	$\widetilde{IS^{min}_{10d}}$	**6.1**	-	-	-	*14.3*	17.8	**31.3**	22.8	41.5	*27.4*	36.7	**58.5**
	$\overline{IS^{max}_{10d}}$	**1640.4**	-	-	-	*7493.2*	7955.2	8663.3	**11316.9**	10464.0	*8312.7*	9066.4	**10847.0**
T	$\widetilde{IS^{max}_{10d}}$	**3028.7**	-	-	-	*1624.8*	4528.9	2446.4	**4986.5**	**10571.8**	5174.4	*4648.8*	5500.7
S	$\overline{PV}$	**3.0**	-	-	-	5.1	5.0	**5.2**	*4.8*	5.7	**6.3**	*5.2*	6.2
T	$\widetilde{PV}$	**3.1**	-	-	-	**4.8**	**4.8**	**4.8**	*4.5*	**6.2**	6.0	*4.9*	6.1
	$\overline{PV^{min}_{10d}}$	**<0.1**	-	-	-	*0.2*	*0.2*	**0.3**	*0.2*	**0.4**	**0.4**	*0.3*	*0.3*
	$\widetilde{PV^{min}_{10d}}$	**0.1**	-	-	-	0.1	*<0.1*	**0.3**	0.2	**0.4**	0.3	0.3	*0.2*
	$\overline{PV^{max}_{10d}}$	**3.3**	-	-	-	6.1	*6.0*	**6.8**	6.3	**7.5**	7.1	*6.3*	7.1
	$\widetilde{PV^{max}_{10d}}$	**3.3**	-	-	-	**6.6**	*5.7*	**6.6**	5.9	**7.4**	**7.4**	*6.3*	6.7
	$\overline{LTPC}$	**194.5**	-	-	-	**203.7**	*161.0*	180.1	183.3	265.4	**287.3**	219.8	*163.3*
	$\widetilde{LTPC}$	**290.0**	-	-	-	110.0	129.0	*77.0*	**140.0**	254.0	**358.0**	234.0	*121.0*
	$\overline{NTPC}$	**12.0**	-	-	-	*10.2*	**13.8**	11.2	10.5	*8.4*	11.5	**12.0**	11.3
	$\widetilde{NTPC}$	**13.0**	-	-	-	*7.0*	**9.0**	*7.0*	*7.0*	*5.0*	**9.0**	7.0	**9.0**
	$\overline{DTP}$	**10.9**	-	-	-	**22.4**	*15.9*	16.8	16.4	21.5	**25.3**	16.6	*14.5*
	$\widetilde{DTP}$	**11.2**	-	-	-	**21.1**	13.1	*11.7*	15.0	20.1	**24.2**	*11.4*	11.8
	%	*0.8*	**3.3**	3.0	0.9	**0.7**	0.4	*0.3*	**0.7**	0.1	**0.3**	-	**0.3**
	$\overline{O_3}$	47.5	*45.7*	61.8	**74.7**	59.5	*53.9*	61.5	**75.4**	-	-	-	-
	$\widetilde{O_3}$	47.5	*44.0*	55.9	**78.8**	57.6	*53.7*	56.8	**69.1**	-	-	-	-
	$\overline{H_2O}$	290.2	*193.3*	289.4	**505.8**	295.9	*138.9*	169.8	**394.1**	-	-	-	-
	$\widetilde{H_2O}$	292.0	*201.6*	355.3	**616.5**	291.4	*105.7*	146.6	**334.4**	-	-	-	-
	$\overline{IS}$	*584.2*	870.8	1538.7	**2373.6**	2599.6	1027.2	*502.8*	**4105.1**	3221.7	2176.9	-	**8640.5**
	$\widetilde{IS}$	*453.8*	549.0	456.0	**785.1**	1714.5	428.0	*193.7*	**3124.8**	3245.4	2193.9	-	**8440.2**
	$\overline{IS^{min}_{10d}}$	45.6	*23.4*	39.0	**64.2**	45.9	*24.8*	41.9	**84.1**	47.4	61.5	-	**121.4**
	$\widetilde{IS^{min}_{10d}}$	42.7	*21.8*	36.1	**60.0**	40.3	*24.1*	42.9	**79.1**	49.7	73.3	-	**121.9**
	$\overline{IS^{max}_{10d}}$	*6585.7*	**12253.1**	10000.0	11603.1	9877.5	*6162.4*	**10717.3**	9057.3	6459.7	8722.3	-	**9674.5**
S	$\widetilde{IS^{max}_{10d}}$	*5999.2*	**13409.8**	7934.1	12116.1	**7955.0**	*3488.1*	7442.6	6971.3	6439.8	**12652.1**	-	9341.7
T	$\overline{PV}$	**0.4**	**0.4**	**0.4**	*0.3*	*0.6*	0.7	**0.8**	*0.6*	**0.9**	0.8	-	0.8
T	$\widetilde{PV}$	**0.4**	*0.3*	*0.3*	*0.3*	*0.6*	0.7	**0.8**	*0.6*	**1.0**	0.8	-	0.8
	$\overline{PV^{min}_{10d}}$	*<0.1*	**0.1**	**0.1**	**0.1**	**0.3**	**0.3**	*0.2*	**0.3**	**0.5**	0.3	-	0.4
	$\widetilde{PV^{min}_{10d}}$	*<0.1*	<0.1	**0.2**	**0.2**	**0.3**	**0.3**	*0.2*	**0.3**	**0.5**	0.3	-	0.3
	$\overline{PV^{max}_{10d}}$	**7.4**	6.1	*5.8*	7.0	**7.0**	6.5	*6.1*	6.5	**7.1**	5.6	-	6.6
	$\widetilde{PV^{max}_{10d}}$	**8.2**	6.0	*5.4*	6.0	**7.0**	6.1	*5.5*	6.3	**7.5**	6.2	-	6.5
	$\overline{LTPC}$	356.9	351.2	*144.2*	**437.6**	221.5	172.1	*118.0*	**256.2**	115.0	195.2	-	**311.8**
	$\widetilde{LTPC}$	345.0	371.0	*131.0*	**505.0**	174.0	106.0	*90.0*	**198.0**	69.0	168.0	-	**313.0**
	$\overline{NTPC}$	*8.1*	**16.2**	15.7	9.6	11.3	13.8	**15.0**	*10.8*	9.4	10.2	-	**12.5**
	$\widetilde{NTPC}$	*5.0*	**14.0**	10.0	7.0	*8.0*	10.0	**13.0**	9.0	9.0	9.0	-	**12.0**
	$\overline{DTP}$	*-18.6*	**-11.6**	-12.9	-13.2	*-18.8*	-14.4	**-6.5**	-13.6	-33.5	-25.0	-	**-23.8**
	$\widetilde{DTP}$	*-19.4*	-13.0	**-10.7**	-12.4	*-15.9*	-11.2	**-4.5**	-12.9	-34.4	-25.0	-	**-18.4**

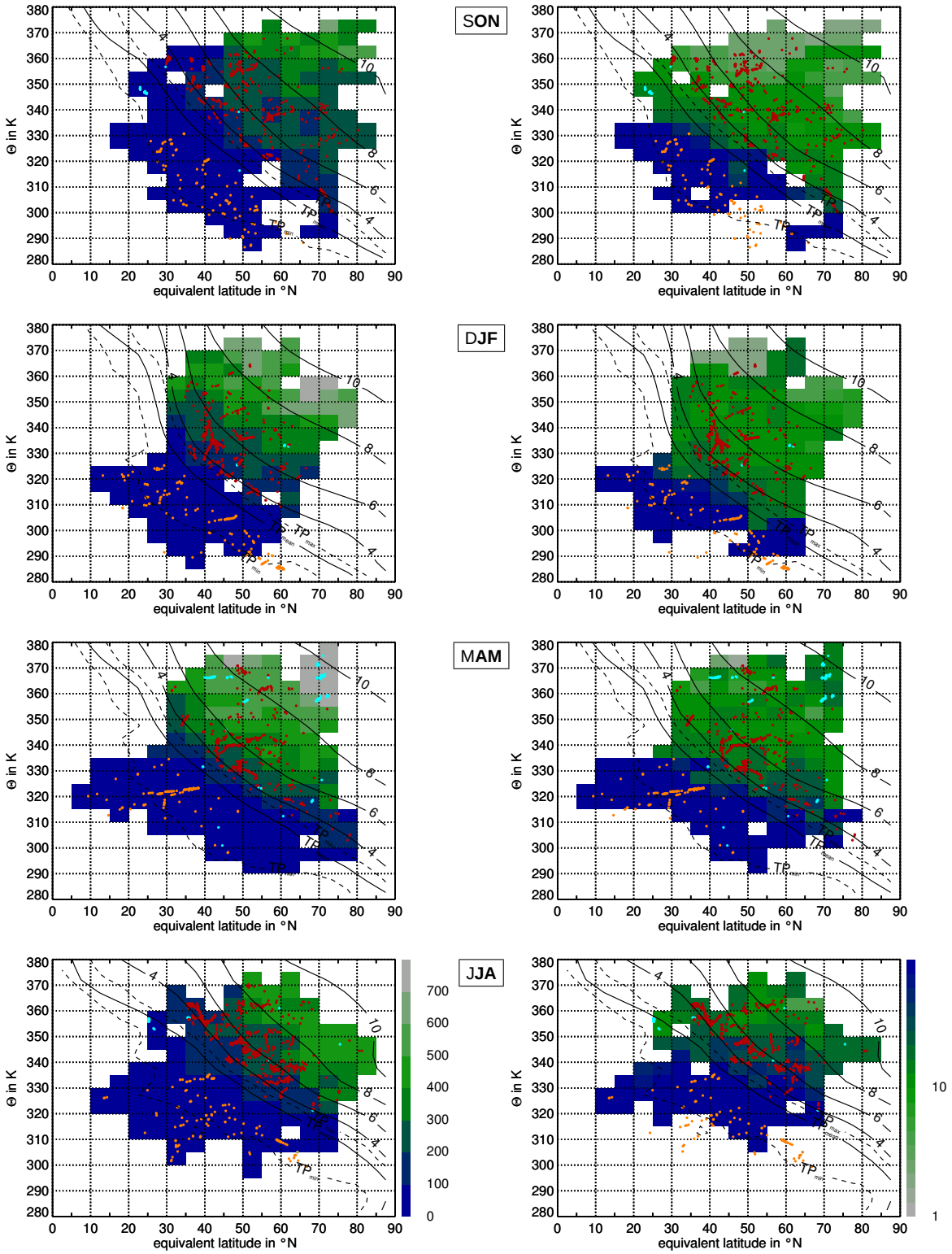

Figure B.2.: As Figure 4.3 but with significant STE trajectories within the previous 30 days.

Appendix C

O_3:H_2O correlations during the POLSTAR 1997/98 and STREAM 1996/97/98 campaigns

In this appendix the correlations used in section 4.3 of *in situ* measured O_3 and H_2O during the POLSTAR $1997/98$ and STREAM $1996/97/98$ campaigns are shown. Thereby, all flight missions are displayed in one scatterplot.

C.1 POLSTAR 1997/98

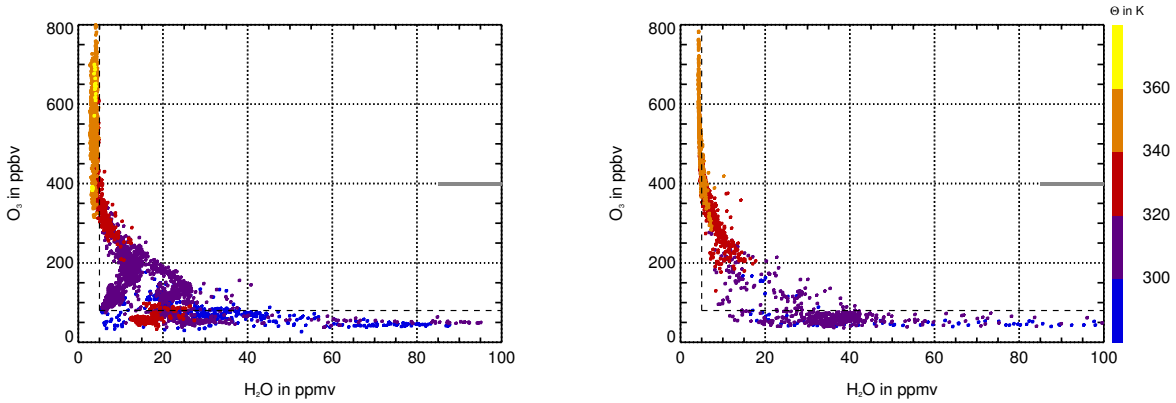

Figure C.1.: Tracer correlations of ozone and total water for the POLSTAR $1997/98$ campaigns. As in Figure 4.7, the horizontal grey bar at the right ordinate in each chart marks the ozone value to which tropospheric air is traceable in the lowermost stratosphere as indicated by total water mixing ratios. The colour coding illustrates the potential temperature in K. (Left: POLSTAR 1997; right: POLSTAR 1998.

C.2 STREAM 1996/97/98

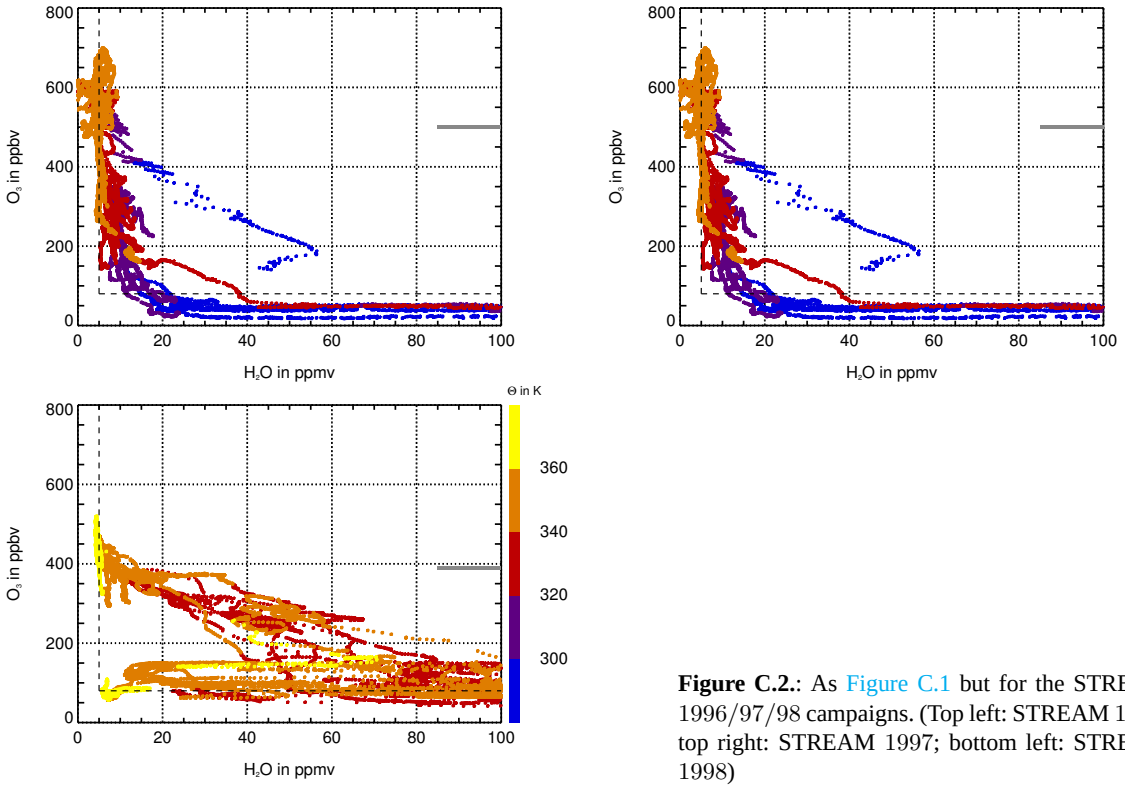

Figure C.2.: As Figure C.1 but for the STREAM 1996/97/98 campaigns. (Top left: STREAM 1996; top right: STREAM 1997; bottom left: STREAM 1998)

Appendix D

Completion of parameters at the tropopause derived from ECMWF analyses

In this part mean parameters at the tropopause during the SPURT time period from August 10, 2001, to July 11, 2003, derived from ECMWF analyses are completed (cf. section 5.2).

Pressure

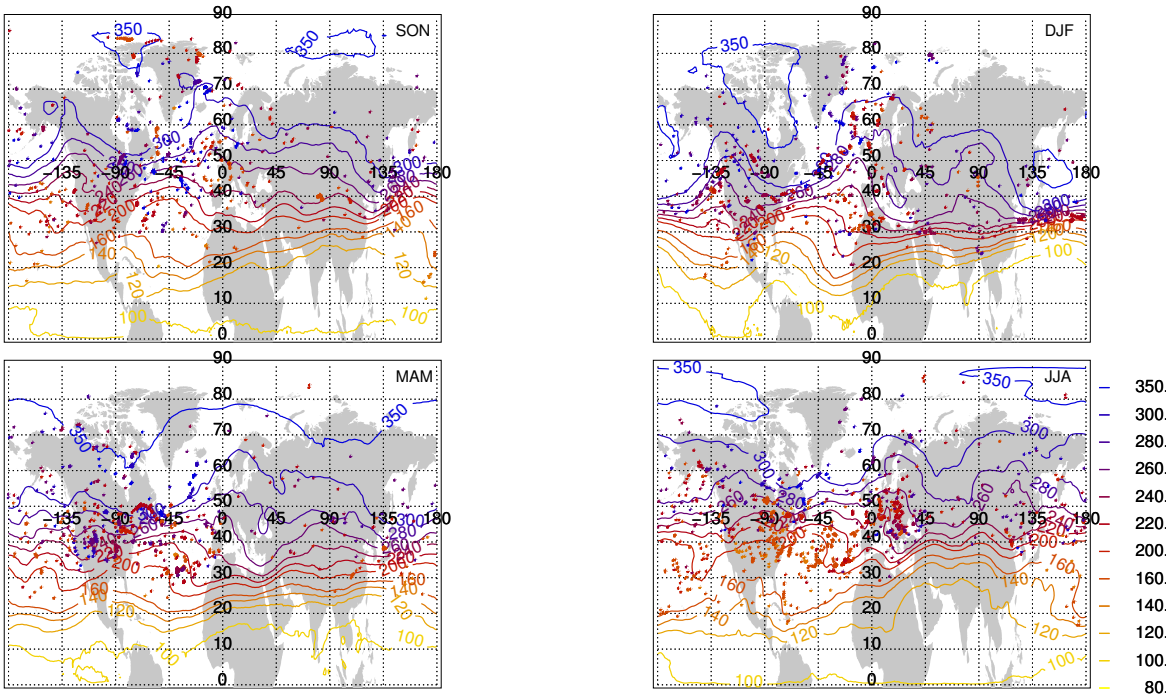

Figure D.1.: Contour fields: pressure p at the tropopause defined by the 2.0 PVU surface (colour coded in hPa). Additionally, locations of last significant tropopause crossings of identified TST trajectories are displayed with p at the exchange location (same colour coding). Clockwise: autumn, winter, summer, and spring.

Geopotential height

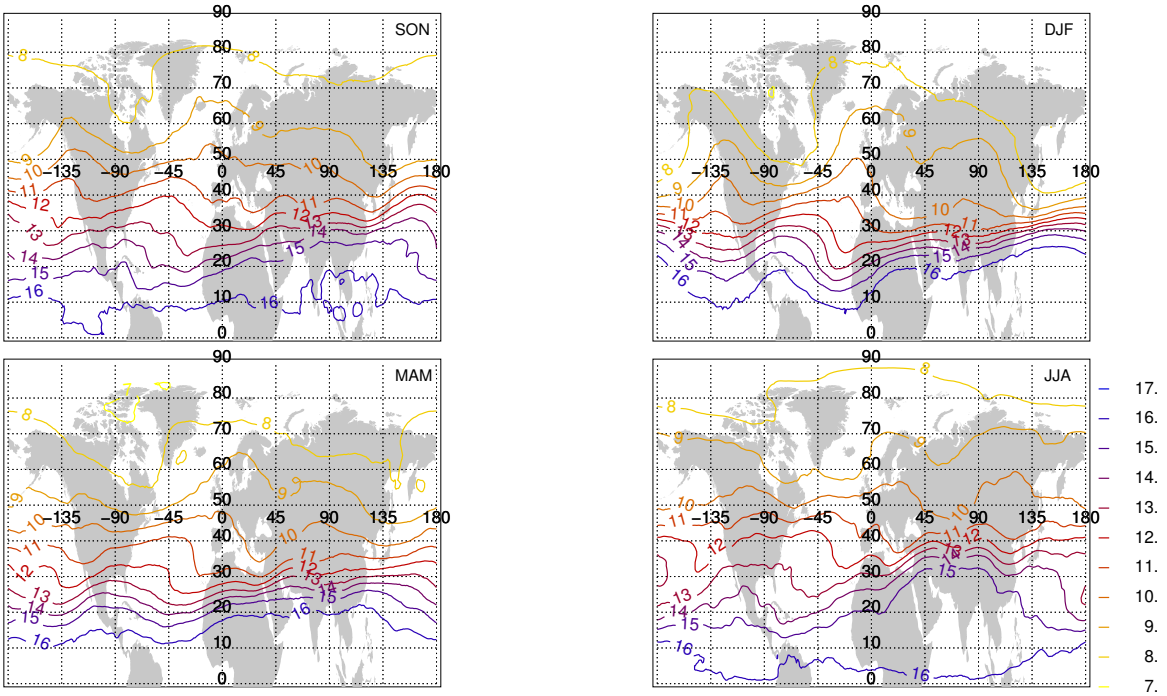

Figure D.2.: Same as Figure D.1 but for geopotential height GPH (colour coded in gpdm).

Potential temperature

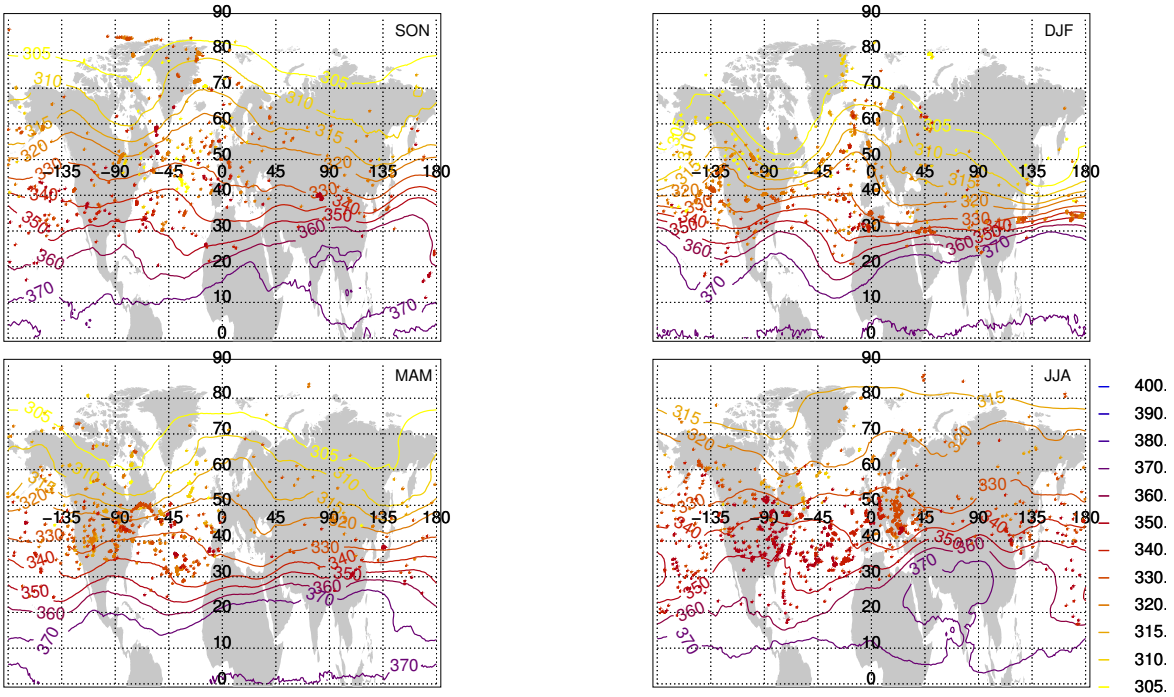

Figure D.3.: Same as Figure D.1 but for potential temperature Θ (colour coded in K).

Ice saturation mixing ratio

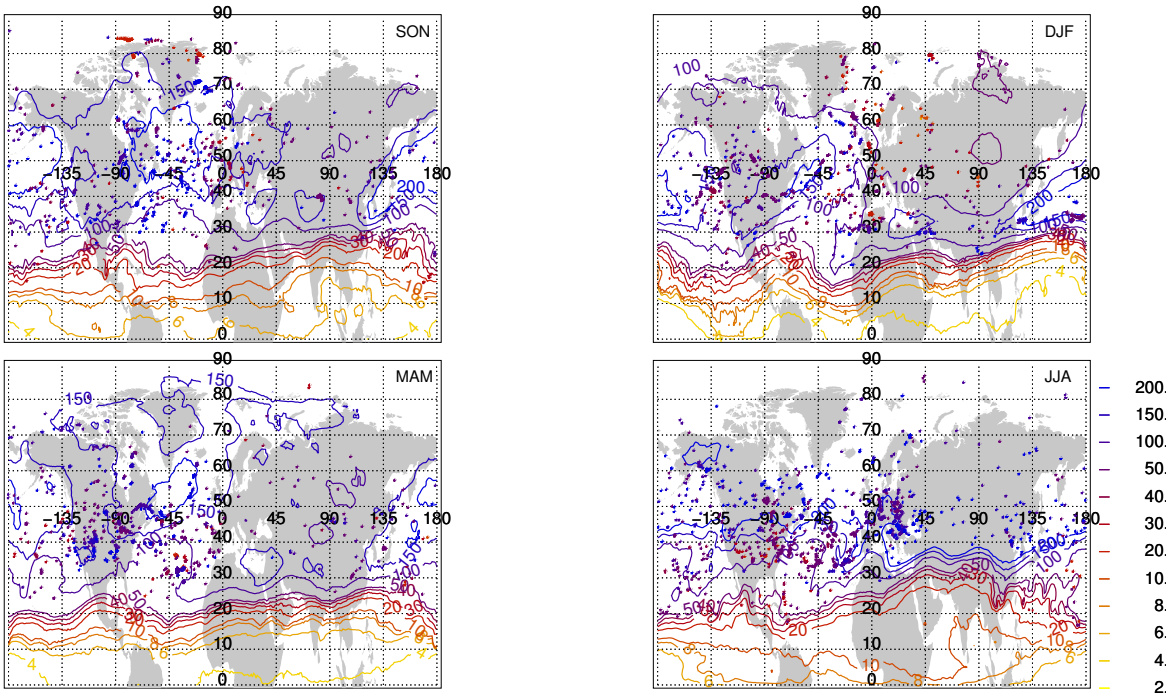

Figure D.4.: Same as Figure D.1 but for ice saturation mixing ratio IS (colour coded in ppmv).

Appendix E

Total water entry values at the extra-tropical tropopause derived from the airborne SPURT measurements

Table E-I: Entry values of total water at the tropopause (H_2O^{TP}, defined at an ozone mixing ratio of 80 ppbv) and the corresponding stratospheric ozone mixing ratio (O_3^{LS}, at a water vapour mixing ratio of 5 ppmv) derived from mixing lines in different potential temperature ranges. For the single mixing lines specific data points are considered. The restrictions for each linear regression are given by the maximum and minimum values of total water, ozone and potential temperature. The abbreviations sb and nb denote southbound and northbound flight directions (dir., only for the SPURT flight missions). An example for deriving the entry values from the mixing lines is displayed in Figure 5.1 for the second mission on May 16, 2002, assigned by an asterisk in the table. A plus sign marks mixing lines not included in Figure 5.2.

campaign	mission	dir.	H_2O^{min}	H_2O^{max}	O_3^{min}	O_3^{max}	Θ^{min}	Θ^{max}	H_2O^{TP}	O_3^{LS}
POLSTAR 1997	0128_1	-	10	15	100	180	300	340	18.2	237.6
POLSTAR 1997	0128_1	-	15	21	150	200	300	320	30.5	204.2
POLSTAR 1997	0128_1	-	15	40	140	200	300	340	32.1	281.2
POLSTAR 1997	0128_1	-	0	15	200	400	320	340	15.9	341.3
POLSTAR 1997	0128_1	-	4	5	300	600	340	360	6.0	259.1
POLSTAR 1997	0130_1	-	10	40	150	300	300	320	51.2	230.2
POLSTAR 1997	0130_1	-	5	15	200	350	300	340	23.8	324.2
POLSTAR 1997	0130_1	-	5	15	200	450	320	340	16.2	388.1
POLSTAR 1997	0130_1	-	0	10	600	800	360	380	8.5	524.5
POLSTAR 1997	0204_1	-	0	40	150	300	300	320	34.7	286.7
POLSTAR 1997	0204_1	-	0	20	200	500	320	340	21.9	353.7
POLSTAR 1997	0204_1	-	4	5	300	500	340	360	5.4	157.0
POLSTAR 1997	0206_1	-	5	10	180	300	300	320	17.4	314.0
POLSTAR 1997	0206_2	-	0	20	200	400	300	320	27.7	321.1
POLSTAR 1997	0206_2	-	0	20	80	400	320	340	18.2	351.0
POLSTAR 1998	0121_1	-	no mixing line inferable							
POLSTAR 1998	0125_1	-	0	8	100	300	340	360	11.7	363.7
POLSTAR 1998	0126_1	-	15	40	80	300	300	320	29.2	280.7
POLSTAR 1998	0126_1	-	0	11	250	400	320	340	16.1	397.4
POLSTAR 1998	0126_2	-	10	15	130	300	300	320	21.2	233.0
POLSTAR 1998	0126_2	-	0	10	200	400	320	340	15.2	400.9
POLSTAR 1998	0126_2	-	0	10	200	400	340	360	13.4	404.0
POLSTAR 1998	0129_1	-	0	40	100	300	280	300	34.3	218.2
POLSTAR 1998	0129_1	-	0	40	100	300	300	320	23.0	275.8
POLSTAR 1998	0129_1	-	0	20	100	400	320	340	19.8	373.0
POLSTAR 1998	0129_1	-	0	10	100	600	340	360	6.7	428.7
POLSTAR 1998	0201_1	-	0	20	200	400	320	340	16.7	382.3
POLSTAR 1998	0201_1	-	0	10	300	600	340	360	6.2	391.8

continued on next page

Table E-I continued from previous page

campaign	mission	dir.	H_2O^{min}	H_2O^{max}	O_3^{min}	O_3^{max}	Θ^{min}	Θ^{max}	H_2O^{TP}	O_3^{LS}
POLSTAR 1998	0204_1	-	0	40	80	300	300	320	34.6	273.3
POLSTAR 1998	0204_1	-	0	15	200	400	320	340	20.7	363.6
POLSTAR 1998	0204_2	-	30	40	80	200	300	320	41.7	259.7
STREAM 1996	0522_1	-	46	60	140	200	300	340	72.9	293.7
STREAM 1996	0522_1	-	46	51	80	100	300	340	51.1	234.4
STREAM 1996	0522_1	-	0	5	300	400	360	380	10.1	288.2
STREAM 1996	0523_1	-	53	65	150	200	300	320	100.6	272.0
STREAM 1996	0523_1	-	0	40	150	250	320	340	76.4	259.7
STREAM 1996	0523_1	-	30	35	100	155	300	340	45.9	263.8
STREAM 1996	0527_1	-	20	40	180	230	330	340	74.3	287.5
STREAM 1996	0527_1	-	15	30	150	200	320	340	62.2	256.2
STREAM 1996	0527_1	-	0	10	200	400	340	360	67.7	303.2
STREAM 1996	0530_1	-	10	40	100	300	300	340	52.1	325.7
STREAM 1996	0530_1	-	5	20	200	400	340	350	28.1	362.0
STREAM 1996	0530_1	-	0	8	200	400	360	380	8.4	266.7
STREAM 1996	0601_1	-	40	60	150	200	300	320	93.1	273.5
STREAM 1996	0601_1	-	15	40	200	400	300	340	60.8	330.3
STREAM 1996	0601_1	-	0	10	200	400	340	360	39.4	354.0
STREAM 1996	0601_1	-	0	10	200	400	360	380	9.0	299.7
STREAM 1997	0314_1	-	10	60	200	450	280	300	73.6	460.9
STREAM 1997	0314_1	-	0	20	250	700	300	320	40.7	355.2
STREAM 1997	0314_1	-	0	20	250	700	320	340	19.7	534.6
STREAM 1997	0321_1	-	0	20	110	150	280	300	22.4	167.8
STREAM 1997	0321_1	-	5	20	100	400	300	320	13.9	425.0
STREAM 1997	0321_1	-	0	20	100	600	320	340	11.7	492.4
STREAM 1997	0323_1	-	9	10	100	150	300	320	11.9	240.1
STREAM 1997	0323_1	-	5	9	100	170	320	340	10.6	357.4
STREAM 1997	0323_1	-	0	10	200	600	340	360	8.2	470.0
STREAM 1997	0325_1	-	21	40	100	200	320	340	40.0	236.8
STREAM 1997	0325_1	-	8	15	310	400	320	340	22.2	393.2
STREAM 1997	0325_1	-	0	5	350	500	340	360	8.5	404.0
STREAM 1998	0703_1	-	45	60	180	230	320	340	87.9	385.0
STREAM 1998	0703_1	-	30	40	100	230	340	360	52.3	423.6
STREAM 1998	0703_1	-	0	5	300	500	360	380	9.1	406.1
STREAM 1998	0705_1	-	no mixing line inferable							
STREAM 1998	0708_1	-	60	75	100	150	320	340	82.0	446.3
STREAM 1998	0708_1	-	35	40	320	350	320	340	72.7	578.4
STREAM 1998	0708_1	-	0	20	400	450	340	360	58.6	437.9
STREAM 1998	0708_1	-	5	7	400	600	360	380	13.0	443.8
STREAM 1998	0712_1	-	38	43	290	310	340	360	96.5	442.4
STREAM 1998	0715_1	-	23	30	80	140	340	360	31.2	275.5
STREAM 1998	0715_2	-	25	45	200	260	320	340	63.8	389.3
SPURT – IOP1	1110_1	sb	10	40	50	400	320	340	40.1	206.1
SPURT – IOP1	1110_1	sb	10	40	50	400	340	360	33.3	563.8
SPURT – IOP1	1110_1+	sb	15	30	50	800	360	380	63.5	713.2
SPURT – IOP1	1110_1	sb	0	5	50	800	360	380	7.3	304.0
SPURT – IOP1	1110_2	sb	40	75	50	200	320	340	60.2	113.6
SPURT – IOP1	1110_2	sb	15	25	50	200	340	360	16.8	124.6
SPURT – IOP1	1111_1	nb	0	40	50	400	300	340	32.4	274.2
SPURT – IOP1	1111_1	nb	20	45	50	200	330	340	41.4	124.2
SPURT – IOP1	1111_1	nb	0	20	50	400	340	360	22.0	312.7
SPURT – IOP1	1111_1	nb	0	10	200	600	360	380	6.2	306.2
SPURT – IOP1	1111_2	nb	0	20	200	300	300	340	42.9	305.9
SPURT – IOP1	1111_2	nb	10	20	100	200	300	340	49.9	177.2
SPURT – IOP1	1111_2	nb	0	8	50	600	340	360	10.7	297.9
SPURT – IOP1	1111_2	nb	0	30	50	600	360	380	5.8	236.9
SPURT – IOP2	0117_1	sb	15	20	150	250	330	340	22.0	468.4
SPURT – IOP2	0117_1	sb	10	15	80	200	320	340	17.3	327.2
SPURT – IOP2	0117_1	sb	5	9	40	400	340	360	16.6	393.6
SPURT – IOP2	0117_2	sb	24	28	120	200	320	340	33.1	325.3
SPURT – IOP2	0117_2	sb	15	25	50	150	320	340	25.1	273.9
SPURT – IOP2	0118_1	sb	25	40	80	150	320	340	36.6	113.9
SPURT – IOP2	0118_1	sb	5	30	80	300	320	340	30.2	225.5
SPURT – IOP2	0118_1	sb	9	12	100	210	340	360	15.0	292.8

continued on next page

Table E-I continued from previous page

campaign	mission	dir.	H_2O^{min}	H_2O^{max}	O_3^{min}	O_3^{max}	Θ^{min}	Θ^{max}	H_2O^{TP}	O_3^{LS}
SPURT – IOP2	0118_2	sb	14	19	80	150	330	340	21.9	161.3
SPURT – IOP2	0119_1	nb	0	40	120	200	310	340	51.2	192.5
SPURT – IOP2	0119_1	nb	0	40	120	300	310	340	37.4	272.8
SPURT – IOP2	0119_1	nb	15	20	250	600	340	360	24.6	744.5
SPURT – IOP2	0119_1	nb	5	8	250	700	340	360	9.0	607.6
SPURT – IOP2	0119_2	nb	7	10	200	400	330	340	15.4	445.4
SPURT – IOP2	0119_2	nb	13	17	150	210	320	340	22.9	336.4
SPURT – IOP2	0119_2	nb	0	7	200	600	350	360	8.0	302.7
SPURT – IOP2	0119_2	nb	0	20	50	700	360	380	6.3	309.1
SPURT – IOP3	0516_1	sb	25	40	190	300	330	340	48.6	449.3
SPURT – IOP3	0516_1	sb	15	25	80	110	340	350	27.8	150.5
SPURT – IOP3	0516_1	sb	18	22	200	400	340	350	27.0	801.6
SPURT – IOP3	0516_1	sb	14	16	50	300	340	360	19.1	503.3
SPURT – IOP3	0516_2*	sb	30	60	80	200	330	340	53.5	199.2
SPURT – IOP3	0516_2*	sb	10	30	100	300	340	360	35.8	369.4
SPURT – IOP3	0516_2*	sb	8	20	450	700	340	360	24.4	680.5
SPURT – IOP3	0516_2*	sb	0	7	300	700	350	360	17.8	552.8
SPURT – IOP3	0516_2*	sb	0	4	400	700	360	380	9.6	403.1
SPURT – IOP3	0517_1	nb	40	80	0	200	300	340	75.2	306.4
SPURT – IOP3	0517_1	nb	0	40	80	800	300	340	36.6	507.3
SPURT – IOP3	0517_1	nb	0	40	80	800	340	360	32.9	551.6
SPURT – IOP3	0517_1	nb	10	18	300	600	340	360	30.3	576.1
SPURT – IOP3	0517_1	nb	0	40	80	800	360	380	6.5	302.5
SPURT – IOP3	0517_2	nb	18	40	80	450	320	330	42.7	615.7
SPURT – IOP3	0517_2	nb	20	35	80	150	340	350	33.7	262.9
SPURT – IOP3	0517_2	nb	0	40	80	700	340	360	30.3	551.0
SPURT – IOP3	0517_2	nb	0	8	80	700	360	380	17.7	522.6
SPURT – IOP4	0822_1	sb	90	100	100	150	320	340	103.9	535.5
SPURT – IOP4	0822_1	sb	50	70	200	300	340	350	88.4	546.5
SPURT – IOP4	0822_1	sb	47	50	180	200	350	360	82.1	337.1
SPURT – IOP4	0822_2	sb	80	100	100	200	320	340	109.0	290.3
SPURT – IOP4	0822_2	sb	20	100	80	500	340	360	87.5	295.4
SPURT – IOP4	0822_2	sb	26	32	150	400	360	380	37.2	999.1
SPURT – IOP4	0823_1	nb	no valid H_2O data							
SPURT – IOP4	0823_2	nb	no valid H_2O data							
SPURT – IOP5	1017_1	sb	5	20	50	300	320	340	27.0	264.1
SPURT – IOP5	1017_1	sb	8	20	130	300	340	360	18.1	259.5
SPURT – IOP5	1017_1	sb	0	20	50	120	340	360	17.6	151.8
SPURT – IOP5	1017_1	sb	0	8	140	180	350	360	9.4	164.6
SPURT – IOP5	1017_2	sb	14	30	50	250	310	340	26.7	354.1
SPURT – IOP5	1017_2	sb	10	11	150	250	340	350	27.8	262.3
SPURT – IOP5	1017_2	sb	0	10	50	400	360	380	6.3	211.0
SPURT – IOP5	1018_1	nb	23	40	100	250	300	340	45.4	319.6
SPURT – IOP5	1018_1	nb	15	25	150	300	340	350	25.4	365.1
SPURT – IOP5	1018_1	nb	0	6	150	280	360	380	7.8	289.3
SPURT – IOP5	1018_2	nb	20	25	220	260	330	340	48.3	334.8
SPURT – IOP5	1018_2	nb	10	25	80	400	340	360	24.2	385.3
SPURT – IOP5	1018_2	nb	6	8	200	400	350	360	12.5	338.7
SPURT – IOP5	1018_2	nb	0	20	80	600	360	380	6.3	274.2
SPURT – IOP6	0215_1	sb	40	60	50	800	310	340	50.6	1136.0
SPURT – IOP6	0215_1	sb	20	30	50	200	310	340	30.4	448.7
SPURT – IOP6	0215_2	sb	30	40	100	220	300	320	43.5	563.4
SPURT – IOP6	0215_2	sb	30	35	200	500	320	340	36.4	1199.4
SPURT – IOP6	0215_2	sb	0	20	80	400	310	340	22.6	750.3
SPURT – IOP6	0216_1	nb	20	38	50	110	320	340	41.8	118.0
SPURT – IOP6	0216_1	nb	10	18	200	400	340	350	29.8	520.1
SPURT – IOP6	0216_1	nb	20	30	150	400	340	350	39.9	568.2
SPURT – IOP6	0216_2	nb	0	22	50	400	300	340	25.4	386.8
SPURT – IOP6	0216_2	nb	20	40	200	400	330	340	35.1	650.6
SPURT – IOP6	0216_2	nb	12	15	350	650	340	350	22.0	1053.1
SPURT – IOP6	0216_2	nb	0	20	50	800	350	360	15.6	857.1
SPURT – IOP6	0216_3	nb	30	40	200	400	310	340	53.1	500.8
SPURT – IOP6	0216_3	nb	27	35	150	250	330	340	32.9	714.4
SPURT – IOP6	0216_3	nb	13	17	180	300	330	340	23.5	482.3

continued on next page

Table E-I continued from previous page

campaign	mission	dir.	H_2O^{min}	H_2O^{max}	O_3^{min}	O_3^{max}	Θ^{min}	Θ^{max}	H_2O^{TP}	O_3^{LS}
SPURT – IOP6	0216_3	nb	17	20	200	600	350	360	25.1	902.7
SPURT – IOP7	0427_1	nb	20	40	200	500	310	340	57.6	680.7
SPURT – IOP7	0427_1	nb	60	80	250	500	310	340	83.4	1166.2
SPURT – IOP7	0427_1	nb	20	25	400	800	340	350	38.3	1277.0
SPURT – IOP7	0427_1	nb	40	42	400	600	340	350	55.0	1675.3
SPURT – IOP7	0427_1	nb	29	31	500	1000	360	380	51.8	1806.3
SPURT – IOP7	0427_2	nb	65	100	120	200	300	320	121.1	238.2
SPURT – IOP7	0427_2	nb	5	20	200	600	300	340	23.5	690.1
SPURT – IOP7	0427_2	nb	27	33	200	400	310	340	43.8	792.6
SPURT – IOP7	0427_2	nb	31	37	340	400	330	340	51.9	818.1
SPURT – IOP7	0427_2	nb	38	55	350	500	330	340	94.8	687.8
SPURT – IOP7	0428_1	sb	5	80	80	700	320	340	73.8	261.7
SPURT – IOP7	0428_1	sb	20	30	80	400	320	340	35.8	652.5
SPURT – IOP7	0428_1	sb	20	25	100	240	340	350	26.5	954.1
SPURT – IOP7	0428_1	sb	5	20	460	700	350	360	20.2	757.0
SPURT – IOP7	0428_2	sb	15	25	200	300	320	340	35.2	487.7
SPURT – IOP7	0428_2	sb	5	40	80	700	320	340	39.7	540.3
SPURT – IOP7	0428_2	sb	0	30	80	700	340	360	35.4	564.5
SPURT – IOP7	0428_2	sb	5	9	400	700	350	360	21.6	581.9
SPURT – IOP7	0428_2	sb	0	6	400	700	360	380	10.1	613.9
SPURT – IOP7	0429_1	nb	30	80	80	210	310	340	80.9	300.9
SPURT – IOP7	0429_1	nb	55	58	240	280	310	340	81.5	639.2
SPURT – IOP7	0429_1	nb	35	40	400	800	350	360	63.4	1048.7
SPURT – IOP7	0429_1	nb	27	28	400	800	360	380	44.0	1181.2
SPURT – IOP8	0709_1	sb	5	150	80	500	320	340	131.0	353.4
SPURT – IOP8	0709_1	sb	25	50	50	400	340	350	50.6	584.5
SPURT – IOP8	0709_1	sb	10	15	50	350	350	360	14.8	383.3
SPURT – IOP8	0709_1	sb	5	10	80	500	360	380	11.0	403.4
SPURT – IOP8	0709_2	sb	20	80	80	400	320	340	72.4	371.3
SPURT – IOP8	0709_2	sb	35	45	100	150	340	350	56.9	217.1
SPURT – IOP8	0709_2	sb	11	12	300	400	350	360	22.3	477.2
SPURT – IOP8	0709_2	sb	0	4	50	500	360	380	9.4	324.8
SPURT – IOP8	0710_1	nb	50	60	300	350	320	340	89.5	637.9
SPURT – IOP8	0710_1	nb	39	50	350	500	340	350	76.9	806.6
SPURT – IOP8	0710_1	nb	20	23	400	600	360	380	40.4	870.4
SPURT – IOP8	0710_2	nb	40	60	400	500	320	340	118.7	638.8
SPURT – IOP8	0710_2	nb	52	60	250	350	330	340	81.0	763.0
SPURT – IOP8	0710_2	nb	20	35	400	600	350	360	54.8	1067.6

Abbreviations and symbols

Organisations and institutes

abbreviation	standing
BMBF	Bundesministerium für Bildung und Forschung (German Ministry for Education and Research)
ECMWF	European Centre for Medium-Range Weather Forecasts
EU	European Union
FZJ	Forschungszentrum Jülich GmbH (Research Centre Jülich)
GFD	Gesellschaft für Flugzieldarstellung
GmbH	Gesellschaft mir beschränkter Haftung (limited liability company)
IACETH	Institute for Atmospheric and Climate Science of the Swiss Federal Institute of Technology Zürich
ICG-I	Institut for Chemistry and Dynamics of the Geosphere I: Stratosphere
IPCC	Intergovernmental Panel on Climate Change
JWGU	Institute for Meteorology and Geophysics, Johann Wolfgang Goethe University of Frankfurt/Main
MPI	Max Planck Institute for Chemistry Mainz
SPARC	Stratospheric Processes and their Role in Climate
WMO	World Meteorological Organization

Aircraft measurement campaigns and programs

abbreviation	standing
AFO2000	Atmosphärenforschung 2000 (federal atmospheric research 2000)
CARIBIC	civil aircraft for the regular investigation of the atmosphere based on an instrument container

continued on next page

continued from previous page

abbreviation	standing
CONTRACE	convective transport of trace gases into the middle and upper troposphere over Europe
MOZAIC	measurement of ozone on airbus in-service aircraft
POLSTAR	polar stratospheric aerosol experiment
SPURT	Spurenstofftransport in der Tropopausenregion (trace gas transport in the tropopause region)
STREAM	stratosphere-troposphere experiment by aircraft measurements
UTOPIHAN-ACT	upper tropospheric ozone: processes involving HO_x and NO_x, the impact of aviation and convectively transported pollutants in the tropopause region

Instruments and measurement principles

abbreviation	standing
CL	chemiluminescence
CLD 790 SR	sensitivity analyser for measuring reactive nitrogen (NO_y), nitrogen monoxide NO), and ozone (O_3) simultaneously
ERBS	Earth Radiation Budget Satellite
FISH	fast *in situ* stratospheric hygrometer
GC	gas chromatography
GHOST II	gas chromatograph for the observation of stratospheric tracer
HALO	high altitude and long range research aircraft
HALOE	Halogen Occultation Experiment
JOE	Jülich ozone experiment
LiCor-6262	instrument to measure primarily CO_2
LIDAR	Light detection and ranging
Ly-α	Lyman-α fluorescence
NDIR	non-dispersive infrared-absorption
POAM	Polar Ozone and Aerosol Measurement (POAM)
SAGE II	stratospheric aerosol and gas experiment II
TDLAS	tunable diode laser
TRISTAR	tracer in situ TDLAS for atmospheric research
UVA	UV absorption

Acronyms

abbreviation	standing
CASL	contour-advective semi-Lagrangian algorithm

continued on next page

continued from previous page

abbreviation	standing
CLaMS	chemical Lagrangian model of the stratosphere
CPT	could point tropopause
CSRT	clear sky radiative tropopause
CTM	chemistry transport model
DJF	December, January, and February (winter season)
DL	length of day in s
DTP	distance from tropopause
DWT	downward transport
FLEXPART	Lagrangian particle dispersion model
HP	hygropause
IOP	intensive operation phase
JJA	June, July, and August (summer season)
LAGRANTO	Lagrangian analyses tool
LMS	lowermost stratosphere
LRT	lapse rate tropopause
LS	lower stratosphere
LSTPC	last significant tropopause crossing
LTPC	last tropopause crossing
MAM	March, April, and May (spring season)
ML	(extra-tropical) mixing layer
NTPC	number of tropopause crossings
OHP	Observatoire de Haute Provence
PJ	polar jet
PDF	probability distribution function
RDF	reverse domain filling
SJ	sub-tropical jet
SH	specific humidity
SON	September, October, and November (autumn season)
STE	stratosphere-troposphere exchange
STR	stratosphere
STT	secondary tropical tropopause (only in section 3.1)
STT	stratosphere-to-troposphere transport
TD	touch down
TO	take off

continued on next page

continued from previous page

abbreviation	standing
TP	tropopause
TP_{tinych}	chemically defined tropopause
TP_{tinyth}	tropopause defined by the temperature lapse rate
TPR	tropopause region
TR	time resolution
TRO	troposphere
TST	troposphere-to-stratosphere transport
TTL	tropical transition layer
TTT	tropical thermal tropopause
UT	upper troposphere
UTC	coordinated universal time
UV	ultraviolet
UWT	upward transport
VMR	volume mixing ratio
VOC	volatile organic compounds

Symbols

abbreviation	standing
°N	degree north
$\partial T/\partial z$	temperature lapse rate
ζ	relative vorticity
κ	Poisson constant, adiabatic exponent (≈ 0.286)
λ	geographical longitude
λ_c	critical Lyapunov exponent
μ, $\triangle\mu$	ambiguous letter for any field that shows a mean monotonic decrease or increase with latitude on a given isentrope (cf. section 4.1)
$\mu^{e}_{H_2O}$	H_2O entry value at the tropopause
ξ	ambiguous letter for any parameter at the tropopause
π	universal constant of the circle (≈ 3.141)
φ	geographical latitude
φe	equivalent latitude
Θ, $\triangle\Theta$	potential temperature, distance to the local tropopause in K
$\dot{\Theta}$	isentropic vertical velocity
ϱ	Spearman's rank correlation coefficient

continued on next page

continued from previous page

abbreviation	standing
τ_{cross}	time for crossing the tropopause
τ_{s}	residence time in the stratosphere
τ_{t}	residence time in the troposphere
ω	vertical velocity in the pressure system
$A(\mu_q)$	area enclosed by the value μ_q on a considered isentrope
ClO	chlorine monoxide
$ClONO_2$	chlorine nitrate
CFC	chlorofluorocarbon
CFC11	$CFCl_3$
CFC12	CF_2Cl_2
CH_4	methane
CO	carbon monoxide
CO_2	carbon dioxide
c_{p}	specific heat constant and constant pressure (1004 J kg^{-1} K^{-1})
D	total number of data points
d_t	total time derivative
e_{sat}	saturation water vapour pressure
FF, $\triangle$FF	horizontal wind velocity, wind speed difference to the jet stream maximum wind speeds
f	coriolis parameter
g	acceleration of gravity (9.81 m s^{-1})
GPH	geopotential height
H_2O	total water
H_2O_{OBS}	observed total water (not corrected to anisokinetic sampling)
HCl	hydrogen chloride
HO_x	reactive hydrogen
IS	ice saturation mixing ratio
N, N_i	number of bins, elements in the i$^{\text{th}}$ bin
N_2O	nitrous oxide
NO	nitric oxide
NO_x	$NO+NO_2+NO_3$
NO_y	reactive nitrogen
O_3	ozone

continued on next page

continued from previous page

abbreviation	standing
OH	hydroxyl radical
p	pressure
p_0	constant reference pressure (1000 hPa)
ppbv	parts per billion volume
ppmv	parts per million volume
PV	potential vorticity
PVU	potential vorticity unit $10^{-6} m^2 s^{-1} K kg^{-1}$
R	individual gas constant of dry air (287.04 J kg^{-1} K^{-1})
RH_{ice}	relative humidity with respect to ice
r	Pearson's rank correlation coefficient
r_e	radius of the Earth
SE	Shannon entropy
$SF6$	sulfur hexafluoride
T	temperature
t	time
U_0	velocity of the free flow
U	flow velocity inside the inlet
u	wind component in easterly direction
v	wind component in northern direction
x	x-coordinate
x	ambiguous letter for any parameter (cf. page 47)
$\bar{x}$	mean value of any parameter (on page 47)
x_i	ambiguous letter for any parameter (on page 47)
y	y-coordinate
y	ambiguous letter for any parameter (cf. page 47)
$\bar{y}$	mean value of any parameter (on page 47)
y_i	ambiguous letter for any parameter (on page 47)
z	z-coordinate

References

Ackerman, M., D. Frimout, C. Muller, and D. J. Wuebbles: 1979, 'Stratospheric methane measurements and predictions'. *Pure Appl. Geophys.* **117**, 367–380. 29

Ancellet, G., and M. Beekmann: 1997, 'Evidence for changes in ozone concentrations in the free troposphere over southern France from 1976–1995'. *Atmos. Env.* **31**, 2835–2851. 26

Ancellet, G., M. Beekmann, and A. Papayannis: 1994, 'Impact of a cutoff low development on downward transport of ozone in the troposphere'. *J. Geophys. Res.* **99**, 3451–3468. 105

Ancellet, G., J. Pelon, M. Beekmann, A. Papayannis, and G. Mégie: 1991, 'Ground-based studies of ozone exchanges between the stratosphere and the troposphere'. *J. Geophys. Res.* **96**, 22401–22421. 5, 105

Appenzeller, C., H. C. Davies, and W. A. Norton: 1996a, 'Fragmentation of stratospheric intrusions'. *J. Geophys. Res.* **101**(D1), 1435–1456. 5, 29, 124

Appenzeller, C., J. H. Holton, and K. H. Rosenlof: 1996b, 'Seasonal variation of mass transport across the tropopause'. *J. Geophys. Res.* **101**(D10), 15071–15078. 23, 36, 37, 54, 59, 105, 142

Appenzeller, C., A. K. Weiss, and J. Staehelin: 2000, 'North Atlantic Oscillation modulates Total Ozone Winter Trends'. *Geophys. Res. Lett.* **27**(8), 1131–1134. 75

Austin, J. F., and M. J. Follows: 1991, 'The ozone record at Payerne: an assessment of the cross-tropopause flux'. *Atmos. Env.* **25A**, 1873–1880. 27, 138

Ayers, G. P., H. Granek, and R. Boers: 1997, 'Ozone in the marine boundary layer at Cape Grim: Model Simulation'. *J. Atmos. Chem.* **27**, 179–195. 26

Bamber, D. J., P. G. W. Healy, B. M. R. Jones, S. A. Penkett, A. F. Tuck, and G. Vaughan: 1984, 'Vertical profiles of tropospheric gases: Chemical consequences of stratospheric intrusions'. *Atmos. Env.* **18**, 1759–1766. 105

Baray, J.-L., G. Ancellet, T. Randriambelo, and S. Baldy: 1999, 'Tropical cyclone Marlene and stratosphere-troposphere exchange'. *J. Geophys. Res.* **104**(D11), 13953–13970. 5

Baray, J.-L., V. Daniel, G. Ancellet, and B. Legras: 2000, 'Planetary-scale tropopause folds in the southern subtropics'. *Geophys. Res. Lett.* **27**(3), 353–356. 5

Beekmann, M., G. Ancellet, S. Blonsky, D. De Muer, A. Ebel, H. Elbern, J. Hendricks, J. Kowol, C. Mancier, R. Sladkovic, H. G. J. Smit, P. Speth, T. Trickl, and P. van Haver: 1997, 'Regional and Global Tropopause Fold Occurence and Related Ozone Flux Across the Tropopause'. *J. Atmos. Chem.* **28**, 29–44. 81, 105

Beekmann, M., G. Ancellet, and Mégie: 1994, 'Climatology of tropospheric ozone in southern Europe and its relation to potential vorticity'. *J. Geophys. Res.* **99**(D6), 12841–12853. 26, 27, 28, 38, 105, 107, 138

Bethan, S., G. Vaughan, and S. J. Reid: 1996, 'A comparison of ozone and thermal tropopause heights and the impact of tropopause definition on quantifying the ozone content of the troposphere'. *Quart. J. R. Met. Soc.* **122**, 929–944. 22, 23, 24, 25, 54, 70, 87, I

Beuermann, J.: 2000, 'Einfluss von Transportprozessen auf die Wasserdampfverteilung in der Tropopausenregion'. PhD, Rheinische Friedrich-Wilhelms-Universität Bonn. 72, 117

Beuermann, J., P. Konopka, D. Brunner, O. Bujok, G. Günther, D. S. McKenna, J. Lelieveld, R. Müller, and C. Schiller: 2002, 'High-resolution measurements and simulation of stratospheric and tropospheric intrusions in the vicinity of the polar jet stream'. *Geophys. Res. Lett.* **29**(12), doi: 10.1029/2001GL014162. 116

Beyerle, G., H.-J. Schäfer, R. Neuber, O. Schrems, and I. S. McDermid: 1998, 'Dual wavelength lidar observations of tropical high-altitude cirrus clouds during the ALBATROSS 1996 campaign'. *Geophys. Res. Lett.* **25**(6), 919–922. 102

Bithell, M., L. J. Gray, and B. D. Cox: 1999, 'A three-dimensional view of the evolution of midlatitude stratospheric intrusions'. *J. Atmos. Sci.* **56**, 673–688. 5, 23

Boering, K. A., E. J. Hintsa, S. C. Wofsy, J. G. Anderson, B. C. Daube Jr., A. E. Dessler, M. Loewenstein, M. P. McCormick, J. R. Podolske, E. M. Weinstock, and G. K. Yue: 1995, 'Measurements of stratospheric carbon dioxide and water vapor at northern midlatitudes: Implications for troposphere-to-stratosphere transport'. *Geophys. Res. Lett.* **22**(20), 2737–2740. 29

Bönisch, H.: 2004. personal communication. 135, 139

Bourqui, M. S.: 2004, 'Stratosphere-to-troposphere exchange from the Lagrangian perspective: a case study and method sensitivities'. *Atmos. Chem. Phys. Discuss.* **4**, 3249–3284. 53, 60, 61

Bregman, A., J. Lelieveld, M. M. P. van den Broek, P. C. Siegmund, H. Fischer, and O. Bujok: 2000, 'N_2O and O_3 relationships in the lowermost stratosphere: A diagnostic for mixing processes as presented by a three-dimensional chemistry-transport model'. *J. Geophys. Res.* **105**(D13), 17279–17290. 2

Brennikmeijer, C. A. M., F. Slemr, C. Koeppel, D. S. Scharffe, M. Pupek, J. Lelieveld, P. Crutzen, A. Zahn, D. Sprung, H. Fischer, M. Hermann, M. Reichelt, J. Heintzenberg, H. Schlager, H. Ziereis, U. Schumann, B. Dix, U. Platt, R. Ebinghaus, B. Martinsson, P. Ciais, D. Filippi, M. Leuenberger, D. Oram, S. Penkett, P. van Velthoven, and A. Waibel: 2005, 'Analyzing Atmospheric Trace Gases and Aerosols Using Passenger Aircraft'. *EOS* **86**(8). 10

Brewer, A. W.: 1949, 'Evidence for a world circulation provided by measurement of helium and water vapor in the stratosphere'. *Quart. J. R. Met. Soc.* **75**, 351–363. 3, 30

Browell, E., E. Danielsen, S. Ismail, G. G, and R. Beck: 1987, 'Tropopause fold structure determined from airborne Lidar and in situ measurements'. *J. Geophys. Res.* **92**, 2112–2120. 24, 107

Bujok, O.: 1998, 'In-situ-Messung langlebiger Spurengase in der untersten Stratosphäre: Entwicklung und Anwendung einer flugzeuggestützten gaschromatischen Nachweismethode'. PhD, Rheinische Friedrich-Wilhelms-Universität Bonn. Berichte des Forschungszentrums Jülich, 3517. 72, 116

Bujok, O., V. Tan, E. Klein, R. Nopper, R. Bauer, A. Engel, M.-T. Gerhards, A. Afchine, D. S. McKenna, U. Schmidt, F. G. Wienhold, and H. Fischer: 2001, 'GHOST - A Novel Airborne Gas Chromatograph for In Situ Measurements of Long-lived Tracers in the Lower Stratosphere: Method and Applications'. *J. Atmos. Chem.* **39**(1), 37–64. doi: 10.1023/A:1010789715871. 13

Butchart, N., and E. E. Remsberg: 1986, 'The area of stratospheric polar vortex as a diagnostic for tracer transport on an isentropic surface'. *J. Atmos. Sci.* **43**, 1319–1339. 51

Chameides, W. L., and J. C. G. Walker: 1973, 'A photochemical theory for tropospheric ozone'. *J. Geophys. Res.* **78**, 8751–8760. 25

Chen, P.: 1995, 'Isentropic cross-tropopause mass exchange in the extratropics'. *J. Geophys. Res.* **100**(D8), 16661–16673. 3, 28, 79, 133

Crutzen, P. J.: 1973, 'A discussion of the chemistry of some minor constituents in the stratosphere and troposphere'. *Pure and Applied Geophysics* **106**, 1385–1399. 25

Crutzen, P. J.: 1974, 'Photochemical reactions initiated by and influencing ozone in unpolluted tropospheric air'. *Tellus* **26**, 47–57. 25

Crutzen, P. J., M. Lawrence, and U. Pöschl: 1999, 'On the background photochemistry of tropospheric ozone'. *Tellus, Ser. AB* **51**, 123–146. 26

Danielsen, E. F.: 1968, 'Stratospheric-tropospheric exchange based upon radioactivity, ozone, and potential vorticity'. *J. Atmos. Sci.* **25**, 502–518. 5, 22, 24, 25, 51, 107

Danielsen, E. F.: 1984, 'Meteorological context for global tropospheric experiments instrument tests'. paper presented to AGU fall meeting, San Francisco, CA. paper number: A21-02, citet after Hoskins (1991, sec. 2). 23

Danielsen, E. F.: 1990, 'In defense of Ertel's potential vorticity and its general applicability as a meteorological tracer'. *J. Atmos. Sci.* **47**, 2013–2020. 51

Danielsen, E. F.: 1993, 'Irreversible transport in the stratosphere by internal waves of short vertical wavelength'. *J. Geophys. Res.* **96**, 17433–17452. 102

Danielsen, E. F., and R. S. Hipskind: 1980, 'Stratospheric-tropospheric exchange at polar latitudes in summer'. *J. Geophys. Res.* **85**, 393–400. 5, 22

Danielsen, E. F., and V. Mohnen: 1977, 'Project Duststorm Report: Ozone transport, in situ measurements, and meteorological analysis of tropopause folding'. *J. Geophys. Res.* **82**, 5867–5877. 105

Davies, T. D., and E. Schuepach: 1994, 'Episodes of high ozone concentrations at the earth's surface resulting from transport down from the upper troposphere/lower stratosphere: a review and case studies'. *Atmos. Env.* **28**, 53–68. 105

Dessler, A. E.: 1998, 'A reexamination of the "stratospheric fountain" hypothesis'. *Geophys. Res. Lett.* **25**(22), 4165–4168. 29

Dessler, A. E., E. J. Hintsa, E. M. Weinstock, J. G. Anderson, and K. R. Chan: 1995, 'Mechanisms controlling water vapor in the lower stratosphere: "A tale of two stratospheres"'. *J. Geophys. Res.* **100**(D11), 23167–23172. 29, 30, 33

Dessler, A. E., and S. C. Sherwood: 2004, 'Effect of convection on the summertime extratropical lower stratosphere'. *J. Geophys. Res.* **109**. doi: 10.1029/2004JD005209. 72

Dethof, A., A. O'Neill, and J. Slingo: 2000, 'Quantification of the isentropic mass transport across the dynamical tropopause'. *J. Geophys. Res.* **105**(D10), 12279–12293. 6, 79, 142

Dritschel, D. G.: 1989, 'Contour dynamics and contour surgery: Numerical algorithms for extended, high-resolution modeling of vortex dynamics in two-dimensional, inviscid, incompressible flow'. *Comp. Phys. Rep.* **10**, 77–146. 116

Dvortsov, V. L., and S. Solomon: 2001, 'Response of the stratospheric temperatures and ozone to past and future increases in stratospheric humidity'. *J. Geophys. Res.* **106**(D7), 7505–7514. 2

Eckardt, S., A. Stohl, H. Wernli, P. James, C. Forster, and N. Spichtinger: 2004, 'A 15-Year Climatology of Warm Conveyor Belts'. *J. Clim.* **17**(1), doi: 10.1175/1520–0442(2004)017<218:AYCOWC>2.0CO;2. 97

Eisele, H., H. E. Scheel, R. Sladkovic, and T. Trickl: 1999, 'High-resolution Lidar measurements of stratosphere-troposphere exchange'. *J. Atmos. Sci.* **56**, 319–330. 5

Elbern, H., J. Kowol, R. Sládkovic, and A. Ebel: 1997, 'Deep stratospheric intrusions: A statistical assessment with model guided analyses'. *Atmos. Env.* **31**, 3207–3226. 105

Eluszkiewicz, J.: 1996, 'A three-dimensional view of the stratosphere-to-troposphere exchange in the GFDL SKYHI model'. *Geophys. Res. Lett.* **23**(18), 2489–2492. 28, 79

Emmons, L. K., D. A. Hauglustaine, J.-F. Müller, M. A. Carroll, G. P. Brasseur, D. Brunner, J. Staehelin, V. Thouret, and A. Marenco: 2000, 'Data composits of airborne observations of tropospheric ozone and its precursors'. *J. Geophys. Res.* **105**(D16), 20497–20538. 9

Engel, A., D. Brunner, H. Bönisch, H. Fischer, M. Hegglin, P. Hoor, R. Maser, T. Peter, C. Schiller, U. Schmidt, T. Szabo, H. Wernli, and V. Wirth: 2004, 'Trace gas transport in the tropopause region (SPURT)'. *AFO 2000 newsletter N. 9*. 135, 139

Ertel, H.: 1942, 'Ein neuer hydrodynamischer Wirbelsatz'. *Meteorolog. Z.* **59**, 277–281. 23

Esler, J. G., D. G. H. Tan, and P. H. Haynes: 2001, 'Stratosphere-troposphere exchange: Chemical sensitivity to mixing'. *J. Geophys. Res.* **106**(D5), 4717–4731. 51

Eyring, V., N. R. P. Harris, M. Rex, G. Sheperd, Theodore, D. W. Fahey, G. Amanatidis, J. Austin, M. P. Chipperfield, M. Dameris, P. Forster, A. Gettelman, H. F. Graf, T. Nagashima, P. A. Newman, M. J. Prather, J. A. Pyle, R. J. Salawitch, B. D. Santer, and D. W. Waugh: 2004, 'Comprehensive Summary on the Workshop on "Process-Oriented Validation of Coupled Chemistry-Climate Models"'. *SPARC newsletter N. 23*. 53

Fairlie, T. D., R. B. Pierce, W. L. Grose, G. Lingenfelser, M. Loewenstein, and J. R. Podolske: 1997, 'Lagrangian forecasting during ASHOE/MAESA: Analysis of predictive skill for analyzed and reverse-domain-filled potential vorticity'. *J. Geophys. Res.* **102**(D11), 13169–13182. 116

Fioletov, V. E., G. E. Bodecker, A. J. Miller, M. R. D, and R. Stolarski: 2002, 'Global and zonal total ozone variations estimated from ground-based and satellite measurements: 1964-2000'. *J. Geophys. Res.* **107**(D22), doi: 10.1029/2001JD001350. 2

Fischer, H., M. de Reus, M. Traub, J. Williams, J. Lelieveld, J. de Gouw, C. Warneke, H. Schlager, A. Minikin, R. Scheele, and P. Siegmund: 2003, 'Deep convective injection of boundary layer air into the lowermost stratosphere at midlatitudes'. *Atmos. Chem. Phys.* **3**, 739–745. 29, 72, 86

Fischer, H., F. G. Wienhold, P. Hoor, O. Bujok, C. Schiller, P. Siegmund, M. Ambaum, H. A. Scheeren, and J. Lelieveld: 2000, 'Tracer correlations in the northern high latitude lowermost stratosphere: Influence of cross-tropopause mass exchange'. *Geophys. Res. Lett.* **27**(1), 97–100. 6, 72

Fishman, J., S. Solomon, and P. J. Crutzen: 1979, 'Observational and theoretical evidence in support of a significant in-situ photochemical source of tropospheric ozone'. *Tellus* **31**, 432–446. 25

Foot, J. S.: 1984, 'Aircraft measurements of the humidity in the lower stratosphere from 1977 to 1980 between 45°N and 65°N'. *Quart. J. R. Met. Soc.* **110**, 303–319. 30

Forster, P. M. d. F., and K. P. Shine: 1999, 'Stratospheric water vapour changes as a possible contributor to observed stratospheric cooling'. *Geophys. Res. Lett.* **26**(21), 3309–3312. 2

Forster, P. M. d. F., and K. Tourpali: 2001, 'Effect of tropopause height changes on the calculation of ozone trends and their radiative forcing'. *J. Geophys. Res.* **106**(D11), 12241–12251. 2

Fujiwara, M., M. Kita, and T. Ogawa: 1998, 'Stratosphere-troposphere exchange of ozone associated with the equatorial Kelvin wave as observed with ozonesondes and rawinsondes'. *J. Geophys. Res.* **103**(D15), 19173–19182. 5

Fusco, A. C., and J. A. Logan: 2003, 'Analysis of 1970-1995 trends in tropospheric ozone at Northern Hemisphere midlatitudes with GEOS-CHEM model'. *J. Geophys. Res.* **108**(D15), doi: 10.1029/2002JD002742. 75

Gary, B.: 1989, 'Observational results using the microwave temperature profiler during the Airborne Antarctic Ozone Experiment'. *J. Geophys. Res.* **94**, 11223–11231. 102

Good, P., and J. Pyle: 2004, 'Refinements in the use of equivalent latitude for assimilating sporadic inhomogeneous stratospheric tracer observations, 1: Detecting transport of Pinatubo aerosol across a strong vortex edge'. *Atmos. Chem. Phys. Discuss* **4**, 635–666. 38, 51

Günther, G.: 2004. personal communication. 57

Günther, G., C. Schiller, P. Konopka, and M. Krebsbach: 2004, 'Simulation of Transport Processes in the Tropopause Region during SPURT using a Lagrangian Model'. *Geophys. Res. Abstr.* **6**, SRef–Id: 1607–7962/gra/EGU04–A–02609. 62, 122, 139, 140, 141

Gurk, C.: 2003, 'Untersuchungen zur Verteilung von Kohlendioxid in der Tropopausenregion'. Mastersthesis, Institut für Physik der Atmosphäre, Universität Mainz. 13

Haagen-Smit, A. J., and M. M. Fox: 1956, 'Ozone formation in photochemical oxidation of organical substances'. *Ind. Eng. Chem. Res.* **48**, 1484–1487. 25

Hauf, T., P. Schulte, R. Alheit, and H. Schlager: 1995, 'Rapid vertical trace gas transport by an isolated midlatitude thunderstorm'. *J. Geophys. Res.* **100**(D11), 22957–22970. 72, 86

Haynes, P., and J. Anglade: 1997, 'The vertical sclae cascade in atmospheric tracers due to large-scale differential advection'. *J. Atmos. Sci.* **54**(9), 1121–1136. 124, 131

Haynes, P., and T. Shepherd: 2000, 'Report on the SPARC Tropopause Workshop, Bad Tölz, Germany, 17-21 April 2001'. *SPARC newsletter N. 17*. 21, 22, 27

Haynes, P., and E. Shuckburgh: 2000, 'Effective diffusivity as a diagnostic of atmospheric transport, 2. Troposphere and lower stratosphere'. *J. Geophys. Res.* **105**(D18), 22795–22810. 124, 133, 138

Haynes, P. H., C. J. Marks, M. E. McIntyre, T. G. Sheperd, and K. P. Shine: 1991, 'On the "downward control" of extratropical diabatic circulations by eddy-induced mean zonal forces'. *J. Atmos. Sci.* **48**, 651–678. 3, 6, 138

Hegglin, M. I.: 2004, 'Airborne NO_y-, NO- and O_3-measurements during SPURT: Implications for atmospheric transport'. PhD, Swiss Federal Institute of Technology Zürich. Diss. ETH No. 15553. 13, 14, 20

Hegglin, M. I., D. Brunner, H. Wernli, C. Schwierz, M. O, P. Hoor, H. Fischer, N. Spelten, C. Schiller, M. Krebsbach, U. Parchatka, U. Weers, J. Staehelin, and T. Peter: 2004, 'Tracing troposphere-to-stratosphere transport above a mid-latitude deep convective system'. *Atmos. Chem. Phys.* **4**, 741–756. SRef-ID: 1680-7324/acp/2004-4-741. 52, 72, 78

Herman, R. L., K. Drdla, J. R. Spackman, D. F. Hurst, P. J. Popp, C. R. Webster, P. A. Romashkin, J. W. Elkins, E. M. Weinstock, B. W. Gandrud, G. C. Toon, M. R. Schoeberl, H. Jost, E. L. Atlas, and T. P. Bui: 2002, 'Hydration, dehydration, and the total hydrogen budget of the 1999/2000 winter Arctic stratosphere'. *J. Geophys. Res.* **108**(D5), doi: 10.10292001JD001257. 86

Highwood, E. J., and B. J. Hoskins: 1998, 'The tropical tropopause'. *Quart. J. R. Met. Soc.* **124**, 1579–1604. 3, 22, 91, 92, 93

Highwood, E. J., B. J. Hoskins, and P. Berrisford: 2000, 'Properties of the Arctic tropopause'. *Quart. J. R. Met. Soc.* **126**, 1512–1532. 2, 23

Hintsa, E. J., K. A. Boering, E. M. Weinstock, J. G. Anderson, B. L. Gary, L. Pfister, B. C. Daube, S. C. Wofsy, M. Loewenstein, J. R. Podolske, J. J. Margitan, and T. P. Bui: 1998, 'Troposhere-to-stratosphere transport in the lowermost stratosphere from measurements of H_2O, CO_2, N_2O and O_3'. *Geophys. Res. Lett.* **25**(14), 2655–2658. 4, 29, 33, 142

Hintsa, E. J., A. E. Weinstock, Elliot M Dessler, J. G. Anderson, M. Loewenstein, and J. R. Podolske: 1994, 'SPADE H_2O measurements and the seasonal cycle of stratospheric water vapor [H_2O]'. *Geophys. Res. Lett.* **21**(23), 2559–2562. 29, 30

Hoerling, M. P., T. K. Schaack, and A. J. Lenzen: 1991, 'Global objective tropopause analysis'. *Mon. Wea. Rev.* **119**, 1816–1831. 23, 25

Hoinka, K. P.: 1999, 'Temperature, Humidity, and Wind at the Global Tropopause'. *Mon. Wea. Rev.* **127**, 2248–2265. 23, 29, 85, 92, III

Hollingsworth, A., and P. Lönneberg: 1989, 'The verification of objective analyses: Diagnostics of analysis system performance'. *Meteorol. Atmos. Phys.* **40**, 3–27. 38

Holton, J. R., P. H. Haynes, M. E. McIntyre, A. R. Douglass, R. B. Rood, and L. Pfister: 1995, 'Stratosphere-troposphere exchange'. *Rev. Geophys.* **33**(4), 403–439. 3, 4, 23, 27, 33, 69, 80

Hood, L., S. Rossi, and M. Beulen: 1999, 'Trends in lower stratospheric zonal winds, Rossby wave breaking behaviour, and column ozone at northern midlatitudes'. *J. Geophys. Res.* **104**(D20), 24321–24339. 80

Hoor, P., H. Bönisch, D. Brunner, A. Engel, H. Fischer, C. Gurk, G. Günther, M. I. Hegglin, M. Krebsbach, R. Maser, T. Peter, C. Schiller, U. Scmidt, N. Spelten, H. Wernli, and V. Wirth: 2004a, 'New Insights into Upward Transport across the Extratropical Tropopause derived from Extensive *in situ* Measurements during the SPURT Project'. *SPARC newsletter N. 22*. 20

Hoor, P., H. Fischer, L. Lange, J. Lelieveld, and D. Brunner: 2002, 'Seasonal variations of a mixing layer in the lowermost stratosphere as identified by the CO-O_3 correlation from in situ measurements'. *J. Geophys. Res.* **107**(D5), doi 10.1029/2000JD000289. 72, 80

Hoor, P., H. Fischer, and J. Lelieveld: 2004b, 'Tropical and extratropical tropospheric air in the lowermost stratosphere over Europe: A CO-based budget'. *Geophys. Res. Lett.* , submitted. 69, 142

Hoor, P., C. Gurk, D. Brunner, M. I. Hegglin, H. Wernli, and H. Fischer: 2004c, 'Seasonality and extent of extratropical TST derived from in-situ CO measurements during SPURT'. *Atmos. Chem. Phys.* **4**, 1427–1442. 6, 20, 23, 43, 53, 56, 61, 73, 80, 83, 141

Hoskins, B. J.: 1991, 'Towards a $PV-\theta$ view of the general circulation'. *Tellus* **43 AB**, 27–35. 3, 30, 53, XXVII

Hoskins, B. J., M. E. McIntyre, and A. W. Robertson: 1985, 'On the use and significance of isentropic potential vorticity maps'. *Quart. J. R. Met. Soc.* **111**, 877–946. 22, 23

Hough, A. M.: 1991, 'Development of a two-dimensional global tropospheric model: Model chemistry'. *J. Geophys. Res.* **96**, 7325–7362. 27

Hu, H., and W. T. Liu: 1998, 'The impact of upper tropospheric humidity from Microwave Limb Sounder on the midlatitude greenhouse effect'. *Geophys. Res. Lett.* **25**(16), 3151–3154. 95

Inamdar, A. K., and V. Ramanathan: 1998, 'Tropical and global scale interactions among water vapor, atmospheric greenhouse effect, and surface temperatures'. *J. Geophys. Res.* **103**(D24), 32177–32194. 2

IPCC: 1999, *Aviaton and the Global Atmospere*. Campbridge, UK: Cambridge University Press. Penner, J E and Lister, D H and Griggs, D J and Dokken, D J and McFarland, M (edts.), 373p. 2

IPCC: 2001, *Climate Change 2001, The Scientific Basis*. Campbridge, UK: Cambridge University Press. Houghton, J T and Ding, Y and Griggs, D J and Noguer, M and van der Linden, P J and Dai, X and Maskell, K and Johnson, C A (edts.), 881p. 2

Jackson, D. R., S. J. Driscoll, E. J. Highwood, J. E. Harries, and J. M. Russell III: 1998, 'Troposphere to stratosphere transport at low latitudes as studied using HALOE observations of water vapour 1992–1997'. *Quart. J. R. Met. Soc.* **124**, 169–192. 4, 29

James, P., A. Stohl, C. Forster, S. Eckhardt, P. Seibert, and A. Frank: 2003a, 'A 15-year climatology of stratosphere-troposphere exchange with a Lagrangian particle dispersion model, 1. Methodology and validation'. *J. Geophys. Res.* **108**(D12), doi: 10.1029/2002JD002637. 23, 57, 140

James, P., A. Stohl, C. Forster, S. Eckhardt, P. Seibert, and A. Frank: 2003b, 'A 15-year climatology of stratosphere-troposphere exchange with a Lagrangian particle dispersion model, 2. Mean climate and seasonal variability'. *J. Geophys. Res.* **108**(D12), doi: 10.1029/2002JD002639. 6, 60, 64

Jensen, E. J., O. B. Toon, L. Pfister, and H. B. Selkirk: 1996a, 'Dehydration of of the upper troposphere and lower stratosphere by subvisible cirrus clouds near the tropical tropopause'. *Geophys. Res. Lett.* **23**(8), 825–828. 101

Jensen, E. J., O. B. Toon, J. D. Selkirk, Henry B Spinhirne, and M. R. Schoeberl: 1996b, 'On the formation and persistence of subvisible cirrus clouds near the tropical tropopause'. *J. Geophys. Res.* **101**(D16), 21361–21376. 5, 101, 102

Jensen, E. J., O. B. Toon, A. Tabazadeh, G. W. Sachse, B. E. Anderson, K. R. Chan, C. W. Twohy, B. Gandrud, S. M. Aulenbach, A. Heymsfield, J. Hallett, and B. Gary: 1998, 'Ice nucleation processes in upper tropospheric wave-clouds observed during SUCCESS'. *Geophys. Res. Lett.* **25**(9), 1363–1366. 99

Kley, D., E. J. Stone, W. R. Henderson, J. W. Drummond, W. J. Harrop, and A. L. Schmeltekopf: 1979, 'In situ measurements of the mixing ratio of water vapor in the stratosphere'. *J. Atmos. Sci.* **36**, 2513–2524. 22

Konopka, P.: 2003. personal communication. 56

Konopka, P.: 2004. personal communication. 57

Konopka, P., J.-U. Grooß, G. Günther, D. S. McKenna, R. Müller, J. W. Elkins, D. Fahey, and P. Popp: 2003, 'Weak impact of mixing on chlorine deactivation during SOLVE/THESEO 2000: Lagrangian Modelling (CLaMS) versus ER-2 in situ observations'. *J. Geophys. Res.* **108**, doi: 10.1029/2001JD000876. 125

Konopka, P., L. Pan, R. Müller, D. McKenna, and E. Browell: 2004a, 'How Can We Quantify the Effect of Mixing in the Vicinity of the Tropopause?'. *Geophys. Res. Abstr.* **6**, SRef–Id: 1607–7962/gra/EGU04–A–04995. 125

Konopka, P., R. Spang, G. Günther, R. Müller, D. S. McKenna, D. Offermann, and M. Riese: 2004b, 'How homogeneous and isotropic is stratospheric mixing?: Comparison of CRISTA-1 observations with transport studies based on the Chemical Lagrangian Model of the Stratosphere (CLaMS)'. *Geophys. Res. Abstr.* **128**, 1–13. 127

Koop, T., B. Luo, A. Tsias, and T. Peter: 2000, 'Water activity as the determinant for homogenious ice nucleation in aqueous solutions'. *Nature* **406**, 611–614. 115

Krämer, M., and A. Afchine: 2004, 'Sampling characteristics of inlets operated at low U/U_0 ratios: new insights from computational fluid dynamics (CFX) modeling'. *J. Aer. Sci.* **35**, 683–694. 115

Lamarque, J. F., and P. G. Hess: 1994, 'Cross-tropopause mass exchange and potential vorticity budget in a simulated tropopause folding'. *J. Atmos. Sci.* **51**(15), 2246–2269. 5

Lamarque, J. F., A. O. Langford, and M. H. Proffitt: 1996, 'Cross-tropopause mixing of ozone through gravity wave breaking: Observation and modeling'. *J. Geophys. Res.* **101**(D17), 22969–22976. 5

Langford, A. O., C. D. Masters, M. H. Proffitt, E.-Y. Hsie, and A. F. Tuck: 1996, 'Ozone measurements in a tropopause fold associated with a cut-off low system'. *Geophys. Res. Lett.* **D23**(18), 2501–2504. 5

Lelieveld, J., and F. Dentener: 2000, 'What controls tropospheric ozone?'. *J. Geophys. Res.* **105**(D3), 3531–3551. 25, 26, 54, 107, 109

Levy, H. I., P. S. Kasibhatla, W. J. Moxim, A. A. Klonecki, A. I. Hirsch, S. J. Oltmans, and W. L. Chameides: 1997, 'The global impact of human activity on tropospheric ozone'. *Geophys. Res. Lett.* **24**(7), 791–794. 26

Levy, H. I., J. D. Mahlman, W. J. Moxim, and S. C. Liu: 1985, 'Tropospheric ozone: The role of transport'. *J. Geophys. Res.* **90**, 3753–3772. 25, 105

Lindzen, R. S.: 1990, 'Some coolness concerning global warming'. *Bull. Am. Meteorol. Soc.* **71**, 288–299. 2

Liu, S. C., M. Trainer, F. Fehsenfeld, D. Parrish, E. J. Williams, D. W. Fahey, G. Hübler, and P. C. Murphy: 1987, 'Ozone production in the rural troposphere and the implications for the regional and global ozone distributions'. *J. Geophys. Res.* **92**, 4191–4207. 27

Logan, J.: 1985, 'Tropospheric ozone: Seasonal behaviour, trends and anthropogenic influence'. *J. Geophys. Res.* **90**, 10463–10482. 26, 27

Logan, J.: 1989, 'Ozone in rural areas of the United States'. *J. Geophys. Res.* **94**, 8511–8532. 26

Logan, J. A.: 1999, 'An Analysis of ozonesonde data for the lower stratosphere: Recommendations for testing models'. *J. Geophys. Res.* **104**(D13), 16151–16170. 27, 37, 59, 75, 131, 138

Logan, J. A., I. A. Megretskaia, A. J. Miller, G. C. Tiao, D. Choi, L. Zhang, R. S. Stolarski, G. J. Labow, S. M. Hollandsworth, G. E. Bodeker, H. Claude, D. De Muer, J. B. Kerr, D. W. Tarasick, S. J. Oltmans, B. Johnson, F. Schmidlin, J. Staehelin, P. Viatte, and O. Uchino: 1999, 'Trends in the vertical distribution of ozone: A comparison of two analyses of ozonesonde data'. *J. Geophys. Res.* **104**(D21), 26373–26399. 2, 59

Luo, B. P., T. Peter, H. Wernli, S. Flueglistaler, M. Wirth, C. Kiemle, H. Flentje, V. A. Yushkov, V. Khattatov, V. Rudakov, A. Thomas, S. Borrmann, G. Toci, P. Mazzinghi, J. Beuermann, C. Schiller, F. Cairo, G. Di Don-Francesco, A. Adriani, C. M. Volk, J. Strom, K. Noone, V. Mitev, R. A. MacKenzie, K. S. Carlslaw, T. Trautmann, V. Santacesaria, and L. Stefanutti: 2003, 'Ultrathin Tropical Tropopause Clouds (UTTCs): II. Stabilization mechanisms'. *Atmos. Chem. Phys.* **3**, 1093–1100. 5

Mahowald, N. M., R. A. Plumb, R. P. J, J. del Corral, F. Sassi, and W. Heres: 2002, 'Stratospheric transport in a three-dimensional isentropic coordinate model'. *J. Geophys. Res.* **107**(D15), 4254. doi: 10.1029/2001JD001313. 57, 142

Mangold, A.: 2004, 'Untersuchingen zur Mikrophysik von Eiswolken: Simulationsexperimente in der Aerosolkammer AIDA'. PhD, Universität Wuppertal. ISSN 0944-2952, in cooperation with the Institute for Chemistry and Dynamics of the Geosphere, ICG-I: Stratosphere. 99

Marenco, A.: 1998, 'Measurement of ozone and water vapor by Airbus in-service aircraft: The MOZAIC program, an overview'. *J. Geophys. Res.* **103**(D19), 25631–25642. 10

Marti, J., and K. Mauersberger: 1993, 'A survey and new measurements of ice vapor pressure at temperatures between 170 and 250 K'. *Geophys. Res. Lett.* **20**, 363–366. 58

Mastenbrook, H. J., and H. J. Oltmans: 1983, 'Stratospheric water vapor variability for Washington, DC/Boulder, CO: 1964–82'. *J. Atmos. Sci.* **40**, 2157–2165. 29

McCormick, M. P., E. W. Chiou, L. R. McMaster, W. P. Chu, J. C. Larsen, D. Rind, and S. Oltmans: 1993, 'Annual variations of water vapor in the stratosphere and upper troposphere observed by the Stratospheric Aerosol and Gas Experiment II'. *J. Geophys. Res.* **98**, 4867–4874. 29

McFarquhar, G. M., A. J. Heymsfield, J. Spinhirne, and B. Hart: 2000, 'Thin and Subvisual Tropopause Tropical Cirrus: Observation and radiative impacts'. *J. Atmos. Sci.* **57**(12), 1841–1853. 5

McKenna, D. S., J.-U. Grooß, G. Günther, P. Konopka, R. Müller, G. Carver, and Y. Sasano: 2002a, 'A new Chemical Lagrangian Model of the Stratosphere (CLaMS),2. Formulation of chemistry scheme and initialization'. *J. Geophys. Res.* **107**, doi: 10.1029/2000JD000113. 18, 38, 56, 125

McKenna, D. S., P. Konopka, J.-U. Grooß, G. Günther, R. Müller, R. Spang, D. Offermann, and Y. Orsolini: 2002b, 'A new Chemical Lagrangian Model of the Stratosphere (CLaMS), 1. Formulation of advection and mixing'. *J. Geophys. Res.* **107**, doi: 10.1029/2000JD000114. 7, 9, 18, 38, 56, 124

McLinden, C. A., S. C. Olsen, B. Hannegan, O. Wild, P. M. J, and J. Sundet: 2000, 'Stratospheric ozone in 3-D models: A simple chemistry and the cross-tropopause flux'. *J. Geophys. Res.* **105**, 14653–14665. 9

Mocrette, J.-J.: 1991, 'Radiation and cloud radiative properties in the european centre for medium range weather forecasts forecasting system'. *J. Geophys. Res.* **96**(D5), 9121–9132. 56, 125

Monks, P. S.: 2000, 'A review of the observations and origins of the spring ozone maximum'. *Atmos. Env.* **34**, 3545–3561. 26, 37, 105

Mote, P. W., T. J. Dunkerton, M. E. McIntyre, E. A. Ray, P. H. Haynes, and J. M. Russell III: 1998, 'Vertical velocity, vertical diffusion, and dilution by midlatitude air in the tropical lower stratosphere'. *J. Geophys. Res.* **103**(D8), 8651–8666. 29

Mote, P. W., K. H. Rosenlof, M. E. McIntyre, E. S. Carr, J. C. Gille, J. R. Holton, J. S. Kinnersley, H. C. Pumphrey, J. M. Russel, and J. W. Waters: 1996, 'An atmospheric tape recorder: The imprint of tropical tropopause temperatures on stratospheric water vapor'. *J. Geophys. Res.* **101**(D2), 3989–4006. 3, 4, 29, 86

Mottaghy, D.: 2001, 'Ozonmessungen in der unteren Stratosphäre'. Mastersthesis, Rheinisch-Westfälische Technische Hochschule Aachen. in cooperation with the Institute for Chemistry and Dynamics of the Geosphere, ICG-I: Stratosphere. 7, 13, 14, 36, 137

Müller, J.-F., and G. P. Brasseur: 1995, 'IMAGES: A three-dimensional chemical transport model of the global troposphere'. *J. Geophys. Res.* **100**(D8), 16445–16490. 26

Murphy, D. M., K. K. Kelly, A. F. Tuck, and M. H. Proffitt: 1990, 'Ice saturation at the tropopause observed from the ER-2 aircraft'. *Geophys. Res. Lett.* **17**, 353–356. 104

Nagurny, A. P.: 1998, 'Climatic characteristics of the tropopause over the Arctic Basin'. *Ann. Geophys.* **16**, 110–115. 93

Nash, E. R., P. A. Newman, J. E. Rosenfield, and M. R. Schoeberl: 1996, 'An objective determination of the polar vortex using Ertel's potential vorticity'. *J. Geophys. Res.* **101**(D5), 9471–9478. 51, 129

Nedoluha, G. E., R. M. Bevilacqua, K. W. Hoppel, J. D. Lumpe, and H. Smit: 2002, 'Polar Ozone and Aerosol Measurement III measurements of water vapor in the upper troposphere and lowermost stratosphere'. *J. Geophys. Res.* **107**(D10), doi: 10.1029/2001JD000793. 30, 86, 97

Newell, R. E., and S. Gould-Steward: 1981, 'A stratospheric fountain?'. *J. Atmos. Sci.* **38**(12), 2789–2796. 5, 95, 97

Norton, W. A.: 2001, 'Longwave Heating of the Tropical Lower Stratosphere'. *Geophys. Res. Lett.* **28**(19), 3653–3656. 57

Oltmans, S. J.: 1981, 'Surface ozone measurements in clean air'. *J. Geophys. Res.* **86**, 1174–1180. 105

Oltmans, S. J., and D. J. Hofmann: 1995, 'Increase in lower-stratospheric water vapour at a mid-latitude Northern Hemisphere site from 1981 to 1994'. *Nature* **374**, 146–149. 30

Oltmans, S. J., and S. J. Levy III: 1994, 'Surface ozone measurements from a global network'. *Atmos. Env.* **28**, 9–24. 27

Oltmans, S. J., H. Vömel, D. J. Hofmann, K. H. Rosenlof, and D. Kley: 2000, 'The increase in stratospheric water vapor from balloonborne frostpoint hygrometer measurements at Washington D.C. and Boulder, Colorado'. *Geophys. Res. Lett.* **27**(21), 3453–3457. 86

Ovarlez, J., J.-F. Gayet, K. Gierens, J. Ström, H. Ovarlez, F. Auriol, R. Busen, and U. Schumann: 2002, 'Water vapour measurements inside cirrus clouds in Northern and Southern hemispheres during INCA'. *Geophys. Res. Lett.* **29**(16), doi: 10.1029/2001GL014440. 101

Ovarlez, J., P. van Velthoven, and H. Schlager: 1999, 'Water vapor measurements from the troposphere to the lowermost stratosphere: Some signatures of troposphere to stratosphere exchanges'. *J. Geophys. Res.* **104**(D14), 16973–16978. 23, 32

Pan, L., S. Solomon, W. J. Randel, J. F. Lamarque, P. Hess, J. C. Gille, E. W. Chiou, and M. P. McCormick: 1997, 'Hemispheric asymmetries and seasonalvariations of the lowermost stratospheric water vapor and ozone derived from SAGE II data'. *J. Geophys. Res.* **102**(D23), 28177–28184. 6, 28, 30, 33, 85, 131

Pan, L. L., E. J. Hintsa, E. M. Stone, E. M. Weinstock, and W. J. Randel: 2000, 'The seasonal cycle of water vapor and saturation vapor mixing ratio in the extratropical lowermost stratosphere'. *J. Geophys. Res.* **105**(D21), 26519–26530. 31, 32, 36

Park, M., W. J. Randel, E. Kinnison, Douglas, and R. R. Gracia: 2004, 'Seasonal variation of methane, water vapor, and nitrogen oxides near the tropopause: Satellite observations and model simulations'. *J. Geophys. Res.* **109**(D03), doi 10.1029/2003JD003706. 29

Parrish, D. D., J. S. Holloway, R. Jakoubek, M. Trainer, T. B. Ryerson, G. Hübler, F. C. Fehsenfeld, J. L. Moody, and O. R. Cooper: 2000, 'Mixing of anthropogenic pollution with stratospheric ozone: A case study from the North Atlantic wintertime troposphere'. *J. Geophys. Res.* **105**(D19), 24363–24374. 6

Peter, T., B. P. Luo, M. Wirth, C. Kiemle, H. Flentje, V. A. Yushkov, V. Khattatov, V. Rudakov, A. Thomas, S. Borrmann, G. Toci, P. Mazzinghi, J. Beuermann, C. Schiller, F. Carso, G. Di Donfrancesco, A. Adriani, C. M. Volk, J. Strom, K. Noone, V. Mitev, R. A. MacKenzie, K. S. Carslaw, T. Trautmann, V. Santacesaria, and L. Stefanutti: 2003, 'Ultrathin Tropical Tropopause Clouds (UTTCs): I. Cloud morphology and occurrence'. *Atmos. Chem. Phys.* **3**, 1083–1091. 5

Pfister, L., H. B. Selkirk, E. J. Jensen, J. Podolske, G. Sachse, M. Avery, M. R. Schoeberl, M. J. Mahoney, and E. Richard: 2003, 'Processes controlling water vapor in the winter Arctic tropopause region'. *J. Geophys. Res.* **108**(D5), doi: 10.1029/2001JD001067. 3, 23, 73, 77, 78, 80, 106

Piani, C., and W. A. Norton: 2002, 'Solid-body rotation in the northern hemisphere summer stratosphere'. *Geophys. Res. Lett.* **29**(23), doi: 10.1029/2002GL016079. 130

Pichler, H.: 1997, *Dynamik der Atmosphäre*, Spektrum-Hochschultaschenbuch. Spektrum Akademischer Verlag GmbH. 3. aktualisierte Auflage, ISBN 3-8274-0134-8. 18, 23

Pierrehumbert, R. T.: 1995, 'Thermostats, radiator fins, and the local runaway greenhouse'. *J. Atmos. Sci.* **52**, 1784–1806. 2

Plumb, R. A.: 1996, 'A "tropical pipe" model of stratospheric transport'. *J. Geophys. Res.* **101**(D2), 3957–3972. 3

Plumb, R. A., and J. Eluszkiewicz: 1999, 'The Brewer-Dobson circulation: Dynamics of the tropical upwelling'. *J. Atmos. Sci.* **56**(6), 868–890. 3

Plumb, R. A., and M. K. W. Ko: 1992, 'Interrelationships between mixing ratios of long-lived stratospheric constituents'. *J. Geophys. Res.* **97**, 10145–10156. 65, 72

Plumb, R. A., D. W. Waugh, and M. P. Chipperfield: 2000, 'The effect of mixing on tracer relationships inthe polar vortices'. *J. Geophys. Res.* **105**(D8), 10047–10062. 72

Postal, G. A., and M. H. Hitchman: 1999, 'A climatology of Rossby wave breaking along the subtropical tropopause'. *J. Atmos. Sci.* **56**(3), 359–373. 123

Potter, B. E., and J. R. Holton: 1995, 'The role of monsoon convection in the dehydration of the lower tropical stratosphere'. *J. Atmos. Sci.* **52**(8), 1034–1050. 5

Poulida, O., R. R. Dickerson, and A. Heymsfeld: 1996, 'Stratosphere-troposphere exchange in a midlatitude mesoscale convective complex: 1. Observations'. *J. Geophys. Res.* **101**(D3), 6823–6836. 5, 22, 29, 72, 86

Prados, A. I., G. E. Nedoluha, R. M. Bevilacqua, D. R. Allen, K. W. Hoppel, and A. Marenco: 2003, 'POAM III ozone in the upper troposphere and lowermost stratosphere: Seasonal variability and comparisons to aircraft observations'. *J. Geophys. Res.* **108**(D7), doi: 10.1029/2002JD002819. 27, 33, 131

Press, W. H., S. A. Teukolsky, W. T. Vetterling, and B. P. Flannery: 1997, *Numerical Recipies in Fortran 77: The Art of Scientific Computing*, Vol. 1 of *Fortran Numerical Recipies*. The Pitt Building, Trumpington Street. Cambridge CB2 1RP: Press Syndicate of the University of Cambridge, 2nd edition. ISBN 0-521-43064-X. 48

Price, J. D., and G. Vaughan: 1992, 'Statistical studies of cut-off low systems'. *Ann. Geophys.* **10**, 96–102. 105

Price, J. D., and G. Vaughan: 1993, 'The potential for stratosphere-troposphere exchange in cut-off low systems'. *Quart. J. R. Met. Soc.* **119**, 343–365. 5, 23, 105

Ramaswamy, V., M. D. Schwartzkopf, and K. P. Shine: 1992, 'Radiative forcing of climate from halocarbon induced global stratospheric ozone loss'. *Nature* **355**, 810–812. 105

Randel, W. J., F. Wu, A. Gettelman, J. M. Russell III, J. M. Zawodny, and S. J. Oltmans: 2001, 'Seasonal variation of water vapor in the lower stratosphere observed in Halogen Occultation Experiment data'. *J. Geophys. Res.* **106**(D13), 14313–14325. 29, 52

Ray, E.: 2004a. email communication. 129

Ray, E.: 2004b. personal communication at AGU fall meeting 2004, San Francisco, CA, USA. 129

Ray, E. A., F. L. Moore, J. W. Elkins, G. S. Dutton, D. W. Fahey, H. Vömel, S. J. Oltmans, and K. H. Rosenlof: 1999, 'Transport into the Northern Hemisphere lowermost stratosphere revealed by in situ tracer measurements'. *J. Geophys. Res.* **104**(D21), 26565–26580. 6, 23, 28, 59, 133, 142

Ray, E. A., K. H. Rosenlof, E. Richard, D. Parrish, and R. Jakoubek: 2004, 'Seasonal Distributions of Ozone in the Region of the Subtropical Jet: An Analysis of *In Situ* Aircraft Measurements'. *J. Geophys. Res.* **109**(D08106), doi: 10.1029/2003JD004143. 38, 131, 133

Regener, V. H.: 1957, 'Vertical flux of atmospheric ozone'. *J. Geophys. Res.* **62**, 221–228. 25

Reid, G. C., and K. S. Gage: 1981, 'On the annual variation in height of the tropical tropopause'. *J. Atmos. Sci.* **38**, 1928–1938. 92

Reid, S. J., A. F. Tuck, and G. Kiladis: 2000, 'On the changing abundance of ozone minima at northern midlatitudes'. *J. Geophys. Res.* **D10**(105), 12169–12180. 2

Reiter, E. R.: 1975, 'Stratoepheric-troposphere exchange processes'. *Rev. Geophys. Space Phys.* **13**(4), 459–474. 80, 105

Richard, E. C., K. C. Aikin, E. A. Ray, K. H. Rosenlof, L. Thompson, Thomas, A. Weinheimer, D. Montzka, D. Knapp, B. Ridley, and A. Gettelman: 2003, 'Large-scale equatorward transport of ozone in the subtropical lower stratosphere'. *J. Geophys. Res.* **108**(D23), doi: 10.1029/2003JD003884. 86

Rind, D., E.-W. Chiou, W. Chu, J. Larsen, S. Oltmans, J. Lerner, M. P. McCormick, and L. McMaster: 1991, 'Positive water vapour feedback in climate models confirmed by satellite data'. *Nature* **349**, 500–503. 2

Rind, D., and P. Lonergan: 1995, 'Modeled impacts of stratospheric ozone and water vapor pertubations with implications for high-speed civil transport aircraft'. *J. Geophys. Res.* **100**(D4), 7381–7396. 2

Roelofs, G.-J., and J. Lelieveld: 1997, 'Model study of the influence of cross-tropopause O_3transport on tropospheric O_3 levels'. *Tellus* **49B**, 38–55. 5

Rood, R. B., A. R. Douglass, M. C. Cerniglia, and W. G. Read: 1997, 'Synoptic-scale mass exchange from the troposphere to the stratosphere'. *J. Geophys. Res.* **102**(D19), 23467–23485. 5

Rood, R. B., A. R. Douglass, M. C. Cerniglia, L. C. Sparling, and E. Nielsen: 2000, 'Seasonal variability of middle-latitude ozone in the lowermost stratosphere derived from probability distribution functions'. *J. Geophys. Res.* **105**(D14), 17793–17805. 23, 79

Rosenlof, K. H., S. J. Oltmans, D. Kley, J. M. Russell III, E.-W. Chiou, W. P. Chu, D. G. Johnson, K. K. Kelly, H. A. Michelsen, G. E. Nedoluha, E. E. Remsberg, G. C. Toon, and M. P. McCormick: 2001, 'Stratospheric water vapor increases over the past half-century'. *Geophys. Res. Lett.* **28**(7), 1195–1198. 86

Rosenlof, K. H., A. F. Tuck, K. K. Kelly, J. M. Russell III, and M. P. McCormick: 1997, 'Hemispheric asymmetries in water vapor and inferences about transport in the lower stratosphere'. *J. Geophys. Res.* **102**(D11), 13213–13234. 29, 143

Scheel, H. E., H. Areskoug, H. Geiss, B. Gomiscel, K. Grandby, L. Haszpra, L. Klasinc, D. Kley, T. Laurila, T. Lindskog, M. Roemer, R. Schmitt, P. Simmonds, S. Solberg, and G. Toupance: 1997, 'On the spatial distribution and seasonal variation of lower-troposphere ozone over Europe'. *J. Atmos. Chem.* **28**, 11–28. 26, 27

Schiller, C.: 2004. personal communication. 74

Schiller, C., A. Afchine, N. Eicke, C. Feigl, H. Fischer, A. Giez, P. Konopka, H. Schlager, T. Tuitjer, F. G. Wienhold, and M. Zöger: 1999, 'Ice particle formation and sedimentation in the tropopause region: A case study based on in situ measurements of total water during POLSTAR 1997'. *Geophys. Res. Lett.* **26**(14), 2219–2222. 100, 114

Schiller, C., R. Bauer, F. Cairo, T. Deshler, A. Dörnbrack, J. Elkins, A. Engel, H. Flentje, N. Larsen, I. Levin, M. Müller, S. Oltmans, H. Ovarlez, J. Ovarlez, J. Schreiner, F. Stroh, C. Voigt, and H. Vömel: 2002, 'Dehydration in the Arctic stratosphere during the SOLVE/THESEO-2000 campaigns'. *J. Geophys. Res.* **107**(D20), doi: 10.1029/2001JD000463. 99

Schoeberl, M. R.: 2004, 'Extratropical stratosphere.troposphere mass exchange'. *J. Geophys. Res.* **109**(D13303), doi: 10.1029/2004JD004525. 142

Schoeberl, M. R., and P. A. Newman: 1995, 'A multiple-level trajectory analysis of vortex filaments'. *J. Geophys. Res.* **100**(D12), 25801–25815. 116

Seidel, D. J., R. J. Ross, J. Angell, and G. C. Reid: 2001, 'Climatological characteristics of the tropocal tropopause as revealed by radiosondes'. *J. Geophys. Res.* **106**(D8), 7857–7878. 3

Seo, K.-H., and K. P. Bowman: 2001, 'A climatology of isentropic cross-tropopause exchange'. *J. Geophys. Res.* **106**(D22), 28159–28172. 80

Shapiro, M. A.: 1980, 'Turbulent mixing within tropopause folds as a mechanism for the exchange of chemical constituents between the stratosphere and the troposphere'. *J. Atmos. Sci.* **37**, 994–1004. 5

Shapiro, M. A., T. Hampel, and A. J. Krueger: 1980, 'The Arctic tropopause fold'. *Mon. Wea. Rev.* **115**, 444–454. 103

Simmons, A. J., A. Untch, C. Jakob, P. Kållberg, and P. Undén: 1999, 'Stratospheric water vapour and tropical tropopause temperatures in ECMWF analyses and multi-year simulations'. *Quart. J. R. Met. Soc.* **125**(553), 353–386. doi: 10.1256/smsqj.55316. 94, 95, 115

Smith, J. B., E. J. Hintsa, N. T. Allen, R. M. Stimpfle, and J. G. Anderson: 2001, 'Mechanisms for midlatitude ozone loss: Heterogeneous chemistry in the lowermost stratosphere?'. *J. Geophys. Res.* **106**(D1), 1297–1309. 102

Sobel, A., R. Plumb, and D. Waugh: 1997, 'Methods of calculating transport across the polar vortex edge'. *J. Geophys. Sci.* **54**, 2241–2260. 52

Solomon, S., S. Borrmann, R. R. Garcia, R. Portmann, L. W. Thomason, L. R. Poole, D. Winker, and M. P. McCormick: 1997, 'Heterogeneous chlorine chemistry in the tropopause region'. *J. Geophys. Res.* **102**(D17), 21411–21429. 3

Solomon, S., R. R. Garcia, and F. Stordal: 1985, 'Transport processes and ozone pertubations'. *J. Geophys. Res.* **90**, 12981–12989. 70

Solomon, S., R. Portmann, R. R. Garcia, W. Randel, F. Wu, R. Nagatani, J. Gleason, L. W. Thomason, L. R. Poole, and M. P. McCormick: 1999, 'Ozone depletion at mid-latitudes: Coupling of volcanic aerosols and temperature variability to anthropogenic chlorine'. *Geophys. Res. Lett.* **25**(11), 1871–1874. 3

SPARC, S.: 2000, 'Assesment of Upper Tropospheric and Stratospheric Water Vapour'. Technical Report 2, BP3, 91371 Verrières le Buisson Cedex, France. WCRP-113, WMO/TD-No. 1043. 2, 86

Sparling, L. C.: 2000, 'Statistical perspectives on stratospheric transport'. *Rev. Geophys.* **38**(3), 417–436. 46, 47

Sparling, L. C., and M. R. Schoeberl: 1995, 'Mixing entropy analysis of dispersal of aircraft emissions inthe lower stratosphere'. *J. Geophys. Res.* **100**(D8), 16805–16812. 43, 46

Sprenger, M., M. C. Maspoli, and H. Wernli: 2003, 'Tropopause folds and cross-tropopause exchange: A global investigation based upon ECMWF analyses for the time period March 2000 to February 2001'. *J. Geophys. Res.* **108**(D12), doi 10.1029/2002JD002587. 23

Sprenger, M., and H. Wernli: 2003, 'A northern hemispheric climatology of cross-tropopause exchange for the ERA15 time period (1979-1993)'. *J. Geophys. Res.* **108**(D12), doi 10.1029/2002JD002636. 6, 39, 60, 62, 64, 69, 142

Srikanth, M., H. K. Kesavan, and P. H. Roe: 2000, 'Probability Density Function Estimation using the MinMax Measure'. *IEEE Transactions on Systems, Man, and Cybernetics – Part C: Applications and Reviews* **30**(1), 77–83. 46

Staehelin, J., N. R. P. Harris, C. Appenzeller, and J. Eberhard: 2001, 'Ozone trends: a review'. *Rev. Geophys.* **39**(2), 231–290. 3

Steinbrecht, W., H. Claude, U. Köhler, and K. P. Hoinka: 1998, 'Correlations between tropopause height and total ozone: Implications for long-term changes'. *J. Geophys. Res.* **103**(D23), 19183–19192. 2

Stohl, A.: 2001, 'A 1-year Lagrangian "climatology" of airstream in the Northern Hemisphere troposphere and lowermost stratosphere'. *J. Geophys. Res.* **106**(D7), 7263–7279. paper number 2000JD900570. 6, 97

Stohl, A., P. Bonasoni, P. Cristofanelli, W. Collins, J. Feichter, A. Frank, C. Forster, E. Gerasopoulos, H. Gäggeler, P. James, T. Kentarchos, H. Kromp-Kolb, B. Krüger, C. Land, J. Meloen, A. Papayannis, A. Priller, P. Seibert, M. Sprenger, G. J. Roelofs, H. E. Scheel, C. Schnabel, P. Siegmund, L. Tobler, T. Trickl, H. Wernli, V. Wirth, P. Zanis, and C. Zerefos: 2003a, 'Stratosphere-troposphere exchange: A review, and what we have learned from STACCATO'. *J. Geophys. Res.* **108**(D12), doi: 10.1029/2002JD002490. 60

Stohl, A., M. Hittenberger, and G. Wotawa: 1998, 'Validation of the Lagrangian Particle Dispersion Model FLEXPART against Large-scale Tracer Experiment Data'. *Atmos. Env.* **32**(24), 4245–4264. 60

Stohl, A., P. James, F. Caroline, N. Spichtinger, A. Marenco, V. Thouret, and H. G. J. Smit: 2001, 'An extension of Measurement of Ozone and Water Vapour by Airbus In-service Aircraft (MOZAIC) ozone climatologies using trajectory statistics'. *J. Geophys. Res.* **106**(D21), 27757–27768. paper number 2001JD000749. 61, 65

Stohl, A., N. Spichtinger-Rakowski, P. Bonasoni, H. Feldmann, M. Memmesheimer, H. E. Scheel, T. Trickl, S. Hübener, W. Ringer, and M. Mandl: 2000, 'The influence of stratospheric intrusions on alpine ozone concentrations'. *Atmos. Env.* **34**, 1323–1354. 5

Stohl, A., and T. Trickl: 1999, 'A textbook example of long-range transport: Simultaneous observation of ozone maxima of stratospheric and North American origin in the free troposphere over Europe'. *J. Geophys. Res.* **104**(D23), 30445–30462. paper number 1999JD900803. 5, 23, 65, 105

Stohl, A., H. Wernli, P. James, M. Bourqui, C. Forster, M. A. Liniger, P. Seibert, and M. Sprenger: 2003b, 'A new perspective of stratosphere-troposphere exchange'. *Bull. Am. Met. Soc.* **84**, 1565–1573. doi: 10.1175/BAMS-84-11-1565. 23, 97

Stone, E. M., L. Pan, B. J. Sandor, W. G. Read, and J. W. Waters: 2000, 'Spatial distributions of upper tropospheric water vapor measurements from the UARS Microwave Limb Sounder'. *J. Geophys. Res.* **105**(D10), 12149–12161. paper number 2000JD900125. 30, 31, 32, 95

Strahan, S. E., M. Loewenstein, and J. R. Podolske: 1999, 'Climatology and small-scale structure of lower stratospheric N_2O based on in situ observations'. *J. Geophys. Res.* **104**(D2), 2195–2208. paper number: 1998JD200075. 51, 53, 59

Sutton, R.: 1994, 'Lagrangian flow in the middle atmosphere'. *Quart. J. R. Met. Soc.* **120**, 1299–1331. 116

Talbot, R. W., J. E. Dibb, E. M. Scheuer, Y. Kondo, M. Koike, H. B. Singh, L. B. Salas, Y. Fukui, J. O. Ballenthin, R. F. Meads, T. M. Miller, D. E. Hunton, A. A. Viggiano, D. R. Blake, N. J. Blake, E. Atlas, F. Flocke, D. J. Jacob, and L. Jaegle: 1999, 'Reactive Nitrogen Budget During the NASA SONEX Mission'. *Geophys. Res. Lett* **26**(20), 3057–3060. 22, 54

Thomas, W., F. Baier, T. Erbertseder, and M. Kästner: 2003, 'Analysis of the Algerian severe weather event in November 2001 and its impact on ozone and nitrogen dioxide distributions'. *Tellus* **55B**, 993–1006. 52

Thorncroft, C. D., B. J. Hoskins, and M. E. McIntyre: 1993, 'Two paradigms of baroclinic-wave life-cycle behaviour'. *Quart. J. R. Met. Soc.* **119**, 17–55. 80

Thouret, V., A. Marenco, P. Nédélec, and C. Grouhel: 1998, 'Ozone climatologies at 9-12 km altitude as seen by the MOZAIC airborene program between September 1994 and August 1996'. *J. Geophys. Res.* **103**, 25653–25679. 22, 54

Tuck, A. F., S. J. Hovde, K. K. Kelly, M. J. Mahoney, M. H. Proffitt, E. C. Richard, and T. L. Thompson: 2003a, 'Exchange between the upper tropical troposphere and the lower stratosphere studied with aircraft observations'. *J. Geophys. Res.* **108**(D23), 4734. doi: 10.1029/2003JD003399. 142

Tuck, A. F., S. J. Hovde, E. C. Richard, D. W. Fahey, R. S. Gao, and T. P. Bui: 2003b, 'A scaling analysis of ER-2 data in the inner Arctic vortex during January–March 1000'. *J. Geophys. Res.* **108**(D5), 8306. doi: 10.1029/2003JD003399. 142

Van Haver, P., D. De Muer, M. Beekmann, and C. Mancier: 1996, 'Climatology of tropopause folds at midlatitudes'. *Geophys. Res. Lett.* **23**(9), 1033–1036. 105

Vaughan, G., J. D. Price, and A. Howells: 1994, 'Transport into the troposphere in a tropopause fold'. *Quart. J. R. Met. Soc.* **120**, 1085–1103. 5

Vaughan, G., and C. Timmis: 1998, 'Transport of near-tropopause air into the lower midlatitude stratosphere'. *Quart. J. R. Met. Soc.* **124**, 1559–1578. 64, 69, 123

Vömel, H., S. J. Oltmans, D. Kley, and P. J. Crutzen: 1995, 'New evidence for stratospheric dehydration mechanism in the equatorial Pacific'. *Geophys. Res. Lett.* **22**(23), 3235–3238. 87

Wang, P.-H., M. Cunnold, Derek, J. M. Zawodny, R. B. Pierce, J. R. Olson, G. S. Kent, and K. M. Skeens: 1998a, 'Seasonal ozone variations in the isentropic layer between 330 K and 380 K as observed by SAGEII: Implications of extratropical cross-tropopause transport'. *J. Geophys. Res.* **103**(D22), 28647–28659. 28

Wang, P.-H., D. J. Jacob, and J. A. Logan: 1998b, 'Global simulation of tropospheric O_3-NO_x-hydrocarbon chemistry: 2. Model evaluation and global ozone budget'. *J. Geophys. Res.* **103**(D22), 10727–10755. 26

Wang, P. K.: 2003, 'Moisture plumes above thunderstorm anvils and their contributions to cross-tropopause transport of water vapor in midlatitudes'. *J. Geophys. Res.* **108**(D6), doi: 10.1029/2002JD002581. 5, 86

Wang, P. K.: 2004a, 'A cloud model interpretation of jumping cirrus avove storm top'. *Geophys. Res. Lett.* **31**, L18106. doi: 10.1029/2004GL020787. 86, 87

Wang, P. K.: 2004b, 'The physical mechanism of irreversible troposphere-to-stratosphere mass transport by deep convection'. *Geophys. Res. Abstr.* **6**, 01256. SRef-Id: 1607-7962/gra/EGU04-A-01256. 86, 87

Waugh, D. W.: 1996, 'Seasonal variation of isentropic transport out of the tropical stratosphere'. *J. Geophys. Res.* **101**(D2), 4007–4023. 3

Waugh, D. W., and R. A. Plumb: 1994, 'Contour advection with surgery: A technique for investigating finescale structure in tracer transport'. *J. Atmos. Sci.* **51**(4), 530–540. 116

Waugh, D. W., R. A. Plump, J. W. Elkins, D. W. Fahey, K. A. Boering, G. S. Dutton, C. M. Volk, E. Keim, R.-S. Gao, B. C. Daube, S. C. Wofsy, M. Loewenstein, J. R. Podolske, K. R. Chan, M. H. Proffitt, K. K. Kelly, P. A. Newman, and L. R. Lait: 1997, 'Mixing of polar vortex air into middle latitudes as revealed by tracer-tracer scatterplots'. *J. Geophys. Res.* **102**(D11), 13119–13134. 65, 72

Wernli, H., and M. Bourqui: 2002, 'A Lagrangian "1-year climatology" of (deep) cross-tropopause exchange in the extratropical Northern Hemisphere'. *J. Geophys. Res.* **107**(D2), doi 10.1029/2001JD000812. 5, 6, 23, 61, 64, 80, 81, 98, 142

Wernli, H., and H. C. Davies: 1997, 'A Lagrangian-based analysis of extratropical cyclones, 1, The method and some applications'. *Quart. J. R. Met. Soc.* **123**, 467–489. 6, 17, 61, 97

Wiederhold, P. R.: 1997, *Water vapor measurements: methods and instruments*. Marcel Dekker, Inc. 58

Wienhold, F., H. Fischer, P. Hoor, V. Wagner, R. Konigstedt, G. Harris, J. Anders, R. Grisar, M. Knothe, W. Riedel, F. Lübken, and T. Schilling: 1998, 'TRISTAR - a tracer in situ TDLAS for atmospheric research'. *App. Phys. B-Lasers and Optics* **67**, 411–417. 13

Wiggins, S.: 1988, 'Stirred but not mixed'. *Nature* **333**, 395–396. 60

Winker, D. M., and M. A. Vaughan: 1994, 'Vertical distribution of clouds over Hampton, Virginia observed by lidar under the ECLIPS and FIRE ETO programs'. *Atmos. Res.* **34**, 117–133. 100

Wirth, V.: 1995, 'Diabatic heating in an axisymmetric cut-off cyclone and related stratosphere-troposphere exchange'. *Quart. J. R. Met. Soc.* **121**, 127–147. 5, 23

Wirth, V.: 2000, 'Thermal versus dynamical tropopause in upper-tropospheric balanced flow anomalies'. *Quart. J. R. Met. Soc.* **126**, 299–317. 22, 23

WMO: 1986a, 'Atmospheric Ozone 1985'. WMO Global Ozone Res. and Monit. Proj. Rep. 20. Geneva. 22, I

WMO: 1986b, 'Atmospheric Ozone, 1985: Atmospheric ozone assessment of our understanding of the processes controlling its present distribution and change.'. Rep. Vol. 1, Geneva, Switzerland. 22

WMO: 1990, 'Scientific assesment of ozone depletion: 1989'. Report No. 20, Geneva. 87

Yang, H., and K. K. Tung: 1998, 'Water vapor, surface temperature, and the greenhouse effect – A statistical analysis of tropical-mean data'. *J. Clim.* **11**, 2686–2697. 2

Zahn, A.: 2001, 'Constraints on 2-way transport across the Arctic tropopause based on O_3, stratospheric tracer (SF_6), and water vapor isotope (D,T) tracers'. *J. Atmos. Chem.* **39**(3), 303–325. 6

Zahn, A., C. A. M. Brenninkmeijer, and P. F. J. van Velthoven: 2004a, 'Passenger aircraft project CARIBIC 1997-2002, Part I: the extratropical chemical tropopause'. *Atmos. Chem. Phys. Discuss.* **4**, 1091–1117. 54

Zahn, A., C. A. M. Brenninkmeijer, and P. F. J. van Velthoven: 2004b, 'Passenger aircraft project CARIBIC 1997-2002, Part II: the ventilation of the lowermost stratosphere'. *Atmos. Chem. Phys. Discuss.* **4**, 1119–1150. 22, 28, 74, 75, 78

Zängl, G., and K. P. Hoinka: 2001, 'The tropopuase in polar regions'. *J. Clim.* **14**, 3117–3139. 23

Zierl, B., and V. Wirth: 1997, 'The influence of radiation on tropopause behaviour and stratosphere-troposphere exchange in an upper tropospheric anticyclone'. *J. Geophys. Res.* **102**(D20), 23883–23894. 5, 29

Zöger, M., A. Afchine, N. Eicke, M.-T. Gerhards, E. Klein, D. S. McKenna, U. Mörschel, U. Schmidt, V. Tan, F. Tuitjer, T. Woyke, and C. Schiller: 1999, 'Fast in situ stratospheric hygrometers: A new family of balloon-borne and airborne Lyman α photofragment fluorescence hygrometers'. *J. Geophys. Res.* **104**(D1), 1807–1816. 7, 13, 14, 137

Acknowledgements

Without the collaboration of good colleagues, without their support, also from friends and my family, I would never have reached this goal. In this place I would like to thank all the people who contributed to this work.

My first thanks are addressed to my supervisor Prof. Dr. Marin Riese (director of the ICG-I) and my adviser Dr. Cornelius Schiller (head of the group ”water vapour and long-lived trace species”) who offered me the opportunity to realise my thesis at the ICG-I of the FZJ. Most of all, I thank you for your trust in my work and the allowed freedom in pursuing scientific questions, for your always open doors and for the opportunity to contribute to interesting scientific conferences and seminars. Thanks for enabling, beneath the SPURT campaigns, my participation in a polar campaign in Kiruna and in an interesting GCC summer school in Montréal.
Martin Riese should further be mentioned for his professional guidance. Many thanks for your time to arrange multitudinous ”PhD. chats” with many interesting discussions and ”collective problem solving”.
Sincere thanks are due to Cornelius Schiller for the exceedingly amazing scientific attendance and support during the last three years. You always had time for questions and for surveying and working through numbering documents, for intensive discussions, for providing valuable advice and, ultimately, for your inexhaustible and constructive criticism and suggestions. Not least I got perfect support and back stabilization from you at every time . Especially pleasant are your familiar attitudes and your ”vis comica”.
I am equally grateful to Prof. Dr. Heini Wernli, who kindly accepted to supervise this thesis as the second examiner and enriched it with many good ideas, especially in section 6.1. I would like to thank you for the interest in my work and your contagious enthusiasm in scientific research.

I owe a debt of gratitude to Dr. Gebhard Günther. Thank you for your all time open door and mind, concerning all kinds of things, for your professional discussions and skilful assistance,

e.g. in CLaMS troubleshooting. You contributed monumentally to the ”factor of amusement”, in particular within the ”relaxing conversations”.

Earnest thanks are due to my room colleagues Nicole Spelten (the woman who I am allowed since January 2005 to sit right opposite and not ”cater-cornered”) and Alexander Mangold. I thank you for good times at the institute and your instruction into the secrets of FISH and the laboratory work as well as for the pleasant working atmosphere.
I further thank Dr. Paul Konopka for taking time to deal with my several questions and for providing scientific support. You should also be dignified for your well-done job as the ”football representative” who organised and realised an absolutely successful ICG-I playing team. Woe betide whom maintaining something else.
Thanks to Reimar Bauer for your very helpful computational advice, especially in IDL programming, to Nicole Thomas for your programming support in CLaMS, Dr. Martina Krämer for useful discussions and Dr. Susanne Rohs for taking time to proofread the thesis.
I would also like to say ”thanks” to the entire ICG-I for the pleasant working atmosphere, the kindness and very supportive cooperation.

My earnest thanks are addressed to the whole SPURT team for unforgettable collegiality and teamwork without which a project like SPURT could not be completed with such great success. Thanks for the lots of work and fun during the campaigns. Special thanks to Rolf Maser, Harald Franke and Dieter Schell of enviscope GmbH for your professional technical support and excellent organisation, and for giving at all times the maximum possible assistance in all kinds of problems.
Great thanks are due to the pilots and the GFD for the excellent operation of the Learjet 35A and the kind atmosphere in the hangar and at the barbecues.
Also ”De Aalversuper” should be mentioned for the warm atmosphere and the steady effort to provide catering for the SPURT team making it impossible to starve.

I send my best wishes and honest thanks to my whole family, my parents for giving me faith, motivation and never ending support. You always accept my ”psychological fog” and know how to deal with it. Thanks for your spiritual and moral succour, your patience and support.
Most sincere and tender thanks belong to my admirable wife, Maria, for her esprit, faith and love. I would like to thank you for all your ”motivation syringes”, for your aid and support and for being very patient during the busy weeks. I am very grateful for the humour and our marvellous times.